# Rosensweig Instability and Droplets in a Quantum Ferrofluid of Dysprosium Atoms

Von der Fakultät Mathematik und Physik der Universität Stuttgart
zur Erlangung des akademischen Grades eines Doktors der
Naturwissenschaften (Dr. rer. nat.) genehmigte Abhandlung

vorgelegt von

**Holger Markus Eberhard Kadau**

aus Backnang

| | |
|---|---|
| Hauptberichter: | Prof. Dr. Tilman Pfau |
| Mitberichter: | Prof. Dr. Martin Dressel |
| Prüfungsvorsitzender: | Prof. Dr. Hans Peter Büchler |
| Tag der mündlichen Prüfung: | 21. April 2016 |

5. Physikalisches Institut
Universität Stuttgart
2016

# Abstract

Quantum gases can act as model systems for condensed matter phenomena, especially dipolar quantum gases can exhibit spontaneous symmetry breaking owing to the long-range and anisotropic character of the interactions. In particular, a Bose-Einstein condensate with dipolar interaction can act as a quantum ferrofluid which, in analogy to a classical ferrofluid, has been predicted to exhibit a Rosensweig instability where the translational symmetry is broken and self-organized structures form. In this thesis, we experimentally observe this effect in a dipolar Bose-Einstein condensate of dysprosium atoms. This manifests itself in a transition from a superfluid to a state with ordered droplet ensembles. Prior to this work, the resulting quantum droplets were expected to collapse at the mean-field level due to an essentially attractive interaction. However, we observe them to be stable and demonstrate quantitatively that quantum fluctuations, a consequence of Heisenberg's uncertainty principle, stabilize the droplets against the expected collapse.

# List of Publications

In the framework of this thesis, the following articles have been published:

- I. Ferrier-Barbut, H. Kadau, M. Schmitt, M. Wenzel and T. Pfau, *Observation of quantum droplets in a strongly dipolar Bose gas*, Phys. Rev. Lett. **116**, 215301 (2016).
- H. Kadau, M. Schmitt, M. Wenzel, C. Wink, T. Maier, I. Ferrier-Barbut and T. Pfau, *Observing the Rosensweig instability of a quantum ferrofluid*, Nature **530**, 194-197 (2016).
- F. Fang, R. Olf, S. Wu, H. Kadau and D. M. Stamper-Kurn, *Condensing magnons in a degenerate ferromagnetic spinor Bose gas*, Phys. Rev. Lett. **116**, 095301 (2016).
- T. Maier, I. Ferrier-Barbut, H. Kadau, M. Schmitt, M. Wenzel, C. Wink, T. Pfau, K. Jachymski and P. S. Julienne, *Broad universal Feshbach resonances in a chaotic spectrum of dysprosium atoms*, Phys. Rev. A **92**, 060702(R) (2015).
- T. Maier, H. Kadau, M. Schmitt, M. Wenzel, I. Ferrier-Barbut, T. Pfau, A. Frisch, S. Baier, K. Aikawa, L. Chomaz, M. J. Mark, F. Ferlaino, C. Makrides, E. Tiesinga, A. Petrov and S. Kotochigova, *Emergence of Chaotic Scattering in Ultracold Er and Dy*, Phys. Rev. X **5**, 041029 (2015).
- T. Maier, H. Kadau, M. Schmitt, A. Griesmaier and T. Pfau, *Narrow-line magneto-optical trap for dysprosium atoms*, Optics Letters **39**, 3138 (2014).
- M. Schmitt, E. A. L. Henn, J. Billy, H. Kadau, T. Maier, A. Griesmaier and T. Pfau, *Spectroscopy of a narrow-line optical pumping transition in atomic dysprosium*, Optics Letters **38**, 637 (2013).

# Contents

# Allgemeinverständliche Zusammenfassung

Wir beschäftigen uns in dieser Arbeit mit ultrakalten Quantengasen. Diese kalten Quantengase sind ein Gaswölkchen mit tausend bis millionen Atomen nah am absoluten Temperaturnullpunkt für die in erster Linie quantenmechanische Eigenschaften wichtig sind. Die Besonderheit von solch kalten Atomen ist die einzigartige hochgenaue Kontrolle von inneren und äußeren Eigenschaften des Systems. Äußere Eigenschaften sind unter anderem elektrische und magnetische Felder sowie die Form und Tiefe der Atomfalle. Wohingegen innere Eigenschaften atomspezifische Merkmale und die Wechselwirkung zwischen mehreren Atomen sind. Es lassen sich verschiedene Wechselwirkungen zwischen den Atomen realisieren, die das Forschungsfeld von kalten Atomen sehr vielfältig macht.

Durch diese genaue Kontrolle sind Hochpräzisionsanwendungen mit solchen Quantensystemen möglich. Unter anderem lassen sich die zur Zeit genauesten Uhren der Welt bauen, die über 1000 mal genauer sind als die üblichen Caesium-Atomuhren, die die Sekunde definieren und die internationale Referenzzeit bestimmen. Uhren mit kalten Atomen haben eine Abweichung von weniger als einer Sekunde in 16 Milliarden Jahren. Als Vergleich: Unser Universum ist etwas weniger als 14 Milliarden Jahre alt. Eine weitere Hochpräzisionsanwendung ist die Bestimmung von fundamentalen Naturkonstanten, wie zum Beispiel der Gravitationskonstante und der Feinstrukturkonstante.

Ein weitere wichtige Motivation für die Erforschung kalter Atome ist, dass in Zukunft mit kalten Atomen Quantencomputer möglich sein können. Sowohl ein klassischer Computer als auch ein Quantencomputer rechnen mit Bits, also mit Einsen und Nullen. Allerdings muss bei einem Quantencomputer ein Bit nicht entweder Null oder Eins sein, wie dies für den klassischen Computer der Fall ist, sondern der Zustand eines Quanten-Bits (Qubit) ist eine Überlagerung oder Summe von Null und Eins. Durch dieses so genannte Superpositionsprinzip können bestimmte Probleme der Informatik effizienter gelöst werden. Aktuelle Versuche mit Quantencomputern können bereits erste Quantenalgorithmen mit mehreren Qubits durchführen.

Eine weitere Motivation für kalte Quantengase ist die Durchführung von Quantensimulationen. Bei Quantensimulationen werden kalte Atome als Modellsystem für kompliziertere Vielteilchensysteme wie Festkörper, Flüssigkeiten und Atomkerne genutzt. Der Vorteil von diesen Modellen mit kalten Atomen ist, dass sie typischerweise 1000-fach größer als die Atomabstände im Festkörper sind und somit direkt optisch beobachtbar sind. Quantensimulationen können helfen bisher nicht komplett verstandene Effekte, wie beispielsweise die Supraleitung, besser untersuchen zu können. Der erste Schritt in diese Richtung war die Simulation eines magnetischen Übergangs.

Auf der Suche nach neuen Modellsystemen mit quantenmechanischen Eigenschaften werden auch häufig neue unerwartete Materiezustände gefunden. Dies können außergewöhnliche Zustände mit extremen Eigenschaften sein. Einerseits können sich Teile des kalten Quantengases wie ein neues Quasiteilchen verhalten oder andererseits in einen anderen extremen Aggregatzustand übergehen und einen neuen Phasenübergang zeigen. Es gibt weitaus mehr als die drei bekannten Aggregatszustände fest, flüssig und gasförmig. Viele weitere Zustände sind eine Mischung aus diesen dreien oder haben eigenständige neue Eigenschaften. Ein ganz besonderes Beispiel ist der bisher noch nicht erzeugte Suprakristall. Es ist ein Materiezustand, der gleichzeitig fest und flüssig ist und dazu keine innere Reibung aufweist.

Motiviert durch diese Möglichkeiten, wurde im Rahmen dieser Arbeit ein ultrakaltes Quantengas aus Dysprosiumatomen erzeugt. Damit haben wir einen neuen Materiezustand gefunden, der sich ähnlich wie ein Flüssigkeitstropfen verhält. Da diese Tröpfchen nur aufgrund von Quanteneffekten existieren können, nennen wir sie *Quanten-Tröpfchen*. Wir haben diesen neuen Zustand gefunden indem wir eine sogenannte *Rosensweig-Instabilität* eingeleitet haben. Diese Rosensweig-Instabilität kannte man bisher nur von Ferrofluiden. In Zukunft könnten diese Quanten-Tröpfchen ein Modellsystem für flüssige Heliumtropfen oder Atomkerne sein.

Für die restliche Zusammenfassung gehen wir genauer auf die durchgeführten Experimente ein. Wir erklären, welche quantenmechanischen Effekte wir nutzen und welche inneren und äußeren Eigenschaften wir kontrollieren können. Wir vergleichen darüber hinaus unsere Ergebnisse aus der Quantenmechanik mit klassischen Beispielen um diese verständlicher darstellen zu können.

In der Welt der Quantenmechanik ist alles anders: Auf Längenskalen von wenigen Nanometern sind klassische Vorstellungen von Materie nicht mehr möglich. In diesem Längenbereich sind die Bausteine der Materie sowohl Welle als auch Teilchen und haben nur noch eine gewisse Wahrscheinlichkeit an einem bestimmten Ort zu sein. Diese Effekte lassen sich in ultrakalten verdünnten Gasen direkt beobachten. Hierfür werden Tausende bis Millionen Atome bis auf wenige Milliardstel Grad über dem absoluten Nullpunkt herabgekühlt. Dann sind die Atome einzeln nicht mehr unterscheidbar und vereinen sich zu einer kollektiven Materiewelle. Dieser ungewöhnliche Zustand nennt sich *Bose-Einstein-Kondensat* und verleiht dem Atomkollektiv erstaunliche Eigenschaften. Diese Materiewelle fließt als Quantenflüssigkeit ohne Viskosität - also völlig reibungsfrei - und wird deshalb Supraflüssigkeit genannt.

Wir haben eine solche Supraflüssigkeit mit starkem magnetischem Verhalten hergestellt. Es handelt sich dabei um ein Bose-Einstein-Kondensat aus Dysprosiumatomen und wir nennen es *Quanten-Ferrofluid*. Da Dysprosium das am stärksten magnetische Element im Periodensystem ist, verhält sich unsere Quantenflüssigkeit wie ein herkömmliches Ferrofluid. Ferrofluide bestehen aus unzähligen winzigen magnetischen Eisenpartikeln, die in Öl oder Wasser gelöst sind. Bereits diese Ferrofluide haben bemerkenswerte Eigenschaften. Sie werden durch ein äußeres Magnetfeld magnetisiert und können sich entsprechend der magnetischen Feldrichtung anordnen. Legt man ein starkes Magnetfeld senkrecht zu der Ferrofluidoberfläche an, wirken verschiedene Kräfte auf das Ferrofluid: die Schwerkraft, die magnetische Kraft und die Oberflächenspannung. Wenn die magnetische Kraft alle anderen Kräfte übertrifft, widerfährt die Oberfläche des Ferrofluids eine Rosensweig-Instabilität. Es bildet sich dann eine igelförmige, regelmäßige Oberflächenstruktur aus vielen Spitzen. Aus der Sicht der magnetischen Teilchen ist dieses Verhalten verständlich: Da sich Nord- und Südpol eines Magneten anziehen, ist es für die Teilchen energetisch vorteilhaft sich entlang der Feldrichtung anzuordnen und somit Spitzen auf der zuvor glatten Oberfläche zu erzeugen. Im Quanten-Ferrofluid übernehmen die Dysprosiumatome die Rolle der Eisenteilchen als winzige atomare Magnete.

Für unsere Untersuchungen haben wir ein pfannkuchenförmiges Wölkchen aus etwa 15.000 Dysprosiumatomen in einer optischen Atomfalle hergestellt. Wir legten ein Magnetfeld an und richteten somit die atomaren Magnete senkrecht zur Pfannkuchenebene aus. In unserem Quanten-Ferrofluid wirken auch verschiedene innere und äußere Kräfte wie bei einem Ferrofluid. Von außen werden die Atome von der optischen Falle gefangen und innere Kräfte sind atomare Wechselwirkungen. Zusätzlich zu der magnetischen Wechselwirkung gibt es noch eine abstoßende Kontaktwechselwirkung zwischen den Atomen. Diese abstoßende Kraft konnten wir präzise verringern und verursachten damit eine magnetische Instabilität. Wir beobachteten, wie bei einer Rosensweig-Instabilität von Ferrofluiden, das Auftreten von geordneten Kristallstrukturen. Diese Strukturen setzen sich aus mikroskopischen Tröpfchen zusammen. Die Tröpfchen haben jeweils Ausmaße kleiner als 1 $\mu$m und ihre Existenz wurde nach dem bisherigen Kenntnisstand nicht für möglich gehalten.

Durch weitere Untersuchungen der Quantentröpfchen haben wir starke Anzeichen, dass *Quantenfluktuationen*, die durch die Heisenberg'sche Unschärferelation hervorgerufen werden, eine entscheidende Rolle für die Stabilität dieser Quantenmaterie spielen. Wir konnten den Ursprung der Stabilität herausfinden, indem wir die Tröpfchen in einer optischen Pinzette einzeln getrennt haben. Dadurch konnten wir die Eigenschaften einzelner Quantentröpfchen untersuchen und ihre inneren Kräfte variieren. Das Verhalten der Tröpfchen entspricht den Erwartungen von theoretischen Modellen, die Quantenfluktuationen einbeziehen. Dies bedeutet auch, dass wir erstmals einen Materiezustand gefunden haben, der nur aufgrund von Quantenfluktuationen existieren kann.

Diese Quantenfluktuationen ermöglichen einen einzigartigen Materiezustand, in dem gegensätzliche Eigenschaften von Gasen, Kristallen und Suprafl üssigkeiten verbunden werden konnten. Diese Verknüpfung könnte ein erster Schritt zu einem sogenannten Suprakristall sein, ein räumlich geordneter Festkörper mit suprafluiden Eigenschaften.

# 1. Introduction

Physical substances exist in distinct forms, so-called *states of matter*, that have well-defined physical properties. In every day life we experience four states of matter: solids, liquids, gases and plasmas. These classical states are connected by *phase transitions* when the substance moves from one state to another under specific physical conditions. For example, by increasing the temperature of a solid, the matter gains thermal energy and becomes more excited and active. If this energy overcomes the inter-particle forces that hold the atoms together, the solid melts and undergoes a phase transition to a liquid, where the characteristic order of a solid is abruptly lost.

However, under extreme physical conditions there exists many other states of matter, often in situations with extremely cold temperatures, extremely high density, extreme pressures or extremely high energy. In the framework of this thesis, we investigate dilute gases of extremely cold atoms, meaning temperatures as close as possible to the absolute zero. Such *ultracold atoms* are typically a few billionth of a degree above absolute zero and are governed by the rules of quantum mechanics. In these *quantum gases* a new state of matter, a *Bose-Einstein condensate*, has been discovered for bosonic alkali atoms in 1995 [1–3]. In a Bose-Einstein condensate (BEC), all atoms occupy the same lowest energy quantum state and cumulate to a single quantum matter wave.

From then on, the field of atomic physics witnessed an enormous increase in the number of groups working on ultracold gases. Some of the early demonstrated important BEC properties are matter-wave interference [4] or the generally accepted proof of superfluidity with quantum vortices [5]. Though, what makes quantum gases truly fascinating are inter-particle interactions. Although quantum gases are dilute, interactions play a dominant role and can strongly change the many-body properties [6]. Early studies focussed on the short-range *contact interaction.* The strength of this contact interaction is characterized by a single parameter: the *scattering length* $a$. This scattering length can be magnetically tuned at will with so-called Feshbach resonances [7, 8]. These Feshbach resonances were used to create molecular BECs [9–11] from fermionic quantum gases [12] and investigate their crossover to a Bardeen-Cooper-Schrieffer BCS-type superfluid [13] or to observe the universal trimer Efimov bound states [14].

Moreover, the external confinement for ultracold quantum gases can be modified to various geometries. This offers also the possibility to use optical lattices [15, 16] to mimic solid state physics. Two famous examples that successfully showed condensed matter behaviour are the superfluid to Mott insulator transition [17] and atoms manifesting the Anderson localization [18, 19]. Recent technical advances even allowed to detect single atoms in optical lattices with optical microscope objectives [20, 21]. With this high control on internal and external properties including the excellent detection methods, it was possible to simulate a magnetic phase transition [22]. This trend to perform *quantum simulations* with high control on internal and external properties [23, 24] as well as to engineer exotic quantum systems that can lead to new states of matter, drives much of the fundamental research in the field of ultracold atoms.

All the achievements mentioned above, were investigated with alkali elements (Li, Na, K, Rb, Cs) that feature only an isotropic short-range atomic interaction. In 2005 the experimental realization of chromium BECs [25] opened the door to the investigation of strong inter-atomic magnetic dipole-dipole interactions in a quantum gas. In strong contrast to the contact interaction, the dipolar interaction is anisotropic and long-range and allows to study fundamentally different phenomena compared to experiments with alkali elements. This dipolar interaction in ultracold gases has attracted a lot of attention, both experimentally and theoretically [26–28]. For ultracold dipolar systems, exotic states of matter have been proposed, including the elusive supersolid state. This state of matter unites properties of solids and superfluids [29, 30]. Self-organized ground states have been predicted [31, 32], that are related to a non-monotonically increasing excitation spectrum displaying a roton minimum [33], similar to the one observed in superfluid helium [34].

Early experimental studies with chromium BECs [25, 35, 36] in Stuttgart and Paris have developed the basic principles of dipolar quantum gases. In particular the dipolar interaction manifests itself in an anisotropic response to external magnetic fields. The ultracold samples have displayed magnetostriction with an elongation along the field direction [36–38] that also modifies the stability criterion of dipolar BECs [39, 40]. If it becomes unstable it exhibits a dynamic collapse that can show a d-wave symmetry [41–43]. Another effect of the anisotropic dipolar interaction is the coupling of the spin degree of freedom to the orbital angular momentum, hence, dipolar collisions do not conserve magnetic quantum numbers [44, 45]. This effect has been used to successfully cool a chromium cloud using demagnetization cooling [46]. The spin relaxation was also observed as an important effect of spinor physics with dipolar BECs [47, 48] as well as for atoms in an optical lattice [49–52]. Last for chromium atoms, the dipolar interaction anisotropically modifies collective mode frequencies [53] and the excitation spectrum [54].

In the last few years plenty of other dipolar systems became available. Dipolar effects are possible for BECs with Rydberg atoms [55, 56] or heteronuclear molecule gases [57] that both present electric dipole moments. Up to date only diatomic molecules composed of alkali atoms are available at ultracold temperatures. In detail these are the two fermionic molecules $^{40}$K$^{87}$Rb [58–60] and $^{23}$Na$^{40}$K [61] and the bosonic molecules $^{7}$Li$^{133}$Cs [62], $^{41}$K$^{87}$Rb [63], $^{85}$Rb$^{133}$Cs [64], $^{87}$Rb$^{133}$Cs [65, 66] and very recently $^{23}$Na$^{87}$Rb [67]. The molecule $^{40}$K$^{87}$Rb was already trapped in an optical lattice and realized a lattice spin model [68]. Besides, weak dipolar effects have even been observed with alkali metals by carefully tuning the contact interaction to vanishing strength [69, 70] or with investigations in spinor gases [71, 72].

Furthermore, the family of magnetic dipolar quantum gases has been extended by two lanthanides: erbium [73, 74] and dysprosium [75, 76]. Both elements exhibit even stronger magnetic dipolar interactions than chromium atoms and have already proven their superiority. For both elements, quantum gases of bosonic and fermionic atoms were created thanks to universal dipolar scattering [77]. Both elements present a dense chaotic spectrum of Feshbach resonances [78, 79] with the possibility to create magnetic molecules [80, 81]. Very recently erbium atoms were trapped in an optical lattice and have shown dipolar interaction to neighbouring lattice sites [82]. For dipolar fermions the anisotropic character of the interaction deformed the Fermi surface [83] and modified the elastic scattering process [84], while Fermi degeneracy allowed, through the Pauli exclusion principle, to control the inelastic processes [85].

### This thesis

In Stuttgart the first dipolar quantum gas was achieved in 2005, followed by the investigation of many fascinating phenomena. However, the range of achievable physics was limited due to fundamental properties of the element chromium and a detection with poor optical resolution. Beginning of 2012, we switched from the element chromium to dysprosium and started to build a new generation apparatus with state of the art experimental tools. With this apparatus we were able to generate a new exotic state of matter, a liquid-like quantum droplet, that is only possible as a consequence of quantum fluctuations.

This thesis introduces in chapter 2 the theory on quantum gases and describes the two apparent inter-particle interactions. These are first the short-range contact interaction and second the long-range dipolar interaction. We introduce a mean-field model to describe dipolar BECs and give two approximations to derive the properties of condensates.

In the third chapter, we describe our new generation apparatus to create dysprosium quantum gases. We shortly mention the cooling methods used and describe the technical tools employed to tune and detect internal parameters. First, we can carefully tune the strength of the contact interaction with a Feshbach resonance. This requires a stable, repeatable magnetic field control. Second, we use a microscope objective that allows to detect the condensate properties *in situ* with a spatial resolution of $1\,\mu$m. This is a unique feature for dipolar quantum gases and allowed the discovery of the new state of matter. The creation and behaviour of this state is very similar to a classical ferrofluid.

Thus, in chapter 4 we compare a classical ferrofluid with a dipolar condensate, that is a *quantum ferrofluid* with superfluid properties. We show that a classical as well as a quantum ferrofluid present a magnetically induced instability: the *Rosensweig instability* and the *roton instability* respectively. For a Rosensweig instability, the surface of a classical ferrofluid surface forms a regular pattern of peaks and valleys [86].

Indeed, we observed the Rosensweig instability also for a quantum ferrofluid in chapter 5 [87]. Surprisingly, we detected stable droplet ensembles, that were theoretically not predicted prior to this work. Each microscopic droplet has a radial size smaller than our resolution limit of $1\,\mu$m. We propose quantum fluctuations as the stabilizing mechanism for our new state of matter.

Finally in chapter 6, we show the distinct evidence that quantum fluctuations stabilize our droplet state [88]. Additionally, we prove that this liquid-like *quantum droplet* is self-confining for relaxed confinement and remains superfluid as we observe matter-wave interference. Thus, this quantum droplet might be a first step to a supersolid state or a quantum model system for superfluid helium droplets or atomic nuclei.

# 2. Dipolar Quantum Gases

The description of dipolar quantum gases requires theoretical notions from quantum mechanics, quantum statistics, atomic physics and classical electrodynamics. A quantum statistical treatment reveals the existence of the Bose-Einstein condensed state, while atomic physics provides the microscopic details about its constituents as well as the tools to create and manipulate it. Finally, the interaction existing between two dipoles results from the laws of classical electrodynamics. Hence, this chapter is a short summary and not an in-depth look at the subject of dipolar quantum gases.

We start this chapter with an overview on degenerate quantum gases and Bose-Einstein condensation. In the following, we give a short introduction[1] to inter-particle interactions and the resulting scattering theory. We first show that Van-der-Waals interactions can be reduced in the ultracold regime to a short-range interaction described with a single parameter, the scattering length $a$. Next, we characterize a second inter-particle interaction: the long-range and anisotropic dipole-dipole interaction. Finally, we combine condensation and inter-particle interactions in a mean-field model resulting in the Gross-Pitaevskii equation (GPE). For this GPE, we present two approximations with analytic feasible solutions to reveal the basic properties of Bose-Einstein condensates.

## 2.1. Bose-Einstein condensation: a superfluid state

The transformation of a thermodynamic system from one phase of matter to another one is called a *phase transition*. During a phase transition certain system properties change discontinuously and often involve a symmetry breaking process. Popular examples are the freezing and evaporation of liquids as a result of a change in temperature. Most transitions are governed by microscopic particle interactions that influence macroscopic phenomena to reach the systems lowest energy.

However, there exists a unique phase transition that can occur in the absence of interactions, but requires quantum statistics: *Bose-Einstein condensation*. In 1924 Bose predicted this phase transition for photons [90] and Einstein extended the work for a gas of non-interacting, massive bosons [91, 92]. They concluded that for a dense and cold enough sample a macroscopic number of particles occupies one single-particle state, resulting in a new form of matter. This state is in many systems the zero-momentum state and nowadays this new phase of matter is called a *Bose-Einstein condensate* (BEC). Such BECs exhibit quantum mechanical effects determining macroscopic phenomena of the many-particle system.

---

[1] For further details, we refer to a thorough review given in [89].

A qualitative explanation at which conditions quantum mechanical effects start to dominate is depicted in figure 2.1a and goes as follows. The quantum-mechanical description associates wave-like attributes to matter. The quantitative relation between a massive particle and the associated wave aspects is given by the de-Broglie wavelength $\lambda_{\mathrm{dB}} = 2\pi\hbar/p$, where $p$ is the particle momentum and $\hbar = h/2\pi$ the reduced Planck constant [93]. For a many-body sample in thermal equilibrium at temperature $T$ the momentum is $p \propto \sqrt{mk_{\mathrm{B}}T}$ with $m$ the particle mass and $k_{\mathrm{B}}$ the Boltzmann constant. If the resulting thermal de-Broglie wavelength $\lambda_{\mathrm{dB}} = \sqrt{2\pi\hbar^2/mk_{\mathrm{B}}T}$ is large compared to the characteristic length scale of the problem, the particles have to be treated as *matter waves* and obey the rules of quantum mechanics. In the case of a many-particle system the characteristic length is given by the inter-particle distance $n^{-1/3}$, where $n$ is the particle density. Combining these considerations, we find that the condition for the emergence of quantum mechanical effects (or coherent many-body effects) is[2]

$$k_{\mathrm{B}}T \lesssim \frac{\hbar^2 n^{2/3}}{m}\,. \tag{2.1}$$

When quantum mechanics emerge for indistinguishable particles that are allowed to occupy the same particle state, quantum statistics play a dominant role. Degenerate particles in the same state experience the exchange interaction[3] [96, 97], that leads to an effective attraction of bosons. Therefore, we concentrate in this thesis on *quantum fluids* [98], involving liquids and gases[4]. We will present detailed fluid mechanics concerning our system in chapter 4.

To observe quantum effects for typical liquids with particle densities of $n \approx 10^{28}\,\mathrm{m}^{-3}$ the temperature has to be on the order of $10\,\mathrm{K}/A$ with $A$ the mass number. Indeed, liquid helium ($^4$He) shows a phase transition at $T = 2.17\,\mathrm{K}$ at saturated vapour pressure and was first observed in 1937 [99, 100]. Below this so-called $\lambda$-point the liquid has two components: a normal one and a superfluid one characterised by a zero viscosity [101]. After the connection between superfluidity to Bose-Einstein condensation in 1938 [102, 103], superfluid helium was considered as the prototype of BECs.

However, every liquid exhibits strong inter-particle interactions. Such strong interactions push particles out of the zero-momentum state and even at absolute zero temperature particles with non-zero momenta are present, although the superfluid fraction is unity. As we shall see later in chapter 5 and 6, this effect is related to the so-called *quantum fluctuations*. One major step was the generalization of Bose-Einstein condensation to interacting systems in 1956 [104, 105]. It was then possible to estimate theoretically the condensed fraction of superfluid helium to be 8 % [104] and the recent measured value with neutron scattering gives a condensed fraction of 7 % [106]. Hence, liquid helium established

---

[2] This condition, only using simple connections, is remarkably close to the full analysis [94, 95] that gives a critical temperature of $k_{\mathrm{B}}T_{\mathrm{c}} = \frac{2\pi}{\zeta(3/2)^{3/2}}\frac{\hbar^2 n^{2/3}}{m} \approx 3.31\frac{\hbar^2 n^{2/3}}{m}$ with $\zeta(x)$ the Riemann zeta function.

[3] The exchange interaction is a quantum mechanical effect that can only occur between identical particles. For fermions, the exchange interaction is called Pauli repulsion.

[4] In most crystalline solids this exchange of neighbouring atoms and the effects of indistinguishability vanish, and hence quantum statistics are negligible [98, p. 2].

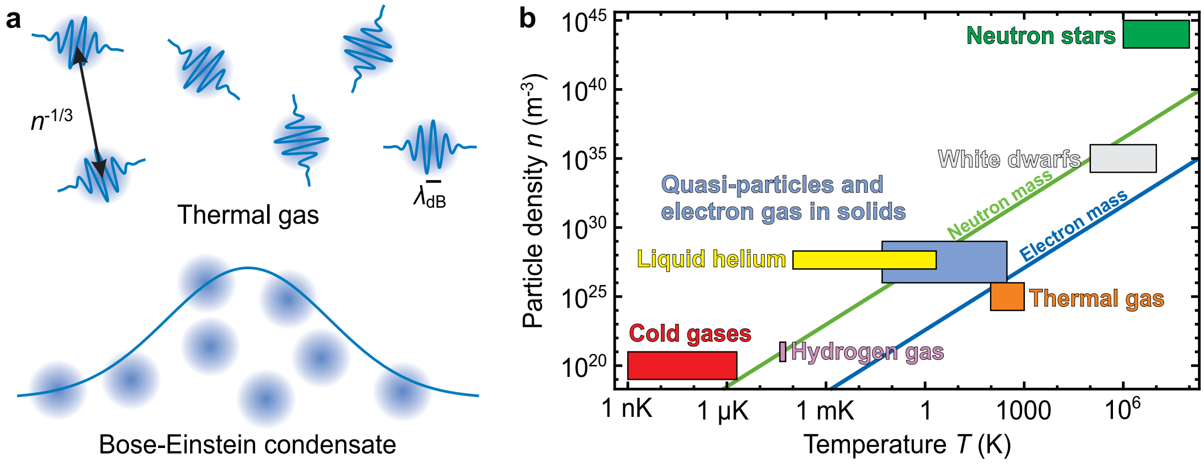

**Fig. 2.1. Degeneracy in quantum fluids.** **a**, Simple image of the phase transition from a thermal gas to a quantum degenerate Bose-Einstein condensate. Important length scales for the system are the particle distance $n^{-1/3}$ and the thermal de-Broglie wavelength $\lambda_{\mathrm{dB}}$. Further explanation is given in the text. **b**, Summary of quantum-degenerate systems and their particle densities and temperatures. Systems with degenerate electrons are above the blue line, which is satisfied for white dwarfs [138] as for quasi-particles and the electron gas in solids. Whereas systems with degenerate atoms or neutrons have to be at least above the green line. This is fulfilled for neutron stars [139], liquid helium [140] and neutral atomic gases as cold as $T \approx 1\,\mathrm{nK}$ [141, 142].

the fundament of quantum fluids, but the reduced occupancy of the zero-momentum state in liquids made it prohibitively difficult to study Bose-Einstein condensation in details.

A superior system would be ultracold gases with reduced inter-particle interactions. The quest for gaseous BECs started in the 1980s when laser cooling and trapping of neutral atoms [107] have been developed (cooling and trapping methods are described in chapter 3). By now, quantum degeneracy has been achieved for several neutral atomic species[5] with typical densities of $n \approx 10^{19} - 10^{21}\,\mathrm{m}^{-3}$ and typical temperatures of $T \approx 50\,\mathrm{nK} - 2\,\mu\mathrm{K}$. In this thesis we use dysprosium atoms ($^{164}$Dy) with an atomic density of $n \approx 10^{20}\,\mathrm{m}^{-3}$ in the BEC phase and cool the atoms as low as $T \approx 70\,\mathrm{nK}$. One should mention that most of these BECs, including ours, are metastable[6], as their true equilibrium state at low temperatures is either liquid or solid. However, the extremely low densities (as comparison the density of air is $n \approx 10^{25}\,\mathrm{m}^{-3}$) suppress the creation rate of molecular states and the subsequent dense equilibrium state.

BECs have also been achieved for quasi-particles with low effective mass at higher temperatures, up to room temperature. Such (quasi-)particles are magnons [143, 144], excitons [145], polaritons [146, 147] and photons [148]. In Figure 2.1b we present a summary of degenerate quantum systems, both bosonic and fermionic.

---

[5] Condensed atomic isotopes: $^{1}$H [108], $^{4}$He* [109, 110], $^{7}$Li [3, 111], $^{23}$Na [2], $^{39}$K [112], $^{41}$K [113], $^{40}$Ca [114], $^{52}$Cr [25], $^{85}$Rb [115], $^{87}$Rb [1], $^{84}$Sr [116, 117], $^{86}$Sr [118], $^{88}$Sr [119], $^{133}$Cs [120], $^{160}$Dy [121], $^{162}$Dy [121], $^{164}$Dy [75], $^{166}$Er [122], $^{168}$Er [73], $^{170}$Er [122], $^{168}$Yb [123], $^{170}$Yb [124], $^{174}$Yb [125], $^{176}$Yb [126]. To complete the atomic list, we mention degenerate Fermi gases: $^{3}$He [127], $^{6}$Li [128, 129], $^{40}$K [12], $^{53}$Cr [130], $^{87}$Sr [131, 132], $^{161}$Dy [76], $^{167}$Er [74], $^{171}$Yb [133], $^{173}$Yb [134].
These fermions can be bound to molecules and form a molecular BEC: $^{6}$Li$_2$ [9, 10], $^{40}$K$_2$ [11].

[6] The only exception is spin-polarized hydrogen, as there exists no triplet bound state [108, 135–137].

## 2.2. Two-body interactions

In the previous section, we mentioned the extremely low densities of ultracold gases to prevent clustering of atoms. Hence, one might expect that inter-particle interactions are insignificant. Despite the diluteness of cold gases, two-body interactions determine fundamental properties of BECs, such as density profile, ground state energy and collective oscillation frequencies. Actually, it is even possible to prepare strongly correlated systems with cold gases [6]. In the following, we discuss aspects of the two-body interactions relevant to the description of a dipolar BEC, which are the isotropic, short-range contact interaction and the anisotropic, long-range dipole-dipole interaction.

### 2.2.1. Short-range contact interaction

At small separations $\boldsymbol{r}$ between two atoms, several interactions contribute to the interaction potential $U(\boldsymbol{r})$ between them. For small distances the electron shells around each atom start to overlap and the strong electrostatic and Pauli repulsion keeps atoms apart. While at larger distances electric induced-dipole-dipole interactions lead to an attractive interaction, known as the *van der Waals interaction* that scales as $-C_6/r^6$ with the element-dependent van der Waals coefficient $C_6$. These forces balance each other at a typical separation which corresponds to the equilibrium distance of bound diatomic molecules. This interatomic potential is called molecular potential and is sketched in figure 2.2b,c.

The molecular potential typically has a depth that corresponds to temperatures higher than 1000 K. This indicates again that a cold atomic gas is not the true ground state of the system, as the energetic minimum is reached with bound molecular states. But at low temperatures the molecule formation is dominated by three-body recombinations [149]. In the considered dilute systems, such inelastic three-body collisions are rare but the elastic two-body collision rates are sufficient to maintain thermal equilibrium. Thus, two-body collisions play a crucial role in the realization of BECs and their fundamental properties.

To make a rough estimate of the molecular interaction range, we estimate it for particles with zero energy by dimensional arguments. If two particles approach a separation $r_0$ they gain the kinetic energy $\Delta p^2/2m_{\mathrm{red}} = C_6/r_0^6$, with $m_{\mathrm{red}}$ the reduced mass. By using the Heisenberg's uncertainty principle $\Delta p \approx \hbar/\Delta x$ with $\Delta x = r_0$, we obtain for typical van der Waals coefficients[7] an interaction range of $r_0 \approx 100\, a_0$ with $a_0$ the Bohr radius. This interaction range is typically much smaller than the mean inter-particle distance for dilute atomic gases of $n^{-1/3} \approx 4000\, a_0$. Therefore, ultracold gases are composed of freely moving atoms that do not interact, except when approaching another atom closer than $r_0$ to collide elastically. This means for the scattering theory that each collision perturbs the atomic wave function only by a small amount. Hence, for only calculating the asymptotic scattering behaviour, it is not crucial to know the exact molecular potential. Following this idea, the molecular potential may be simplified with a so-called *two-body pseudo potential* that yields the same scattering properties.

---

[7] The interaction range reads finally $r_0 = (2m_{\mathrm{red}}C_6/\hbar^2)^{1/4}$ and by using the van der Waals coefficient for dysprosium atoms $C_6^{\mathrm{Dy}} = 2003\, E_{\mathrm{h}} a_0^6$ [79] (with $E_{\mathrm{h}}$ the Hartree energy) we get a range of $r_0^{\mathrm{Dy}} = 156\, a_0$.

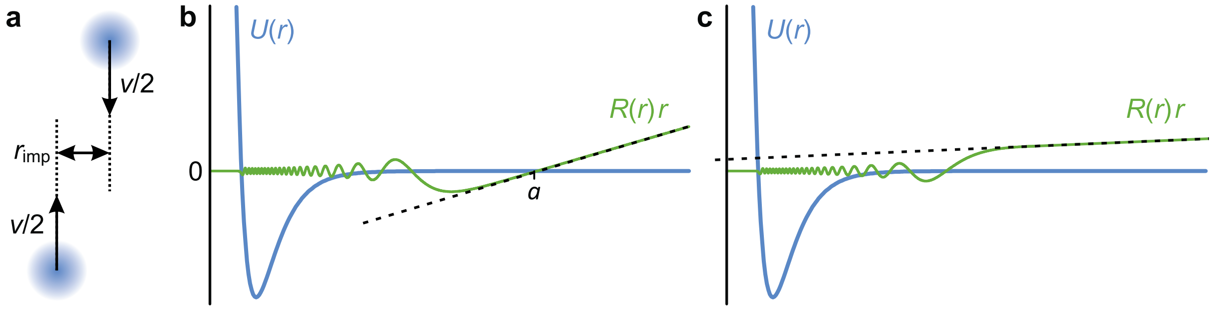

**Fig. 2.2. Scattering of two neutral atoms. a**, Two colliding atoms with relative velocity $v$ in their center of mass frame. The impact parameter $r_{\text{imp}}$ determines their relative angular momentum. **b**,**c**, Molecular potential $U(r)$ (blue line) and its radial wave function $R(r)r$ (green line) for zero energy. The extrapolation of the wave function from large $r$ is drawn as dashed line that crosses the horizontal $r$-axis at the scattering length $a$. Slightly different potentials can result in a positive (**b**) or a negative (**c**) scattering length $a$. Adapted from [150].

To get insight into the properties and symmetries needed for such pseudo potentials, we consider the simple case of two colliding particles in the center of mass frame [151], see figure 2.2a. This pair moves with a relative velocity $v$ and the impact parameter $r_{\text{imp}}$, resulting to the relative angular momentum $\hbar l \simeq r_{\text{imp}} m_{\text{red}} v$ with $l$ the quantum number of the relative angular momentum. At low temperatures, we may express the relative velocity with the de-Broglie wavelength $\lambda_{\text{dB}} = 2\pi\hbar/m_{\text{red}}v$. For a collision to happen, the impact parameter $r_{\text{imp}}$ has to be less than the interaction range $r_0$. Thus, we find the condition for the angular momentum $l \leq 2\pi r_0/\lambda_{\text{dB}}$. As discussed in section 2.1 the de-Broglie wavelength for BECs is much larger than the interaction range and as the relative angular momentum $l$ is quantized, the only solution possible is $l = 0$. In this zero angular momentum regime, independent of the actual interaction potential, the scattered wave function is a spherical wave or a so-called *s-wave*.

Evidently, we can replace the interaction potential by a spherical pseudo potential. The simplest pseudo potential describing the isotropic two-body short-range interaction is

$$U_{\text{contact}}(\boldsymbol{r}) = g\,\delta(\boldsymbol{r}) = \frac{4\pi\hbar^2 a}{m}\,\delta(\boldsymbol{r}) \tag{2.2}$$

with $\delta(\boldsymbol{r})$ the Dirac delta function, $g$ the so-called *contact coupling strength*, that is only dependent on the *s-wave scattering length* $a$. A positive scattering length $a$ means a repulsive potential, while negative $a$ represents an attractive one. The value of the scattering length $a$ can be traced back to the real molecular potential $U(r)$. When numerically calculating the wave function of the molecular potential for zero energy, the wave function shows many oscillations for $r < r_0$. But for large distances $r > r_0$ the intercept of the asymptotic wave function on the $r$-axis restores the scattering length $a$, as shown in figure 2.2b. The parameter $a$ is very large (negative or positive) when the last molecular state (virtual state or bound state) of the specific potential is close to zero energy (figure 2.2c shows the case of a virtual state above zero energy) [152]. The dependence of $a$ on molecular states is more discussed in section 3.3.1 on Feshbach resonances.

### 2.2.2. Long-range dipole-dipole interaction

Ultracold quantum gases in the degenerate regime have been achieved for many different elements[5] and most phenomena can be explained with solely including the short-range contact interaction of section 2.2.1. Though, a few successfully cooled atomic species feature further non-negligible inter-particle interactions. These are the three elements chromium, erbium and dysprosium each with a strong magnetic dipole moment $\mu_\mathrm{m}$ of $6\,\mu_\mathrm{B}$, $7\,\mu_\mathrm{B}$ and $10\,\mu_\mathrm{B}$, where $\mu_\mathrm{B}$ is the Bohr magneton. Dipolar interactions can result in unusual effects for BECs, that gained large interest in the field of atomic physics [26–28]. We now introduce the dipole-dipole interaction available in dipolar quantum gases.

In the presence of an external magnetic field $\boldsymbol{B}$, the magnetic dipoles align in the same direction $z$ such that the sample gets polarized, as depicted in figure 2.3a. For two aligned dipoles the *dipole-dipole interaction potential* reads

$$U_\mathrm{dd}(\boldsymbol{r}) = \frac{\mu_0 \mu_\mathrm{m}^2}{4\pi} \frac{1 - 3\cos^2\vartheta}{r^3}, \tag{2.3}$$

with $\mu_0$ the vacuum permeability and $\vartheta$ the angle between the polarization direction $\boldsymbol{\mu}_\mathrm{m}$ and the relative position $\boldsymbol{r}$ of the dipoles. The dipole-dipole interaction has two main properties: it is long-range and anisotropic. The latter anisotropic character is illustrated in figure 2.3b and evidently depends on the relative position of the two dipoles, which can be easily seen in two limiting cases. The interaction potential is attractive for a head-to-tail configuration ($\vartheta = 0°$), while it is repulsive in a side-by-side configuration ($\vartheta = 90°$).

The long-range character implies that the systems interaction energy depends on global system properties, such as the total atom number. Contrary, the short-range interaction energy depends only on local properties, such as the local density. To quantify this statement and define the long-range character of interactions, we test the convergence of the interaction energy for large distances [153]. For this we consider the potential energy for a single particle in the center of a sphere of radius $R$ with homogeneously distributed particles with density $n$. We further assume the interaction potential to be proportional to $1/r^\alpha$ with $\alpha$ the defining parameter for the interaction range. We obtain for the single particle in a three-dimensional sphere with constant density the interaction energy

$$E_\odot = \int_b^R 4\pi r^2\, n \frac{1}{r^\alpha}\, \mathrm{d}r \propto \left[r^{3-\alpha}\right]_b^R \tag{2.4}$$

with $b$ being a small but finite cut-off radius. For increasing radius $R$, hence increasing the volume of the sphere, the volume contribution to the energy can be neglected when $\alpha > 3$, but diverges if $\alpha \leq 3$. We define the latter case to be long-range potentials, as global parameters such as the size are important. Hence, the dipolar interaction is long-range in three dimensions[8].

As the interaction range is not finite anymore, in principle all partial waves with angular momenta $l > 0$ contribute to the scattering process. This forbids the possibility to describe

---

[8] This definition can be generalized to systems with $D$ dimensions in the same manner. Accordingly the interaction is called long-range if the interaction fulfils $\alpha/D \leq 1$.

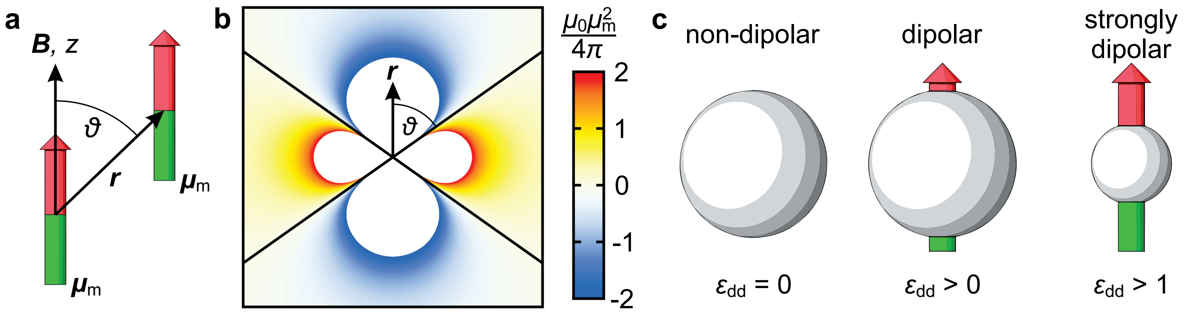

**Fig. 2.3. Dipole-dipole interaction.** **a**, Two dipoles with magnetic moment $\boldsymbol{\mu}_\mathrm{m}$ are polarized by an external magnetic field $\boldsymbol{B}$ along the $z$-direction. The dipole-dipole interaction is dependent on the separation $\boldsymbol{r}$ and the angle $\vartheta = \measuredangle(\boldsymbol{\mu}_\mathrm{m}, \boldsymbol{r})$. **b**, The dipole-dipole interaction potential showing its anisotropic character. Regions with attractive character (negative potential) are drawn blue, while repulsive ones (positive potential) are yellow and red. The black lines depict the angle with zero interaction. The central white region is due to a cutoff of the potential at $\pm 2\mu_0\mu_\mathrm{m}^2/4\pi$. **c**, Illustration of the inter-particle interactions. A non-dipolar BEC consists of atoms that can be seen as hard spheres with the scattering length $a$ as radius. A dipolar BEC includes an additional atomic magnetic moment and we specify it to be strongly dipolar for $\varepsilon_\mathrm{dd} > 1$.

the scattering correctly with a short-range pseudo potential [154], as done in section 2.2.1 for the molecular potential. Nevertheless, for low enough scattering energies, the dipolar scattering can be approximated to be universal and scatters only into s-wave channels [77, 155]. Additionally, the anisotropy of the potential couples orbital angular momentum with spin angular momentum. This results in state-changing collisions, called dipolar relaxation [44].

For further discussion of different dipolar systems, it is convenient to define various parameters to quantify the strength of the dipolar interaction. Similar to the scattering length $a$ for the contact interaction, we introduce the *characteristic dipolar length*

$$a_\mathrm{dd} = \frac{\mu_0 \mu_\mathrm{m}^2 m}{12\pi\hbar^2} \tag{2.5}$$

and the *dipolar coupling strength*

$$g_\mathrm{dd} = \frac{4\pi\hbar^2 a_\mathrm{dd}}{m} = \frac{\mu_0\mu_\mathrm{m}^2}{3}\,. \tag{2.6}$$

The numerical factors are chosen such that a three-dimensional, homogeneous dipolar condensate becomes unstable for $a_\mathrm{dd} > a$, as shown in section 4.4.2. The ratio of dipolar and contact coupling strength is defined as *relative dipolar strength*

$$\varepsilon_\mathrm{dd} = \frac{g_\mathrm{dd}}{g} = \frac{a_\mathrm{dd}}{a} = \frac{\mu_0\mu_\mathrm{m}^2 m}{12\pi\hbar^2 a}\,. \tag{2.7}$$

This interplay of both interactions is shown as a simple illustration in figure 2.3c with the contact interaction pictured as hard spheres.

Unusual effects in dipolar gases are mainly predicted for dominating dipolar interaction in the strongly dipolar regime, meaning $\varepsilon_{\mathrm{dd}} > 1$. In table 2.1, we mention the parameters quantifying the interaction strength for different atomic species. Only the two isotopes of dysprosium $^{162}$Dy and $^{164}$Dy are in the strongly dipolar regime. However, so-called Feshbach resonances are an important tool to tune the contact interaction and manipulate the scattering length $a$ [8], as described later in section 3.3.1. With this technique even condensates of chromium atoms could reach the strongly dipolar regime by decreasing the contact interaction strength [36].

To conclude this section on inter-particle interactions, the full binary pseudo potential of contact and dipolar interaction, that is used in the following sections to describe the many-body behaviour of condensates, reads

$$U_{\mathrm{int}}(\boldsymbol{r}) = g\,\delta(\boldsymbol{r}) + \frac{3}{4\pi} g_{\mathrm{dd}} \frac{1 - 3\cos^2\vartheta}{r^3}\,. \tag{2.8}$$

## 2.3. Mean-field description of dipolar gases

In the previous section the two-body interactions were introduced, namely the isotropic short-range contact interaction and the anisotropic long-range dipole-dipole interaction. In this section we give a description of interacting Bose-Einstein condensates, that consist typically of more than 10,000 atoms. This description requires a many-body theory of a complex system where each particle interacts with all others. Such many-body systems with interactions are in general difficult to solve exactly. A simple approximation is the so-called mean-field theory, where the effect of all inter-particle interactions on a test particle is averaged to an effective mean field. This reduces the many-body-problem to a single particle problem with mean-field interaction potentials.

In this section we present the mean-field model of dipolar quantum gases and obtain the Gross-Pitaevskii equation. This equation is a nonlinear, partial differential equation and needs further approximation to be solved analytically. We demonstrate two easy approaches: the variational method and the Thomas-Fermi approximation.

### 2.3.1. Gross-Pitaevskii equation

The fundamental starting point for a many-body problem is the description in second quantization. The many-body Hamiltonian for $N$ interacting bosons confined by an external potential $V_{\mathrm{ext}}$ is given by [158]

$$\begin{aligned} \hat{H} = &\int \mathrm{d}^3 r\, \hat{\Psi}^\dagger(\boldsymbol{r}) \left( -\frac{\hbar^2 \nabla^2}{2m} + V_{\mathrm{ext}}(\boldsymbol{r}) \right) \hat{\Psi}(\boldsymbol{r}) \\ &+ \frac{1}{2} \int \mathrm{d}^3 r\, \mathrm{d}^3 r'\, \hat{\Psi}^\dagger(\boldsymbol{r}) \hat{\Psi}^\dagger(\boldsymbol{r}') U_{\mathrm{int}}(\boldsymbol{r} - \boldsymbol{r}') \hat{\Psi}(\boldsymbol{r}') \hat{\Psi}(\boldsymbol{r})\,, \end{aligned} \tag{2.9}$$

where $\hat{\Psi}^\dagger(\boldsymbol{r})$ and $\hat{\Psi}(\boldsymbol{r})$ are the bosonic field operators that create and annihilate a particle at position $\boldsymbol{r}$ and fulfil the normalization $N = \int \mathrm{d}^3 r\, \langle \hat{\Psi}^\dagger(\boldsymbol{r}) \hat{\Psi}(\boldsymbol{r}) \rangle$ with the angle brackets

| | $^{87}$Rb | $^{52}$Cr | $^{162}$Dy | $^{164}$Dy | $^{166}$Er | $^{168}$Er | $^{170}$Er |
|---|---|---|---|---|---|---|---|
| $a\,(a_0)$ | 100.4(1) | 102.5(4) | 122(10) | 92(8) | 72(13) | 137(1) | -221(22) |
| $\mu_\mathrm{m}\,(\mu_\mathrm{B})$ | 1 | 6 | 9.93 | 9.93 | 6.98 | 6.98 | 6.98 |
| $a_\mathrm{dd}\,(a_0)$ | 0.7 | 15.1 | 129.2 | 130.8 | 65.4 | 66.2 | 67.0 |
| $\varepsilon_\mathrm{dd}$ | 0.007 | 0.15 | 1.06 | 1.42 | 0.91 | 0.48 | -0.30 |
| Refs. | [156] | [45] | [157] | [81, 157] | [122] | [82] | [122] |

**Tab. 2.1. Dipolar and contact interaction parameters.** S-wave scattering length $a$, magnetic dipole moment $\mu_\mathrm{m}$, characteristic dipolar length $a_\mathrm{dd}$ and relative dipolar strength $\varepsilon_\mathrm{dd}$ for different atomic species. Alkali atoms are represented by rubidium that are almost non-dipolar. To observe dipolar effects, $\varepsilon_\mathrm{dd}$ has to be non-negligible, as it is the case for chromium, dysprosium and erbium atoms. Comparing these species, only dysprosium is in the strongly dipolar regime.

denoting the expectation value. In the Heisenberg representation the field operators are time dependent and change with time described by the Heisenberg equation[9] [94, p. 38]

$$\begin{aligned} i\hbar\frac{\partial}{\partial t}\hat{\Psi}(\boldsymbol{r},t) &= \left[\hat{\Psi}(\boldsymbol{r},t),\hat{H}\right] \\ &= \left(-\frac{\hbar^2\nabla^2}{2m} + V_\mathrm{ext}(\boldsymbol{r}) + \int \mathrm{d}^3r'\,\hat{\Psi}^\dagger(\boldsymbol{r}',t)U_\mathrm{int}(\boldsymbol{r}-\boldsymbol{r}')\hat{\Psi}(\boldsymbol{r}',t)\right)\hat{\Psi}(\boldsymbol{r},t)\,. \end{aligned} \tag{2.10}$$

Starting from now, we include approximations for a mean-field description of many-bosons quantum systems as formulated by Bogolyubov in 1947 [159]. The key point is to separate the condensate wave function out of the field operators. In the thermodynamic limit of high atom numbers $N \gg 1$, the two states with $N$ and $N+1 \simeq N$ correspond to the same physical configuration and consequently the field operator can then be decomposed to [158, p. 11]

$$\hat{\Psi}(\boldsymbol{r}) = \Psi(\boldsymbol{r}) + \delta\hat{\Psi}(\boldsymbol{r})\,, \tag{2.11}$$

where $\Psi(\boldsymbol{r}) = \langle\hat{\Psi}(\boldsymbol{r})\rangle$ is the condensate wave function and $\delta\hat{\Psi}(\boldsymbol{r})$ is a small perturbation, that may be called *quantum fluctuations.* These quantum fluctuations are crucial for the results presented in this thesis, and hence we focus on fluctuations in chapters 5 and 6. Nevertheless, to introduce the basic static and dynamic properties of condensates, we neglect any quantum fluctuations in the following. By inserting the field operator from eq. (2.11) in eq. (2.10), we obtain the non-linear, *time-dependent Gross-Pitaevskii equation (GPE)*

$$i\hbar\frac{\partial}{\partial t}\Psi(\boldsymbol{r},t) = \left(-\frac{\hbar^2\nabla^2}{2m} + V_\mathrm{ext}(\boldsymbol{r}) + \Phi_\mathrm{int}(\boldsymbol{r})\right)\Psi(\boldsymbol{r},t)\,, \tag{2.12}$$

with the *mean-field interaction potential* $\Phi_\mathrm{int}$ using the density $n(\boldsymbol{r},t) = |\Psi(\boldsymbol{r},t)|^2$

$$\Phi_\mathrm{int}(\boldsymbol{r}) = \int \mathrm{d}^3r'\,U_\mathrm{int}(\boldsymbol{r}-\boldsymbol{r}')\,n(\boldsymbol{r}',t)\,. \tag{2.13}$$

---

[9] We use the commutation relations $\left[\hat{\Psi}(\boldsymbol{r},t),\hat{\Psi}^\dagger(\boldsymbol{r}',t)\right] = \delta(\boldsymbol{r}-\boldsymbol{r}')$ and $\left[\hat{\Psi}(\boldsymbol{r},t),\hat{\Psi}(\boldsymbol{r}',t)\right] = 0$.

To easily obtain the static properties of condensates within this formalism of mean-field theory, we write the condensate wave function as $\Psi(r,t) = \psi(\boldsymbol{r})\,\mathrm{e}^{-i\mu t/\hbar}$ with $\mu$ the chemical potential of the condensate. We insert this ansatz into eq. (2.12) and use the two-body interaction potential from eq. (2.8), resulting in the *stationary Gross-Pitaevskii equation*

$$\mu\psi(\boldsymbol{r}) = \left(-\frac{\hbar^2\nabla^2}{2m} + V_{\mathrm{ext}}(\boldsymbol{r}) + g\,n(\boldsymbol{r}) + \Phi_{\mathrm{dip}}(\boldsymbol{r})\right)\psi(\boldsymbol{r})\,, \tag{2.14}$$

with $\Phi_{\mathrm{dip}}$ the mean-field dipolar potential

$$\Phi_{\mathrm{dip}}(\boldsymbol{r}) = \int \mathrm{d}^3r'\,U_{\mathrm{dd}}(\boldsymbol{r}-\boldsymbol{r}')\,n(\boldsymbol{r}')\,. \tag{2.15}$$

One can see that the dipolar interaction adds a non-local term, due to its long-range character. In contrast, the contact interaction depends only on the local density.

For completeness we give the important *energy functional* of a dipolar quantum gas [26]

$$E(n) = \int \mathrm{d}^3r\,\left[\frac{\hbar^2\nabla^2}{2m}\,n(\boldsymbol{r}) + V_{\mathrm{ext}}\,n(\boldsymbol{r}) + \frac{g}{2}\,n(\boldsymbol{r})^2 + \frac{\Phi_{\mathrm{dip}}(\boldsymbol{r})}{2}\,n(\boldsymbol{r})\right]\,. \tag{2.16}$$

The different terms in the energy functional describing the total energy correspond to kinetic, potential and interaction energy. Minimizing the total energy with a variational method and a suitable trial density function is a convenient way to approach fundamental properties of condensates in a simple manner. In the next two sections, we present two established analytical methods.

### 2.3.2. Variational method: Gaussian density profile

To perform experiments with ultracold gases, the atoms have to be trapped in an external potential $V_{\mathrm{ext}}$. In this thesis, the experiments are performed in harmonic traps which we consider to be anisotropic for generality. The three-dimensional harmonic oscillator potential is

$$V_{\mathrm{ext}}(\boldsymbol{r}) = \frac{m}{2}\,\left(\omega_x^2x^2 + \omega_y^2y^2 + \omega_z^2z^2\right)\,, \tag{2.17}$$

with the trap frequencies $\omega_j$ $(j = x, y, z)$ and we define the geometric mean of the trap frequencies $\overline{\omega} = (\omega_x\omega_y\omega_z)^{1/3}$. Such harmonic trapping leads to an inhomogeneous density distribution of the gas and hence the necessity for calculating its spatial extent. For a non-interacting quantum gas[10] the stationary GPE (2.14) simplifies to the well-known Schrödinger equation. For a harmonic external potential (2.17) the solutions are the Hermite functions, as shown in figure 2.4a. A condensate will form in the energetically lowest state, that has a Gaussian wave function

$$\psi_{\mathrm{G}}(\boldsymbol{r}) = \left(\frac{N}{\pi^{3/2}a_xa_ya_z}\right)^{1/2}\exp\left(-\frac{x^2}{2a_x^2} - \frac{y^2}{2a_y^2} - \frac{z^2}{2a_z^2}\right)\,, \tag{2.18}$$

---

[10] The critical temperature for a trapped non-interacting sample differs from eq. (2.1) and reads $k_{\mathrm{B}}T_{\mathrm{c}} \approx 0.94\hbar\overline{\omega}N^{1/3}$ [158].

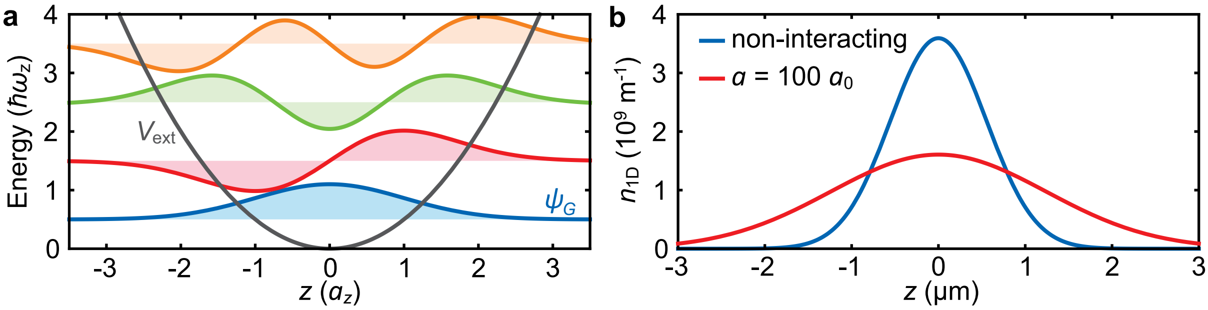

**Fig. 2.4. Gaussian wave function.** **a**, Representation of the wave functions for the first four bound eigenstates. The horizontal axis shows position $z$ in units of the harmonic oscillator length $a_z$. The vertical axis gives the energy for the harmonic external potential $V_{\text{ext}}$ and indicates the state energies. **b**, Integrated density profiles with and without interactions. The figure shows the one-dimensional density $n_{\text{1D}}(z)$, that is the density $n(\boldsymbol{r})$ integrated along the $x$- and $y$-direction, for a BEC with 10,000 $^{164}$Dy atoms in a spherical harmonic trap with $\overline{\omega} = \omega_z = 2\pi \cdot 100\,\text{Hz}$. The blue line is the case of a non-interacting ideal gas with a harmonic oscillator length of $a_z \approx 0.79\,\mu\text{m}$ and a central density of $n_0 \approx 3.7 \cdot 10^{21}\,\text{m}^{-3}$. Including a typical contact interaction strength with a scattering length of $a = 100\,a_0$ (green line) reduces dramatically the central density to $n_0 \approx 3.3 \cdot 10^{20}\,\text{m}^{-3}$ and increases the Gaussian width[12] to $\sigma_z \approx 1.76\,\mu\text{m}$.

where the harmonic oscillator lengths $a_j$ $(j = x, y, z)$ are given by $a_j = \sqrt{\hbar/m\omega_j}$ and we define the characteristic oscillator length $\overline{a} = (a_x a_y a_z)^{1/3} = \sqrt{\hbar/m\overline{\omega}}$. Consequently, the density distribution $n_G(\boldsymbol{r}) = |\psi_G(\boldsymbol{r})|^2$ is a Gaussian with the central density $n_0 = N/\pi^{3/2}\overline{a}^3$.

However, inter-particle interactions strongly change the density of the ultracold gas. For instance of repulsive interactions the size of the sample will increase with respect to the non-interacting case (see figure 2.4b). To get physical insight into the behaviour of interacting gases, we adopt the Gaussian wave function (2.18) to a variational trial function with the density distribution[11] given as [95, p. 165]

$$n_{\text{trial}}(\boldsymbol{r}) = \frac{N}{\pi^{3/2}\sigma_x\sigma_y\sigma_z} \exp\left(-\frac{x^2}{\sigma_x^2} - \frac{y^2}{\sigma_y^2} - \frac{z^2}{\sigma_z^2}\right) \tag{2.19}$$

with the Gaussian widths $\sigma_j$ as variational parameters. By substituting this trial function in the energy functional (2.16) one yields energy expressions. Minimizing the total energy for given external potentials and interactions with respect to the parameters $\sigma_j$, leads to the variational ground state. With this simple variational approach, early studies on stationary properties [160, 161] as well as dynamics [162, 163] of non-dipolar gases have been performed. In the same manner dipolar gases have been investigated [39, 164] and we give the energy terms for a cylindrical symmetric trap in appendix A.6.

Although the Gaussian trial function is successful for the energy contributions and can be easily calculated, it fails in describing the realistic density profile of atomic BECs. Hence, the next section introduces another approach: the Thomas-Fermi approximation.

---

[11] The trial function still satisfies the normalization condition $N = \int \mathrm{d}^3 r\, n(\boldsymbol{r})$.

[12] By neglecting the kinetic energy term in the energy functional (2.16), one derives an analytical expression [95, p. 166] for the Gaussian width $\sigma_j = \left(\frac{2}{\pi}\right)^{1/10} \left(\frac{Na}{\overline{a}}\right)^{1/5} \frac{\overline{\omega}}{\omega_j}\,\overline{a}$, resulting in $\sigma_z \approx 1.74\,\mu\text{m}$ for figure 2.4.

### 2.3.3. Interaction dominated regime: Thomas-Fermi approximation

For sufficiently large total atom number $N$, that includes sufficiently high densities $n$, the interaction terms in the energy functional (2.16) dominates over the kinetic energy term. Hence, a better approximation for the condensate density distribution for large number of atoms may be obtained by excluding the kinetic energy term and then solving the stationary GPE (2.14). For a non-dipolar condensate, we find that the GPE in the so called *Thomas-Fermi approximation*[13] simplifies to

$$\mu = V_{\mathrm{ext}}(\boldsymbol{r}) + g\, n_{\mathrm{TF}}(\boldsymbol{r})\,. \tag{2.20}$$

This equation has an analytical solution by using the external potential $V_{\mathrm{ext}}$ from eq. (2.17) and ensuring the normalization criterion $N = \int \mathrm{d}^3 r\, n_{\mathrm{TF}}(\boldsymbol{r})$. Then, the density in Thomas-Fermi approximation follows a parabolic distribution

$$n_{\mathrm{TF}}(\boldsymbol{r}) = |\psi_{\mathrm{TF}}(\boldsymbol{r})|^2 = \frac{15N}{8\pi R_x R_y R_z}\left[1 - \frac{x^2}{R_x^2} - \frac{y^2}{R_y^2} - \frac{z^2}{R_z^2}\right] \text{ for } n_{\mathrm{TF}} \geq 0\,, \tag{2.21}$$

mimicking the external potential and featuring an ellipsoidal shape with lengths $R_j$ along the semi-principal axes given by

$$R_j = 15^{1/5}\left(\frac{Na}{\overline{a}}\right)^{1/5} \frac{\overline{\omega}}{\omega_j}\,\overline{a}\,. \tag{2.22}$$

In the following, we will call these lengths *Thomas-Fermi radii.* By defining the central density for the inverted parabola to be $n_0 = 15N/8\pi R_x R_y R_z$, the constant chemical potential from eq. (2.20) can be also written as $\mu = g\, n_0$. This again indicates the local character of the contact interaction, as the chemical potential $\mu$ only depends on the local density value.

Figure 2.5a shows the density distribution in Thomas-Fermi approximation in comparison with the Gaussian trial function. The solutions from both approaches present a difference in shape and central density. When comparing them with numerically calculations of the GPE [165] or experimentally measured density profiles [166], it agrees very well with the Thomas-Fermi approximation. We show in figure 2.5b an exact numerical solution and the approximation with an inverted parabola distribution for an atom number $N = 10{,}000$ and scattering length $a = 100\, a_0$. They agree in absolute central density and spatial extent. However, the approximation fails in the region close to the Thomas-Fermi radii $R_{\mathrm{j}}$. In fact, the inverted parabolic distribution is not differentiable at $R_{\mathrm{j}}$ and accordingly the kinetic energy would diverge. Hence, the exact density distribution has to show a smooth behaviour to vanishing density.

The corresponding energy terms for a dipolar gas in Thomas-Fermi approximation are

---

[13] This approximation is valid if the parameter $Na/\overline{a} \gg 1$ is very large [94, p. 164]. As $a$ is on the order of nanometers and $\overline{a}$ is typically in the micrometer range, atom numbers $N$ higher than 10,000 validate this approximation.

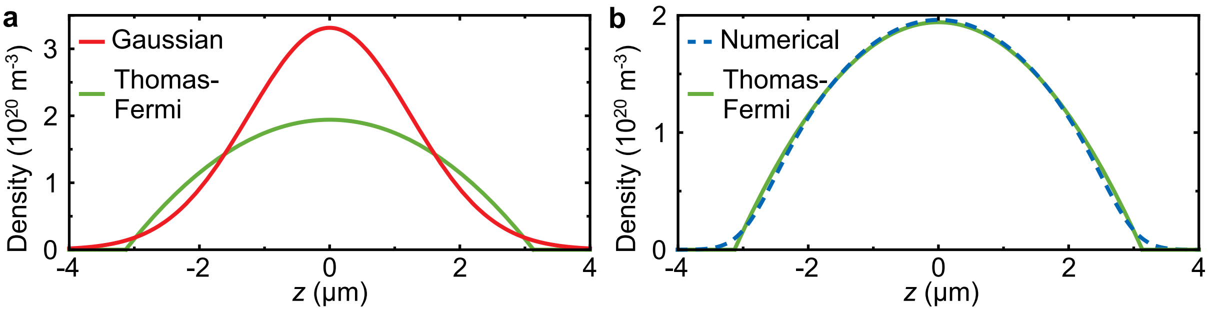

**Fig. 2.5. Thomas-Fermi approximation.** **a**, Density distribution in Gaussian and Thomas-Fermi approximation. The profiles show the density $n(\boldsymbol{r})$ along the $z$-direction for a non-dipolar BEC with 10,000 $^{164}$Dy atoms in a spherical harmonic trap with $\overline{\omega} = \omega_z = 2\pi \cdot 100\,\mathrm{Hz}$ and $a = 100\,a_0$. The Gaussian has a width of $\sigma_z \approx 1.76\,\mu\mathrm{m}$ and a central density of $n_0 \approx 3.3 \cdot 10^{20}\,\mathrm{m}^{-3}$, while the inverted parabola has a Thomas-Fermi radius of $R_z = 3.13\,\mu\mathrm{m}$ and a central density of $n_0 \approx 1.9 \cdot 10^{20}\,\mathrm{m}^{-3}$. **b**, Numerically calculated and approximated density profiles for the same parameters as before. The exact solution coincides very well with the Thomas-Fermi profile and both agree with central density and spatial extent. There are minor differences close to the Thomas-Fermi radius.

presented in appendix A.5. The discussion on static properties of dipolar gases will be continued in section 4.5 when we have introduced fluid mechanics for liquids and gases with dipolar interactions.

# 3. Producing a Dysprosium BEC with high-resolution Imaging

In 2005 the first dipolar quantum gas, consisting of chromium atoms, was achieved in Stuttgart [25]. Then, pioneering work on static and dynamic properties of dipolar quantum gases was performed [36, 39, 41]. But soon the accessible range of physics was limited due to fundamental properties of the element chromium and an atom detection with poor optical resolution. Consequently, we have built a new generation apparatus that now overcomes these restrictions.

Motivated by the first creation of dysprosium condensates in 2011 [75] and the expected phenomena for strongly dipolar gases, we started in the beginning of 2012 to build an experiment that can routinely generate dysprosium quantum gases in a glass cell with high optical access. Finally, we condensed dysprosium atoms in June 2014 for the first time in our research group and imaged them *in situ* with high resolution in April 2015. The way of this research journey is reported in 7 bachelor theses [167–173] and 4 master theses [174–177]. A very detailed description of the recent setup and experimental sequence is given in Thomas Maier's Ph.D. thesis [178].

This chapter only gives a short summary of the experimental setup and production of dysprosium BECs. First, we introduce the rare-earth metal dysprosium and its optical transitions utilized for laser cooling. Second, we summarize briefly the complex cooling process of dysprosium atoms down to quantum degeneracy, and third we introduce our main technical tools for tuning and detecting internal properties of dysprosium BECs. This includes our feature, unique for dipolar quantum gases, to image the atoms *in situ* with a high spatial resolution.

## 3.1. Dysprosium: properties and optical transitions

Dysprosium is a rare earth element with 66 protons in the lanthanide series and possesses seven stable isotopes, with four having a high natural abundance. These are the two bosonic isotopes $^{162}$Dy (25.5 %) and $^{164}$Dy (28.3 %) as well as two fermionic isotopes $^{161}$Dy (18.9 %) and $^{163}$Dy (24.9 %) [179]. Dysprosium has a relatively high melting point (1412 °C) and boiling point (2567 °C) compared to other metals [180].

The electronic ground state configuration [Xe]4f$^{10}$6s$^{2}$ offers an open 4f shell inside closed other shells, which leads to a large orbital angular momentum of $L = 6$. With four unpaired electrons in the f-shell, dysprosium has a total electronic spin of $S = 2$, and hence a total angular momentum of $J = 8$. This $^{5}\mathrm{I}_{8}$ ground state is the origin of the high magnetic moment of $\mu_\mathrm{m} = 9.93\,\mu_\mathrm{B}$. This is, together with the element terbium, the highest magnetic moment of all elements. In contrast to the bosonic isotopes, which have no nuclear spin, the fermionic isotopes possess a nuclear spin of $I = 5/2$ leading to six additional hyperfine levels from $F = 11/2$ to $F = 21/2$ in the electronic ground state.

Due to this complex electronic structure, dysprosium and other lanthanides feature a rich atomic energy spectrum (shown for dysprosium in figure 3.1a) with several possible optical transitions and decay channels. Hence, it was not obvious that lanthanides feature suitable closed cycling transitions. Despite the existence of numerous decay channels, important early studies with erbium atoms showed that laser cooling is possible [181]. Meanwhile there are plenty different laser cooling schemes for lanthanides such as dysprosium [75, 182, 183], holmium [184, 185], erbium [186, 187], thulium [188, 189] and the special case of ytterbium [190, 191], that has a more simple energy spectrum due to a filled f-shell. In addition, these rich energy spectra allow measurements of a possible time variation of the fine structure constant using dysprosium atoms [192, 193] and to have the currently most accurate atomic clocks using ytterbium atoms [194, 195].

Up to now, only two experiments created dysprosium quantum gases[14] and they differ in the laser cooling transitions used, that we show in figure 3.1 with relevant parameters. An essential part of every experiment creating ultracold atoms is a so-called *magneto-optical trap* (MOT), consisting of six laser beams and a magnetic gradient field. This results in optical cooling and a magneto-optical confinement for the atoms [107]. If the used optical transition has a high decay rate $\Gamma$ or natural linewidth $\gamma$, the corresponding MOT is then able to capture atoms from an atomic beam with a velocity of a couple meters per second. But, a high decay rate or linewidth also limits the lowest possible temperature, defined by the so-called Doppler temperature $T_\mathrm{Doppler} = \hbar\Gamma/2k_\mathrm{B}$.

Therefore, for the first achieved dysprosium BEC in Illinois/Stanford, the researchers started with a MOT using the strongest cooling transition with a wavelength of 421 nm and a natural linewidth of $\gamma_{421} = 32.2\,\mathrm{MHz}$ [182]. To reach colder atomic samples they used a subsequent second stage MOT operating at the very narrow transition at 741 nm with a small linewidth of $\gamma_{741} = 1.78\,\mathrm{kHz}$ [75]. In contrast, our approach is based on a narrow-line MOT using the transition at 626 nm with a linewidth of $\gamma_{626} = 136\,\mathrm{kHz}$. This enables the MOT to directly capture atoms from an atomic beam and offers a low cooling temperature at the same time [183]. This cooling scheme is inspired by experiments on erbium [187] and ytterbium atoms [191] with a similar transition.

Actually, a magneto-optical trap is only a single technical part of experiments creating ultracold gases. Starting with solid dysprosium and to finally generate a gaseous condensate is a complex production process. It consists of many steps that all have to be properly quantified and are very time-sensitive, partially on a $10\,\mu$s time scale. Additionally as a BEC is a metastable state and is generally destroyed when detecting it, we have to create a new sample every 20 seconds. In the next section, we present the experimental setup and summarize the production of dysprosium quantum gases.

---

[14] There are many groups working on further experiments using ultracold dysprosium gases, for example in Mainz, Innsbruck, Paris, Pisa and São Carlos

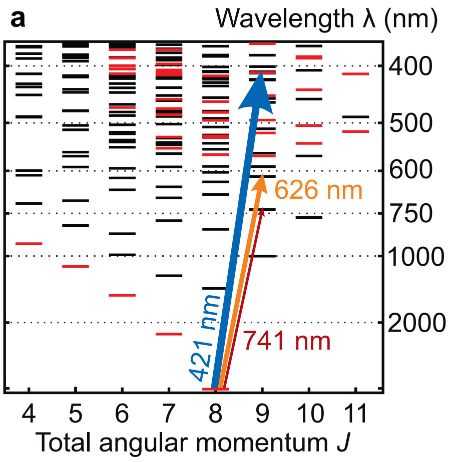

**b** Optical Cooling transitions

| | Blue (421) | Orange (626) | Red (741) |
|---|---|---|---|
| $\lambda$ (nm) | 421.291 | 626.082 | 740.963 |
| $\gamma$ | 32.2(8) MHz | 136(4) kHz | 1.78(2) kHz |
| $\Gamma$ (1/s) | $2.02 \cdot 10^8$ | $8.55 \cdot 10^5$ | $1.12 \cdot 10^4$ |
| $\tau$ | 4.94 ns | 1.17 $\mu$s | 89.3 $\mu$s |
| $I_{\mathrm{sat}}$ | 56.3 mW/cm$^2$ | 72 $\mu$W/cm$^2$ | 590 nW/cm$^2$ |
| $T_{\mathrm{Doppler}}$ | 773 $\mu$K | 3.3 $\mu$K | 42.7 nK |
| $T_{\mathrm{recoil}}$ | 329 nK | 149 nK | 106 nK |
| Refs. | [196] | [197] | [196] |

**Fig. 3.1. Atomic energy spectrum of dysprosium. a**, A part of the atomic dysprosium energy spectrum where the levels are sorted to their respective angular momentum $J$ [198]. The scale gives the wavelength $\lambda$ of an optical transition from the electronic ground state. Energy states with even (odd) parity are shown as red (black) line. The coloured arrows indicate three optical transitions that are used for laser cooling of dysprosium atoms. **b**, The table gives relevant parameters for these optical cooling transitions. The vacuum wavelength $\lambda$, natural linewidth $\gamma$, decay rate $\Gamma = 2\pi\gamma$, decay constant $\tau = 1/\Gamma$, saturation intensity $I_{\mathrm{sat}} = 2\pi^2\hbar c\Gamma/3\lambda^3$, Doppler temperature $T_{\mathrm{Doppler}} = \hbar\Gamma/2k_{\mathrm{B}}$ and recoil temperature $T_{\mathrm{recoil}} = \hbar^2k^2/2mk_{\mathrm{B}}$ with the wave number $k = 2\pi/\lambda$.

## 3.2. Experimental setup and production of dysprosium BECs

We give an overview of the steps used to generate a dysprosium condensate. It includes basics of laser cooling, magneto-optical trapping and optical trapping that are explained in reviews and textbooks [95, 107, 151]. Here, we can only give a brief description on these techniques and give recent, important experimental numbers. Instead of describing the mostly home-built laser systems and their frequency stabilization, we concentrate on the main steps given in this list:

1. Deceleration of the hot atomic beam with a Zeeman slower
2. Cooling and trapping in a magneto-optical trap (MOT)
3. Transfer to the optical tweezers and transport to a glass cell
4. Transfer to a crossed optical dipole trap (ODT) and post-cooling
5. Forced evaporation to quantum degeneracy
6. Tuning and detection of internal parameters

With these steps we will shortly describe the sequential production of condensates and the vacuum chamber that protects the gaseous atom clouds from the environment. The vacuum chamber consists of three main parts: the oven chamber, the MOT chamber and the glass cell. A more thorough description of our preparation sequence of quantum gases can be found in the Ph.D. thesis [178], that also includes the laser systems.

### Effusion cell and Zeeman slower

This part describes the preparation of dysprosium in the gas phase and the collimation of the atoms in a decelerated atomic beam. First, a high-purity dysprosium granulate[15] (99.9 %) is put in a molybdenum crucible, as dysprosium reacts with any ceramic crucible at high temperatures. The crucible is placed in a high-temperature effusion cell[16] that sublimates atoms at $T$ = 1200-1250 °C. The whole effusion cell is placed in the oven vacuum chamber with a pressure of $p \approx 10^{-9}$ mbar (see figure 3.2a). The crucible has only a small aperture and collimates the atomic beam. Further collimation of the atomic beam is achieved by a transversal cooling stage with a two-dimensional optical molasses using blue light[17] (421 nm) that is red detuned by -1 $\gamma_{421}$. By using an intensity of up to 9 $I_{\mathrm{sat},421}$ per beam, we can increase the atomic flux by a factor of up to five [183].

The collimated atomic beam has a mean velocity of 450 m/s and as mentioned before a MOT can only capture atoms with a velocity of a few m/s. Hence, we longitudinally decelerate the atomic beam with a spin-flip *Zeeman slower*. Our Zeeman slower consists of a long tube (90 cm), through which the atomic beam travels, a blue laser beam with a red detuning of -17.5 $\gamma_{421}$ and a power of 80 mW and a well-chosen magnetic field that varies spatially along the tube direction. The magnetic field is designed such that the Zeeman shift exactly compensates the Doppler shift for a certain velocity class [199]. At the entrance the blue beam is first resonant for atoms with a velocity of ~600 m/s and as the atoms propagate along the tube, the resonance shifts to lower and lower velocity classes down to a final velocity of 10-15 m/s at the exit, attached to the MOT chamber.

Furthermore the ZS acts as a differential pumping stage to have a two orders of magnitude lower pressure ($p \approx 10^{-11}$ mbar) in the MOT chamber than in the oven chamber ($p \approx 10^{-9}$ mbar).

### Narrow-line magneto-optical trap

The decelerated dysprosium atoms are captured in a narrow-line MOT in the MOT vacuum chamber (see figure 3.2b). The MOT operates with orange light[18] red-detuned to the optical transition at 626 nm with a linewidth of $\gamma_{626} = 136$ kHz. To accomplish a large capture and trapping volume, the beams have a diameter of 22.5 mm and an intensity of up to 250 $I_{\mathrm{sat},626}$ per beam. Additionally, we employ a commercial spectral broadener[19] to increase the laser linewidth to ~70 $\gamma_{626}$, that further increases the capture velocity. We typically load more than $10^8$ atoms with a temperature of about 500 $\mu$K in 4 seconds at a central detuning of -35 $\gamma_{626}$ and with an axial magnetic field gradient of $|\nabla B| = 3$ G/cm.

---

[15] HMW Hauner: 6672002

[16] Createc Fischer: HTC-40-10-2000-SHM with water cooling WK 63-40 and the power supply CU-3504-S1-DC-700

[17] The laser source are two optically pumped titanium-sapphire laser (Coherent, MBR110) operating at a wavelength of 842 nm with both up to 4.5 W optical power. This infrared light is frequency doubled in a self-built monolithic cavity with a non-linear, Brewster-cut lithium triborate crystal (LBO). We can achieve blue powers of up to 2 W for a single laser system [169].

[18] We create the orange 626 nm light by sum-frequency generation of two infrared fiber lasers at 1050 nm and 1550 nm with a power up to 5 W (NKT Photonics: HPA Y10 and HPA E15) in a periodically poled lithium niobate crystal (Covesion: MSFG626-0.5-40). We achieve up to 2 W for the orange laser power.

[19] Electro-optical modulator with a resonance frequency of 105 kHz. Qubig: EO-F0.1M3-VIS

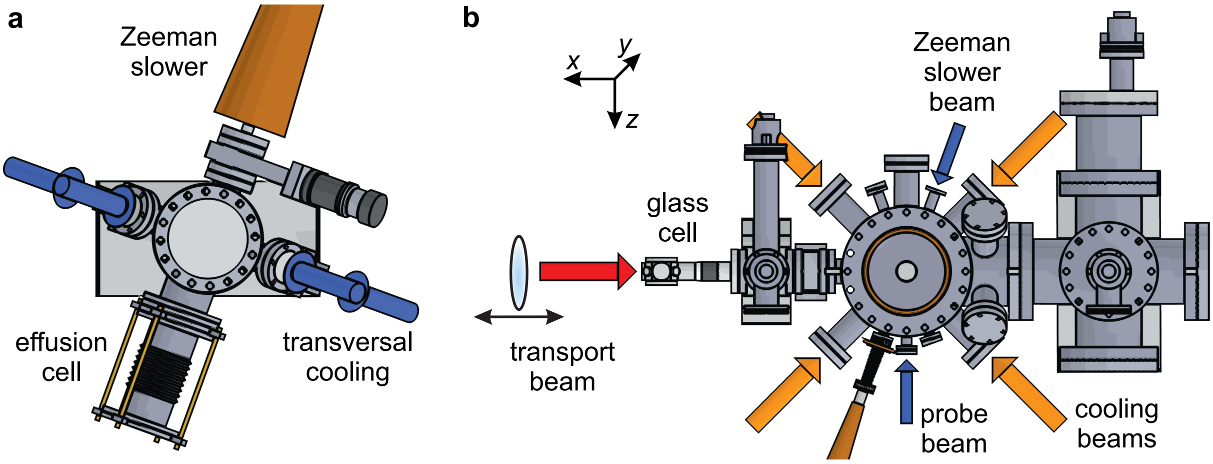

**Fig. 3.2. Experimental vacuum chamber and laser beams. a**, Oven chamber with effusion cell and transversal cooling. The dysprosium atoms are sublimated from the effusion cell, transversally cooled with blue light (blue arrows) and then decelerated in the Zeeman slower. **b**, MOT chamber and glass cell. After the atoms exit the Zeeman slower they are captured by the orange MOT (orange arrows). The atoms can be imaged from the bottom with the probe beam. The atoms from the MOT are transferred into the transport beam (red arrow) and subsequently transported with a moveable lens over 375 mm into the glass cell.

At this stage of the MOT, the temperature is far from being limited by the Doppler temperature $T_{\mathrm{Doppler},626} = 3.3\,\mu$K. To reduce the temperature and to increase the atomic density, the MOT is compressed in 170 ms by decreasing the detuning to -5 $\gamma_{626}$ and the intensity to 0.24 $I_{\mathrm{sat},626}$. We end up with a temperature of about 10 $\mu$K that allows us to load the atoms directly in an optical dipole trap.

### Transport beam

We create the optical tweezers [200] or transport beam with a focused broadband fiber laser[20] operating at 1070 nm with a maximum power of 72 W at the MOT position. The laser is focussed down to a beam waist of 37.3(1.2) $\mu$m, which creates a trap depth of $\sim$640 $\mu$K at maximum intensity. The last focussing lens of the optical tweezers is mounted on an air-bearing translation stage[21] with 40 cm translation range and 0.5 $\mu$m accuracy and repeatability [168]. This allows to move the focus of the transport beam inside the vacuum chamber from the MOT chamber to the glass cell.

The compressed MOT still has a Gaussian width of around 400 $\mu$m, which is a factor of 10 larger than the radial size of the transport beam at focus. Therefore, we do not transfer the atoms at the focal point as this limits the spatial overlap between transport beam and MOT. Instead we employ the moveable lens to move the focus 15 mm away from the MOT position. The waist size at this position is 170 $\mu$m, which increases the trapping area by nearly a factor of 18, but also decreases the potential depth by the same amount. After compressing the MOT we superimpose the transport beam for 120 ms and then release

---

[20] IPG Laser: YLR-100-LP-WC, linewidth of 2 nm

[21] AeroTec: Linear Stage ABL15040 with Controller HLE10-60-A-MXH-B

the atoms from the MOT. The atoms are then only trapped by the transport beam. As the atoms are trapped in an out-of-equilibrium position, they would start to oscillate. To suppress this oscillation, we rapidly move the transport beam in 47 ms, such that the focal point is at the prior MOT position.

After that, we transfer the atoms within 2 s from the MOT chamber into the glass cell by moving the last focusing lens over a range of 375 mm. We typically end up with $10^7$ atoms with a temperature of $100\,\mu$K in the glass cell. We measure the same values in the MOT chamber without moving the last lens. This indicates that the optical transport is lossless and without additional heating. We found that this is the case provided the power is $> 60$ W, that can be only supported for broadband fiber lasers. Unfortunately, this broadband frequency mode structure induces a heating due to two-photon Raman transitions [201]. Thus, further cooling steps are performed in a narrow single-mode ODT.

**Optical dipole trap and evaporation**

We transported the atoms to the glass cell to have two major advantages. The octagonal glass cell offers high optical access and the reduction of magnetizable parts close to the atoms in comparison to a steel vacuum chamber. On a quartz-glass frame[22] 9 high quality windows[23] are bonded (see figure 3.3a). The bondage technique allows for inside and outside anti-reflection coatings for the windows to minimize stray reflections. The two large windows (diameter 50.8 mm) allow a large optical access for the high-resolution objective, that is specified in section 3.3.3. This objective might be also used to write time-averaged potentials with an electro-optical deflector (EOD), that is shown in chapter 7 as outlook. Three side windows (29.4 mm) and further four small windows (14.9 mm) allow optical access for laser beams and the glass-metal transition is non-magnetic.

Once in the glass cell, the atoms in the transport beam are transferred to a crossed optical dipole trap (cODT) within 200 ms. The cODT consists of two dipole traps that we name ODT 1 and ODT 2. Both traps are created by a 55 W solid-state laser[24], that is very narrow in frequency (1 kHz) and has a wavelength of 1064 nm. Both dipole traps are coupled in polarization-maintaining fibers suitable for high powers[25] to optimize pointing stability and are actively intensity stabilized with an acousto-optic modulator[26]. The dipole trap ODT 1 along the $x$-direction, superimposed with the transport beam, is radial symmetric and has a radial beam waist of $39(2)\,\mu$m with a maximum power of 12 W, while the ODT 2 along the $y$-direction is elliptically shaped with beam waists horizontally of $119(5)\,\mu$m and vertically of $31(2)\,\mu$m with a power up to 8 W.

We transfer typically $5\cdot 10^5$ atoms to the crossed ODT with a temperature of typically $35\,\mu$K, while most of the atoms are trapped in ODT 1. Thus, to increase the atom number in the crossed region, we employ another laser cooling step using orange light along the $y$-direction. The beam has a very low intensity of $\sim 0.03\,I_{\mathrm{sat},626}$ with a red-detuning of

---

[22] Precision Glassblowing of Colorado

[23] Gooch & Housego: Corning 7980-OA fused silica, flatness $\lambda/20$

[24] Coherent: Mephisto MOPA 55W

[25] OZ Optics: PMJ-A3HPC,A3HPC-1064-10/125-5AS-2-1-LMA

[26] AA opto-electronic: AA.MTS80-A3-1064Ac, center frequency 80 MHz and we use a two-frequency driver setup to minimize beam movement at different parameter settings [202].

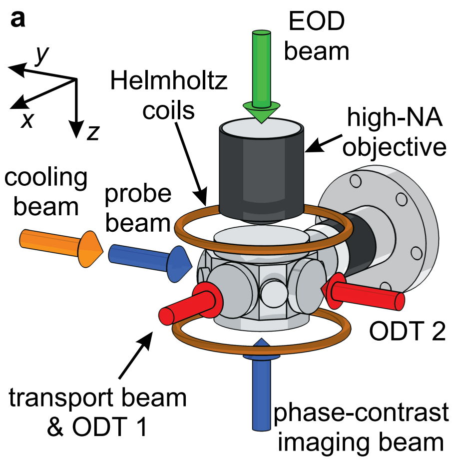

| **b** | $N$ | $T$ | $n_0$ ($\mathrm{m}^{-3}$) | $n_0^{-1/3}$ (nm) | $\lambda_{\mathrm{dB}}$ (nm) |
|---|---|---|---|---|---|
| Oven | - | 1500 K | $5\cdot10^{20}$ | 100 | 0.004 |
| ZS | - | $\sim$2 K | $\sim10^{12}$ | $10^5$ | 0.1 |
| MOT | $10^8$ | 500 $\mu$K | $4\cdot10^{15}$ | 6,000 | 6 |
| cMOT | $10^8$ | 10 $\mu$K | $5\cdot10^{16}$ | 3,000 | 40 |
| Transp | $10^7$ | 100 $\mu$K | $10^{19}$ | 500 | 15 |
| ODT | $5\cdot10^6$ | 35 $\mu$K | $3\cdot10^{18}$ | 700 | 23 |
| cODT | $3\cdot10^6$ | 20 $\mu$K | $2\cdot10^{19}$ | 350 | 30 |
| BEC | $2\cdot10^4$ | 100 nK | $10^{20}$ | 200 | 400 |

**Fig. 3.3. Glass cell and cooling parameters. a**, The figure shows a schematic view of the glass cell. The transport beam transfers the atoms from the MOT vaccum chamber to the glass cell. There, they are loaded into a crossed optical dipole trap created by ODT 1 and ODT 2. In the crossed ODT we employ laser cooling with orange light. The atoms may be imaged from two directions: Time-of-flight absorption imaging from the side in $y$-direction and phase-contrast imaging from the bottom in $z$-direction. The latter allows high-resolution in situ images due to a high numerical aperture objective. The objective may be also used to write tailored potentials with an EOD system. Close to the glass cell we attached a pair of Helmholtz coils capable to generate homogeneous magnetic fields. **b**, The table presents a summary of the different cooling steps and the according atom number $N$, temperature $T$, peak density $n_0$, particle distance $n_0^{-1/3}$ and thermal de-Broglie wavelength $\lambda_{\mathrm{dB}}$. The cooling steps are: dysprosium atoms in the gas phase within the crucible (Oven), at the exit of the Zeeman slower (ZS), captured in the magneto-optical trap (MOT), compressed MOT (cMOT), after the transport to the glass cell (Transp), in the narrow-line optical dipole trap (ODT), in the post-laser cooled crossed ODT (cODT) and finally for the phase transition to a BEC.

-1 $\gamma_{626}$ and is illuminated on the atoms for 500 ms. After this cooling step, we still have typically $3\cdot10^6$ atoms in ODT 1 and $5\cdot10^5$ atoms in the crossed region, both with a temperature of 20 $\mu$K.

To finally achieve a quantum degenerate gas, we utilize *forced evaporative cooling* [203]. This technique is commonly used to achieve densities and temperatures that cannot be reached with laser cooling. Evaporative cooling is based on removing the hottest atoms from the system to reach a lower equilibrium temperature after thermalization due to elastic two-body collision processes. An atom can leave our system if its thermal energy is higher than the potential trap of the cODT. Hence, for a constant trap depth this cooling method would stagnate at some point. Thus, we lower in an optimized way the trap depth, which is proportional to the intensity of the dipole traps, to further decrease the sample temperature. After 6.3 s of forced evaporation, we finally generate a dysprosium condensate consisting of typically 15,000 atoms and a temperature of 70-100 nK.

To conclude this section on the production of dysprosium quantum gases, we give in figure 3.3b a summary of all the mentioned cooling steps with respective parameters important for the onset of quantum degeneracy.

## 3.3. Tuning and detection of internal properties

Strongly dipolar quantum gases, such as a dysprosium quantum gas, can act as a model system for condensed matter phenomena. But novel phenomena are mostly predicted in a small parameter range. Hence, in the field of ultracold atomic physics, two technical main tools are needed: control on internal and external properties and a reliable detection of the atomic cloud properties.

In this section, we describe the possibility to tune the contact interaction strength by utilizing magnetic Feshbach resonances. Hence, we need an accurately controlled and reproducible homogeneous magnetic field. Last, we present the high-resolution in situ imaging to extract the condensate properties.

### 3.3.1. Feshbach resonances: tuning the contact interaction

In the previous section 2.2.1, we introduced the molecular potential $U(\boldsymbol{r})$ and that it can be reduced in the ultracold regime to a scattering process solely described with the scattering length $a$ as single parameter. We also mentioned that if the potential $U(\boldsymbol{r})$ supports a molecular bound state close to the kinetic energy of the particles, that is essentially zero energy in the ultracold regime, the absolute value of the scattering length $a$ is large. If the bound state is slightly lower than zero energy, then $a$ is positive, while it is negative, if the bound state is a virtual state with an energy higher than zero [95, 152]. In principle the molecular potential, and hence the energy levels, can be modified with static electric fields due to an induced dipole-dipole interaction between polarized atoms [204]. Unfortunately, the required electric fields are on the order of 100 kV/cm, which is very challenging for experiments in a vacuum chamber. Instead for our experiments, we utilize so-called *Feshbach resonances* [8], that are magnetically controlled.

Atoms are not point-like particles, but exhibit an internal structure with angular quantum numbers. Thus, they do not only feature one single molecular potential, they provide a manifold of possible collision channels, each with different quantum numbers. When these different potentials or channels are coupled, the scattering behaviour can be strongly modified. Theoretical predictions were carried out independently by Feshbach in the context of nuclear physics [205] and by Fano approaching the problem in the background of atomic physics [206]. The elementary properties of such a Feshbach resonance can be understood from a simple picture [8].

We consider two molecular potentials $U(r)$ and $U_\mathrm{c}(r)$, as shown in figure 3.4a. The potential $U(r)$ describes the interaction of two atoms with a small kinetic energy $E$. This channel is asymptotically the one of two unbound atoms in the collision process and represents the energetically open channel. The other potential $U_\mathrm{c}(r)$ is an energetically closed channel, where the atoms are in a different angular momentum state. However, this channel remains important as it can support a bound molecular state at the energy level $E_\mathrm{c}$ near the threshold of the open channel. If the energy $E_\mathrm{c}$ approaches the energy $E$ of the incident particles, then even weak coupling can lead to a strong mixing between the two channels. If the corresponding magnetic moments of the two channels are different, the

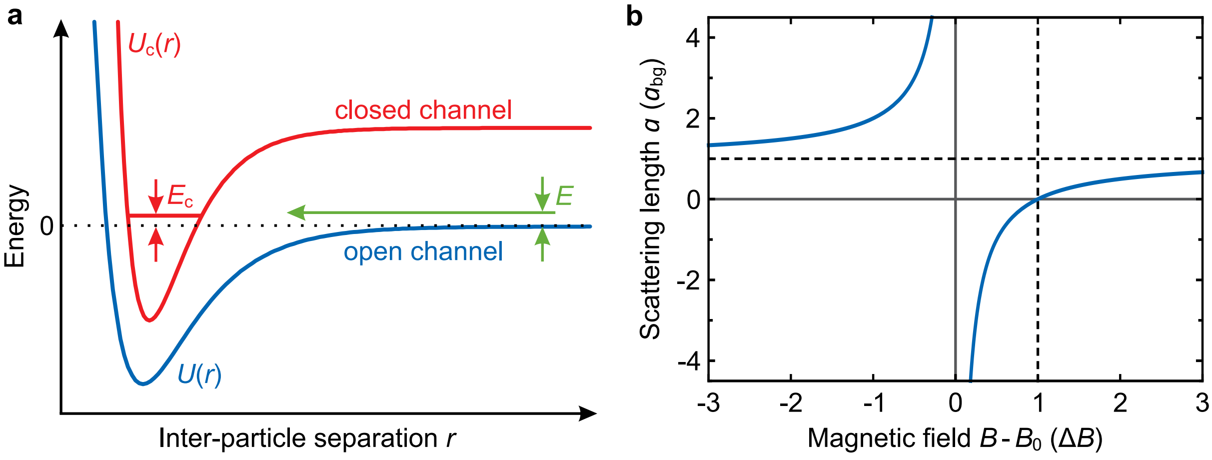

**Fig. 3.4. Feshbach resonance.** **a**, Basic two-channel model for a Feshbach resonance. Atoms with collision energy $E$ (green) can enter the open channel $U(r)$ (blue line), while the closed channel $U_c(r)$ (red line) features a bound state at energy $E_c$. The energy level $E_c$ can be tuned in resonance with a magnetic field via a Zeeman shift. This leads, due to a coupling of different molecular states, to a mixing of the two states and a change of the scattering length $a$. Based on [8]. **b**, Scattering length $a$ as a function of magnetic field $B$ in the vicinity of a Feshbach resonance. The Feshbach resonance is located at $B_0$ and has a width of $\Delta B$. Far away from any resonance the scattering length approaches the value $a_{bg}$, while it vanishes at the magnetic field $B_0 + \Delta B$.

energy difference can be controlled with a magnetic field via the Zeeman shift. This leads to a magnetically tunable Feshbach resonance with a resonant behaviour of the scattering process, where the scattering length $a$ diverges at a given magnetic field. The change in scattering length around the resonance can be described by [8]

$$a(B) = a_{bg}\left(1 - \frac{\Delta B}{B - B_0}\right) \tag{3.1}$$

with $a_{bg}$ the background scattering length far away from the resonance, $\Delta B$ the resonance width and $B_0$ the resonance position, where the scattering length $a$ diverges. Figure 3.4b shows this resonance expression. An important point is the zero crossing of the scattering length, that occurs at a magnetic field of $B = B_0 + \Delta B$.

Feshbach resonances for dysprosium show remarkable properties. Due to its complex internal atomic structure, we observe a dense spectrum of many Feshbach resonances with a mean density of 4.4 resonances per Gauss [79, 207]. Additionally, a statistical analysis of the spacings between resonances has shown correlations that induced a distribution reminiscent of quantum chaos [78, 79]. Despite this dense and chaotic spectrum of Feshbach resonances there are specific resonances that decouple from the chaotic background and present a broad resonance width [81]. Further studies on scattering properties have yielded a background scattering length of $a_{bg} = 92(8)\,a_0$ for $^{164}$Dy [81, 157]. These results have established the possibility to tune the interactions in a dysprosium quantum gas. The next section describes our magnetic field control and the particular Feshbach resonance that we used for the results in this thesis.

### 3.3.2. Magnetic field control

A controllable homogeneous magnetic field is required to utilize a Feshbach resonance and tune the contact interaction. To attach coils close to the glass cell, we built a plastic holder that has openings for coils and the glass cell windows (see figure 3.5a). The plastic holder is designed such that the optical access is not restricted. We can apply a homogeneous magnetic field along the $z$-direction with a coil pair in Helmholtz configuration. The coils have each $3 \times 3$ turns with a diameter of around 88 mm and create a magnetic field of 1.67 G/A. A bipolar actively stabilized current source[27] with a maximal current of 6 A supplies the coils.

Additionally, to compensate residual magnetic fields, such as earth magnetic field, or to apply a weak magnetic field in an arbitrary direction, we implemented three orthogonal large Helmholtz coil pairs (not shown in the figure). Each coil has a slightly different diameter of around 1 m, is centered to the glass cell and features $5 \times 3$ turns . We use three home-built bipolar current sources[28] that offer a maximal current of 6 to 8 A, dependent on the specific coil. Each coil can reach a maximum field of 1.5 G in its respective direction.

Lastly, we attached a coil pair in an anti-Helmholtz configuration along the $z$-direction to the plastic holder (shown in figure 3.5a). Each coil has $5 \times 18$ turns, a diameter of 105 mm and the coil pair generates a magnetic gradient of 3.57 G/A cm in the axial $z$-direction. This coil pair can be used to compensate gravitational force or to weaken the trap confinement of the optical dipole traps, respectively. For the results shown in chapters 5 and 6, we use it to compensate partially or completely gravity.

With these mentioned coils we can properly control the external magnetic field for the atoms and study specific Feshbach resonances. In earlier studies[29] we detected 309 Feshbach resonances up to a field of 70 G with a resolution of 14.5 mG [79]. These resonances were mapped with atom-loss spectroscopy, that consists in recording the number of atoms left after a given wait time as a function of magnetic field. On a Feshbach resonance, inelastic three-body collisions are amplified [208] such that it shows strong atom losses visible as a minimum in final atom number.

For the work presented in this thesis, we use one particular Feshbach resonance close to a field of 7 G, that is not strongly affected by other neighbouring resonances. We measure its properties with atom-loss spectroscopy on $N = 2 \cdot 10^5$ atoms evaporated to a temperature of $T = 400\,\mathrm{nK}$ in the crossed optical dipole trap. We then set the magnetic field to the target value (with a step size of 5 mG), where the atoms are held for 500 ms. During this time, inelastic three-body recombination causes atom loss and at the resonance position $B_0$ the atom number is minimal, as shown in figure 3.5b with blue circles. With this method, we locate the resonance position to be $B_0 = 7.117(3)\,\mathrm{G}$.

To measure the resonance width $\Delta B$, we search for the zero crossing of the scattering length $a$. As the cross section $\sigma$ of elastic collisions due to the contact interaction scales like $\sigma = 8\pi a^2$, evaporation is ineffective for vanishing contact interaction strength. As

---

[27] HighFinesse: BCS6_12_M2014, relative current stability is $< 2.5 \cdot 10^{-5}$

[28] Based on OPA549

[29] For these studies, we used a different pair of coils along the $y$-direction, that were attached to another plastic holder [178].

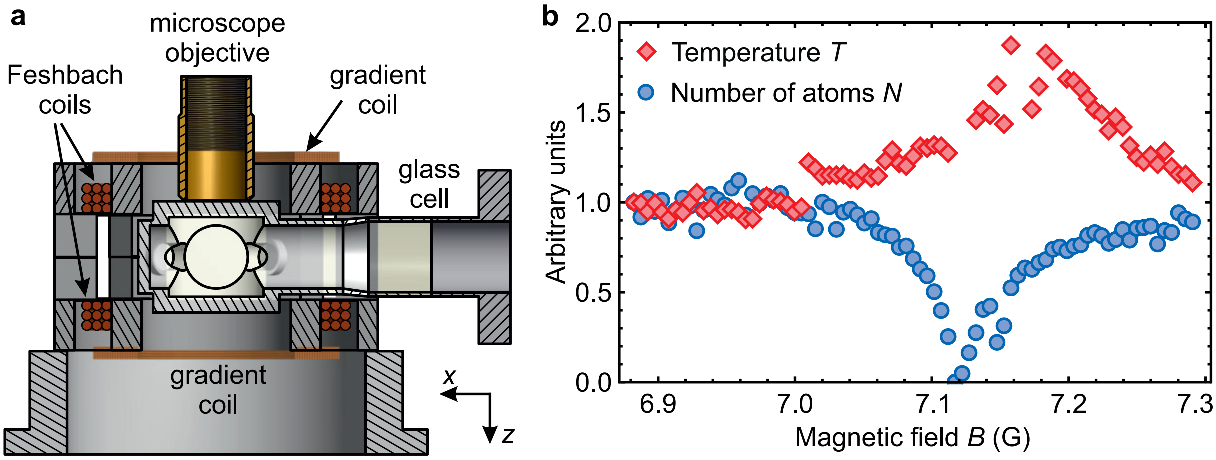

**Fig. 3.5. Magnetic field control and Feshbach resonance. a**, Sectional view of the glass cell. For mounting the Feshbach coils and gradient coils close to the glass cell, we implemented a plastic holder. Adapted from [178]. **b**, Atom-loss spectroscopy mapping a Feshbach resonance of $^{164}$Dy. The number of atoms (blue circles) and temperature (red diamonds) are normalized. The atom number minimum shows the center of the Feshbach resonance at $B_0 = 7.117(3)\,\text{G}$, while the temperature is maximized at $B_0 + \Delta B$, with the resonance width $\Delta B = 51(15)\,\text{mG}$.

a consequence the temperature after some evaporation is maximal at the magnetic field $B_0 + \Delta B$. For such a thermalization measurement, we changed the magnetic field already 1.2 s before the evaporation process ends and observed the maximal temperature at the position $B_0 + \Delta B$, with $\Delta B = 51(15)\,\text{mG}$ (as shown in figure 3.5b with red diamonds). Note that on the right side of the Feshbach resonance appears another very narrow resonance. This resonance slightly changes the zero crossing position, and hence we take this systematic error into account in the uncertainty on the resonance width $\Delta B$.

Tuning the contact interaction strength by using this Feshbach resonance is the first of two key tools to study dipolar quantum gases. The second is a microscope with high spatial resolution to detect the atomic density distribution in situ, which is explained in the next section.

### 3.3.3. High-resolution phase contrast imaging

Probing a trapped condensate directly in the trap needs a suitable imaging technique that provides a high spatial resolution and is not distorted by refractive effects of the dense atomic sample. Hence, we use a microscope objective and apply an imaging technique that relies on a dispersive phase shift instead of a direct absorption of photons.

First, we concentrate on the microscope objective. As the typical size of a trapped condensate is on the order of some $\mu$m, the resolution of the microscope has to be around $1\,\mu$m and the image has to be magnified to be larger than typical CCD pixel sizes. Thus, we use two custom-made objectives, that are diffraction-limited for the imaging wavelength $\lambda = 421\,\text{nm}$ as well as for trapping light at $\lambda = 532\,\text{nm}$ (see outlook in chapter 7). The first microscope objective is mounted above the glass cell (see figure 3.5a) and has an effective focal length of $f_1 = 25\,\mathrm{mm}$ and is corrected for the upper window of our glass cell. The clear aperture of the objective is 17 mm, yielding a numerical aperture of NA = 0.32 given by the Rayleigh criterion. This gives a theoretical resolution of 800 nm and we measured the resolution to be at least $1\,\mu\mathrm{m}$ for blue light [172, 176]. To be able to align the microscope objective[30], it is mounted to a brass tube connected to translation and tilt stages (see figure 3.6a). Rough alignment is done with a home-built non-magnetic $xyz$ linear translation stage, while the fine alignment works with a piezo $xyz$ stage[31] and a tilt stage[32]. The image is then magnified by a second commercial objective[33] with a focal length of $f_2 = 1250\,\mathrm{mm}$ leading to a magnification factor of 50. The magnified image is guided to an EMCCD camera[34] which has a pixel size of $16 \times 16\,\mu\mathrm{m}$. Thus, one pixel width corresponds to 320 nm.

Now, we describe the imaging technique used for dense atomic samples (see schematic setup in figure 3.6b). Phase-contrast polarization imaging was first introduced with lithium atoms [111] and relies on the dispersive phase shift instead of direct absorption giving rise to the atomic density. We use an off-resonant blue beam, close to the 421 nm transition, with a red-detuning of $\delta = \text{-}1.1\,\mathrm{GHz} = \text{-}35\,\gamma_{421}$ to suppress absorption. The imaging beam is linearly polarized and we apply the magnetic field in the beam propagation direction such that the atoms see a mixture of left- and right-handed circularly polarized light. In our case the dysprosium atoms are fully spin-polarized in the lowest lying Zeeman state $m_J = -8$. Thus the atoms couple mainly to the $\sigma^-$ optical transition, while the $\sigma^+$ transition is suppressed by a factor of $\sim$150 due to a ratio of 1/150 in the Clebsch-Gordan coefficients for the two transitions. Hence, the atoms show a strong circular birefringence or optical rotation. If both coupled and uncoupled polarizations are combined on a linear polarizer, with the angle $\theta$ between the initial linear polarization direction and the axis of the polarizer, the transferred intensity distribution depends on the dispersive shift of the atoms.

In order to extract the atomic column density independently of the camera properties, we take a series of three images for each sample. The first image with intensity distribution $I_1$ is taken with atoms and includes the information of the atoms, the second image with intensity $I_2$ is taken without atoms and the third one ($I_3$) is taken without imaging light. Then the column density is given by [176]

$$n_{\mathrm{2D}} = 8\,\frac{3\lambda^2}{2\pi}\,\frac{\delta}{\gamma_{421}}\left[\theta - \arccos\left(\sqrt{\frac{I_1 - I_3}{I_2 - I_3}}\cdot\cos\theta\right)\right] \tag{3.2}$$

recalling the detuning of the imaging light $\delta$ and the polarizer angle $\theta$. The atom number per camera pixel is calculated by $N_{\mathrm{pix}} = (16\,\mu\mathrm{m}/50)^2\,n_{\mathrm{2D}}$, where the prefactor is the imaged area on a single pixel.

---

[30] Special Optics: Microscope objective, 54-17-1250-532/421nm

[31] Physik Instrumente (PI): Nanopositioning stage P-563.3CD with travel ranges $300 \times 300 \times 300\,\mu\mathrm{m}$ and controller E-725.3CDA.

[32] Newport Spectra-Physics: M-TTN80.

[33] Special Optics: Objective, 54-17-25-532/421nm

[34] Andor: iXon DU897 ECS-EXF, $512 \times 512$ active pixels with a pixel size of $16\,\mu\mathrm{m}$

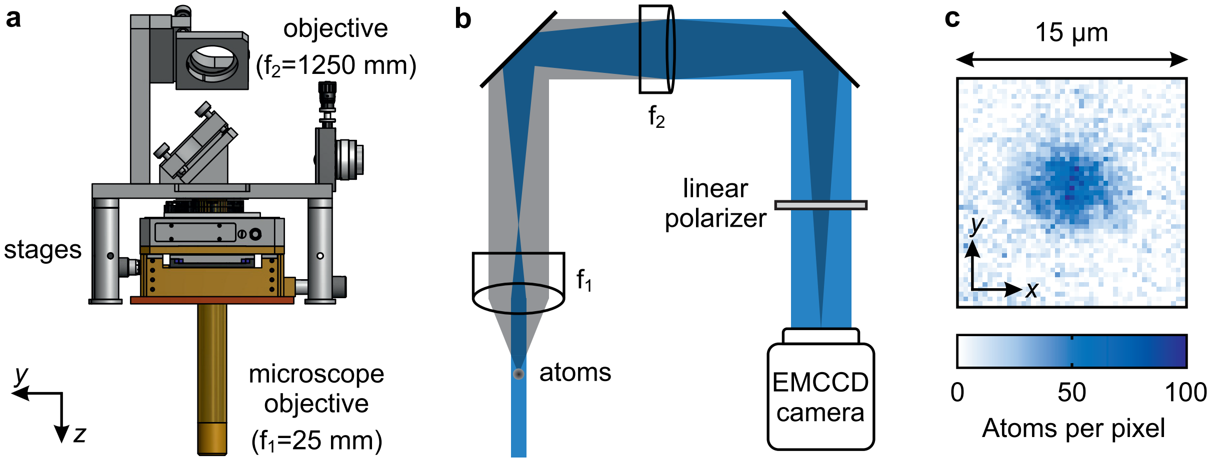

**Fig. 3.6. High-resolution imaging of a dipolar quantum gas.** **a**, Mechanical setup of the microscope imaging. The microscope objective ($f_1 = 25\,\mathrm{mm}$) is mounted on a brass tube, that can be adjusted with translation and tilt stages. The image is magnified by a factor of 50 with a collimation objective ($f_2 = 1250\,\mathrm{mm}$) also attached to translation stages. Adapted from [178]. **b**, Schematic setup of phase-contrast polarization imaging. A far detuned collimated imaging beam (blue) is guided on the atoms and magnified with the microscope objective and the second objective. Before the beam is imaged with an EMCCD camera it is directed through a linear polarizer. The atomic plane (grey) is also magnified and focussed on the camera. **c**, Single sample image of a dysprosium Bose-Einstein condensate. Here, each camera pixel has a physical size of $16\,\mu$m. As the magnification factor is 50, the field of view in this image is $15\,\mu\mathrm{m}\times 15\,\mu\mathrm{m}$.

For the experiments shown here, the polarizer angle is $\theta = 15°$, the image beam is detuned by $\delta = \text{-}35\,\gamma_{421}$ and the figure 3.6c shows an in situ image of a condensate consisting of 15,000 $^{164}$Dy atoms.

# 4. Classical and Quantum Ferrofluids: a Comparison

Fluid mechanics is the branch of physics that studies the motion of fluids (liquids and gases). It only considers macroscopic phenomena rather than the microscopic ones. Hence, the fluid is regarded as a continuous medium that deforms or flows when subjected to a force. By applying general conservation laws of mass, momentum and energy, one derives equations for the macroscopic variables pressure, density and fluid velocity.

In this chapter we compare classical ferrofluids (magnetic liquids) with quantum ferrofluids (magnetic gaseous condensates). Although they show differences in their basic properties (such as compressibility, magnetic polarization or superfluidity), they share similar relations and deformed states. First, we introduce properties and applications of classical ferrofluids and concentrate on the Rosensweig instability. After deriving the equations needed for the dispersion relation, we focus on the deformation of ferrofluid drops. As a comparison, we develop in the exact same manner equations describing quantum ferrofluids and present their excitation spectrum for a homogeneous gas. Finally, we characterize trapped inhomogeneous condensates and depict their anisotropic deformation and stability threshold.

## 4.1. Ferrofluids - Properties and Applications

Liquids that exhibit magnetization in the presence of a magnetic field, meaning a ferromagnetic material, are called ferrofluids [209]. However, since no substance is known whose Curie point exceeds its melting point [209, p. 33], ferrofluids are not found in nature and have to be synthesized. The rest of this section is on the composition, properties and applications of these synthesized ferrofluids.

Such magnetic fluids can be realized by forming a colloidal suspension of solid single-domain magnetic particles with a typical dimension of 10 nm in a liquid carrier. The magnetic particles are magnetite, maghemite or cobalt ferrite and the carrier liquid is water or an organic solvent. In order to avoid agglomeration, the magnetic particles are coated with a molecular layer of dispersant that acts as surfactant [210]. Dependent on carrier liquid, surfactant, the magnetic particles and their concentrations, characteristics like solubility, viscosity, saturation magnetization and permeability are controllable. Since the first generation of stable synthetic ferrofluids in 1965 [211], two main properties are used for technical applications [210, 212]: magnetic position control and absorption of electromagnetic energy [213].

Being ferromagnetic, ferrofluids are attracted by magnetic field maxima, and hence are used for dynamic sealing [214]. Ferrofluidic sealings are designed to protect sensitive environments and machinery components, but still maintain the rotational degree of freedom for a mechanical shaft. For this, a small amount of ferrofluid bridges the gap between a stationary magnet and a magnetizable rotating shaft. This is used for instance in hard disk drives that operate in a dust-free environment. The tiniest particle would be larger than the gap between head and disk of typically 3 nm and would result in a head crash and loss of data. As these sealings can permit pressure differences in the range of one atmospheric pressure, they are also used for rotational feedthroughs in high vacuum applications. One further mechanical usage of magnetic fluids is in loudspeakers[35] [215].

Additionally, there are biomedical applications for ferrofluids [216]. The property of ferrofluids to absorb electromagnetic energy at frequencies that differ from the water resonance frequency allows localized hyperthermia treatment. This technique was already used to treat brain tumours in human studies [217]. Further medical applications are in localized drug targeting by external fields [218] and contrast enhancement for Magnetic Resonance Imaging (MRI) [219].

Finally, magnetic fluids are an interdisciplinary topic that combine features of magnetism and fluid behaviour in one medium. As a response on magnetic fields, these fluids can display novel phenomena. These responses include spontaneous formation of labyrinth patterns [220] and the normal-field or Rosensweig instability [86]. Both effects are shown in figure 4.1 with a thin layer of ferrofluid[36] and as a second non-magnetic medium a chemiluminescent fluid. Despite all progress in the well-established field of ferrofluids, recent progress still rises novel applications with magnetic control [221]. One example is the self-assembly of magnetic nanoparticles in multipolar geometries [222].

In the next section, we use the theory of ferrohydrodynamics describing fluid motion with strong forces of magnetic polarization [209]. This is the basis to identify the underlying mechanisms responsible for a normal-field instability and the deformation of ferrofluids.

## 4.2. Normal-field instability of a classical ferrofluid

When a uniform magnetic field is applied perpendicular to a pool of magnetic fluid, it can destabilize the interface with air or a non-magnetic fluid [223]. If the magnetic field exceeds a critical value, a static ordered pattern deforms the surface. This spontaneous pattern formation is called normal-field or Rosensweig instability [86]. To get insight in this phenomenon, we present a description for the magnetic fluid motion that can be derived using ferrohydrodynamics [209].

---

[35] A loudspeaker uses the Lorentz force on the voice coil, that is attached to the membrane, placed in a permanent magnetic field. Most of the energy fed into a loudspeaker is wasted as dissipated heat to the membrane or air. As this is not an effective cooling process, the ferrofluid closes any air gap and conducts the heat away from the coil. In addition the fluid passively damps the movement of the speaker and avoids resonant response characteristics.

[36] Ferrotec Educational Ferrofluid Type EFH1. The carrier liquid is a light mineral oil.

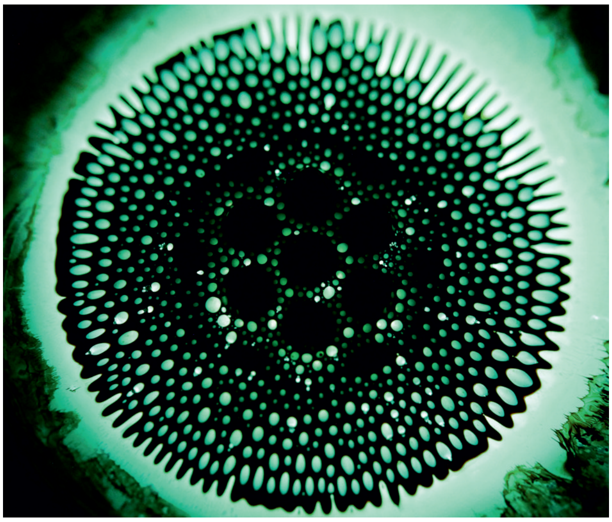

**Fig. 4.1. A patterned instability in a ferrofluid mixture.** A thin layer of ferrofluid (EFH1) with an unmixable non-magnetic chemiluminescent fluid taken from a glow stick. We applied a magnetic field perpendicular to the plane of view with a permanent magnet. One can observe in the center the normal-field instability with a triangular pattern of seven droplets. On the outer region the two fluids exhibit a static pattern that is related to the labyrinth instability. It exhibits a pattern of glowing bubbles within domains of ferrofluid, that convert at the most outside region to fingers of magnetic fluid. The picture was taken with the Canon EF 100mm f/2.8 USM Macro lens, ISO-3200 and an exposure time of 2 s.

### 4.2.1. Hydrodynamic equations of an incompressible ferrofluid

To describe the mechanics of fluids with mass density $\rho = \rho(\boldsymbol{r}, t)$ one introduces the velocity field $\boldsymbol{v} = \boldsymbol{v}(\boldsymbol{r}, t)$, which is a vector field that gives the velocity of an element of fluid at position $\boldsymbol{r}$ and time $t$. As total mass or particle number are conserved, the density and velocity field follow the *continuity equation*[37]

$$\frac{\partial \rho}{\partial t} + \nabla \cdot (\rho \boldsymbol{v}) = 0 \ . \tag{4.1}$$

Ferrofluids can in general be considered as incompressible [209, p. 20] such that the density $\rho$ is constant and the continuity equation reduces to a divergence-free velocity field

$$\nabla \cdot \boldsymbol{v} = 0 \ . \tag{4.2}$$

The continuity equation (4.1) describes the spatial dependence of the flow field $\boldsymbol{v}$, while the time dependence for incompressible fluids is well described by the *Navier-Stokes equation*

$$\rho \left( \frac{\partial \boldsymbol{v}}{\partial t} + (\boldsymbol{v} \cdot \nabla) \boldsymbol{v} \right) = -\nabla p + \rho \eta \nabla^2 v + \boldsymbol{f} \ , \tag{4.3}$$

---

[37] The continuity equation occurs in any field theory with a conserved quantity. In electromagnetism the electric charge is conserved, while for quantum mechanics the probability density is a conserved quantity.

with $\nabla p$ the thermodynamic pressure gradient, $\eta$ the dynamical viscosity and $\boldsymbol{f}$ the sum of all force densities that act throughout the whole volume[38]. Explicitly, for a ferrofluid and assuming non-viscous flow the equation of motion simplifies[39] to [209, p. 178]

$$\rho\frac{\partial \boldsymbol{v}}{\partial t} + \frac{\rho\nabla v^2}{2} = -\nabla p + \rho\boldsymbol{g}_0 + \mu_0 M\nabla H \ , \tag{4.4}$$

where $\boldsymbol{g}_0$ is the local gravitational acceleration[40] and $\mu_0 M\nabla H$ is the *Kelvin force density* [224, p. 144], [225], with $H$ the magnitude of the auxiliary magnetic field and $M$ the magnitude of the magnetization field[41]. For the magnetic force density we neglect magnetostriction of the single magnetic nanoparticles, meaning that we assume the microscopic magnetic moment to be constant [209, p. 111] and assume collinearity of magnetization and magnetic field. In conclusion, equations (4.2) and (4.4) are known as the incompressible *Euler equations* of ferrofluid dynamics.

In the following, we further simplify the Euler equations by investigating only potential flows. This assumption involves only irrotational velocity fields that fulfil $\nabla \times \boldsymbol{v} = 0$. Hence, the velocity field $\boldsymbol{v}$ can be described as the gradient of a scalar function

$$\boldsymbol{v} = \nabla\Phi \ , \tag{4.5}$$

the so-called *velocity potential* $\Phi(\boldsymbol{r}, t)$. By using the first part of the Euler equations (4.2), the velocity potential obeys *Laplace's equation* [226, p. 21]

$$\nabla^2\Phi = \Delta\Phi = 0 \ . \tag{4.6}$$

This equation needs further boundary conditions to be solved, especially for time-dependent problems or surfaces to other media. Hence, we will insert the velocity potential from eq. (4.5) to the second part of the Euler equations (4.4) and perform a volume integral to derive the *Bernoulli's equation* for unsteady potential flow [226, p. 19]

$$\rho\frac{\partial \Phi}{\partial t} + \frac{\rho v^2}{2} + p + \rho g_0 z - \mu_0 M H = f(t) = 0 \ , \tag{4.7}$$

where the gravitational force $\boldsymbol{g}_0$ is antiparallel to the $z$-direction and $f(t)$ is an arbitrary function of time, resulting from the integration. However, this function can be put equal to zero by transforming the velocity potential with $\Phi' = \Phi - \int f(t)\,\mathrm{d}t$, as the resulting velocity field remains unchanged. For steady flow (assuming the velocity potential is independent of time) eq. (4.7) simplifies to Bernoulli's principle or equation.

---

[38] A force density is defined as the force per unit volume. The force acting on a given volume $V$ is defined with the volume integral $\boldsymbol{F} = \int_V \boldsymbol{f}\,\mathrm{d}V$.

[39] In addition the vector relation $(\boldsymbol{v}\cdot\nabla)\boldsymbol{v} = \nabla v^2/2$ is used.

[40] The gravitational force is a body force density defined as force per volume and density. The total force acting throughout the body is $\boldsymbol{F} = \int \rho\boldsymbol{g}_0\,\mathrm{d}V$.

[41] The relation between $B$, $H$ and $M$ is in SI units $\boldsymbol{B} = \mu_0(\boldsymbol{H} + \boldsymbol{M})$. The magnetization field is the distribution of magnetic moments per volume and the magnetic moment is $\boldsymbol{\mu}_\mathrm{m} = \int \boldsymbol{M}\,\mathrm{d}V$. As the terminology for magnetic fields is far from being clear due to historical reasons, we use the following expressions: $\boldsymbol{B}$ is the magnetic field, while $\boldsymbol{H}$ is the auxiliary magnetic field or auxiliary field.

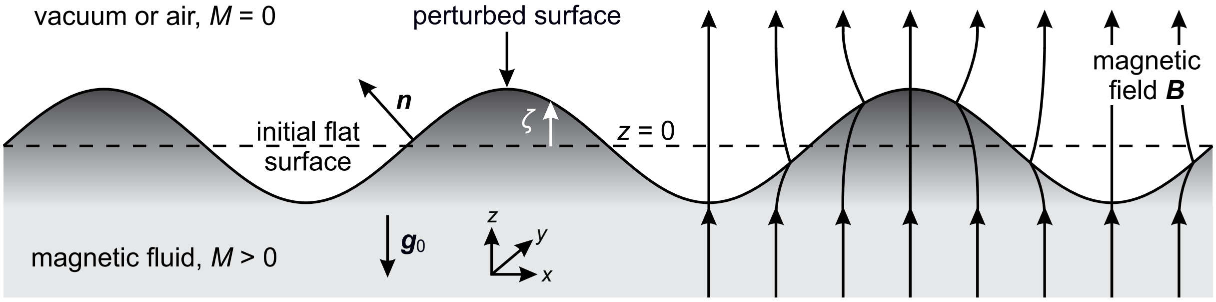

**Fig. 4.2. Qualitative sketch for a surface disturbance in a ferrofluid.** Initially the magnetic fluid occupies the region $z < 0$ with a flat surface, while the upper region is a non-magnetic phase (dashed line). The applied uniform magnetic field is perpendicular to the initial surface. The deflection of the surface is denoted with $\zeta$ with its normal vector $\boldsymbol{n}$. The gravitational force acts anti-parallel to the $z$-direction. Surface displacements perturb the magnetic field $\boldsymbol{B}$ whereby the magnetic field is focused at wave crests. Based on [209].

### 4.2.2. Dispersion relation of surface waves in a ferrofluid

Fluid surfaces tend to form a plane under the influence of gravitation. Applying a uniform magnetic field perturbs the ferrofluid surface and can induce a normal-field instability. Such external perturbations induce surface waves, that are discussed in this section to derive a dispersion relation. We follow a similar approach as presented in [226, chapter 12 and 61].

To obtain the dispersion relation we consider an initially flat volume of ferrofluid occupying the region of space $z < 0$. The upper half $z > 0$ is a non-magnetic phase, e.g. air with a pressure $p_0$ acting on the ferrofluid surface (see figure 4.2). To describe the surface behaviour, we use Laplace's equation[42] (4.6) and Bernoulli's equation (4.7). Starting with Laplace's equation, we define the boundary conditions: a surface wave propagating along the $x$-axis that is uniform along the $y$-axis and without spatial boundaries in all directions, meaning an infinite large plane. Consequently, we start with a simple harmonic assumption for the velocity potential $\Phi = f(z)\cos(kx - \omega t)$ with the wave number $k = 2\pi/\lambda$. It fulfils Laplace's equation

$$\Delta\Phi = \frac{\partial^2\Phi}{\partial x^2} + \frac{\partial^2\Phi}{\partial z^2} = \frac{\partial^2 f}{\partial z^2} - k^2 f = 0 \tag{4.8}$$

for $f(z) = A\mathrm{e}^{kz} + B\mathrm{e}^{-kz}$. We only take the first term as our fluid occupies the region $z < 0$ and the velocity potential has to remain finite. Thus, we obtain for the velocity potential

$$\Phi = A\mathrm{e}^{kz}\cos(kx - \omega t)\ . \tag{4.9}$$

The dispersion relation is still undefined, so we must set further boundary conditions. As we deal with a surface, we have to take into account the *surface tension* as a boundary condition. If the surface is curved, the pressures in the two media are different. This is

---

[42] This equation limits the solutions on an irrotational velocity field, however, this is non-relevant for this section that focuses on surface waves.

expressed in the *Laplace formula* or *Young-Laplace equation*

$$\Delta p = p_0 - p = \sigma_s \left( \frac{1}{R_x} + \frac{1}{R_y} \right) , \tag{4.10}$$

where $\sigma_s$ is the surface tension coefficient and $R_x, R_y$ are the principal radii of curvature of the surface at a given point. The velocity potential also has to fulfil the Bernoulli's equation (4.7). This equation is simplified by considering surface waves with amplitudes much smaller than the wavelength $\lambda$. Hence, the velocity of moving fluid particles is comparatively small such that we can neglect[43] the second term in eq. (4.7) and insert eq. (4.10)

$$\rho \frac{\partial \Phi}{\partial t} + \rho g_0 z - \sigma_\mathrm{s} \left( \frac{1}{R_x} + \frac{1}{R_y} \right) - \mu_0 M H = p_0 \ . \tag{4.11}$$

We define a small surface perturbation $\zeta = \zeta(x, y, t)$ that represents the $z$-coordinate of a point on the surface, where the equilibrium state is $\zeta = 0$ (see figure 4.2). To remove the constant pressure $p_0$ from the equation above, we redefine the potential $\Phi' = \Phi + (p_0/\rho)t$, as the resulting velocity field remains unchanged. Hence, by dropping the primes, eq. (4.11) results in

$$\rho \frac{\partial \Phi}{\partial t} + \rho g_0 \zeta - \sigma_\mathrm{s} \left( \frac{\partial^2 \zeta}{\partial x^2} + \frac{\partial^2 \zeta}{\partial y^2} \right) - \mu_0 M \frac{k \mu_\mathrm{r} M \zeta}{1 + \mu_\mathrm{r}} = 0 \ , \tag{4.12}$$

with $\mu_\mathrm{r}$ the relative permeability[44] and where we have replaced the auxiliary field $H$ by its expression obtained in appendix A.8 with eq. (A.46). The vertical component of the velocity is $v_z = \partial \zeta / \partial t$ and according to the definition of the velocity potential also $v_z = \partial \Phi / \partial z$ applies. Finally, by differentiating the relation (4.12) with respect to $t$ and afterwards replacing the time derivative $\partial \zeta / \partial t$ by a spatial derivative $\partial \Phi / \partial z$, we obtain the boundary condition on the potential $\Phi$

$$\rho \frac{\partial^2 \Phi}{\partial t^2} + \rho g_0 \frac{\partial \Phi}{\partial z} - \sigma_\mathrm{s} \frac{\partial}{\partial z} \left( \frac{\partial^2 \Phi}{\partial x^2} + \frac{\partial^2 \Phi}{\partial y^2} \right) - \frac{\mu_0 \mu_\mathrm{r} k M^2}{1 + \mu_\mathrm{r}} \frac{\partial \Phi}{\partial z} = 0 \ . \tag{4.13}$$

At last, inserting the potential $\Phi$ from eq. (4.9) in the condition (4.13) results in the dispersion relation of surface waves in a ferrofluid [209, p. 189]

$$\rho \omega^2 = \rho g_0 k + \sigma_\mathrm{s} k^3 - \frac{k^2 \mu_0 \mu_\mathrm{r} M^2}{1 + \mu_\mathrm{r}} \ . \tag{4.14}$$

The first term on the right-hand side corresponds to gravity waves existing at the fluid surface with the gravitational force acting as a restoring force [226, p. 39]. They dominate the right side of eq. (4.14), when $k$ is small or correspondingly when the wavelength is

---

[43] This approximation can be understood as follows: During one oscillation period $\tau$ the fluid particles travel the amplitude $a$ of the wave, hence their velocity is on the order of $v = a/\tau$. The velocity varies noticeably for time intervals on the order of $\tau$ or distances on the order on the wavelength $\lambda$. Therefore comparing the terms on the left hand side of eq. (4.4) the condition $\nabla v^2 \ll \partial v / \partial t$ is equivalent to $a^2/\lambda\tau^2 \ll a/\tau^2$ or $a \ll \lambda$. Hence, the oscillation amplitude has to be small compared to the wavelength.

[44] The relative permeability is the ratio of the medium permeability $\mu_\mathrm{med} = \mu_0(1 + \chi_\mathrm{med})$ to the vacuum permeability $\mu_0$, with $\chi_\mathrm{med}$ the magnetic susceptibility. Or in other words $\mu_\mathrm{r} = 1 + \chi_\mathrm{med}$.

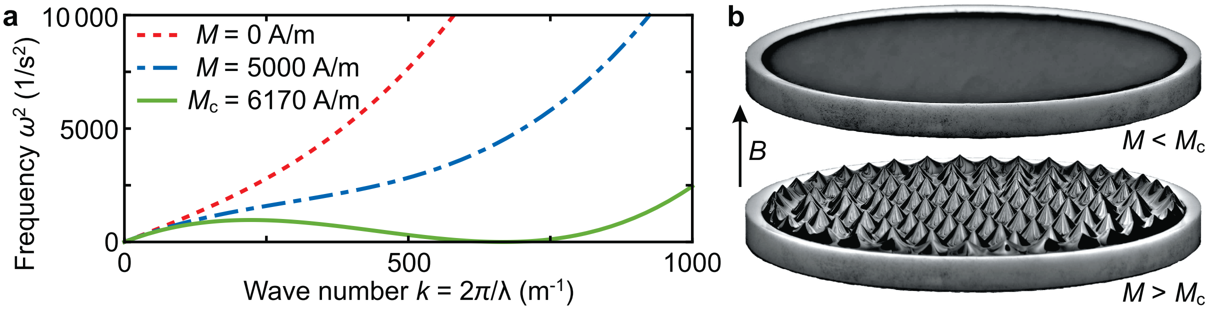

**Fig. 4.3. Dispersion relation of ferrofluid surface waves. a**, The dispersion relation of surface waves in a ferrofluid shown in the $\omega^2$-$k$ plane for different values of magnetization $M$. For the calculated example shown here, we used the measured properties [227] of the magnetic fluid EFH1 ($\rho = 1169\,\mathrm{kg/m^3}$, $\sigma_s = 0.0258\,\mathrm{N/m}$, $\mu_r = 2.552$). **b**, A ferrofluid in the presence of an applied magnetic field perpendicular to the surface remains flat for small magnetization. If the magnetic field (induced magnetization) exceeds a critical value, the surface develops a triangular pattern of spikes due to a softening of excitations. Images taken from [228].

long. Wind-generated ocean waves are an example of gravity waves. The second term is dominant for high values of $k$ and such waves are called capillary waves [226, p. 238]. These waves also travel at the inter-phase boundary of the fluid but in contrast to gravity waves the dynamics is dominated by the surface tension $\sigma_s$. Typically capillary waves on a water surface are ripples with a wavelength of a few centimeters. The dispersion relation of waves is shown in figure 4.3a as red dashed line. For small values of $k$ the graph starts linear, while for higher values the cubic capillary term dominates.

The last term is of importance for intermediate values of $k$, when a magnetic field is present. It describes a magnetic field concentration at the peaks of a surface disturbance, as depicted in figure 4.2. As a ferrofluid is attracted by field maxima it gives a negative contribution to the dispersion. Additionally, as $\omega$ appears squared, the negative magnetic term can lead to an imaginary $\omega$. For a critical magnetization[45] $M_c$ the dispersion relation becomes zero for a finite value of $k$ (green line in figure 4.3a) and the Rosensweig instability occurs [86]. This instability describes the phenomenon of a flat ferrofluid surface developing surface perturbations for a critical external field. These perturbations create a regular pattern, typically triangular, of surface spikes, as shown in figure 4.3b. This transition from a flat surface of surface spikes presents a hysteresis, closely related to first-order phase transitions [229].

## 4.3. Deformation of a ferrofluid drop in a uniform magnetic field

Magnetostriction is a property of magnetic materials that causes to change their shape due to a change in magnetization. In 1842 James Joule identified the magnetostrictive

---

[45] The critical magnetization is calculated by $M_c^2 = \frac{2}{\mu_0 \mu_r}(1+\mu_r)\sqrt{\rho g_0 \sigma_s}$ with the corresponding critical wave number $k_c = \sqrt{\rho g_0/\sigma_s}$ [209, p. 191].

effect on an iron bar exposed to a magnetic field [230]. Similar effects on the shape of a magnetizable fluid are possible under particular conditions. The starting point is a spherical magnetic fluid drop in the absence of any external force. The surface tension maintains the spherical shape in equilibrium as the surface energy is minimized with the smallest surface area. By applying a uniform homogeneous magnetic field, the drop deforms into a prolate spheroid, whose long axis is along the magnetic field lines to minimize its magnetic energy. Therefore, the magnetic forces counteract the surface tension and can even induce a jump in elongation.

Experiments showing these effects were performed for an immiscible ferrofluid drop in a non-magnetic fluid [231, 232]. Both fluids have the same density such that the magnetic drop is levitating against gravity. This instability or jump in shape can be understood from a balanced interplay between magnetic energy and interfacial tension energy. In the following, we present the contributing energy terms and find stable shapes by minimizing the total energy.

In the absence of a magnetic field, a levitating ferrofluid drop has a spherical shape with a radial size of $R_0$ in equilibrium. In the presence of a magnetic field, the drop forms a shape close to a prolate spheroid with semi-major axis length $R_\mathrm{c}$ and semi-minor axis length $R_\mathrm{a}$. In the following, we use a constant volume of $V = \frac{4}{3}\pi R_0^3 = \frac{4}{3}\pi R_\mathrm{a}^2 R_\mathrm{c}$ during any state of deformation. So, the product of the surface tension coefficient $\sigma_\mathrm{s}$ and the spheroid surface gives the surface energy[46]

$$E_\mathrm{s}(\kappa) = 2\pi\sigma_\mathrm{s} R_0^2 \kappa^{-1/3}\left(\kappa + \epsilon^{-1}\arcsin\epsilon\right) \tag{4.15}$$

with the aspect ratio $\kappa = R_\mathrm{a}/R_\mathrm{c}$ and the eccentricity $\epsilon(\kappa) = \sqrt{1-\kappa^2}$. The surface tension shows an energetic minimum for the smallest surface, which are round spheres with an aspect ratio of $\kappa = 1$.

On the contrary, the magnetic energy for a spheroidal drop exposed to a homogeneous field takes the form [232]

$$E_\mathrm{m}(\kappa) = -\frac{V\mu_0 H^2}{2}\left(\frac{1}{\mu_\mathrm{r}-1} + D_\mathrm{m}(\kappa)\right)^{-1} \tag{4.16}$$

with the shape dependent deformation factor[47] [234, p. 211-215]

$$D_\mathrm{m}(\kappa) = \frac{\kappa^2}{1-\kappa^2} - \frac{\kappa^2 \operatorname{artanh}\sqrt{1-\kappa^2}}{(1-\kappa^2)^{3/2}}\,. \tag{4.17}$$

---

[46] The surface area of a prolate spheroid is given as $A = 2\pi R_\mathrm{a} R_\mathrm{c}\left(\kappa + \epsilon^{-1}\arcsin\epsilon\right)$. In the limit of a sphere with $R_\mathrm{a} = R_\mathrm{c} = R_0$ the surface area simplifies by using $\kappa = 1, \epsilon = 0$ and $\lim_{\epsilon\to 0}\epsilon^{-1}\arcsin\epsilon = 1$ to $A = 4\pi R_0^2$.

[47] Here the deformation factor or *demagnetization factor* $D_\mathrm{m}$ is used to describe the magnetic material's response to a magnetic field. The factor $D_\mathrm{m}$ is defined such that a uniformly magnetized object $\boldsymbol{M}$ in a uniform magnetic field $\boldsymbol{B}$ shows a magnetic auxiliary field interior of the medium with $\boldsymbol{H}_\mathrm{med} = \boldsymbol{B}/\mu_0 - D_\mathrm{m}\boldsymbol{M}$. Evidently, the auxiliary field inside the medium $\boldsymbol{H}_\mathrm{med}$ points oppositely to the magnetic field $\boldsymbol{B}$ when the magnetization field $\boldsymbol{M}$ is sufficiently strong. Outside the medium the relation $\boldsymbol{B}/\mu_0 = \boldsymbol{H}$ is always true.

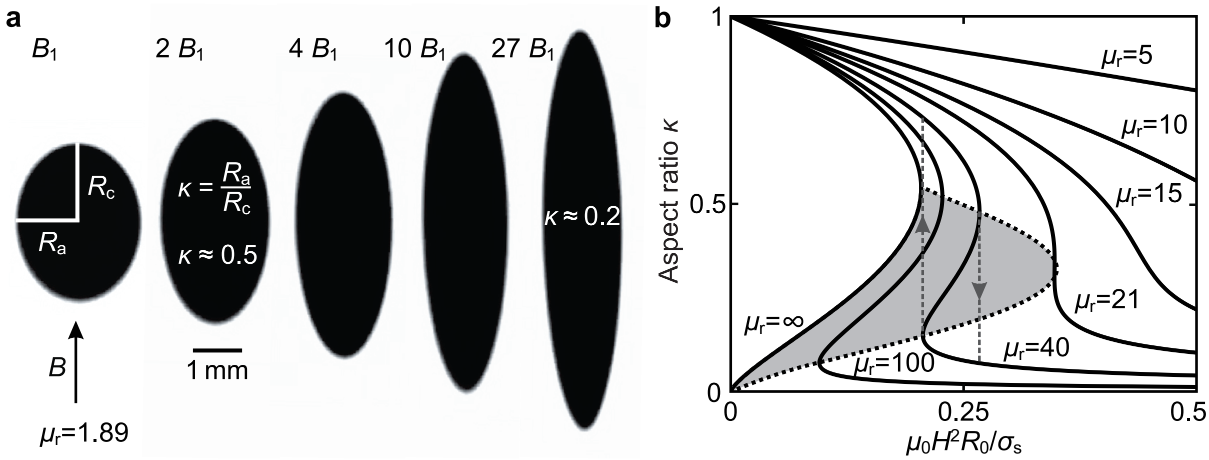

**Fig. 4.4. Deformation of a ferrofluid drop. a**, Photographs of a ferrofluid drop at different magnetic field strengths. The first image was taken at $B_1 = \mu_0 H_1 \approx 76\,\mathrm{G}$ and the drop elongates further for increasing magnetic field. The drop shape is described by a spheroid with axes $R_\mathrm{a}, R_\mathrm{c}$ and the aspect ratio $\kappa = R_\mathrm{a}/R_\mathrm{c}$. Measured parameters for the drop are $\mu_\mathrm{r} = 1.89, \sigma_\mathrm{s} = 0.0135\,\mathrm{N/m}$ and $R_0 = 1.29\,\mathrm{mm}$ leading to the value $\mu_0 H_1^2 R_0/\sigma_\mathrm{s} \approx 4.4$ [233]. **b**, Variation of the aspect ratio $\kappa$ for increasing magnetic field, shown for different relative permeabilities $\mu_\mathrm{r}$ (black lines). For $\mu_\mathrm{r} \gtrsim 21$ it shows an s-shaped curve and unstable regions (grey filled area). Due to this behaviour the drop can become unstable and turns to a different elongated state (grey dashed lines).

In this case of a spheroid it has the limits $D_\mathrm{m}(1) = 1/3$ (sphere) and $D_\mathrm{m}(0) = 0$. As a consequence the magnetic energy is minimized for fully elongated drops with $\kappa \to 0$. With this interplay of surface and magnetic forces, the drop adapts to elongated spheroids along the field direction to reach its energy minimum, as shown in figure 4.4a.

In order to give a quantitative expression for the drop shape with aspect ratio $\kappa$, we search for extrema in the total energy $E_\mathrm{s} + E_\mathrm{m}$ with respect to $\kappa$ for a given field $H$ and size $R_0$. This results in the expression $\mu_0 H^2 R_0/\sigma_\mathrm{s} = g(\kappa)$ [232], where the function $g(\kappa)$ is given in appendix A.9 with eq. (A.49). Figure 4.4b gives the calculated aspect ratio $\kappa$ against the function $g(\kappa)$. The horizontal axis is regarded as an axis of magnetic field squared. First, one sees the obvious behaviour that a magnetic drop elongates to lower aspect ratio $\kappa$ for increasing magnetic field. Second, for increasing relative permeability $\mu_\mathrm{r}$, the function goes from a monotonic curve to an s-shaped one. The transition between these two shapes appears for $\mu_\mathrm{r} \gtrsim 21$, a value found for ferrofluids with high concentrations of magnetic particles[48]. Further analysis of the energy functional shows that a part of the s-shaped curves corresponds to a local maximum in total energy, that is marked in figure 4.4b as grey area . Therefore, this part is unstable and for increasing magnetic field the magnetic drop can become unstable and subsequently must go to a stable point with a much more elongated shape. By again decreasing the magnetic field, the deformation shows a hysteresis effect in relation to a first order phase transition. Such an instability of ferrofluid magnetic drops including the hysteresis has been observed experimentally in [232] with a very concentrated ferrofluid phase with $\mu_\mathrm{r} \approx 40$.

---

[48] The record for the relative permeability of ferrofluids is $\mu_\mathrm{r} \approx 180$ at a temperature of -50°C [235, 236].

Finally, studies on the deformation of a non-levitating ferrofluid drop on a superhydrophobic surface, lead also to an elongation along the direction of the field [237, 238]. This deformation is illustrated in figure 4.5a,b for a ferrofluid drop submitted to a vertical magnetic field. However, when including a vertical magnetic gradient acting on the drop this first again leads to a deformation of the drop into a spiked cone and for a critical field strength to cleavage into two smaller drops [239], see figure 4.5c-e. For onward increasing magnetic field, the drops split further into drop patterns showing a static self-assembly of ferrofluid drops into ordered structures with mainly triangular symmetry, see figure 4.5f,g. The drop division is related to the Rosensweig instability from section 4.2, but differs from it in several ways. For instance, the Rosensweig instability appears also in a homogeneous magnetic field, while for the drop patterns one requirement is a magnetic gradient. Further, a Rosensweig pattern is reversible, while the drop patterns are irreversible when the field is removed (see figure 4.5h). The irreversibility preventing convergence is due to a repulsion between the drops and the non-wetting nature of the substrate, which ensures that the drops are not physically connected.

Herewith, the overview on classical ferrofluids ends. The rest of the chapter concentrates on quantum ferrofluids and points out the similarities of classical and quantum ferrofluids.

## 4.4. Softening of excitations in a quantum ferrofluid

In many-body physics elementary excitations are non-trivial and important, as they can describe properties such as superfluidity and its critical velocity [101, 159, 240]. First evidence for elementary excitations in a dilute condensate has been observed in 1996 as collective oscillations [241] in agreement with hydrodynamic equations for superfluids [226, p. 507]. Hence, in the following section we derive the quantum hydrodynamics in close similarity to classical hydrodynamics. After that, we use this description to determine the excitation spectrum of a homogeneous gas and consider phonon and roton softening, which lead to instabilities.

### 4.4.1. Hydrodynamic equations of a compressible quantum ferrofluid

Describing a quantum ferrofluid in a similar way as a classical ferrofluid may be achieved by using an equivalent set of equations for the GPE (2.12). These equations are dependent on the density $n = |\Psi|^2$ and the gradient of the phase, which is proportional to the local velocity of the condensate. To understand the nature of the velocity of the condensate, we follow a similar approach as described in [94, p. 41] and [95, p. 184].

We start with the dipolar non-local GPE (2.12), multiply it by $\Psi^*(\boldsymbol{r}, t)$ and subtract the complex conjugate of the resulting equation[49]. One derives the equation

$$\frac{\partial|\Psi|^2}{\partial t} + \nabla \cdot \left[\frac{\hbar}{2mi}(\Psi^*\nabla\Psi - \Psi\nabla\Psi^*)\right] = 0 \ , \tag{4.18}$$

---

[49] Subtracting the complex conjugated part is equal to twice the imaginary part.

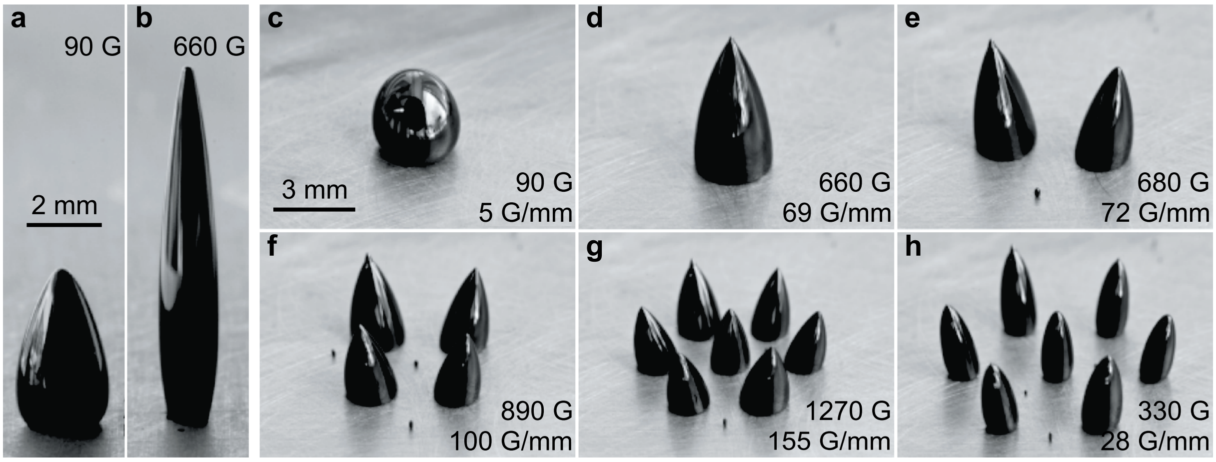

**Fig. 4.5. Ferrofluid drop on a superhydrophobic surface.** **a**,**b**, Photographs of a $20\,\mu$l ferrofluid drop exposed to a nearly uniform magnetic field perpendicular to the surface. The drop elongates along the magnetic field direction and its ellipticity increases for higher fields (field values given in figure). **c**-**h**, Ferrofluid drop upon increasing a non-uniform field with a strong magnetic gradient (the vertical magnetic field and gradient values are shown in the figure). The state of the drop is as follows: **c**, near-zero field (nearly spherical drop); **d**, strong field (conical spiked drop); **e**, above critical field (two daughter drops); **f**,**g**, increasing field leads to more drops; **h**, decreasing field shows strong hysteresis. Adapted from [239, Supplementary Materials].

that is the same as one obtains from a usual linear Schrödinger equation, as all non-linear potentials in the GPE are real. Eq. (4.18) is the *continuity equation* for the particle density $n = |\Psi|^2$ and may be written as

$$\frac{\partial n}{\partial t} + \nabla \cdot (n\boldsymbol{v}) = 0 \ , \tag{4.19}$$

where the *velocity of the condensate* is defined by

$$\boldsymbol{v} = \frac{\hbar}{2mi} \frac{\Psi^* \nabla \Psi - \Psi \nabla \Psi^*}{|\Psi|^2} \ . \tag{4.20}$$

The continuity equation (4.19) has now exactly the same form as eq. (4.1) for classical fluids. Here the conserved quantity is the probability density or particle density, while for the classical fluid it is the total mass or particle number. However, a gas is compressible, in contrast to an incompressible fluid with constant density described in section 4.2.1.

By expressing the wave function into an amplitude and a phase, we might write it as $\Psi(\boldsymbol{r},t) = \sqrt{n(\boldsymbol{r},t)}\, \mathrm{e}^{iS(\boldsymbol{r},t)}$ and in this case the velocity of the condensate is with eq. (4.20)

$$\boldsymbol{v} = \frac{\hbar}{m} \nabla S \ . \tag{4.21}$$

This equation describes the condensate with potential flows and the velocity potential is $\Phi = \hbar S/m$, in equality with eq. (4.5) for classical fluids. Hence, this condition is only valid for irrotational motions of the condensate that meet $\nabla \times \boldsymbol{v} = 0$.

By inserting the previously defined wave function $\Psi = \sqrt{n}\,\mathrm{e}^{iS}$ in the GPE (2.12) and separating imaginary and real part[50], we end up with the continuity equation (4.19) for the imaginary part and the real part reads

$$-\hbar\frac{\partial S}{\partial t} = -\frac{\hbar^2}{2m\sqrt{n}}\nabla^2\sqrt{n} + \frac{mv^2}{2} + V_{\mathrm{ext}}(\boldsymbol{r}) + gn + \Phi_{\mathrm{dip}}(\boldsymbol{r}) \ . \tag{4.22}$$

We find the *equation of motion for the velocity* by taking the gradient of the last equation

$$m\frac{\partial \boldsymbol{v}}{\partial t} + \frac{m\nabla v^2}{2} = -\frac{\nabla p}{n} - \nabla V_{\mathrm{ext}} - \nabla\Phi_{\mathrm{dip}} + \nabla\left(\frac{\hbar^2}{2m\sqrt{n}}\nabla^2\sqrt{n}\right) \tag{4.23}$$

with $\boldsymbol{v}$ given by eq. (4.21) and we define the pressure $p = n^2g/2$. Comparing eq. (4.23) with the Euler equation of a ferrofluid (4.4) shows a close similarity. They both include a kinetic energy term proportional to $\nabla v^2$, a pressure gradient $\nabla p$, an external force that causes trapping and an internal magnetic interaction. The only difference between the two equations is the last term in eq. (4.23) that corresponds to the zero-point energy, sometimes called *quantum pressure.*

Another minor difference exists in the magnetic interaction terms $\nabla\Phi_{\mathrm{dip}}$ and the Kelvin force $\mu_0 M\nabla H$ from eq. (4.4). A quantum ferrofluid is in the ultracold regime, and hence the magnetic constituents are fully spin polarized for magnetic fields[51] exceeding $\sim 10\,\mathrm{mG}$. Thus, for quantum ferrofluids the dipolar interaction energy is typically independent of the magnetic field strength, while for classical ferrofluids the magnetization usually increases for higher magnetic fields

### 4.4.2. Dispersion relation of a homogeneous dipolar gas

We now use the hydrodynamic equations to get a dispersion relation for quantum gases. By considering a three-dimensional (3D) homogeneous gas without external trapping and introducing small density perturbations to linearize the equations, we examine the excitation spectrum and possible instabilities. We obtain (calculated in appendix A.2) the *Bogoliubov excitation spectrum* [159, 242] of a dipolar homogeneous condensate

$$E(\boldsymbol{q}) = \hbar\omega(\boldsymbol{q}) = \sqrt{\left(\frac{\hbar^2q^2}{2m}\right)^2 + \frac{\hbar^2q^2}{2m}2n_0\left[g - g_{\mathrm{dd}}(1 - 3\cos^2\alpha)\right]} \ , \tag{4.24}$$

where $\alpha$ is the angle between the polarization direction $\boldsymbol{\mu}_{\mathrm{m}}$ and the wave propagation $\boldsymbol{q}$. For high values of $q$ the dispersion relation is well described with a quadratic dispersion with $E_{\mathrm{free}}(q) = \hbar^2q^2/2m$ the free particle energy. Whereas for small momenta, the excitations show a linear sound-like dispersion that can be related to modes of phonon quasi-particles. Indeed, the sound velocity is defined as $c_{\mathrm{s}}(\alpha) = \lim_{q\to 0}E(q)/q$ and reads

---

[50] The separation is done with following relations: $i\frac{\partial\Psi}{\partial t} = i\frac{\partial\sqrt{n}}{\partial t}\mathrm{e}^{iS} - \frac{\partial S}{\partial t}\sqrt{n}\,\mathrm{e}^{iS}$ with $\frac{\partial n}{\partial t} = 2\sqrt{n}\frac{\partial\sqrt{n}}{\partial t}$ and $-\nabla^2\Psi = (-\nabla^2\sqrt{n} + \sqrt{n}(\nabla S)^2 - i\sqrt{n}\nabla^2 S - 2i\nabla\sqrt{n}\nabla S)\,\mathrm{e}^{iS}$ with $\frac{1}{\sqrt{n}}\nabla(n\nabla S) = \sqrt{n}\nabla^2 S + 2\nabla\sqrt{n}\nabla S$

[51] The Zeeman energy has to be similar to the thermal energy. Thus, the rough estimate $\mu_{\mathrm{B}}B \approx k_{\mathrm{B}}T$ yields $B = 10\,\mathrm{mG}$ for $T = 700\,\mathrm{nK}$.

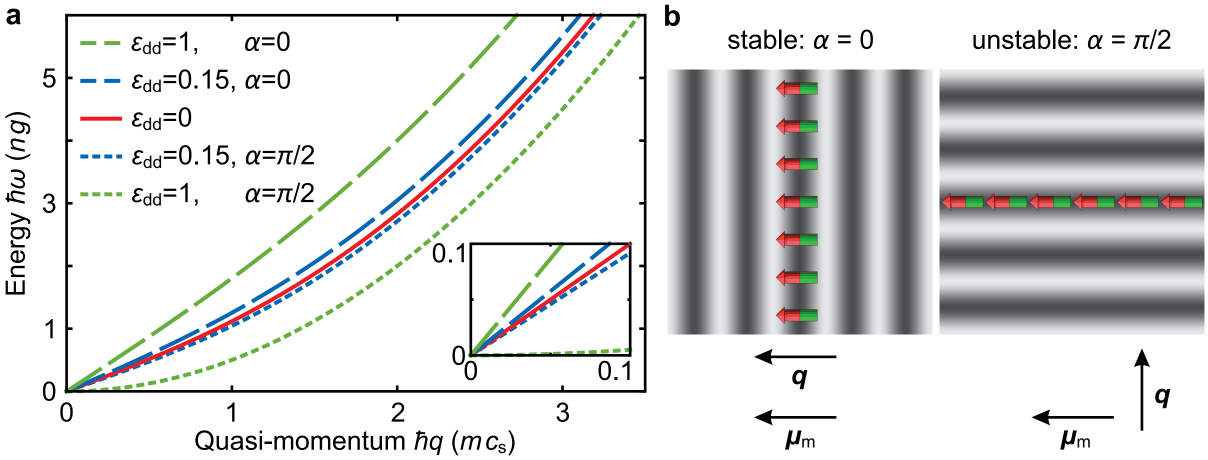

**Fig. 4.6. Excitations in a homogeneous quantum gas. a**, Universal dispersion relation of a 3D homogeneous dipolar Bose gas in dimensionless units with the sound velocity $c_s = \sqrt{n_0 g/m}$. Without dipolar interactions (red solid line) the dispersion relation starts linearly with a transition to a quadratic free particle behaviour. Weak dipolar interactions (blue lines) stiffen the dispersion for phonons travelling parallel ($\alpha = 0$) in polarization direction $\boldsymbol{\mu}_m$, while softening in the perpendicular direction ($\alpha = \pi/2$). Strong dipolar interactions (green lines), change the dispersion dramastically (see inset) and can lead to a phonon instability. **b**, Illustrating the phonon instability for strongly dipolar gases. Density waves perturb the homogeneous gas and create lines of increased density (grey shaded area). Dependent on the phonon propagation direction, the created lines show dipolar repulsion and are stable ($\alpha = 0$) or show dipolar attraction and are unstable ($\alpha = \pi/2$).

$c_s(\alpha) = \sqrt{n_0 g/m}\sqrt{1 - \varepsilon_{dd}(1 - 3\cos^2\alpha)}$. The dipolar interaction induces an anisotropic sound velocity (see figure 4.6a). It is maximal for excitations propagating along the magnetization direction ($\alpha = 0$), while it is minimal in the perpendicular direction ($\alpha = \pi/2$). This anisotropy of the excitation spectrum[52] has been investigated with Bragg spectroscopy [245] in a chromium BEC with $\varepsilon_{dd} = 0.15$ [54].

Strong dipolar interactions ($\varepsilon_{dd} \gtrsim 1$) reveal the anisotropy of the excitation spectrum (see inset of figure 4.6a). While the phonon modes in magnetization direction ($\alpha = 0$) are stiffened and show real and positive excitation energies, the opposite happens in the perpendicular direction. There ($\alpha = \pi/2$) the dipolar interaction softens the modes and leads for $g_{dd} > g$ to imaginary excitation energies, indicating a so-called *phonon instability*. The phonon instability occurs for phonons with the lowest possible momentum $q \to 0$.

Figure 4.6b intuitively illustrates this anisotropic behaviour. A phonon with $\boldsymbol{q}$ in the magnetization direction $\boldsymbol{\mu}_m$ creates planes of higher density where the dipoles point out of the density plane. In this configuration the dipoles interact repulsively leading to an increased energy and hence a stable configuration. This is again the opposite for the perpendicular direction. Here, the lines of increased density are aligned with the dipoles, introducing an attractive dipolar interaction. The system can lower its energy by populating this unstable mode that finally leads to a phonon instability.

---

[52] For trapped condensates in Thomas-Fermi approximation the averaged sound velocity is decreased by the factor $32/15\pi$ [243, 244].

To conclude this section, let us compare the results in a homogeneous dipolar gas with a classical ferrofluid. In section 4.2 we focused on incompressible ferrofluids and hence neglected any local density changes needed for sound waves[53]. However, anisotropic sound velocities have been predicted [246] and measured [247] for compressible ferrofluids with vicious flow. Here, the anisotropy arises from a change in the ferrofluid microstructure that modifies the viscosity, but the actual mechanism is very complicated and remains unclear. One possible process might be the formation of magnetic particle chain clusters [248]. A detailed view into the acoustics of magnetic fluids is given in [249, section 3.9].

### 4.4.3. Roton excitations in a two-dimensional geometry

In the previous section we presented the property of homogeneous condensates to become dynamically unstable for dominating dipolar interactions ($\varepsilon_{\mathrm{dd}} \geq 1$). For this part, we will show that in contrast to 3D condensates a quasi-two-dimensional (2D) gas is stable even for strongly dipolar BECs ($\varepsilon_{\mathrm{dd}} \gg 1$). This situation is achieved by adding a strong harmonic trapping potential in the polarization direction with trapping frequency $\omega_z$. If the confinement is sufficiently strong[54] the density distribution is restricted to the ground state of the harmonic oscillator. Consequently, the excitations along the $z$-direction are exponentially suppressed, which prevents softening of phonon modes propagating along the dipole direction [250].

By assuming the above mentioned, we can analytically calculate (see appendix A.3) the excitation spectrum of a two-dimensional homogeneous dipolar BEC [250, 251]

$$E(q_\perp) = \sqrt{\left(\frac{\hbar^2 q_\perp^2}{2m}\right)^2 + \frac{\hbar^2 q_\perp^2}{2m} 2n_0 \left[g + 2g_{\mathrm{dd}} H_{\mathrm{2D}}\left(\frac{q_\perp \sigma_z}{\sqrt{2}}\right)\right]} \tag{4.25}$$

with $q_\perp$ the absolute value of the quasi-momentum perpendicular to the confinement and dipole direction, $H_{\mathrm{2D}}(x) = 1 - \frac{3\sqrt{\pi}}{2}|x|\,\mathrm{erfc}(x)\mathrm{e}^{x^2}$ with erfc(x) the complementary error function and we recall $\sigma_z = \sqrt{\hbar/m\omega_z}$. By comparing the dispersion relations of the 3D (eq. (4.24)) and 2D homogeneous case they exhibit a similar structure. However, they feature one major difference in the 2D case, as the effective dipolar contribution is dependent on the absolute value of the quasi-momentum $q$ and is proportional to the monotonously decreasing function $H_{\mathrm{2D}}(q_\perp \sigma_z/\sqrt{2})$, depicted in figure 4.7a.

As already mentioned the reduction to two dimensions changes the stability properties. Considering the phonon instability for momentum $q \to 0$, one gets the 2D stability criterion $g + 2g_{\mathrm{dd}} > 0$. If this condition fails, the dispersion energy becomes imaginary, indicating the missing existence of a ground state. However, due to the momentum dependence of the dipolar interaction, there exists one further possible instability: The dispersion relation may show a local minimum at finite values of $q_\perp$ for $g_{\mathrm{dd}} > g$, as seen in figure 4.7b. In analogy to the excitations in superfluid helium [34, 240, 252] the quasi-particles related to

---

[53] The derivation of sound waves in fluids is well established [226, p. 245], but the anisotropic sound velocity is beyond the scope of this thesis.

[54] This means it has to satisfy the condition $\mu = n_0(g + 2g_{\mathrm{dd}}) \ll \hbar\omega_z$.

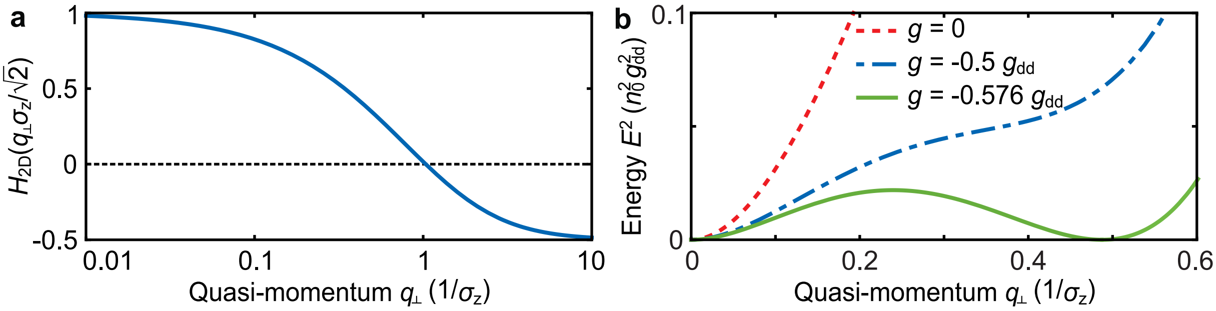

**Fig. 4.7. Excitation spectrum of a 2D homogeneous dipolar gas. a**, The function $H_{2D}$ characterizing the momentum dependence for the effective 2D dipolar interaction. For $q_\perp < \sigma_z = \sqrt{\hbar/m\omega_z}$ the effective dipolar interaction is repulsive, while for higher momenta it is attractive. **b**, Dispersion relation for a 2D homogeneous dipolar gas. We plot three different contact interaction strengths: purely dipolar case (red dashed line), attractive regime (blue dash-dot line) and for values at the roton instability with a local minimum (green solid line). For the plot we used following values for dysprosium atoms: $n_0 = 10^{20}\,\mathrm{m}^{-3}$, $n_0 g_{dd}/\hbar = 2\pi \cdot 536\,\mathrm{Hz}$ and $\omega_z = 2\pi \cdot 2\,\mathrm{kHz}$.

this minimum are called *rotons*. The excitation spectrum with such a *roton minumum* is often referred to a *roton-maxon spectrum* [33]. This roton-maxon-spectrum is observable in a small parameter range of interaction strengths, as shown in figure 4.7b. If the minimum reaches zero energy (in the figure achieved by decreasing the contact interaction strength $g$) a *roton instability* occurs, that is fundamentally different to a phonon instability. While a phonon instability happens at zero momentum, a roton instability is related to a finite momentum, meaning the instability exhibits a characteristic roton length scale.

Following the main message of this chapter, we again compare the demonstrated properties of a quantum ferrofluid with a classical ferrofluid. The roton-maxon-spectrum shown here in a 2D quantum ferrofluid is similar to the excitation spectrum of surface waves in classical ferrofluids presented in section 4.2.2. For example, they both feature a dispersion relation with local minimum at a finite length scale. Furthermore, in both cases tuning the internal interaction properties of the fluid can drive the fluid to an instability: the Rosensweig instability for the classical case and the roton instability for the quantum one. Subsequent to the instability, a classical ferrofluid undergoes spontaneous deformation into regular surface patterns. A very similar pattern formation has been theoretically predicted for an interface of a dipolar condensate [253].

Finally, we mention a short list of predicted roton-related effects for trapped dipolar condensates in three dimensions. All the mentioned effects were calculated using numerical methods to evaluate the Gross-Pitaevskii equation (2.12). Analytical approximations as shown in section 2.3.2 and 2.3.3 are not feasible predicting such unusual effects.

Under certain circumstances an oblate shaped dipolar BEC assumes a biconcave shape, with its maximum density off-center [31, 32]. These biconcave condensates can become unstable due to azimuthal excitations, a so-called angular roton [254]. Perturbation theory has shown that the unstable density modulation has a wavelength characteristic of the roton length scale [255]. Last, the roton-maxon spectrum remains for three dimensions, but is broadened as its shape is density dependent [256, 257].

## 4.5. Deformation and stability of a trapped dipolar condensate

Now, we discuss the static properties of trapped inhomogeneous dipolar condensates, such as deformation and stability conditions. Recalling section 2.3.3, we introduced the density distribution of a non-dipolar condensate in the Thomas-Fermi approximation to be an inverted parabola given by eq. (2.21). As the short-range contact interaction is isotropic and only dependent on local properties, the Thomas-Fermi radii in the three different directions are independent, see eq. (2.22). Whereas, when considering a dipolar condensate, the occurring dipolar interaction is anisotropic and long-range, and hence depends on global properties, such as the complete spatial extent. Thus, we expect the Thomas-Fermi radii to be coupled with each other and to show an anisotropic behaviour.

In this section we focus on the static behaviour of quantum gases, such as magnetostriction or instabilities. Both are an important source of information about the nature of dipolar condensates. But first, we have to introduce the hydrodynamic equations in Thomas-Fermi approximation.

### 4.5.1. Hydrodynamics in Thomas-Fermi approximation

Now, we utilize the Thomas-Fermi approximation, that we already introduced in section 2.3.3 and give the theoretical tools needed to describe static properties of dipolar condensates. The Thomas-Fermi approximation neglects the kinetic term in the stationary GPE (2.14). Equally, neglecting the quantum pressure term of the hydrodynamic equations (4.19) and (4.23) results in the Thomas-Fermi limit valid for dominant interactions. The presence of the non-local dipolar mean-field potential $\Phi_{\text{dip}}$ (2.15) means that the hydrodynamic equations are integral equations that are not trivial to solve. Nevertheless, by adopting an inverted parabola ansatz for the density profile[55] with eq. (2.21), the dipolar mean-field potential contains only terms that are constant or quadratic in the spatial coordinates. This leads to the remarkable effect that even by including dipolar interactions the density distribution remains an inverted parabola. This behaviour has been investigated extensively for trapped [258, 259] and free expanding condensates [36–38]. In the following short summary, we will focus on static inhomogeneous trapped quantum ferrofluids in Thomas-Fermi approximation, whose equilibrium state is described with

$$\mu = V_{\text{ext}}(\boldsymbol{r}) + g\, n(\boldsymbol{r}) + \Phi_{\text{dip}}(\boldsymbol{r})\,, \tag{4.26}$$

that is the stationary case ($\boldsymbol{v} = 0$) of eq. (4.22) neglecting the quantum pressure term.

First, to simplify the discussion on trapped quantum ferrofluids, we choose a trapping potential with a cylindrical symmetry along the polarization direction $z$ of the magnetic dipoles. The external trap then reads $V_{\text{ext}}(\rho, z) = m/2\,(\omega_\rho \rho^2 + \omega_z z^2)$ with $\rho^2 = x^2 + y^2$ and

---

[55] Although this section is about static properties, we give for completeness the respective velocity of the condensate as $\boldsymbol{v}(\boldsymbol{r}, t) = \frac{1}{2}\nabla\left[\alpha_x(t)x^2 + \alpha_y(t)y^2 + \alpha_z(t)z^2\right]$, where the parameters $\alpha_j = \dot{R}_j/R_j$ describe the radii change in time.

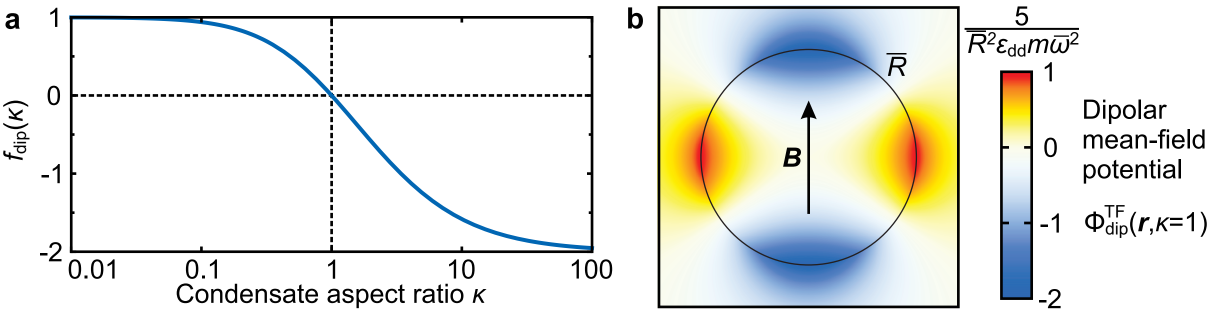

**Fig. 4.8. Geometry dependent dipolar mean-field potential. a**, The dipolar anisotropic function $f_{\mathrm{dip}}(\kappa)$. Its asymptotic values are $f_{\mathrm{dip}}(0) = 1$ and $f_{\mathrm{dip}}(\kappa \to \infty) = -2$, while it vanishes for $\kappa = 1$. **b**, The dipolar mean-field potential for $\kappa = 1$. It presents a saddle-like shape: attractive along the polarization axis $\boldsymbol{B}$ and repulsive perpendicular. The circle with radius $\overline{R}$ marks the spatial extent of the condensate.

we define the *trap aspect ratio* $\lambda = \omega_z/\omega_\rho$. Second, for the density distribution we adopt an inverted parabola with cylindrical symmetry and corresponding Thomas-Fermi radii $R_\rho$ in radial direction and $R_z$ in axial direction. We may also define the *condensate aspect ratio* $\kappa = R_\rho/R_z$, as was done for the treatment of classical ferrofluid drops in section 4.3. The evaluation of the dipolar mean-field potential $\Phi_{\mathrm{dip}}$ (2.15) over the parabolic density distribution can be achieved analytically through the use of spheroidal coordinates [258, 259]. It results in a potential inside the condensate region, given by

$$\Phi^{\mathrm{TF}}_{\mathrm{dip}}(\rho, z, \kappa) = n_0 g_{\mathrm{dd}} \left[ \frac{\rho^2}{R_x^2} - \frac{2z^2}{R_z^2} - f_{\mathrm{dip}}(\kappa) \left( 1 - \frac{3}{2} \frac{\rho^2 - 2z^2}{R_x^2 - R_z^2} \right) \right] \tag{4.27}$$

with the geometry dependent *dipolar anisotropic function*

$$f_{\mathrm{dip}}(\kappa) = \frac{1 + 2\kappa^2}{1 - \kappa^2} - \frac{3\kappa^2 \operatorname{artanh}\sqrt{1 - \kappa^2}}{(1 - \kappa^2)^{3/2}} \,. \tag{4.28}$$

The dipolar anisotropic function is illustrated in figure 4.8a and is a monotonically decreasing function that changes sign at $\kappa = 1$. It is very similar to the deformation factor of classical ferrofluids mentioned in eq. (4.17). As stated before the terms in $\Phi^{\mathrm{TF}}_{\mathrm{dip}}$ are either constant or quadratic in the spatial coordinates, just like the contributions of the harmonic trap or contact interaction to eq. (4.26). Thus an inverted parabola remains a self-consistent solution to the dipolar hydrodynamic equations.

To get an intuitive picture how the dipolar mean-field potential alters the condensate shape, we consider a spherical symmetric trap ($\lambda = 1$) with frequency $\overline{\omega}$. For a weakly dipolar condensate ($\varepsilon_{\mathrm{dd}} \ll 1$) the density distribution remains nearly spherical ($\kappa = 1$) with a Thomas-Fermi radius $\overline{R}$. Then the calculated dipolar mean-field potential is [260]

$$\Phi^{\mathrm{TF}}_{\mathrm{dip}}(\boldsymbol{r}, \kappa = 1) = \varepsilon_{\mathrm{dd}} \frac{m\overline{\omega}^2}{5} \left( 1 - 3\cos^2\vartheta \right) \begin{cases} r^2 & \text{for } r \leq \overline{R} \\ \frac{\overline{R}^5}{r^3} & \text{for } r > \overline{R} \end{cases} \,. \tag{4.29}$$

For this case, as shown in figure 4.8b, the dipolar mean-field potential $\Phi^{\mathrm{TF}}_{\mathrm{dip}}$ is saddle-shaped.

It is attractive along the polarization axis and repulsive perpendicular to it. The potential outside the condensate corresponds obviously to a field generated by $N$ dipoles located at the center of the condensate. Therefore, a dipolar condensate becomes elongated along the polarization axis due to the anisotropic, mean-field dipolar potential. Such a change of the cloud shape due to internal magnetic forces is called magnetostriction and will be discussed in the next section.

## 4.5.2. Magnetostriction of quantum ferrofluids

We have seen in the previous section that a parabolic density profile is a solution of the hydrodynamic equation (4.26) in Thomas-Fermi approximation. It remains to determine the Thomas-Fermi radii such that they satisfy the hydrodynamic equation. Substituting the dipolar mean-field potential (4.27) in the hydrodynamic equation (4.26) and comparing constant and quadratic coefficients in respect to the spatial coordinates, yields three coupled equations. The first equation, due to the constant terms, determines the chemical potential

$$\mu = n_0 \left[ g - g_{\mathrm{dd}} f_{\mathrm{dip}}(\kappa) \right] = g\, n_0 \left[ 1 - \varepsilon_{\mathrm{dd}} f_{\mathrm{dip}}(\kappa) \right] . \tag{4.30}$$

This equation indicates that the effect of the dipolar interaction lowers the chemical potential[56] for prolate condensates ($\kappa < 1$), while raising it for oblate condensates ($\kappa > 1$). The second and third equation are obtained from the quadratic coefficients and determine the Thomas-Fermi radii [258, 259]

$$R_\rho = 15^{1/5} \left( \frac{Na}{\overline{a}} \right)^{1/5} \left( \lambda^{2/3} \kappa \right)^{1/5} \left[ 1 + \varepsilon_{\mathrm{dd}} \left( \frac{3}{2} \frac{\kappa^2 f_{\mathrm{dip}}(\kappa)}{1-\kappa^2} - 1 \right) \right]^{1/5} \overline{a} \tag{4.31}$$

and $R_z = R_\rho/\kappa$ with[57] the condensate aspect ratio $\kappa$, determined by solving the transcendental equation

$$\lambda = \kappa \left( \frac{1 + 2\varepsilon_{\mathrm{dd}} - \frac{3\varepsilon_{\mathrm{dd}} f_{\mathrm{dip}}(\kappa)}{1-\kappa^2}}{1 - \varepsilon_{\mathrm{dd}} + \frac{\kappa^2}{2} \frac{3\varepsilon_{\mathrm{dd}} f_{\mathrm{dip}}(\kappa)}{1-\kappa^2}} \right)^{1/2} . \tag{4.32}$$

Figure 4.9a shows typical density profiles of non-dipolar and dipolar condensates in a spherical trap ($\lambda = 1$). For increasing dipolar interaction the condensate becomes more prolate than the external trap and it always presents $\kappa < \lambda$. Or in other words, a dipolar condensate elongates along the polarization direction showing magnetostriction due to the interplay of external trapping, short-range interactions and anisotropic dipolar interactions. Evidently, the condensate and trap aspect ratio are equal in the non-dipolar case and the radii simplify back to eq. (2.22) derived in section 2.3.3.

We take a closer look at the transcendental equation (4.32) with figure 4.9b. Usually in experimental realizations the external confinement remains constant, while one changes the

---

[56] Note that this also changes the validity criterion for the Thomas-Fermi approximation compared to section 2.3.3. The approximation is suitable if $N(a - f_{\mathrm{dip}}(\kappa) a_{\mathrm{dd}})/\overline{a} \gg 1$ is fulfilled. A systematic discussion in [261] results in more accurate values describing the very prolate case $N(a - a_{\mathrm{dd}})\kappa^{5/3}/\overline{a} \gg 1$ and the very oblate case $N(a + 2a_{\mathrm{dd}})/\kappa^{10/3}\overline{a} \gg 1$.

[57] Recalling the characteristic oscillator length $\overline{a} = \sqrt{\hbar/m\overline{\omega}}$ with $\overline{\omega} = (\omega_\rho^2 \omega_z)^{1/3}$.

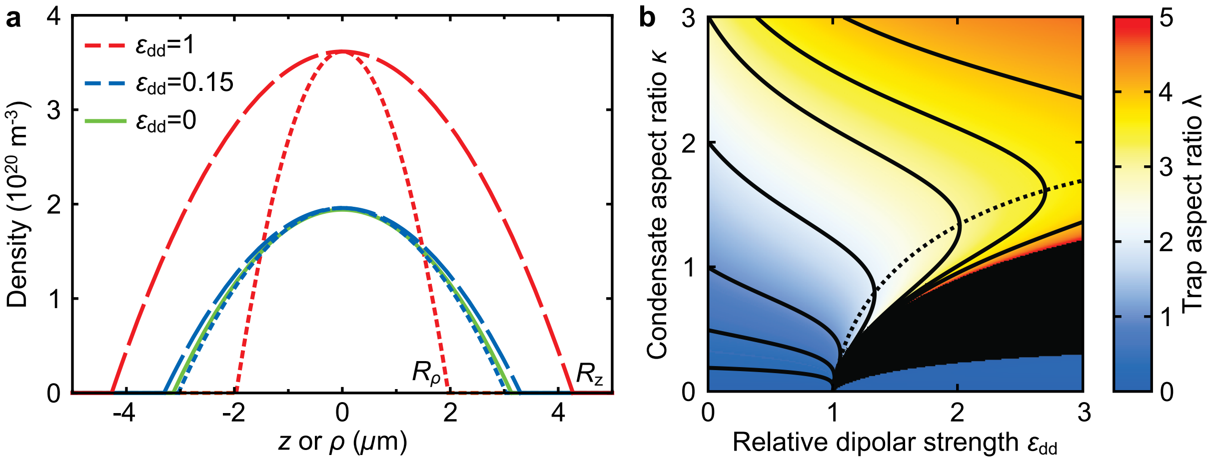

**Fig. 4.9. Magnetostriction of a quantum ferrofluid. a**, Density profiles of non-dipolar and dipolar condensates. Density distributions in Thomas-Fermi approximation along the radial or axial direction for condensates with 10,000 atoms with the mass of $^{164}$Dy in a spherical trap ($\lambda = 1$) with $\overline{\omega} = 2\pi \cdot 100\,\mathrm{Hz}$ and $a = 100\,a_0$. A non-dipolar BEC is also spherical ($\kappa = 1$) with a Thomas-Fermi radius of $\overline{R} = 3.13\,\mu\mathrm{m}$ (green line). Adding weak dipolar interactions ($\varepsilon_{\mathrm{dd}} = 0.15$) perturbs slightly the aspect ratio to $\kappa \approx 0.92$, meaning an elongation along the polarization direction $z$ (dashed and dotted blue line). Strong dipolar interactions ($\varepsilon_{\mathrm{dd}} = 1$) modify strongly the central density and the aspect ratio to $\kappa \approx 0.42$ with a radial radius of $R_\rho \approx 2.0\,\mu\mathrm{m}$ (dotted red line) and an axial one of $R_z \approx 4.3\,\mu\mathrm{m}$ (dashed red line). **b**, Condensate aspect ratio $\kappa$ as a function of the relative dipolar strength $\varepsilon_{\mathrm{dd}}$. It shows solutions of the transcendental equation (4.32) dependent on the trap aspect ratio $\lambda$. The value of $\lambda$ is presented as false colour and each black line is a single value of $\lambda$ that can be read off by noting that $\lambda = \kappa$ for $\varepsilon_{\mathrm{dd}} = 0$. For increasing dipolar interactions the condensate shrinks radially and elongates axially until it reaches the stability threshold marked with a dashed black line. Every solution below this line is not an energetic minimum and the BEC collapses radially to $\kappa \to 0$. The black region indicates imaginary solutions and the blue region below corresponds to solutions with imaginary Thomas-Fermi radii.

internal interactions. Hence, we focus on a constant trap aspect ratio $\lambda$ and increase the relative dipolar strength $\varepsilon_{\mathrm{dd}}$, depicted as black lines in figure 4.9b. As long as $0 \leq \varepsilon_{\mathrm{dd}} \leq 1$ there exists a single solution for any chosen $\lambda$. As expected, the condensate aspect ratio $\kappa$ decreases for stronger dipolar interactions. But for $\varepsilon_{\mathrm{dd}} > 1$, the transcendental equation develops imaginary solutions (black region) and exhibits further possible solutions (below the dashed black line). This may indicate an instability of a dipolar condensate and is the subject of what follows.

As one might expect, any solutions below the dashed line in figure 4.9b are unstable solutions that do not belong to an energetic minimum. This would be very similar to the deformation of a classical ferrofluid drop, introduced in section 4.3. A ferrofluid drop also elongates along the magnetic field direction and eventually undergoes an instability for sufficiently strong dipolar interactions. The previous analysis of the interplay of surface energy and magnetic energy explained stable and unstable regions in figure 4.4. Therefore, to be fully convinced for the case of a quantum ferrofluid, we analyse the energy functional (2.16) evaluated for a parabolic density profile in the next section.

### 4.5.3. Instability due to deformation

In order to get a more quantitative insight into the instability of a dipolar condensate, we calculate the energy functional (2.16) in Thomas-Fermi approximation. We again consider an external radially symmetric trapping and evaluate the energy functional over a general radially symmetric parabolic density profile with Thomas-Fermi radii $R_\rho$ and $R_z$ as variational parameters. We mention the resulting energy expressions in appendix A.5, that are used in the following.

To obtain the instability region, we investigate the energy landscape $E(R_\rho, R_z)$ and search for energy minima. We give a detailed discussion about the case of a dipolar BEC in a trap with aspect ratio $\lambda = 3$, shown in figure 4.10a-d, and keep figure 4.9b in mind. For $\varepsilon_{\mathrm{dd}} < 1$ the energy landscape supports a global minimum for $\lambda = 3$ and also for any other harmonic external trap (figure 4.10a). When lowering the contact interaction to $\varepsilon_{\mathrm{dd}} > 1$, the absolute ground state of the system is an infinitely thin BEC with $\kappa \to 0$. Depending on the trap shape there can exist a local minimum in the energy landscape corresponding to a metastable state. We call it metastable as this minimum is energetically disconnected by a barrier from the absolute ground state. For example in the case of $\lambda = 3$, we show a metastable state with $\varepsilon = 1.1$ in figure 4.10b. Reminding figure 4.9b, the solutions below the dashed line correspond to the saddle-shaped barrier in the energy landscape and hence an unstable solution. Finally, when the scattering length is further decreased the local minimum vanishes at $a_{\mathrm{crit}}$ (figure 4.10c) and hence the missing existence of any stable or metastable state with $a < a_{\mathrm{crit}}$ (figure 4.10d).

For each trap aspect ratio there exists a specific critical scattering length $a_{\mathrm{crit}}$ when the local minimum vanishes and we show this dependence in the so-called stability diagram with figure 4.10e as orange line. Dipolar condensates in prolate shaped traps with $\lambda < 1$ are unstable for positive scattering length with $a < a_{\mathrm{dd}} = a_{\mathrm{crit}}$. The condensate is elongated along the polarization direction and the dipoles mainly attract each other. The dipolar energy contribution is then negative and has a destabilizing character for the system. Hence, only sufficiently strong repulsive contact interaction stabilizes the system. In contrast, dipolar condensates in strongly oblate traps with $\lambda \gg 1$ can be stabilized for $a < a_{\mathrm{dd}}$. In this geometry the dipoles sit mainly side-by-side and repel each other, which is a positive dipolar energy contribution and stabilizes the system. Here, it may be possible to generate stable systems with attractive contact interactions.

In the previous section 2.3.2 we also introduced another variational method utilizing a Gaussian density profile. When using a Gaussian density distribution as a trial function, one derives energy expressions written in appendix A.6. The expressions imply the quantum pressure, a finite atom number effect, that is neglected in the Thomas-Fermi approximation. By performing the same analysis on the energy functional as stated above, the resulting stability diagram is slightly different as before and is shown in figure 4.10e as red line. The main difference is for dipolar condensates in prolate traps that are slightly more stable, as the quantum pressure can counteract some of the attractive interactions. Note that the Gaussian approximation gives exactly the same results as the Thomas-Fermi approximation if the atom number goes to infinity ($N \to \infty$).

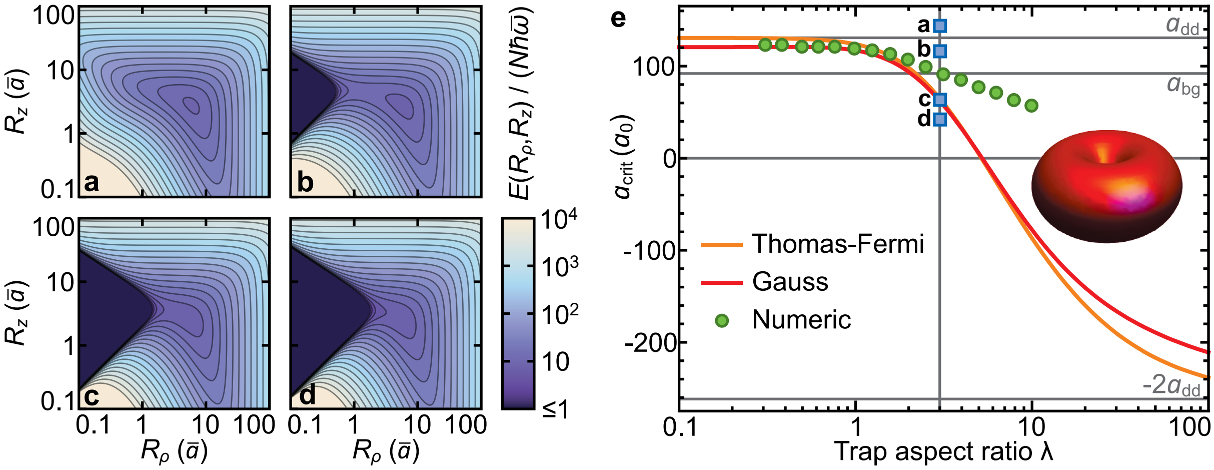

**Fig. 4.10. Stability diagram of a trapped dysprosium condensate.** The figure shows stability properties of a condensate with 10,000 $^{164}$Dy atoms in a radial symmetric trap with trap aspect ratio $\lambda$ and $\overline{\omega} = 2\pi \cdot 100\,\mathrm{Hz}$. **a-d**, Energy landscape $E(R_\rho, R_z)$ in the variational calculations for $\lambda = 3$ and different relative dipolar strength $\varepsilon_{\mathrm{dd}}$ (blue dots in **e**): **a**, $\varepsilon_{\mathrm{dd}} = 0.9$ with a global minimum; **b**, $\varepsilon_{\mathrm{dd}} = 1.1$ exhibits a metastable local minimum; **c**, for $\varepsilon_{\mathrm{dd}} = 2$ the minimum vanishes; **d**, for $\varepsilon_{\mathrm{dd}} = 3$ exists no stable state anymore. **e**, Critical scattering length $a_{\mathrm{crit}}$ as a function of trap aspect ratio $\lambda$. Stability thresholds were calculated in Thomas-Fermi (orange line) and Gaussian approximation (red line). Green dots are numerical simulations and reveal density distributions with a peak density off-center (red isodensity surface).

Finally, to judge on the practicability for both approximations, we performed exact numerical simulations for the time-dependent GPE (2.12) without any restrictions to the density distribution and searched for the stability threshold[58] as well. The results are shown as dots in figure 4.10e and they are in excellent agreement with the Gaussian approximation for prolate traps with $\lambda < 1$, but disagree with both approximations for oblate traps with $\lambda > 1$. This can be explained with the different instability mechanism occurring for these two different regimes. In the prolate configuration the dipoles experience mainly attractive dipolar interaction, and the instability mechanism is a phonon instability as described in section 4.4.2. To recall, a phonon instability leads to collapse with the lowest possible momentum, and hence to the center of the trap. Contrary for mainly repulsive dipolar interaction, as present in an oblate configuration, a dipolar condensate undergoes a roton instability as stated in section 4.4.3. As reminder, a roton instability is related to a finite momentum, and hence may exhibit a peak density off-center [31, 32] with a resulting collapse off-center [254]. Hence, this discrepancy for the stability properties can be already seen as an indirect evidence for the existence of rotonic structures [262].

Indeed, we present in this thesis that the stability mechanism is well described with the numerical results including rotons. However, we also present unexpected long-lived stable states after the roton instability. This main achievement of this thesis is now discussed in the following two chapters.

---

[58] We first performed imaginary time evolution to find the energetic ground state and then let it evolve in real time evolution. Mostly the dipolar BEC became unstable in real time evolution.

# 5. Rosensweig Instability in a Quantum Ferrofluid

Self-organized structure formation is a fundamental phenomenon of nature determining the properties of matter. Self-organization typically leads to a spontaneous breaking of continuous translation symmetry, corresponding to phase transitions. The search for exotic phases of matter drives much of the fundamental research in condensed matter physics. Phases displaying different types of order at once are of particular interest. The prime example is a supersolid breaking simultaneously two continuous symmetries, namely the phase invariance in a superfluid state and the translational symmetry in a crystal.

In this chapter, we report on the first observation of the spontaneously broken translational symmetry for the density distribution in a superfluid. For this purpose, we use a dipolar condensate that acts as a quantum ferrofluid. In analogy to a classical ferrofluid, a quantum ferrofluid exhibits a Rosensweig instability, where the translational symmetry is broken and self-organized structures form in a superfluid - a first step to a supersolid phase. But these structures were expected to collapse using mean-field theory. Hence, we present possible beyond mean-field effects including quantum fluctuations and three-body collisions, that would both prevent a collapse.

## 5.1. Observation of droplet formation in a quantum ferrofluid

In the previous chapters, we introduced all theoretical and technical tools needed to describe and produce a strongly dipolar condensate. Especially, we described the characteristics of classical and quantum ferrofluids and their intriguing responses to magnetic fields. For example, ferrofluids undergo a Rosensweig instability when the internal dipolar interaction exceeds all other fluid forces. The fluid then forms a regular pattern of peaks and valleys that results in separated droplets on a hydrophobic surface (sections 4.2 and 4.3).

For our measurements presenting the Rosensweig instability of a quantum ferrofluid, we first prepared a stable strongly dipolar condensate. For this, we used the technical tools described in chapter 3 such as optical trapping, Feshbach resonances and high-resolution imaging and keep the stability properties of a dipolar condensate in mind (section 4.5). Then we induced an instability in the quantum ferrofluid that we identified as a Rosensweig or roton instability (section 4.4.3). Subsequent, we observe long-lived droplet patterns [87], that are not expected within the mean-field description derived in section 2.3. Finally, we determine the nature of this instability and give prospects for a supersolid state.

### 5.1.1. Preparation of a stable dipolar condensate

To prepare a strongly dipolar condensate consisting of $^{164}$Dy atoms, we perform all steps described in section 3.2. After the final step of forced evaporative cooling in a crossed optical dipole trap (cODT) (see figure 5.1a), we achieve condensates with typically 15,000 atoms and a temperature of $T = 70\,\mathrm{nK}$. As shown in section 4.5, the external trapping configuration and the respective magnetic field direction determine the stability of a dipolar condensate. To obtain a stable strongly dipolar BEC with $\varepsilon_{\mathrm{dd}} > 1$, the final evaporation trap is oblate-shaped with harmonic trap frequencies of around $(\omega_x, \omega_y, \omega_z) = 2\pi \cdot (60, 50, 150)\,\mathrm{Hz}$ giving a trap aspect ratio of $\lambda \approx 3$. Additionally the external magnetic field polarizes the magnetic dipoles along the $z$-direction, the direction with the strongest confinement. In this configuration, the magnetic dipoles predominantly repel each other and a condensate can be stabilized even for $\varepsilon_{\mathrm{dd}} > 1$.

Reminding the stability diagram of a trapped dysprosium condensate in figure 4.10e, one sees that the critical scattering length is close to the background scattering length ($a_{\mathrm{crit}} \approx a_{\mathrm{bg}}$) for a trap[59] with aspect ratio $\lambda = 3$. We recall the background scattering length for $^{164}$Dy to be $a_{\mathrm{bg}} = 92(8)\,a_0$ [81, 157]. Hence, we prepare the BEC in the vicinity of a Feshbach resonance located at $B_0 = 7.117(3)\,\mathrm{G}$ with a width of $\Delta B = 51(15)\,\mathrm{mG}$ (recalling figure 3.5b), to magnetically tune[60] the scattering length $a$ to higher values above $a_{\mathrm{bg}}$. For this, we apply a vertical field along the $z$-axis with field values lower than $B_0$ during the last evaporation process. With the knowledge on the Feshbach resonance and equation (3.1), we get the scattering length $a$ dependent on the magnetic field strength as shown in figure 5.1b. The BEC is created at a field of $B_{\mathrm{BEC}} = 6.962(3)\,\mathrm{G}$ corresponding to a scattering length of $a_{\mathrm{BEC}} = 115(20)\,a_0$, which is close to the characteristic dipolar length $a_{\mathrm{dd}} = 131\,a_0$ of dysprosium atoms (recalling table 2.1).

To use magnetic Feshbach resonances, the magnetic field has to be repeatedly controlled and known with high precision. For this, we frequently calibrate our magnetic coils with radio-frequency spectroscopy between the two lowest Zeeman sub-levels of dysprosium atoms. For this method, we apply radio-frequency radiation with a constant frequency for typically one second after the forced evaporative cooling. If the Zeeman splitting matches the energy of the applied radio-frequency, the atoms are transferred to higher Zeeman sub-levels. This heats up the sample and atoms are lost from the trap. With this technique we calibrated the coil pair creating a homogeneous field along the $z$-direction to address the Feshbach resonance and adjusted the three orthogonal Helmholtz coil pairs to compensate residual magnetic fields along the $x$- and $y$-direction.

Before we use the dipolar condensate for experiments, we shape the external trap to fit our needs, as shown in figure 5.1c. Within 100 ms the intensities of both dipole trap lasers are slightly reduced to get harmonic trap frequencies of $(\omega_x, \omega_y, \omega_z) = 2\pi \cdot (46, 44, 133)\,\mathrm{Hz}$

---

[59] Note that in figure 4.10 we used a mean trapping frequency of $\overline{\omega} = 2\pi \cdot 100\,\mathrm{Hz}$, which is slightly higher than our trap after forced evaporation with $\overline{\omega} \approx 2\pi \cdot 77\,\mathrm{Hz}$. However, the critical scattering length changes only slightly, by less than $2\,a_0$.

[60] We did all the following mentioned investigations also on a second, even narrower resonance located at $B_0 = 1.326(3)\,\mathrm{G}$ with a width of $\Delta B = 8(5)\,\mathrm{mG}$. All the results remain qualitatively the same, indicating the independence of a particular Feshbach resonance.

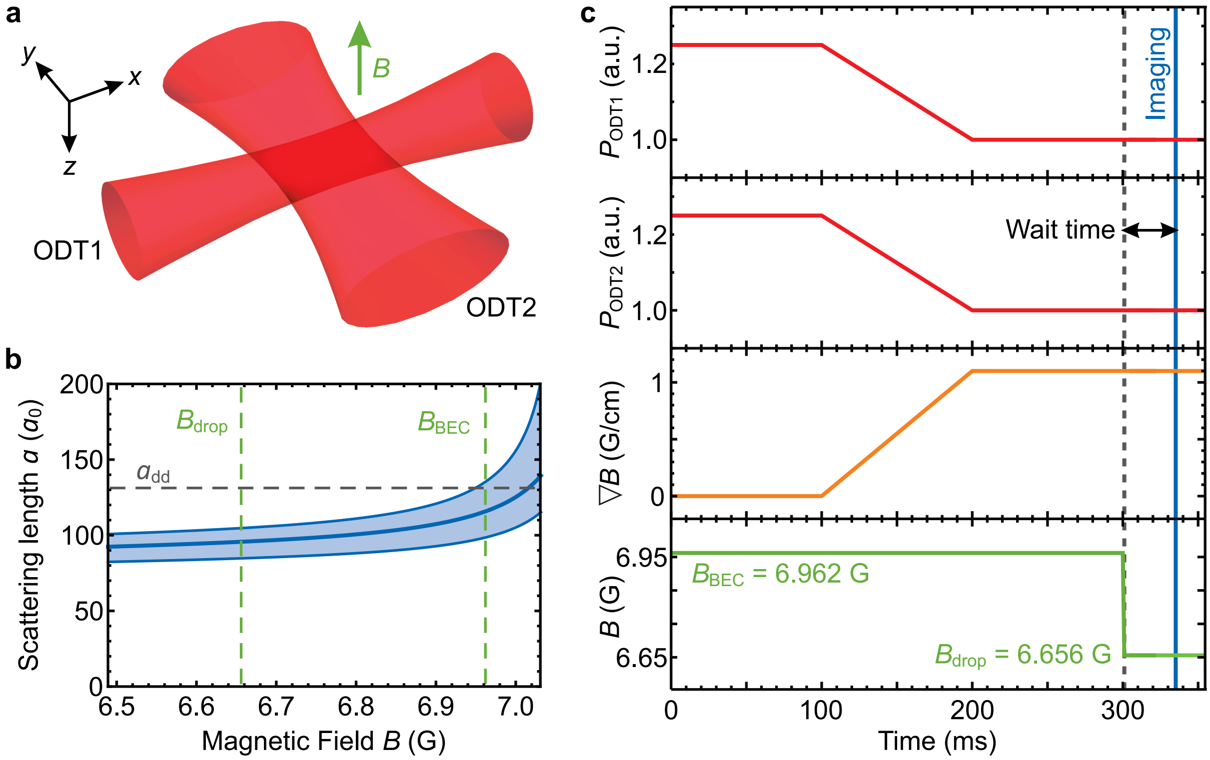

**Fig. 5.1. Crossed optical dipole trap and scattering length. a**, Crossed optical dipole trap (cODT) and magnetic field in the experiment. ODT 1 is a round laser beam, while ODT 1 is elliptical. The magnetic field points perpendicular to both dipole trap directions. **b**, Scattering length $a$ versus magnetic field $B$ for the Feshbach resonance located at 7.117 G. We show the confidence interval for the scattering length and the characteristic dipole length $a_{\mathrm{dd}}$ is indicated as a dashed grey line. The field $B_{\mathrm{BEC}}$ at which we create the condensate and the field $B_{\mathrm{drop}}$ where we induce the droplet state are indicated as dashed green line. **c**, Experimental sequence to shape the cODT and tune the magnetic field. We use a homogeneous field to tune the contact interaction with the Feshbach resonance

resulting in a radially quasi-symmetric trap confinement with a trap aspect ratio very close to $\lambda = 3$. As this trap is very shallow and hardly holds the atoms against gravity, we partially compensate gravity by applying an additional magnetic gradient of 1.1 G/cm at the same time along the $z$-direction[61]. In this reshaped trap we let the condensate settle for further 100 ms, before we tune and detect its internal properties.

For the experiments mentioned in the following, we abruptly change the magnetic field within 0.5 ms to $B_{\mathrm{drop}} = 6.656(3)\,\mathrm{G}$ that corresponds to a scattering length of $a_{\mathrm{drop}} = 95(13)\,a_0$ close to the background scattering length $a_{\mathrm{bg}} = 92(8)\,a_0$. We let the atomic sample then evolve for some wait time and image it in situ with the high-resolution phase contrast imaging explained in section 3.3.3. The results of this experimental sequence are presented in the next sections.

---

[61] A magnetic gradient field of 2.9 G/cm would compensate gravity completely and the atoms would levitate as the forces cancel each other ($\mu_{\mathrm{m}} \nabla B = m g_0$). We use this in section 6.2.2 to levitate non-trapped atoms for a few ms.

### 5.1.2. Droplet patterns

By reducing the scattering length $a$ below the stability threshold close to $a_{\mathrm{bg}}$, the dipolar interaction overcomes any other interactions in the quantum fluid. For dominant dipolar interactions, we expect an angular roton instability [31, 254] to occur in an oblate-shaped trap (section 4.4.3), that can lead to a periodic perturbation of the atomic density distribution [253]. This is closely connected to the Rosensweig instability in a classical ferrofluid [86]. Indeed by reducing the scattering length $a$ from $a_{\mathrm{dd}}$ ($B_{\mathrm{BEC}} = 6.962(3)\,\mathrm{G}$) to $a_{\mathrm{bg}}$ ($B_{\mathrm{drop}} = 6.656(3)\,\mathrm{G}$), we observed a finite-wavelength instability that triggered an unexpected transition to ordered states, as depicted in figure 5.2a. The ordered states we observe consist of multiple tiny droplets arranging in a triangular pattern. The stability mechanism of these droplets is investigated in this thesis.

In figure 5.2b, we show typical in situ images of the resultant triangular patterns for the quantum ferrofluid with different numbers of droplets, $N_{\mathrm{d}}$, ranging from two to ten. Note that up to now, we have no direct control on how many droplets form and it remains a statistical process. Hence, any analysis remains statistical and we have to average detected internal properties for many experimental realizations. To analyse the average number of atoms per droplet, we count the number of droplets $N_{\mathrm{d}}$ in relation to the total number of atoms $N$. The statistical analysis is shown in figure 5.2c indicating a linear dependence between $N_{\mathrm{d}}$ and the number of atoms, with a slope of 1,750(300) atoms per droplet. For $N_{\mathrm{d}} = 2$, we observed a mean droplet distance of $d = 3.0(4)\,\mu\mathrm{m}$. The droplets, which have a large effective dipole moment of $N\mu_{\mathrm{m}}$, strongly repel each other while the radial trapping applies a restoring force. Hence, the distance $d$ can be calculated using a simplified one-dimensional classical system by minimizing the total energy of the system.

For this model, we assume two strongly dipolar particles with 1,750 times the mass and magnetic moment of a dysprosium atom that are confined in a harmonic trap. After a short analysis of the total energy of a trapped system of two such dipoles, we find that the energy is minimized if each particle sits off-center and they have a respective distance of

$$d = 2\left(\frac{9a_x^4 a_{\mathrm{dd}} N}{16}\right)^{1/5} = \left(\frac{3N\mu_0\mu_{\mathrm{m}}^2}{2\pi m\omega_x^2}\right)^{1/5} \tag{5.1}$$

with $a_x$ the harmonic oscillator length $a_x = \sqrt{\hbar/m\omega_x}$. For our experimental parameters, we get a distance of $d = 3.3\,\mu\mathrm{m}$, in agreement with the observed distance[62]. For $N_{\mathrm{d}} > 2$, the droplets arrange mostly in triangular structures, and form a microscopic crystal with a droplet distance of $d = 2$-$3\,\mu\mathrm{m}$. Owing to the isotropy of the repulsion between droplets in the radial plane, we expect the triangular configuration to have the lowest energy, which was for example shown in [263].

Comparing our quantum ferrofluid with a classical ferrofluid, very similar behaviour and patterns have been observed on a superhydrophobic surface, as shown in figure 4.5 [239]. In this classical-ferrofluid system, a single droplet first deforms as the external magnetic field is increased, and then divides into two droplets when some critical field

---

[62] In the next chapter 6 we will see in a more advanced analysis that the droplets cannot be considered as point-like particles anymore.

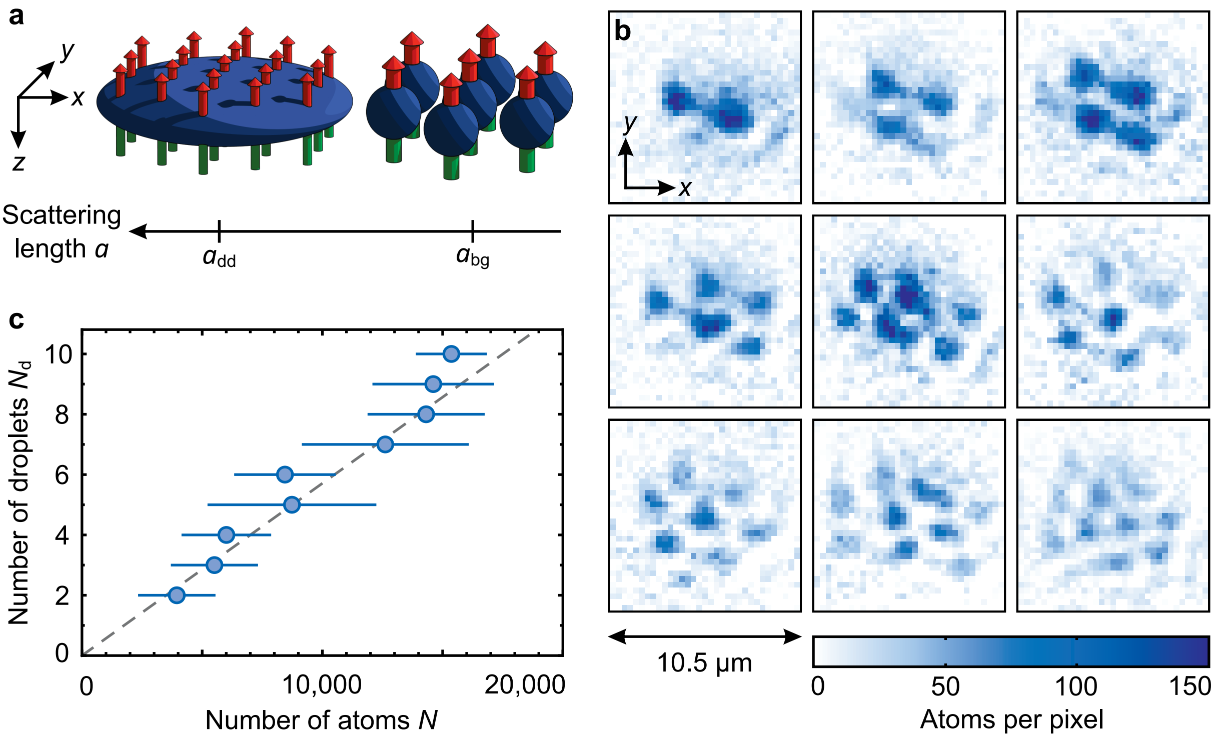

**Fig. 5.2. Growth of a microscopic droplet crystal.** **a**, Schematic of the experimental procedure. We prepared a stable, strongly dipolar dysprosium BEC with $a \approx a_{\mathrm{dd}}$ in an oblate trap (left). By decreasing the scattering length $a$, we induced an instability close to $a \approx a_{\mathrm{bg}}$. Following this instability, the atoms clustered to droplets in a triangular pattern (right). **b**, Representative single samples of droplet patterns imaged in situ, with droplet numbers, $N_{\mathrm{d}}$, ranging from two to ten. Each image has a field of view with $10.5\,\mu\mathrm{m} \times 10.5\,\mu\mathrm{m}$. **c**, We used a set of 112 realizations with different numbers of droplets and atoms for a statistical analysis. The plot shows the mean number of atoms $N$ as a function of the number of droplets $N_{\mathrm{d}}$, with error bars indicating the standard deviation. The fitted linear relation (grey dashed line) has a slope of 1,750(300) atoms per droplet. This shows that increasing the number of atoms results in growth of the microscopic droplet crystal.

is reached. For a quantum ferrofluid, a single droplet should be unstable for $a < a_{\mathrm{dd}}$, owing to the attractive part of the dipolar interaction, and so should collapse. Although, the counteracting quantum pressure, the zero-point energy that exists as a result of an external trapping potential, can compensate attraction and prevent collapse [111], mean field calculations predict this not to be the case [254]. However, in our system the collapse is stopped leading to the creation of tiny droplets, each with a detected radius smaller than $1\,\mu$m limited by the resolution of our imaging.

The very small size of the droplets also indicates a high peak density. Our experimental observation can only give a lower bound of $n_0 \gtrsim 2{\cdot}10^{20}\,\mathrm{m}^{-3}$ due to the missing knowledge on the exact spatial extent of the droplet. In the next section, we will therefore focus on the dynamics and lifetime of the droplets. The decrease in atom number for longer times should be mainly dependent on the three-body losses. With this idea we can then give a further estimate for the peak density of the droplets.

### 5.1.3. Dynamics and lifetime of the droplets

For further quantitative statistical analysis, we have to introduce a parameter that describes the appearance and disappearance of the droplet pattern and is automatically computed for several hundred samples. The counting of the number of droplets $N_\mathrm{d}$, as done for figure 5.2c remained a manual evaluation procedure with a possible subjective impreciseness. Hence, we come up with the following objective quantitative statistical analysis.

We computed the Fourier spectrum $S(k)$ of the obtained images, as described in the figure 5.3a-c and its caption. The patterns are visible as a local maximum in $S(k)$ at finite momentum $k = 2\pi/d \approx 2.5\,\mu\mathrm{m}^{-1}$, whereas the spectrum of a BEC monotonically decreases with $k$. We define the spectral weight

$$\mathrm{SW} = \sum_{k=1.5\,\mu\mathrm{m}^{-1}}^{5\,\mu\mathrm{m}^{-1}} S(k)\,, \tag{5.2}$$

which is a quantity that represents the strength of the structured states, and normalize it such that a BEC has $\mathrm{SW}_\mathrm{BEC} = 1$. After a quench of the interactions from $a \approx a_\mathrm{dd}$ to $a \approx a_\mathrm{bg}$, we statistically investigated the pattern-formation time and the lifetime of these patterns with figure 5.3d. We repeated this measurement 13 times and found statistically that the pattern is fully developed after $\sim 7\,\mathrm{ms}$, and has a 1/e-lifetime of about 300 ms. The decay of the droplet structure is accompanied by a decrease in the number of atoms, with a 1/e-lifetime of about 130 ms, while the residual thermal cloud had constant atom number. Owing to the decreasing number of atoms, the structures evolve back to lower numbers of droplets, $N_d$, until there are no droplets left (insets of Fig. 2d).

We expect that mainly three-body losses limit the lifetime of the droplet patterns. Hence, we compared this lifetime with a non-structured BEC at a field of $B_\mathrm{BEC}$. We followed an analysis of the atom number decay as described in [264]. There, the three-body collision rates resulting to losses are calculated in the Thomas-Fermi limit with a parabolic density distribution[63]. This leads to an atom number decay that reads

$$N(t) = N_0 \left(1 + \frac{t}{\tau_3}\right)^{-5/4}\,, \tag{5.3}$$

with $N_0$ the initial atom number at $t = 0$ and the three-body decay constant $\tau_3$. We measured the decay constant to be $\tau_3 = 6(2)\,\mathrm{s}$ for a condensate with an initial peak density of $n_0 = 1.5(5) \cdot 10^{20}\,\mathrm{m}^{-3}$. With this knowledge we can calculate the three-body loss coefficient for a condensate to be $L_3 = 21/8n_0^2\tau_3 = 1.9^{+5}_{-1.3} \cdot 10^{-41}\,\mathrm{m}^{-6}/\mathrm{s}$.

By doing the same analysis for the droplet patterns (which is likely to be oversimplified), we get $\tau_3 = 120(30)\,\mathrm{ms}$ corresponding to a peak density of $n_0 \approx 10^{+10}_{-5} \cdot 10^{20}\,\mathrm{m}^{-3}$. In section 6.2 we come back to the calculated density of the droplets using a more advanced analysis.

---

[63] A three-body decay is described with $\mathrm{d}N/\mathrm{d}t = -L_3\langle n^2\rangle N$, with $\langle n^2\rangle_{t=0} = 21/8n_0^2$ using the peak density $n_0$ in Thomas-Fermi approximation for the initial conditions. By inserting the atom number dependent Thomas-Fermi radii one sees $\langle n^2\rangle \propto N^{4/5}$, which gives $N^{-9/5}\mathrm{d}N = \mathrm{d}t/\tau_3$ with $\tau_3 = 21/8n_0^2L_3$. Integrating the last equation with an initial atom number $N_0$ results in eq. (5.3).

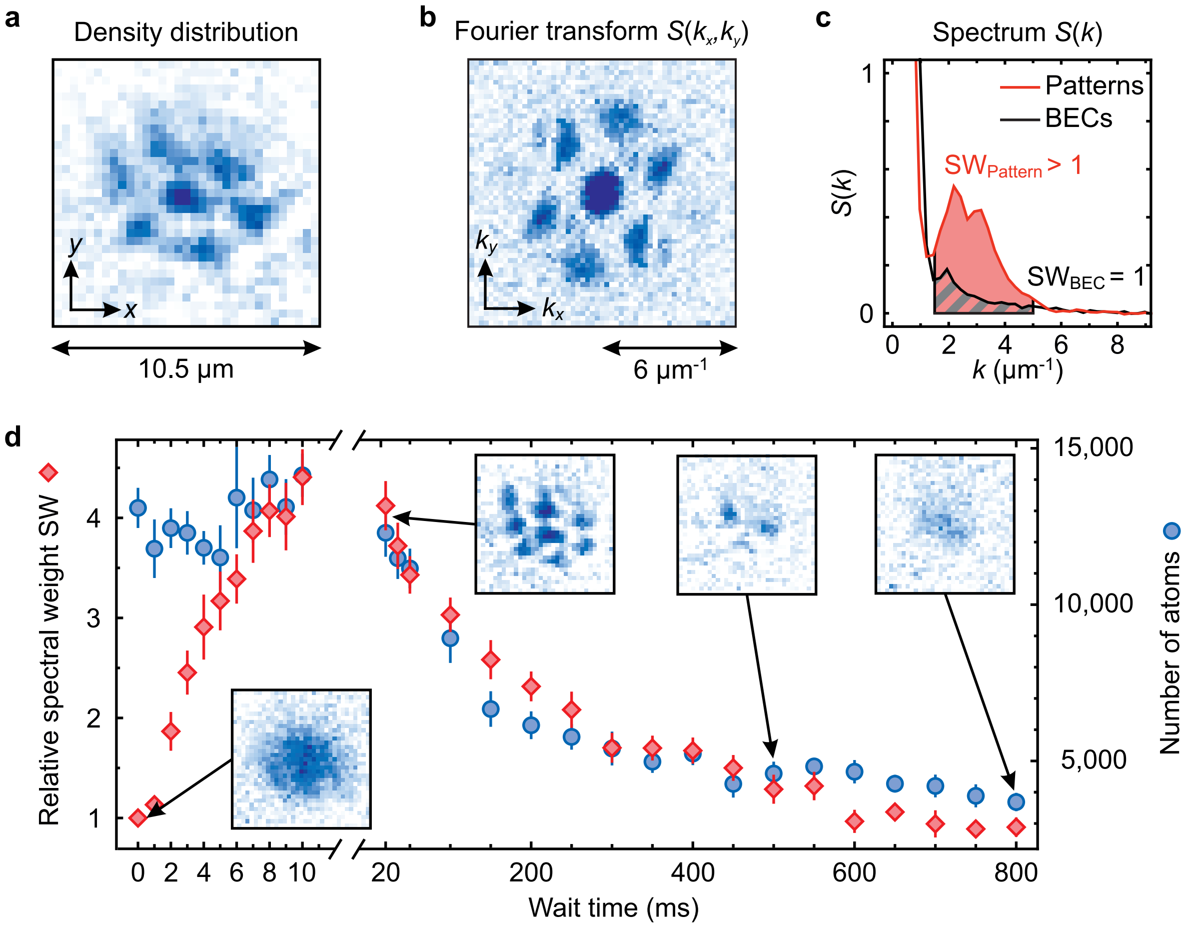

**Fig. 5.3. Evaluation of the structures and lifetime analysis.** Illustration of our statistical evaluation procedure. We began with the spatial density distribution (**a**), and then calculated the absolute value of the two-dimensional Fourier transform $S(k_x, k_y)$ (**b**) and radially averaged over $k = (k_x^2 + k_y^2)^{1/2}$ to obtain the spectrum $S(k)$ (**c**). We removed the white noise from the spectrum $S(k)$ such that $S(k) = 0$ for $k > 7\,\mu\text{m}^{-1}$, which corresponds to structures below our resolution. The spectra in **c** represent an average of 13 images for both BECs and patterns at a wait time of 10 ms. For patterns in the spatial density distribution, we observe enhanced signal for $k \approx 2.5\,\mu\text{m}^{-1}$ in the spectrum (red line), whereas the spectrum of BECs (black line) shows monotonic decay for increasing momentum. We define the sum of these spectra over a momentum range as the relative spectral weight SW (shaded areas, as defined in the text), which is a quantity for the strength of the structured states. **d**, We performed a sudden quench (over 0.5 ms) of the BEC below the instability to $B_{\text{drop}} = 6.656(3)$ G for varying wait times. To determine the creation time and lifetime of the patterns, we plot the relative spectral weight SW (red diamonds) against wait time. Each point is an average of 13 realizations, with error bars indicating the standard error. The plot shows rapid pattern formation within 7 ms without accompanied atom losses and afterwards a surprisingly long 1/e-lifetime of about 300 ms. This lifetime seems to be limited by a decrease in the number of atoms (blue circles). The insets are typical spatial density distributions of a single sample before pattern formation (BEC; bottom left), and at three different wait times.

### 5.1.4. Transition with bistability and hysteresis

The droplet formation due to the occurrence of the Rosensweig instability seems to break the translational symmetry of a continuous quantum ferrofluid. Such a symmetry breaking is a typical indication of a phase transition in the thermodynamic limit. For classical ferrofluids we have discussed first-order phase transition for the Rosensweig instability an the deformation of a single drop. For the drop deformation, we have explicitly shown bistability, that means the system has two stable equilibrium states visible as local minima in the energy potential (see figure 4.4b). Additionally, such a bistability is often accompanied by hysteresis, evident for classical ferrofluids. Due to the strong similarity of classical and quantum ferrofluids, we expect also for the observed droplet formation a hysteretic behaviour with bistability.

We thus performed experiments to explore this hysteretic behaviour. The experimental sequence is depicted in figure 5.4a and it includes to induce the droplet formation and to come back to the initial state. For this, we prepared the BEC close to the Feshbach resonance with $a \approx a_{\mathrm{dd}}$ and ramped the magnetic field linearly to varying values near the instability point. We ensured that the structures were formed within 10 ms, even for values of the magnetic field close to the stability threshold, and waited at the chosen value for twice this time. Figure 5.4b shows a clear hysteresis. For the return, we observe the same spectral weights as for the way down, but for magnetic fields that are about 20 mG greater. This demonstrates that our system features bistability in the transition region. In the thermodynamic limit, such behaviour is a clear signature of a first-order phase transition and the existence of latent heat in the crystallization process. Note that the spectral weight for the return remains slightly higher due to residual defects in the BEC.

To verify that we are not dealing with an energetically excited state resulting from quench dynamics, we performed forced evaporative cooling at a constant magnetic field far away from any Feshbach resonance with $a \approx a_{\mathrm{bg}}$. We observed very similar self-organized structures, which started to occur for temperatures near the expected critical temperature for the phase transition to a BEC, as shown in figure 5.4c. This strongly indicates that multiple tiny droplets are energetically favourable compared to a single, larger condensate. But as we will see later the droplet patterns are not the true ground state of the system and is metastable.

The measurement showing hysteresis presented that droplet structures can melt back into a single BEC. Additionally, with the forced evaporative cooling to droplet patterns occurring at the expected critical temperature, it is quite plausible that the droplets are superfluid individually. Hence, we have seen that the Rosensweig instability in a quantum ferrofluid presents features of a first-order crystallisation phase transition in a superfluid phase. Though, this is still not the evidence of a supersolid state, where two continuous symmetries are broken at the same time. To establish the superfluid character one has to observe long-range phase coherence, thus an inter-droplet phase coherence. But if the individual droplets still share the same phase via weak links or lose their mutual phase coherence remains unclear. We assess the prospects for a supersolid state in the next section.

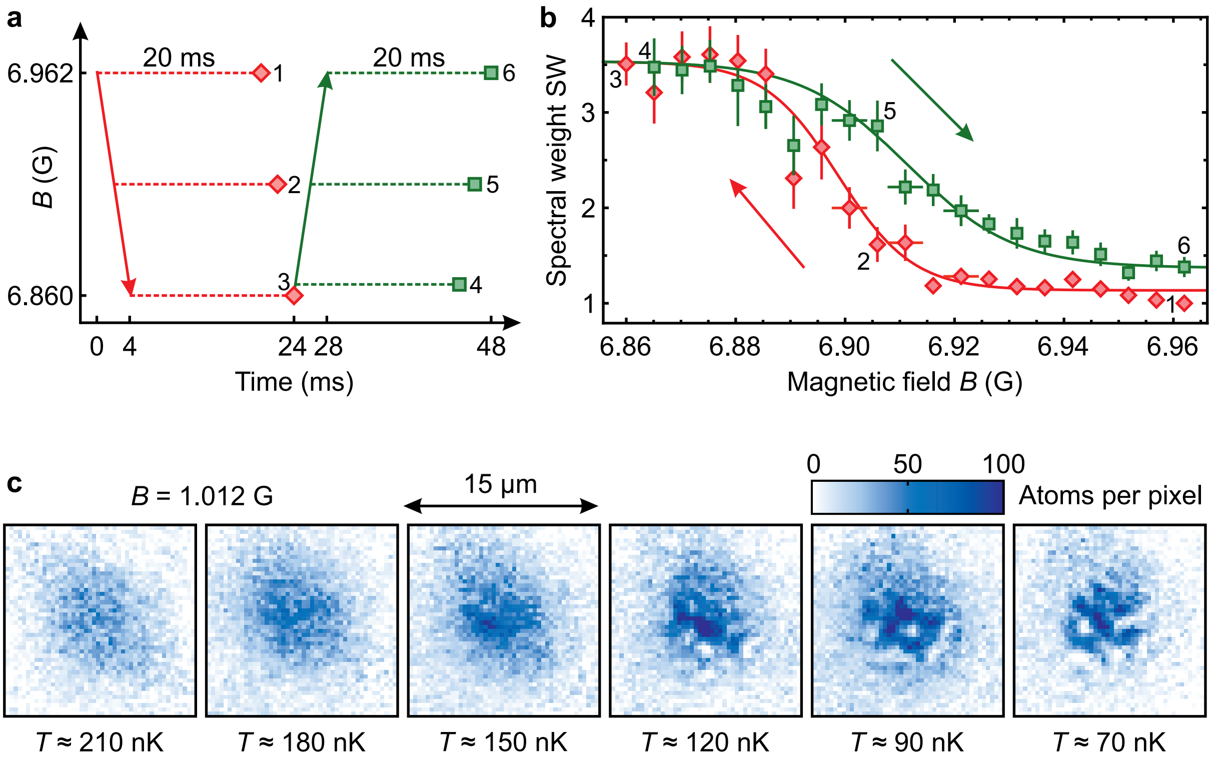

**Fig. 5.4. Hysteresis of pattern formation and evaporation to patterns. a**, A timeline of the experiment in which we observed hysteresis. We prepared the Dy BEC close to the Feshbach resonance at $B_{\mathrm{BEC}} = 6.962(3)\,\mathrm{G}$ and ramped down the magnetic field linearly to different values, with a constant change rate, the lowest of which was $B = 6.680(3)\,\mathrm{G}$. To ensure that the structures had enough time to form, we waited for 20 ms at each value before imaging the atomic sample in situ. For the way back, we first waited at the lowest field value for 20 ms and then increased the magnetic field with the same ramp speed to higher values, once again holding for 20 ms at each value before imaging the sample in situ. **b**, Hysteresis plot for the structured patterns, which shows the spectral weight SW against magnetic field as it is decreased (red diamonds and line) and then increased (green squares and line). Each point is an average of 14 realizations, with the vertical error bars indicating standard errors. We determined the long-term field stability to be 3 mG, as shown by the horizontal error bars for selected points. A clear hysteresis is visible, although the total time is twice as long for the way back. The labels 1-6 in **a** and **b** indicate data points at particular field values to help the understandability; the lines in **b** serve as a guide to the eye. **c**, Evaporation to droplet patterns. We prepared a dipolar BEC with forced evaporative cooling as shown in section 5.1.1, but we kept the magnetic field at a field of $B = 1.012\,\mathrm{G}$, far away from any Feshbach resonances. This means, we evaporated the dysprosium atoms at a scattering length of $a \approx a_{\mathrm{bg}}$. Instead to observe a transition to a condensed matter wave, we observed a transition to very similar droplet patterns. This transition happens at the expected critical temperature of $T_{\mathrm{c}} \approx 150\,\mathrm{nK}$ for 60,000 atoms in a trap with $\overline{\omega} \approx 2\pi \cdot 80\,\mathrm{Hz}$.

### 5.1.5. Prospects of a supersolid state

A supersolid is a spatially ordered material with superfluid properties [265–267]. We take the following definition for a supersolid: spontaneous breaking of a continuous translation symmetry and of phase invariance [268]. It seems hard to merge these very different and seemingly conflictive solid and superfluid behaviours into a single phase of matter. The supersolid phase remains elusive and the search for this phase has focused mainly on solid helium, where claims of its discovery [269, 270] have been withdrawn recently [271].

Another approach starts with a superfluid of Bose-condensed ultracold atoms, which seems to be an excellent system with strong control on inter-particle interactions. These interactions can be tuned and one can create two-body potentials that can lead to the occurrence of a supersolid phase. We will discuss two physical systems, both realizable in experiments using cold atoms or molecules, which were proposed to provide a stable supersolid phase.

By utilizing the Rydberg blockade or dipole blockade [272] one can realize a repulsive potential that flattens off and remains constant below a characteristic cut-off distance. For a condensate with such inter-particle interactions, it was predicted that it shows roton excitations in three dimensions and can form superfluid droplets. Furthermore, the droplets arrange in a triangular structure and such a droplet crystal can turn to a supersolid when tunnelling between neighbouring droplets takes place and phase coherence is established across the whole system [273, 274]. The droplet size in this system is mainly determined by the characteristic cutoff distance of the Rydberg blockade and the particular form of the potential is not crucial. This means the long-range behaviour is largely irrelevant and the supersolid phase is a consequence of the flatness at short-distances. However, a supersolid can also be achieved with only long-range interactions.

We consider atoms or molecules possessing a magnetic or electric dipole moment that are confined to a two dimensional plane. The dipoles are aligned perpendicular to the plane with an external electric or magnetic field. In such a configuration the dipolar interaction can act purely repulsive and a first-order transition from a superfluid to a crystalline phase has been predicted [263, 275]. In three-dimensions any structure close to a supersolid state will undergo subsequent instabilities and collapse [276]. However, our droplet patterns remain stable and could be a good candidate for a supersolid state even in three dimensions, although it is not the ground state of the system.

In our droplet system we have indeed long-range order and expect each droplet to be superfluid, but we did not probe the relative phase between individual droplets. Figure 5.5 exemplifies the difference between a supersolid state compared to a droplet crystal without phase coherence. Experiments that are capable to detect phase coherence could be interference measurements of individual overlapping droplets. The randomness in the droplet ensembles creation mechanism has so far prevented a precise measurement of the relative phase. Indeed one needs stable starting conditions because phase coherence is established by a reproducibility of interference patterns for different samples. Nevertheless, we performed such measurements as shown in section 6.2.2, that do not show the relative phase coherence but give further information on the droplets.

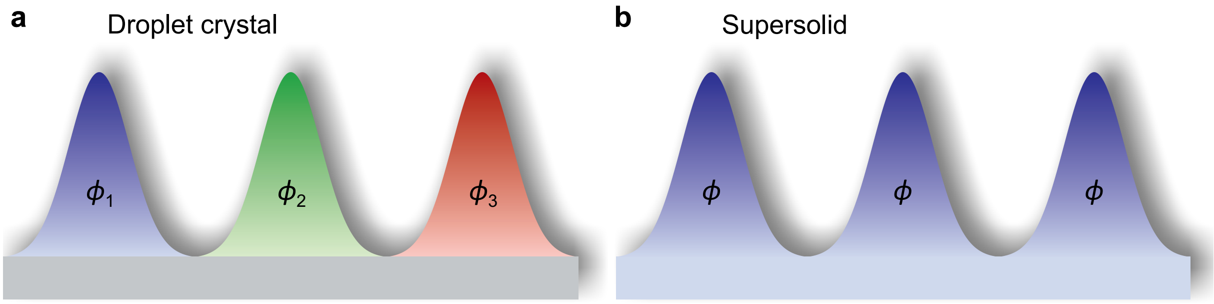

**Fig. 5.5. Droplet crystal and supersolid. a**, Droplet crystal with a background of incoherent atoms (grey). Each droplet exhibits a different phase relation. **b**, Supersolid state with a coherent background that remains phase coherence of the individual droplets.

In the next section, we focus on the stability mechanism of our droplets. We attribute the stability to beyond mean-field effects, which are quantum fluctuations and repulsive three-body collisions. Recent theoretical studies, using these mechanism unfortunately expect that individual droplets loose their phase coherence on a short time scale for our recent experimental parameters [277, 278].

## 5.2. Beyond mean-field effects

When we derived the Gross-Pitaevskii equation (2.12), we only considered binary interactions and neglected any quantum fluctuations in eq. (2.11), which resulted in the energy mean-field contributions (2.16). We derived the energy density due to the contact interaction to be

$$\frac{E_{\mathrm{contact}}}{V} = \frac{g\,n^2}{2}\,, \tag{5.4}$$

recalling the contact interaction strength $g = 4\pi\hbar^2 a/m$ from eq. (2.2). This expression was already found in 1929 by Lenz [279]. However, the mean-field approximation neglects fluctuations around mean values that are inherent to quantum mechanical systems. In 1957, Lee, Huang and Yang included quantum fluctuations as a perturbation around the expectation value and calculated explicitly for binary short-range potentials a higher order correction term for a homogeneous density [280, 281]. Two years later Wu and others extended this work to the next order correction term by studying three-particle collisions through the two-body potential [282–284]. Considering these corrections gives an energy density for the short-range contact interaction that reads

$$\begin{aligned}\frac{E_{\mathrm{contact}}}{V} &= \frac{g\,n^2}{2}\left\{1 + \frac{128}{15\sqrt{\pi}}\sqrt{na^3} + \left[\frac{8(4\pi - 3\sqrt{3})}{3}\ln(Cna^3)\right] na^3 + \ldots\right\} \\ &= \frac{g\,n^2}{2}\left\{1 + \frac{128}{15\sqrt{\pi}}\sqrt{na^3}\right\} + \frac{g_3\,n^3}{6} + \ldots \end{aligned} \tag{5.5}$$

with a term proportional to $(na)^{5/2}$ due to quantum fluctuations and a term proportional to $(na)^3$. The numerical prefactor of the quantum fluctuation term is constant, whereas the latter depends on the constant $C$ in the argument of the logarithm, that can be in principle calculated from knowledge on the short-range details of the interaction potential [285, 286]. In the following, we will call this prefactor $g_3$ giving the scale of the three-body correction. We expect quantum fluctuations to influence the condensate properties much earlier than the three-body correction, as the latter has the higher order scaling. Hence, we will neglect for now the three-body correction term.

## 5.2.1. Quantum fluctuations

In this section, we discuss the quantum fluctuations. We expand the correction term for dipolar interactions and calculate the energy functional with these corrections. We present observed beyond mean-field effects for non-dipolar quantum gases and discuss the arising stability properties for a dipolar system.

The expressions above were only derived by assuming short-range inter-particle interactions. However, additional long-range dipolar interactions modify the quantum fluctuation term. This correction was formally derived including microscopic properties of the interaction potential by avoiding pseudo-potentials [287]. With these calculated quantum fluctuations and using the local density approximation[64] for trapped inhomogeneous gases [288, 289], the resulting beyond mean-field equation for the chemical potential of a dipolar quantum gas reads [290, 291]

$$\mu = V_{\mathrm{ext}}(\boldsymbol{r}) + g\, n(\boldsymbol{r}) + \frac{32}{3} g \sqrt{\frac{n(\boldsymbol{r})^3 a^3}{\pi}} Q_5(\varepsilon_{\mathrm{dd}}) + \Phi_{\mathrm{dip}}(\boldsymbol{r}) \tag{5.6}$$

with the respective energy functional for the density distribution $n = n(\boldsymbol{r})$

$$E\left[n(\boldsymbol{r})\right] = \int \mathrm{d}^3 r \left[ V_{\mathrm{ext}}\, n + \frac{g}{2} n^2 + \frac{64}{15} g\, n^2 \sqrt{\frac{n a^3}{\pi}} Q_5(\varepsilon_{\mathrm{dd}}) + \frac{\Phi_{\mathrm{dip}}}{2}\, n \right] . \tag{5.7}$$

In both equations the quantum fluctuation term is multiplied with the correction factor $Q_5(\varepsilon_{\mathrm{dd}})$ dependent on the relative dipolar strength [291]

$$Q_5(x) = (1-x)^{5/2}\, {}_2F_1\left(-\frac{5}{2}, \frac{1}{2}; \frac{3}{2}; \frac{3x}{x-1}\right) \overset{\text{Taylor}}{\approx} 1 + \frac{3}{2}x^2 + \frac{1}{7}x^3 - \frac{3}{56}x^4 + \dots \tag{5.8}$$

with ${}_2F_1(a, b; c; z)$ the ordinary hypergeometric function[65]. We show the function $Q_5(\varepsilon_{\mathrm{dd}})$ in

---

[64] A trapped dilute BEC can usually be divided into regions with an extent much larger than the range of the inter-particle interactions, but still much smaller than the scale of the spatial variation of the density distribution $n(\boldsymbol{r})$. In these regions, the gas can be considered as locally homogeneous and eq. (5.5) remains valid for trapped condensates.

[65] The ordinary hypergeometric function ${}_2F_1(a, b; c; z)$ includes many other special functions as specific cases. For example ${}_2F_1(a, b; b; z) = (1-z)^{-a}$ and ${}_2F_1(\frac{1}{2}, \frac{1}{2}; \frac{3}{2}; z^2) = \arcsin(z)/z$. Additionally, there exists linear identities that are true for any hypergeometric function, explicitly we use the relation ${}_2F_1(a, b; c; z) = \frac{b}{b-a}{}_2F_1(a, b+1; c; z) - \frac{a}{b-a}{}_2F_1(a+1, b; c; z)$ to simplify the function $Q_5$ [292, chapter 2.8, eq. (32)]. By using this relation three times on ${}_2F_1(-\frac{5}{2}, \frac{1}{2}; \frac{3}{2}; z)$ from eq. (5.8), we get the identity ${}_2F_1(-\frac{5}{2}, \frac{1}{2}; \frac{3}{2}; z) = \frac{1}{6}{}_2F_1(-\frac{5}{2}, \frac{3}{2}; \frac{3}{2}; z) + \frac{5}{24}{}_2F_1(-\frac{3}{2}, \frac{3}{2}; \frac{3}{2}; z) + \frac{5}{16}{}_2F_1(-\frac{1}{2}, \frac{3}{2}; \frac{3}{2}; z) + \frac{5}{16}{}_2F_1(\frac{1}{2}, \frac{1}{2}; \frac{3}{2}; z)$.

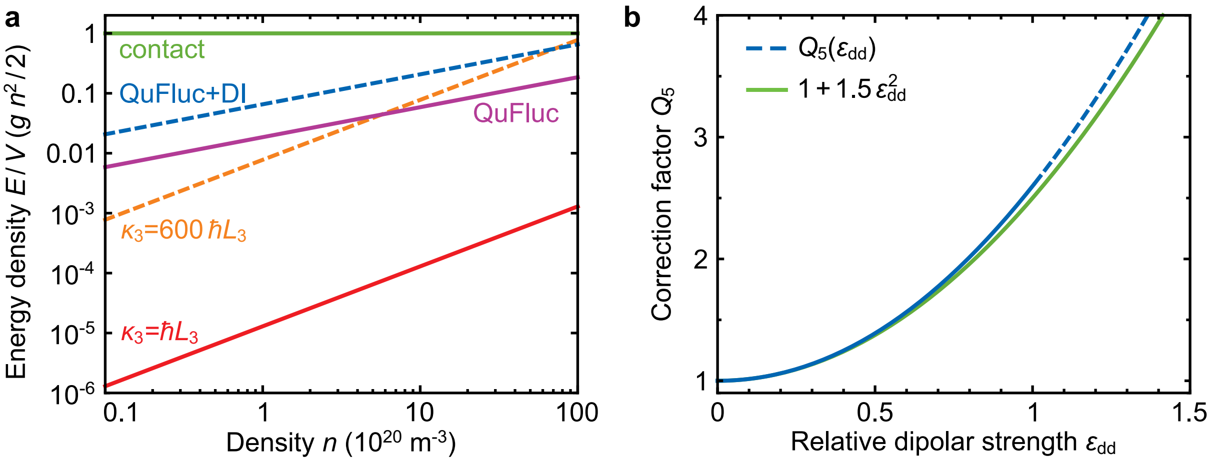

**Fig. 5.6. Corrections for the energy density. a**, Energy density corrections normalized to the contact energy (green). We show the contribution due to quantum fluctuations without dipolar interaction (purple) and with included dipolar interactions with $\varepsilon_{\mathrm{dd}} = 1.3$ (blue dashed line). Additionally, we present the (in the next section introduced) three-body contribution (red) with $\kappa_3 = \hbar L_3 \approx 10^{-41}\,\hbar\,\mathrm{m}^{-6}/\mathrm{s}$ and with 600 times this value (orange dashed line). **b**, Correction function $Q_5(\varepsilon_{\mathrm{dd}})$ which governs the energy correction on the relative dipolar strength $\varepsilon_{\mathrm{dd}}$ (blue). For $\varepsilon_{\mathrm{dd}} > 1$ the function $Q_5$ has a small imaginary part and the real part is negative. Thus, the dashed blue line is $|\mathrm{Re}(Q_5)|$. We approximate $Q_5$ with a second order Taylor series (green).

figure 5.6b and its lowest order Taylor expansion at the point $x = 0$. The function $Q_5(\varepsilon_{\mathrm{dd}})$ is discontinuous at $\varepsilon_{\mathrm{dd}} = 1$ and has a very small imaginary part for $\varepsilon_{\mathrm{dd}} > 1$. However, it is expected that the correction factor remains valid even in the strongly dipolar regime for oblate shaped traps [287]. Hence, we will use in the following $Q_5(\varepsilon_{\mathrm{dd}}) \approx 1 + \frac{3}{2}\varepsilon_{\mathrm{dd}}^2$ to effectively circumvent the discontinuity and the very small imaginary part of $Q_5(\varepsilon_{\mathrm{dd}} > 1)$.

In figure 5.6a we show the energy density of quantum fluctuations (purple line) normalized to the mean-field contact interaction energy (green line). By including dipolar interactions the quantum fluctuations increase by a factor of 3.5 for $\varepsilon_{\mathrm{dd}} = 1.3$ (blue) compared to the non-dipolar case. Quantum fluctuations are a common feature for systems with high density or the presence of strong interactions and have been already observed to alter the many-body behaviour of non-dipolar quantum gases. The first observation was made in strongly interacting Fermi gases. These offer the possibility to bind two fermions to one bosonic dimer and study molecular Bose-Einstein condensates. In systems working with fermionic $^6$Li the molecular BEC had, due to quantum fluctuations, increased collective oscillation frequencies [293], a modified density distribution [294] and a decreased pressure [295]. Furthermore in a strongly interacting atomic BEC of $^7$Li, the same modified spatial density distribution was observed in situ [296]. Finally for strongly interacting bosonic $^{85}$Rb atoms, the excitation spectrum showed the onset of quantum fluctuations [297].

If quantum fluctuations are the stabilization mechanism for the droplets, our observations would be the first many-body state in quantum gases only existing as a consequence of quantum fluctuations. Thus, it is of interest to develop a variational approach similar to section 4.5.3 to investigate the energy functional including quantum fluctuations. For this we use an inverted parabola ansatz for the density distribution (section 2.3.3) which is described with the two variational width parameters $R_\rho$ and $R_z$. Evaluating the energy functional[66] of eq. (5.7), gives the energy landscapes shown in figure 5.7a-d. We use trap and atomic parameters that agree with the experiments shown in the previous section 5.1.

Depending on the scattering length $a$, we find either one or two minima that lie on two distinct solution branches with very different energy (figure 5.7e). The two branches differ by their radial extent $R_\rho$ and the associated cloud aspect ratio $\kappa = R_\rho/R_z$ as well as the peak density $n_0$, as shown in figure 5.7f-h. We thus associate the state with a lower density to the condensate phase and the other with a higher density to the droplet state.

The tendency of a ferrofluid to elongate along the magnetic field direction and to show an instability to much more elongated states was shown for the classical case in section 4.3 and figure 4.4b. For a quantum ferrofluid one certainly needs the quantum fluctuations as a stabilizing effect for the elongated state. Then the occurrence of bistability related to first order phase transitions is also possible. This is the reason for the lack of a stable very elongated state within the mean-field discussion in section 4.5. Very recent theoretical investigations have shown such quantum stabilization in a bosonic non-dipolar mixture with competing attraction and repulsion [298] and for our dipolar system [299, 300].

There are a few more interesting features in figure 5.7. Both the condensate and droplet state can be energetically metastable (local energetic minimum) or the global energetic minimum depending on the scattering length. The energy of the droplet and condensate state intersects at a transition point with $a_{\text{inter}} \approx 90\,a_0$. This transition point is very close to the background scattering length of $^{164}$Dy with $a_{\text{bg}} = 92(8)\,a_0$, where we observed the Rosensweig instability. For further reduced scattering length, the droplet becomes a strongly bound state with negative energy compared to non-interacting atoms. This bound droplet state shows a constant peak density independent of atom number (figure 5.7i), which is a typical property of a liquid with a homogeneous density.

Finally, we compare the variational calculations with the experimental observations. Most importantly, we could identify one possible stability mechanism for the droplets that can stop the collapse. Furthermore, the intersection point of the condensate and droplet state agrees very well with the observed occurrence of the droplets. However, for the experiments we observe many droplets arranging in a regular pattern, whereas the calculations consider only a single droplet. We expect the angular roton instability that induces the condensate to collapse off-center to prevent the formation of a single droplet. Instead the roton instability creates a ring with higher density that is the origin of multiple droplet formation. Very recent numerical simulations started with our experimental parameters and used two paths to the droplet state [301]. The first path was only decreasing the scattering length and resulted in multiple droplets. Contrarily, the second path additionally changed the trap to a prolate case and back to the original state while decreasing the scattering length. This circumvented the roton instability and resulted in a single droplet that had in addition a much lower total energy than multiple droplets. Thus our observed droplet patterns are not the true ground state our system.

---

[66] We give explicitly the energy terms in the appendix A.5 with the quantum fluctuation term in eq. (A.25).

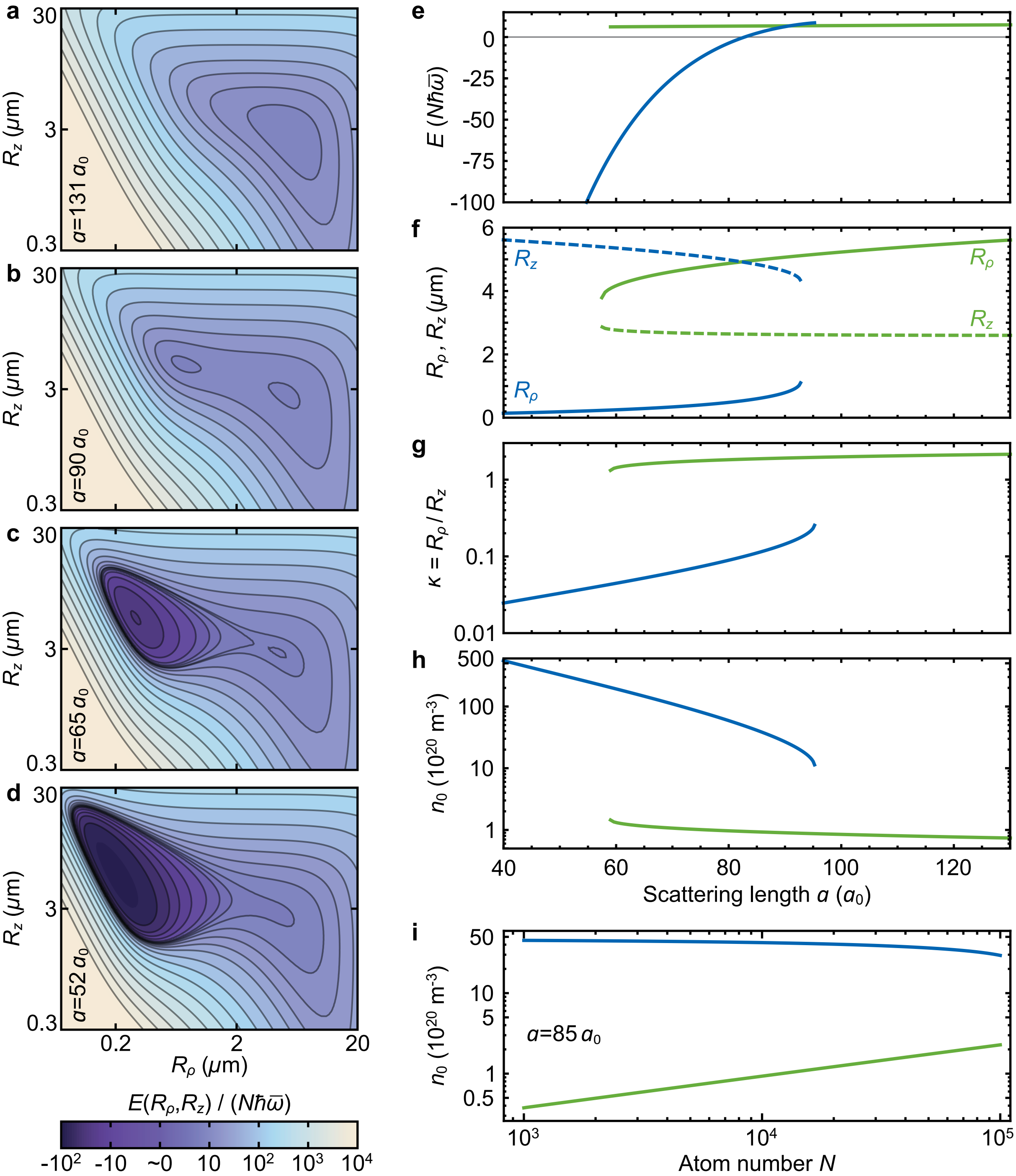

**Fig. 5.7. Properties of dipolar condensates including quantum fluctuations.** We show properties of condensates with $N = 10{,}000$ $^{164}$Dy atoms in a radial symmetric trap with aspect ratio $\lambda = 3$ and $\bar{\omega} = 2\pi \cdot 65\,\text{Hz}$. **a-d**, Energy landscape for variational calculations with inverted parabolic ansatz as a function of $R_\rho$ and $R_z$. Up to two minima are found as a function of scattering length $a$, whose value is stated in the figure. **e-h**, We track the two minima for variable scattering length $a$ and present the condensate state as green line and the droplet state as blue line. We give respectively the energy of the minimum (**e**), Thomas-Fermi radii $R_{\rho,z}$ (**f**), aspect ratio $\kappa$ (**g**) and the peak density $n_0$ (**h**). **i**, We show the peak density $n_0$ in dependence of the atom number $N$. A BEC increases its density proportional to $N^{2/5}$, while the droplet state has a nearly constant density that is slightly decreasing for higher atom numbers.

### 5.2.2. Repulsive three-body interactions

In this section, we discuss the impact of three-body corrections and their applicability to stabilize a droplet state. Hence, we neglect quantum fluctuations and only consider three-body corrections. The three-body correction factor $g_3$ is expected to be very small [285]. Thus, we include additional three-body collisions, which could appear as a consequence of an additional three-body interaction potential. This three-body potential gives a correction for the Gross-Pitaevskii equation that can be written as $g_3' n^2/2$. Here, $g_3'$ is the complex three-body coupling strength that can describe elastic and inelastic three-body scattering. The elastic part is the (real) three-body coupling strength $\kappa_3 = \mathrm{Re}(g_3')$ and the inelastic part is used for the three-body recombination rate $L_3 = \mathrm{Im}(g_3')/\hbar$, that we already introduced in section 5.1.3 describing atom losses. Up to now elastic three-body scattering that should modify many-body effects has not been observed for ultracold quantum gases.

It is expected that the non-measured elastic three-body collisions have a coupling strength $\kappa_3$ that is on the same order of magnitude as the low three-body loss coefficient: $\kappa_3 \approx \hbar L_3 \approx 10^{-41}\,\hbar\,\mathrm{m}^{-6}/\mathrm{s}$. With this argument, the expected value of $\kappa_3$ leads to a three-body contribution to the total energy density which is more than 100 times weaker than the contribution of quantum fluctuations (red line in figure 5.6a). But depending on the microscopic three-body interaction potential, it may be possible that the three-body coupling strength $\kappa_3$ overcomes the inelastic three-body collisions.

With such high elastic three-body interactions, theoretical investigations in the early 2000s predicted stable states with a high atomic density. For instance, a non-dipolar quantum gas with an attractive contact interaction and a repulsive three-body interaction has shown a first-order liquid-gas phase transition apparent with a strong change in density [302, 303]. This work has also been extended to bosons and fermions with the observation of stable so-called *quantum droplets* [304]. Very recent numerical investigations have presented stable droplet patterns in a dipolar quantum gas with repulsive three-body collisions [277, 278], but they had to assume a very high three-body coupling strength compared to the three-body loss coefficient $L_3$ ($\kappa_3 \gtrsim 600\,\hbar L_3 \approx 600 \cdot 10^{-41}\,\hbar\,\mathrm{m}^{-6}/\mathrm{s}$). Furthermore, recent variational calculations with a Gaussian ansatz have also shown bistability related to a first-order phase transition for such a system [301]. We will do a similar approach with an inverted parabola ansatz and estimate a minimal three-body coupling strength $\kappa_3$ to observe stable droplets with our experimental parameters.

We evaluate the energy functional including a repulsive three-body coupling by using a parabolic density distribution as done in the previous section[67]. For sufficiently high $\kappa_3$, we observe very similar properties as for the case with quantum fluctuations, that we have shown in the previous figure 5.7. As one example we present an energy surface in figure 5.8a showing a bistability with two minima. In the following, we focus on the dependence of the minima in respect to the three-body coupling strength $\kappa_3$. We map the intersection point $a_{\mathrm{inter}}$, where the minimum energy of the condensate and droplet state is equal and show it in figure 5.8b. For scattering lengths lower than $a_{\mathrm{inter}}$ the droplet state is energetically favourable compared to the condensate state. We expect $a_{\mathrm{inter}}$ to be in the

---

[67] We mention the energy terms in the appendix A.5 with the three-body term in eq. (A.26).

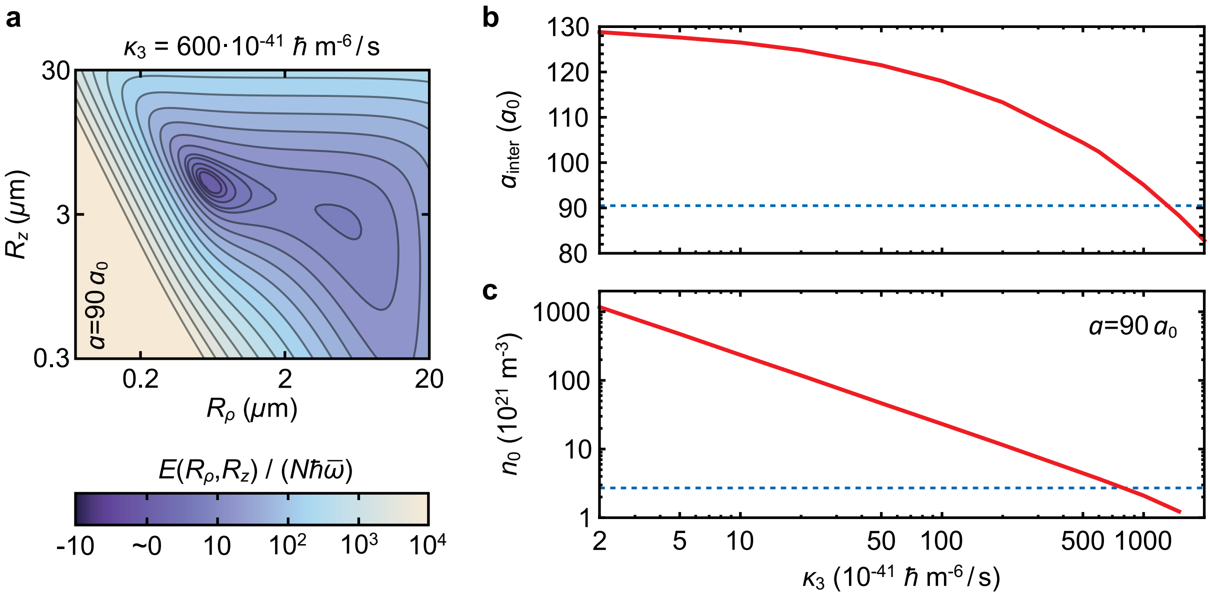

**Fig. 5.8. Properties of dipolar condensates including three-body repulsion.** We show properties of condensates with $N = 10{,}000$ $^{164}$Dy atoms in a radial symmetric trap with aspect ratio $\lambda = 3$ and $\overline{\omega} = 2\pi\cdot 65\,\mathrm{Hz}$. **a**, Energy landscape for variational calculations using a parabolic density distribution as a function of $R_\rho$ and $R_z$. For a very strong three-body repulsion with $\kappa_3 = 600{\cdot}10^{-41}\,\hbar\,\mathrm{m}^{-6}/\mathrm{s}$ there exists two minima with similar energy at $a = 90\,a_0$. **b**, We track the intersection point $a_\mathrm{inter}$, where the energy of the droplet and condensate state is equal, dependent on the three-body coupling strength $\kappa_3$ (red line). The intersection point $a_\mathrm{inter}$ is in the range of the background scattering length $a_\mathrm{bg}$ for $\kappa_3 = 500\text{-}2000{\cdot}10^{-41}\,\hbar\,\mathrm{m}^{-6}/\mathrm{s}$. We show $a_\mathrm{inter}$ for quantum fluctuations as a dashed blue line. **c**, Peak density for the droplet state at a scattering length of $a = 90\,a_0$ for variable three-body coupling strength $\kappa_3$, shown as red line. The peak density reaches the observed density on the order of $n_0 \approx 10^{21}\,\mathrm{m}^{-3}$ again only for very high three-body repulsion with $\kappa_3 > 500{\cdot}10^{-41}\,\hbar\,\mathrm{m}^{-6}/\mathrm{s}$. The peak density including quantum fluctuations is the dashed blue line.

range of $a_\mathrm{bg}$, which is the case for $\kappa_3 \gtrsim 600\,\hbar L_3$. Additionally, we show the peak density $n_0$ at a scattering length of $90\,a_0$ for the droplet state in dependence of $\kappa_3$. Again we can only reach experimental observed densities on the order of $n_0 \approx 10^{21}\,\mathrm{m}^{-3}$ if the three-body coupling strength is $\kappa_3 \gtrsim 500\,\hbar L_3$. In contrast the quantum fluctuations reached the expected values of $a_\mathrm{inter}$ and peak density $n_0$ without any changeable parameter (shown as dashed line in figure 5.8b,c). Due to this behaviour, that repulsive three-body collisions can only reproduce our observations with exceptionally high $\kappa_3$, whereas quantum fluctuations explain the stability without any free parameter, we strongly favour the explanation with quantum fluctuations. In the next chapter we strengthen the quantum fluctuations to be the stabilization reason, as we perform more advanced measurements of the density for the quantum droplets and the stability dependence on the scattering length $a$.

# 6. Quantum Droplets

In the previous section we reported on the observation of a new state of matter which appeared as a product of the Rosensweig instability in a quantum ferrofluid. We observed droplet ensembles that can exist due to a competition of different energy density contributions. They experience an effective attractive mean-field contribution with a scaling of $n^2$ and a repulsive part that scales $n^{2+\alpha}$. This interplay results in liquid-like droplets. Such energy functionals with higher order terms are also used to reliably describe liquid helium droplets [305] and atomic nuclei [306]. Hence, our quantum droplets might be a model system for other quantum matter phenomena. We showed in section 5.2 that the stability of our droplet ensembles could be explained by quantum fluctuations or alternatively by an extremely strong three-body repulsion.

In this chapter, we present discriminating experiments that allow us to establish that the droplets are stabilized by quantum fluctuations. We realized an investigation method to detect properties of the droplets. The main idea is to isolate the droplets by releasing them into an optical waveguide. We present the preparation method and the subsequent propagation of droplets in such a waveguide. We observed inter-droplet repulsion and use this measurement to calculate the spatial extent of a droplet. Further, we examine the scaling behaviour of the density in dependence of the scattering length and obtain agreement with the quantum fluctuations. Finally, we expand the droplets in the absence of gravity to prove that each droplet remains superfluid as well as the peak density agrees with theoretical predictions including quantum fluctuations. All results give strong evidence for quantum fluctuations, and hence we call our new state *quantum droplets* [88].

## 6.1. Quantum droplets in an optical waveguide

In this section, we perform studies on quantum droplets in an optical waveguide. These studies were inspired by a similar experimental sequence performed for bright solitons in non-dipolar quantum gases [307, 308]. Such solitons are self-confining matter waves that means they are stable even when the external confinement along one direction is removed. This means solitary waves can propagate over long distances in a waveguide with neither attenuation nor change in shape. These solitary waves arise from a compensation of natural dispersion by an attractive interaction. The existence of solitary waves is a very general feature of nonlinear wave equations and they have been also observed in many other physical systems including water waves and optics amongst others. If more than a single soliton is apparent, the possibility arises to study soliton collision processes that are dependent on the relative phases of the individual solitons [309, 310].

In the context of dipolar condensates, bright solitons have been predicted in a two-dimensional geometry, where the magnetic dipoles are artificially turned negative or when they are polarized along the plane resulting in an effective attraction [311, 312]. However, we want to stress out that these predictions feature a very different configuration than in our experiments. Additionally, the natural dispersion arising from kinetic energy is known not to stabilize droplets against the mean-field collapse. In consequence although, we observe self-confined quantum droplets that are not solitons or solitary waves in the strict sense. In fact the droplets are again more related to classical ferrofluids, where a surface object was observed that remains localized along two dimensions [313].

Quantum droplets arise from the competition between three contributions. First, the mean-field interactions that tends to create high density elongated states along the magnetic field direction. Second, the repulsive quantum fluctuations that prevent the droplet density from getting too high. And third, the trap confinement constraining the droplets along the field direction. In fact, the droplets remain essentially unchanged when the radial confinement is removed [301]. As a consequence of this effect, we can investigate isolated quantum droplets in an optical waveguide. We will observe their self-confinement and propagation in the waveguide, as well as evidence for collisions between droplets.

### 6.1.1. Preparation of droplets in a waveguide

To perform systematic measurements on the quantum droplets, we place them in an optical waveguide. This relaxes their confinement in one direction and they are allowed to propagate along this $x$-direction. The waveguide is a single optical dipole trap (ODT 1) that creates a tight confinement around the $x$-axis. The release in this waveguide is performed as shown in figure 6.1a. We first created as already explained in section 5.1.1 a stable BEC containing $\sim$10,000 $^{164}$Dy atoms in a crossed optical dipole trap at a magnetic field of $B = B_{\mathrm{BEC}} = 6.96(1)\,\mathrm{G}$ with a weak magnetic gradient to compensate partially gravity. We then lowered the magnetic field within 1 ms to a lower field of $B_{\mathrm{drop}} = 6.66(1)\,\mathrm{G}$ and created as described before in section 5.1.2 droplet ensembles. After further 10 ms, one dipole trap (ODT 2) was turned off in 10 ms, while the power of the other one (ODT 1) was increased. This increase is performed to ensure that the atoms are not pulled out of the trap by gravity. The droplets were then allowed to move in the waveguide for $t_{\mathrm{WG}}$ and were imaged in situ with the high-resolution imaging (section 3.3.3).

In figure 6.1c we present in situ images during the reshaping of the optical dipole traps. The droplet patterns in a triangular structure are compressed along the $y$-direction but are allowed to propagate freely along the $x$-direction. We then observe the following: The condensed atoms remain fragmented into up to six droplets and down to one droplet. Some atoms originally in the condensate do not form quantum droplets, but this fraction is hard to quantify since it is hard to tell apart from a residual thermal fraction in our images. Second, during the evolution time $t_{\mathrm{WG}}$ the initial confinement energy is turned into relative kinetic energy and the droplets move apart. Additionally, we expect the droplets to repel each other as a consequence of the effectively repulsive dipolar interaction between them.

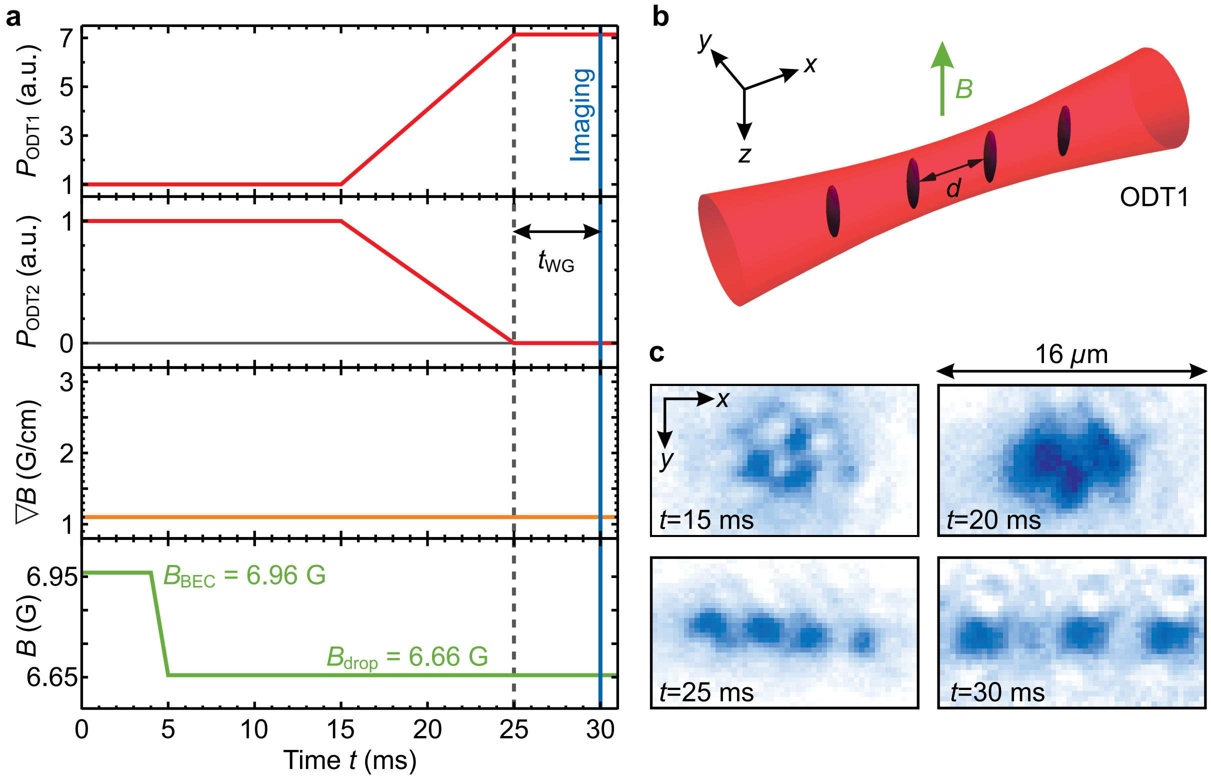

**Fig. 6.1. Preparation of droplets in a waveguide.** **a**, Experimental sequence to release the droplets in an optical waveguide. The droplets were generated with a change in magnetic field from $B_{\mathrm{BEC}}$ to $B_{\mathrm{drop}}$ in 1 ms and a wait time of 10 ms such that the droplets could develop. Afterwards ODT 2 was turned off in 10 ms, while the power $P_{\mathrm{ODT1}}$ was increased to hold the atoms against the partially compensated gravity. The droplets were then released to the waveguide for the time $t_{\mathrm{WG}}$. **b**, Schematic representation of the droplets in the waveguide created by ODT 1 along the $x$-direction. The droplet elongation along the magnetic field direction $z$ is depicted and their respective distance $d$ is indicated. **c**, Representative single sample images during the reshaping of the optical traps. The droplet patterns in an oblate trap ($t = 15\,\mathrm{ms}$) are compressed along the $y$-direction that creates occasionally a zigzag droplet structure (t=20 ms). Then the droplets are released to a waveguide ($t = 25\,\mathrm{ms}$) and are allowed to expand freely along $x$ and can increase their respective distance ($t > 25\,\mathrm{ms}$). Each image shows a field of view of $16\,\mu\mathrm{m} \times 9\,\mu\mathrm{m}$.

The final experimental configuration of droplets in a waveguide is shown in figure 6.1b with their respective separation $d$. The optical waveguide features trap frequencies of $\omega_y = 2\pi \cdot 123(5)\,\mathrm{Hz}$ and $\omega_z = 2\pi \cdot 100(10)\,\mathrm{Hz}$. Along the $x$-direction the trap frequency is $\omega_x < 2\pi \cdot 1\,\mathrm{Hz}$, which is too weak to hold the atoms and they are pulled either by a residual magnetic field gradient or the gravitation.

In the next two sections, we investigate the properties of the droplets within this waveguide. With systematic measurements, we can see self-confining droplets and can calculate their spatial extent. These fundamental properties of the quantum droplets will help in section 6.2 to unravel their nature and confirm quantum fluctuations to be the mechanism ensuring stability.

### 6.1.2. Propagating and self-confining droplets

After placing the quantum droplets in the waveguide, they were allowed to move along the $x$-direction. We then imaged them as a function of time in the waveguide $t_{\mathrm{WG}}$ using our high-resolution imaging. We show representative images in figure 6.2b. We observe atom numbers of $N = 800(200)$ in the droplets. The droplets move away from each other, but remain constant in their size. We extract the in situ size with a fit to a Gaussian function with the Gaussian width as a fit parameter. Note that in this section the Gaussian width is defined using the variance $\mathrm{Var}(x) = \sigma^2_{\mathrm{Var},x}$, which leads to widths that are a factor of $\sqrt{2}$ smaller than previously defined[68] in eq. (2.19). With this definition, we observe an in situ size of $\sigma_{\mathrm{Var},x} \approx 900\,\mathrm{nm}$, that does not evolve for the shown period under observation of $t_{\mathrm{WG}} = 20\,\mathrm{ms}$, as shown in figure 6.2c with blue circles. This size is mainly limited by our optical resolution of $\sim 1\,\mu\mathrm{m}$ and hence we can only state this as an upper bound for the radial droplet size.

By measuring the separation between droplets $d$, we observe a significant increase up to a factor of four, as depicted in figure 6.2d. These facts that a single droplet appears to be stable and that their spatial size remains constant when they move apart, indicates strongly that they are self-confining. Thus, we can exclude already any long-range mechanism between the droplets as a stability process.

To illustrate the self-confinement, we compare it with the evolution of a condensate that is not separated into droplets and subject it to the same experimental sequence. For this measurement, we did the same sequence as shown in figure 6.1a, but kept the magnetic field throughout at a value of $B = B_{\mathrm{BEC}} = 6.96(1)\,\mathrm{G}$. The results of this slightly changed sequence is shown in figure 6.2a. The condensate expands as a whole in the waveguide, at the time of release to the waveguide ($t_{\mathrm{WG}} = 0\,\mathrm{ms}$) it has an axial size of $\sigma_{\mathrm{Var},x} \approx 5\,\mu\mathrm{m}$ which increases by a factor of 10 for the longest observation time of $t_{\mathrm{WG}} = 20\,\mathrm{ms}$, as presented in figure 6.2b with red diamonds. This strong expansion is due to a release of kinetic and interaction energy. The axial size undergoes in the first 10 ms a linear growth[69] with rates of $\dot{\sigma}_{\mathrm{Var},x} \approx 1\mu\mathrm{m/ms}$. This expansion rate can be described in terms of the released energy $E_x = \frac{1}{2} m \dot{\sigma}_{\mathrm{Var},x}$ [314], which results in $E_x \approx 4.5\,\hbar\omega_x^{\mathrm{init}}$, with $\omega_x^{\mathrm{init}} = 2\pi\,46\,\mathrm{Hz}$ the initial trap frequency along the $x$-direction. We will come back to expansion dynamics in section 6.2.2 to measure the density of the droplets.

Since the confinement along the $x$-direction is very weak, residual magnetic gradients or the gravitation pull the atoms away from the imaging region of the waveguide. To keep them within the field of view and measure the droplet repulsion, we need a small confinement along the $x$-direction. For this, we kept the other dipole trap (ODT 2) turned on at a very reduced power[70]. This second set of experiments is shown in the next section and can be used to give a spatial extent for the droplets.

---

[68] The Gaussian density function such that the squared Gaussian width is equal to the variance reads $f(x) = \frac{1}{\sqrt{2\pi}\sigma_{\mathrm{Var}}} \exp\left(\frac{(x-x_0)^2}{2\sigma^2_{\mathrm{Var}}}\right)$. The Gaussian width $\sigma$ from eq. (2.19) and $\sigma_{\mathrm{Var}}$ have a relation that reads $\sigma = \sqrt{2}\sigma_{\mathrm{Var}}$.

[69] For longer times the atomic cloud is accelerated along the $x$-direction, which speeds up the expansion of the condensate.

[70] The trap had a power of $P_{\mathrm{ODT2}} = 0.14$ given in relative units of figure 6.1a.

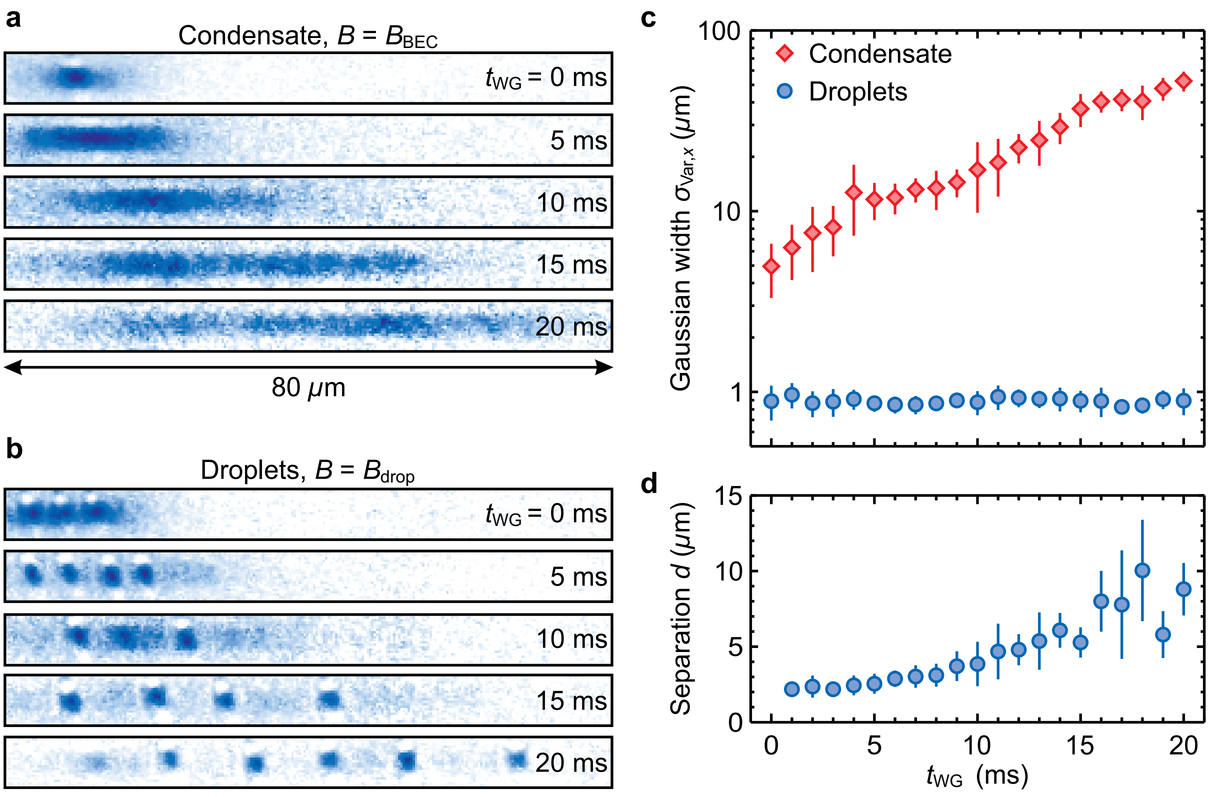

**Fig. 6.2. Condensates and droplets in a waveguide. a,b**, Examples of in situ single sample images after release in the waveguide (field of view is $80\,\mu\mathrm{m} \times 6.4\,\mu\mathrm{m}$). Images were taken at propagation times in the waveguide $t_{\mathrm{WG}} = 0, 5, 10, 15, 20\,\mathrm{ms}$. The samples were released to the waveguide as a condensate kept at a magnetic field of $B_{\mathrm{BEC}} = 6.96\,\mathrm{G}$ (**a**) and in comparison as droplets at a magnetic field of $B_{\mathrm{drop}} = 6.66\,\mathrm{G}$ (**b**). While the condensate expands strongly along the $x$-direction, the size of the droplets remains unchanged. This indicates that the droplets are self-confining. **c**, This evolution of the Gaussian width $\sigma_{\mathrm{Var},x}$ is shown for condensates (red diamonds) and is compared to droplets (blue circles). Each point is an average of 5 realizations and the error bars give the standard deviation. **d**, Separation $d$ between the droplets as a function of time $t_{\mathrm{WG}}$. We used the data taken for **c** to extract the separation $d$ and show it with an error of one standard deviation.

### 6.1.3. Periodic quantum droplet oscillations

In this section, the quantum droplets were released to a prolate trap. This prolate trap was created by the optical waveguide (ODT 1) and a second perpendicular dipole trap (ODT 2) that created a weak confinement along the $x$-direction. This results in a prolate trap with harmonic trap frequencies of $(\omega_x, \omega_y, \omega_z) = 2\pi \cdot (14.5(1), 123(5), 110(10))$ where the magnetic field is still pointing along $z$. This trap has a high trap aspect ratio[71] of $\lambda = \omega_{y,z}/\omega_x \approx 8$. In this trap we can investigate the repulsive interaction between the droplets and use a refined analysis of the droplet distance to calculate the spatial extent of the droplets.

---

[71] The trap aspect ratio is slightly different used as defined before. Previous traps were radial symmetric along the magnetic field direction $z$. Here, the trap is radial symmetric along the $x$-direction.

By releasing the droplets to the prolate-shaped trap, we observe an oscillatory motion of the droplets along the $x$-direction with the weak confinement of $\omega_x = 2\pi \cdot 14.5(1)\,\mathrm{Hz}$. We show this behaviour qualitatively in figure 6.3a with a set of in situ images taken for increasing oscillation time $t_{\mathrm{trap}}$ in the prolate trap. For the shown examples each image has four to six droplets and we can observe an oscillatory motion of the separation $d$ between the droplets, which is represented in figure 6.3b. The oscillation frequency is very close to the trap frequency $\omega_x$ and one observes a strong damping of the oscillations. This damping is at least in part due to the coupling of the droplet relative motion to the background of atoms that are not inside droplets. This background consists mainly of non-condensed thermal atoms, but we also expect a remnant condensed fraction that is not inside the droplets. This background is excited as well and presents a breathing mode that can be also seen in figure 6.3a as the diffuse background. This breathing mode is strongly damped for $t_{\mathrm{trap}} > 30\,\mathrm{ms}$, which in turn slows down the droplets relative motion. Future studies with a reduced thermal background would allow to test the elasticity of the droplet collisions and that the oscillation frequency shows a possible deviation from the trap frequency.

For long observation times $t_{\mathrm{trap}}$ the droplets equilibrate at a distance of $d = 2.5(5)\,\mu\mathrm{m}$. Furthermore, when we first adiabatically loaded a stable condensate in the prolate trap and then induced the Rosensweig instability by changing the field from $B_{\mathrm{BEC}}$ to $B_{\mathrm{drop}}$, we observed the same distance. This distance is smaller than the length obtained by a simple analysis of the problem assuming point-like dipoles. This analysis results in $d = (3N\mu_0\mu_{\mathrm{m}}^2/2\pi m\omega_x^2)^{1/5} \approx 4.5\,\mu\mathrm{m}$, as shown in eq. (5.1). This indicates that the separation is reduced by a finite extent of the droplets along the $z$-direction. Thus, we cannot assume the droplets to be point-like and need a more refined analysis.

To quantitatively determine the separation $d$ and relate it to the spatial extent, we calculate the dipolar energy $E_{\mathrm{dd,inter}}$ between two droplets at a distance $d$ in the Gaussian ansatz with cylindrical symmetry. The calculation to obtain this inter-droplet interaction is shown in appendix A.4 and the final result for $E_{\mathrm{dd,inter}}$ is written in eq. (A.22). The dipolar interaction is in our geometry effectively repulsive at long range and depends on the separation $d$ as well as the spatial extents $\sigma_{\mathrm{Var},\rho}$ and $\sigma_{\mathrm{Var},z}$. There exists always a global minimum for $d = 0$ as the dipolar interaction is for overlapping droplets effectively attractive. For $d > 0$, the dipolar repulsion is counteracted by the harmonic trap energy that reads $E_{\mathrm{trap}} = Nm\omega_x^2 d^2/4$ for two droplets with the mass of $N$ dysprosium atoms.

We then search for energy minima in the sum of dipolar energy ($E_{\mathrm{dd,inter}}$) and trap energy ($E_{\mathrm{trap}}$) as a function of the droplet separation $d$. For low enough droplet sizes such that $d \gg \sigma_{\mathrm{Var},\rho}$, the individual density distributions are only weakly overlapping, and there exists a local minimum. In figure 6.3c we present the distance $d$ of this local minimum obtained as a function of the Gaussian widths $\sigma_{\mathrm{Var},\rho}$ and $\sigma_{\mathrm{Var},z}$ for 800 atoms in a droplet. When a local minimum exists, its separation $d$ depends mainly on $\sigma_{\mathrm{Var},z}$. The experimentally observed separation of $d = 2.5(5)\,\mu\mathrm{m}$ is only possible within the region delimited by the dashed line visible in figure 6.3c. From this we see that the experimental value can be only fulfilled for $\sigma_{\mathrm{Var},z} = 2.5(5)\,\mu\mathrm{m}$ and for the radial extent we can only give an upper bound of $\sigma_{\mathrm{Var},\rho} \lesssim 500$ nm.

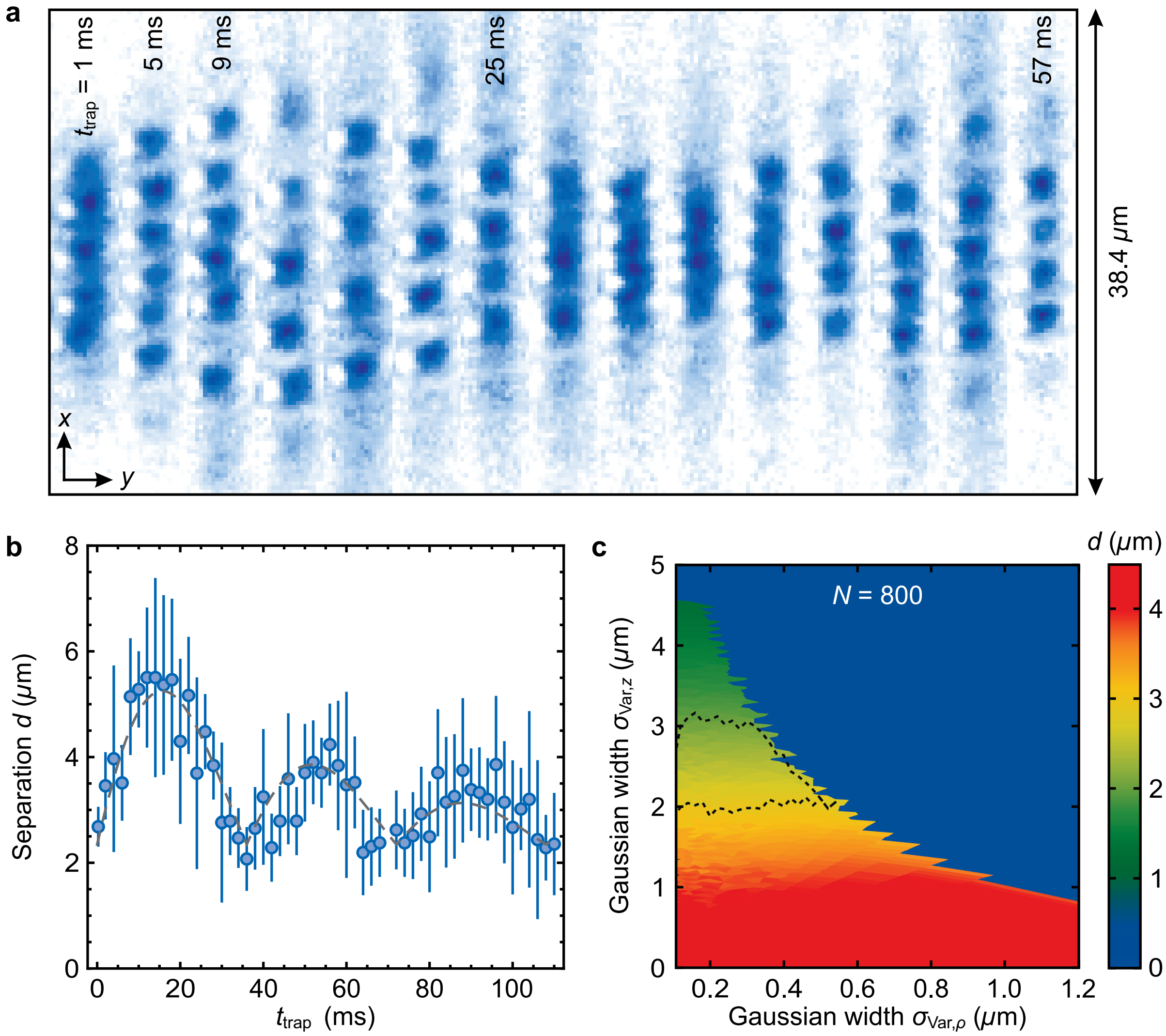

**Fig. 6.3. Quantum droplets in a prolate trap.** **a**, After the creation of the quantum droplets we transfer them to a prolate trap with trap frequencies $(\omega_x, \omega_y, \omega_z) = 2\pi \cdot (14.5, 123, 110)\,\text{Hz}$. The droplets then oscillate along the $x$-direction in the harmonic trap and are allowed to collide. We show in situ images for a time sequence of multiple oscillating droplets with the oscillation time $t_{\text{trap}}$ mentioned in the figure. Each image has a field of view of $38.4\,\mu\text{m} \times 5.5\,\mu\text{m}$. **b**, Separation between the droplets $d$ as a function of wait time $t_{\text{trap}}$ in the prolate trap. Each point is an average of 5 realizations with the standard deviation as error bars. The separation $d$ oscillates with the axial frequency $\omega_x$ and shows a strong damping. The grey dashed line is a guide to the eye with a frequency of $\omega_x$. At long times the droplets equilibrate with a separation of $d = 2.5(5)\,\mu\text{m}$. **c**, Droplet separation $d$ that locally minimizes the total energy of two repelling droplets in a harmonic confinement with trap frequency $\omega_x$. The separation $d$ is a function of the droplet widths $\sigma_{\text{Var},\rho}$ and $\sigma_{\text{Var},z}$. The local energy minimum for $d > 0$ only exists in a certain range of parameters. If a minimum exists the separation $d$ only depends on $\sigma_{\text{Var},z}$. The area within the dashed line shows the possible values of $\sigma_{\text{Var},\rho}$ and $\sigma_{\text{Var},z}$ for our experimentally observed separation of $d = 2.5(5)\,\mu\text{m}$.

## 6.2. Evidence of quantum fluctuations

In the previous section, we used our measurements to show that the droplets are strongly elongated along the magnetic field direction with an aspect ratio of $\kappa \lesssim 0.2$. Inside a droplet, this results in a dipolar interaction that is mainly attractive and since $\varepsilon_{\mathrm{dd}} > 1$ this attraction is stronger than the repulsive contact interaction. Hence, the droplets are expected to be unstable in the mean-field description, as discussed in section 4.5.3. In section 5.2, we presented how beyond mean-field effects can stabilize these droplets. For example in figure 5.7g we calculated the aspect ratio for droplets including quantum fluctuations and got similar values with $\kappa < 0.2$. However, the same is true including additional repulsive three-body interactions. But quantum fluctuations and three-body interactions differ in their atomic density scaling for the energy density. Thus, measuring the droplet density should unravel the nature of the stabilizing mechanism.

In this section, we identify quantum fluctuations to be the stabilization mechanism, as we measure further properties of the droplets. The following experiments determine the droplet atomic density and its dependence on the scattering length $a$. The measured properties agree very well with corrections that include quantum fluctuations and are incompatible with three-body repulsion.

### 6.2.1. Lifetime of quantum droplets

The droplets are dense and thus exhibit enhanced three-body recombination losses. We have shown indeed in section 5.1.3 the droplet ensembles reduced lifetime compared to a condensate. By extracting the droplet lifetime, we could estimate a droplet peak density. In this section, we measure the droplet lifetime for different values of the scattering length $a$. When using quantum fluctuations as stabilization mechanism, we have seen a strong increase of the density for decreasing $a$ in figure 5.7h. In contrast when including three-body repulsion the scaling of the density with $a$ is much weaker [301]. In turn, we expect also that the three-body recombination losses, that strongly increase for higher densities, show a strong dependence on the scattering length $a$.

The experimental sequence is identical to the previous section 6.1.3 where we released the droplets in a prolate trap. The only difference is that we investigated it here for much longer times $t_{\mathrm{trap}}$. For this time, we tuned the magnetic field to varying final values $B_{\mathrm{f}}$ to control the final scattering length $a_{\mathrm{f}}$ and map the total atom number $N$ of the sample. As a result of these measurements, we show three exemplary atom number decay curves in figure 6.4a for varying magnetic field $B_{\mathrm{f}}$. We observe initially a decay with a fast time scale, that we call $\tau_{\mathrm{f}}$ and is typically a few hundred ms. This fast decay stops at atom numbers of $N = 4000(250)$ and then follows a decay with a much longer time scale of several seconds. We associate the fast one to the lifetime of the droplets, before a remnant cloud with 4000 atoms is left, that is too dilute to form droplets and thus decays much more slowly. We do in fact only observe droplets during the initial fast decay. The lifetime of the droplets is then extracted with a fit to an exponential decay. By allowing the long-term atom number to change between 3750 and 4250, we get an uncertainty on $\tau_{\mathrm{f}}$.

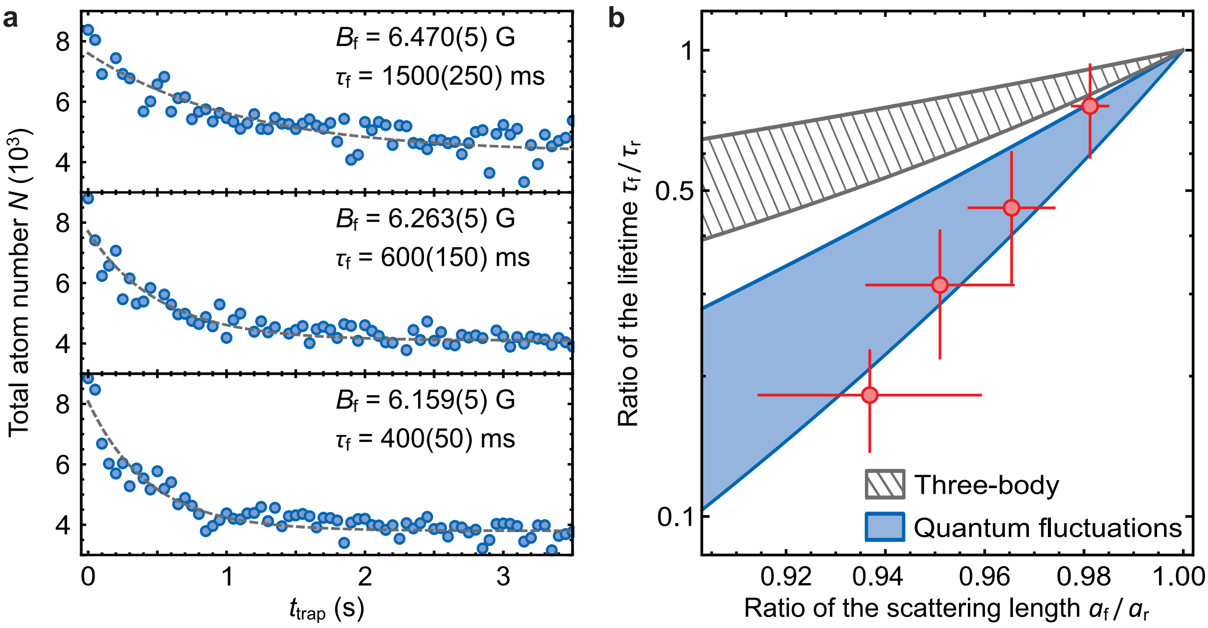

**Fig. 6.4. Lifetime of quantum droplets.** **a**, Atom number lifetime measurements in the prolate trap. We performed lifetime measurements at varying magnetic field $B_\mathrm{f}$ for five different values ranging from 6.573(5) G to 6.159(5) G. The figure shows the total atom number $N$ as a function of $t_\mathrm{trap}$ for three different final magnetic fields $B_\mathrm{f}$ and the existence of two time scales is evident. From the fast initial dynamics, we extract the droplet lifetime $\tau_\mathrm{f}$. **b**, Droplet lifetime $\tau_\mathrm{f}$ versus the scattering length $a$. The figure shows the ratio of the droplet lifetime $\tau_\mathrm{f}/\tau_\mathrm{r}$ as a function of the ratio of the scattering length $a_\mathrm{f}/a_\mathrm{r}$, where the reference lifetime is taken with $a_\mathrm{r} = 94(12)\,a_0$ at $B_\mathrm{r} = 6.573(5)$ G. The filled blue and hatched grey areas represent the expected scaling using quantum fluctuations and three-body repulsion. The areas take into account the uncertainty range on the droplets aspect ratio $0 \leq \kappa \leq 0.2$.

We present the measured lifetimes $\tau_\mathrm{f}$ as red circles normalized to the reference lifetime $\tau_\mathrm{r}$ at $B_\mathrm{r} = 6.573(5)$ G in figure 6.4b against their scattering length $a_\mathrm{f}$ given in units of the reference scattering length $a_\mathrm{r} = 94(12)\,a_0$. The data is presented in unitless variables not only for simplicity, it also leads to a more convenient theoretical analysis. The ratio of the lifetimes fulfils the relation

$$\frac{\tau_\mathrm{f}}{\tau_\mathrm{r}} = \frac{\langle n_\mathrm{r}^2 \rangle}{\langle n_\mathrm{f}^2 \rangle} = \frac{n_{0,\mathrm{r}}^2}{n_{0,\mathrm{f}}^2}\,, \tag{6.1}$$

where the decay lifetime is given as $\tau = 1/L_3\langle n^2 \rangle$. We used a constant three-body loss rate $L_3$ independent of the scattering length $a$ and the fact that the droplet density is independent of the atom number (as shown in figure 5.7i).

A simple analytic calculation to estimate the peak density $n_0$ in dependence of the scattering length $a$ including beyond mean-field effects is shown in appendix A.7. The squared ratio of the peak densities taken at different scattering lengths is then only dependent on the two dimensionless variables $\frac{a_\mathrm{f}}{a_\mathrm{r}}$ and $\frac{a_\mathrm{dd}}{a_\mathrm{r}}$, as shown with eq. (A.34) and (A.35). In particular for three-body repulsion, the ratio is independent on the three-body coupling constant $\kappa_3$. We present in figure 6.4b the scaling behaviour of these ratios using quantum fluctuations (blue area) and three-body repulsion (grey hatched area).

The data points are incompatible with the scaling predicted by three-body repulsion while without any fit parameter they follow the scaling of quantum fluctuations. This demonstrates explicit that quantum fluctuations constitute the stabilizing mechanism. But, a value for the central peak density is still missing, that is derived in the final section.

### 6.2.2. Expansion and interference of droplets

The last investigation method used in this thesis for the quantum droplets is their time of flight (ToF) expansion in free space. However, the droplet expansion is not yet completely understood and needs further theoretical and experimental effort. There has been predictions that liquid-like droplets exhibit an absence of growth without external confinement [277, 298]. On the other hand the expansion of dipolar gases is well studied in the mean-field approximation [36–38], but is in our case modified by beyond mean-field effects [291]. Therefore, to quantitatively express the droplet expansion, we measure the released energy and use these measurements to obtain the atomic density of the droplets.

For the expansion measurements, we used the experimental sequence as shown in figure 6.5a. As before we transferred the droplets in the optical waveguide and turned off the waveguide after $t_{\mathrm{WG}} = 4\,\mathrm{ms}$. In order to keep the atoms at the focal position of our high-resolution imaging system, we increased the magnetic field gradient to compensate completely gravity. At the same time we may have quenched the magnetic field $B_{\mathrm{ToF}}$ in $50\,\mu\mathrm{s}$ to values ranging from $B_{\mathrm{drop}}$ to $7.01\,\mathrm{G}$, which tuned the short-range contact interaction. The droplets then levitated for the time $t_{\mathrm{ToF}}$ and were imaged for various times after release. Figure 6.5b shows examples of this expansion measurement for $B = B_{\mathrm{drop}}$ and $B = 6.86\,\mathrm{G}$.

We first discuss the case of a constant magnetic field (no quench) at $B = B_{\mathrm{drop}}$. We record the sizes $\sigma_{\mathrm{Var},x}$ and $\sigma_{\mathrm{Var},y}$ as a function of the time $t_{\mathrm{ToF}}$. We show in figure 6.5c the size along the $y$-direction with blue circles and observe that the droplets expand. The sizes undergo a linear growth with a rate of $\dot{\sigma}_{\mathrm{Var},x} = 0.17(3)\,\mu\mathrm{m/ms}$ and $\dot{\sigma}_{\mathrm{Var},y} = 0.24(3)\,\mu\mathrm{m/ms}$. We qualitatively express the expansion dynamics in terms of a released energy $E_i = \frac{1}{2}m\dot{\sigma}^2_{\mathrm{Var},i}$ [314], which is the sum of kinetic and interaction energy [94, p. 168]. This results in $E_x = 0.045(4)\,\hbar\omega_y$ and $E_y = 0.09(1)\,\hbar\omega_y$, which are remarkably low energies and demonstrates that kinetic energy plays only a marginal role as expected. However, a full theory is presently not available to describe the free-space dynamics for our system after the release. To circumvent the absence of a theoretical model for the droplet dynamics, we investigate only relative changes in the released energy for increasing contact interactions.

Hence, we consider now the droplet expansion for $B_{\mathrm{ToF}} > B_{\mathrm{drop}}$. For increasing fields $B_{\mathrm{ToF}}$ the scattering length $a$ is increased. Thus, we release additional interaction energy, that can be measured as faster expansion. The droplets' size becomes comparable to or larger than their relative distance such that neighbouring ones overlap. In this case, we observed matter-wave interference fringes along the $x$-direction as exemplified on the right side of figure 6.5b. The presence of these fringes demonstrates that each droplet individually is phase coherent and thus superfluid. Their observation opens the door to studies of the relative phase coherence between droplets, which is compelling evidence for

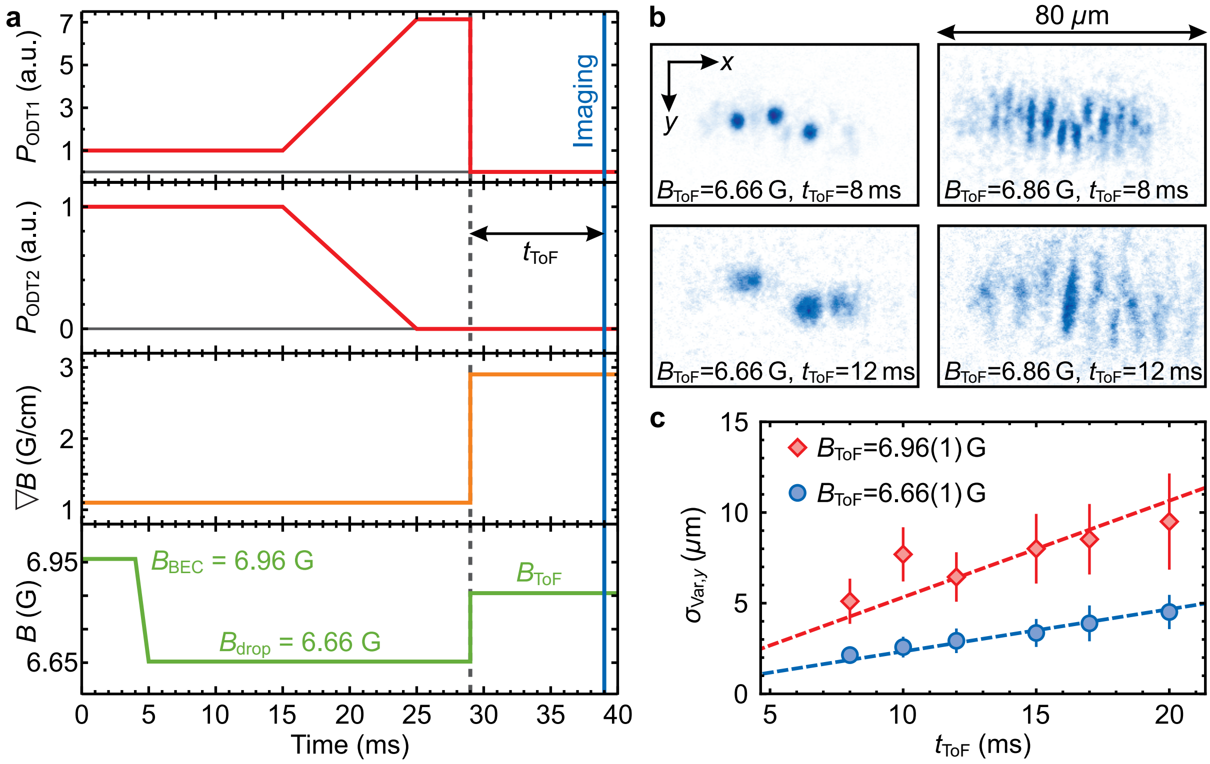

**Fig. 6.5. Expansion and interference of droplets. a**, Experimental sequence for time of flight expansion measurements. The droplets were transferred in the waveguide with $t_{\mathrm{WG}} = 4\,\mathrm{ms}$ at a field of $B_{\mathrm{drop}} = 6.66(1)\,\mathrm{G}$. When the droplets were released from the optical trap for free expansion, we completely compensated gravity with a magnetic gradient and quenched the magnetic field to different values $B_{\mathrm{ToF}}$ for the expansion time $t_{\mathrm{ToF}}$. **b**, Examples for a time of flight expansion measurement with a field of view of $80\,\mu\mathrm{m} \times 48\,\mu\mathrm{m}$. For the two left images the magnetic field was kept at $B_{\mathrm{drop}}$ during expansion, while for the two right images it was quenched to $B = 6.86\,\mathrm{G}$. We can observe clear interference fringes along the $x$-axis while we can still measure the expanded width along the $y$-direction. **c**, Gaussian width $\sigma_{\mathrm{Var},y}$ as a function of time of flight $t_{\mathrm{ToF}}$. We show examples for varying field $B_{\mathrm{ToF}}$: Blue circles show expansion at $B_{\mathrm{ToF}} = B_{\mathrm{drop}}$ and red diamonds at $B_{\mathrm{ToF}} = B_{\mathrm{BEC}}$. Each point is an average of 30-40 realizations with one standard deviation as error bars. By assuming a linear time dependence (dashed lines), we can evaluate the released energy $E_y = \frac{1}{2} m \dot{\sigma}^2_{\mathrm{Var},y}$.

a supersolid state discussed in section 5.1.5. In the present case we do not observe fringe patterns that allow us to measure the droplets relative phase, but this is mainly due to shot-to-shot noise in the in-situ position and relative spacing of the droplets since we are not yet in the far-field regime.

Although the droplets start to overlap along the $x$-direction and show interference fringes, we can still measure their size along the $y$-direction. As an example, we show in Figure 6.5c the widths $\sigma_{\mathrm{Var},y}$ for $B_{\mathrm{ToF}} = B_{\mathrm{BEC}} = 6.96\,\mathrm{G}$ as red diamonds and observe again a linear growth in the size with slope $\dot{\sigma}_{\mathrm{Var},y}$. By repeating this measurement for varying magnetic field $B_{\mathrm{ToF}}$, we get the released energy $E_y(B_{\mathrm{ToF}})$. For increasing magnetic field the contact interaction is changed by an amount of $\Delta a_{\mathrm{ToF}} = a(B_{\mathrm{ToF}}) - a(B_{\mathrm{drop}})$ with $a(B_{\mathrm{drop}}) = 95(13)\,a_0$.

We present in figure 6.6a in blue circles the difference in released energy $\Delta E_y = E_y(B_{\text{ToF}}) - E_y(B_{\text{drop}})$ in dependence of the change in scattering length $\Delta a_{\text{ToF}}$. As can be seen, the released energy and the corresponding expansion rate is strongly increased. Given the short quench time of $50\,\mu$s for the magnetic field, the initial density distribution of a single droplet does not have time to adapt to the interaction quench. One thus expects that the change in released energy is given by

$$\Delta E \simeq \frac{1}{N}\int \mathrm{d}^3r\,\frac{\Delta g}{2}n^2 = \frac{\Delta g}{2}\langle n\rangle = \begin{cases} \frac{1}{4\sqrt{2}}\,\Delta g\, n_0 & \text{with Gaussian ansatz} \\ \frac{2}{7}\,\Delta g\, n_0 & \text{with inverted parabola} \end{cases}, \tag{6.2}$$

with $\Delta g = 4\pi\hbar^2\Delta a_{\text{ToF}}/m$. Since we are dealing with the difference in total energy here, the variation of the beyond mean-field corrections is negligible. Thus, we can adjust eq. (6.2) to our measured data in figure 6.6a using the density as a single fit parameter. The result is shown as green line with a green shaded confidence interval and we obtain $\langle n\rangle = 1.7(7)\cdot 10^{20}\,\mathrm{m}^{-3}$. Using the Gaussian ansatz this yields $n_0^{\mathrm{G}} = 4.9(2.0)\cdot 10^{20}\,\mathrm{m}^{-3}$, while for the inverted parabola we obtain $n_0^{\mathrm{TF}} = 3.0(1.2)\cdot 10^{20}\,\mathrm{m}^{-3}$.

The final last step is to verify if the obtained peak density values are compatible with predictions including quantum fluctuations. For this verification, we consider the chemical potential of a dipolar quantum gas with beyond mean-field correction terms, as given in eq. (5.6). We use a Gaussian function or an inverted parabola for the density distribution[72] and analyse the mechanical stability condition[73] $\frac{\partial\mu}{\partial n} \geq 0$ at the central trap position with the peak density $n_0$

$$\left.\frac{\partial\mu}{\partial n}\right|_{r=0} = g\,[1 - \varepsilon_{\text{dd}} f_{\text{dip}}(\kappa)] + \begin{cases} 16g\sqrt{n_0 a^3/\pi}\,(1 + \frac{3}{2}\varepsilon_{\text{dd}}^2) & \text{Quantum fluctuations} \\ \kappa_3 n_0 & \text{Three-body repulsion} \end{cases}. \tag{6.3}$$

For our experimental values of $\varepsilon_{\text{dd}} \approx 1$ and $f_{\text{dip}}(\kappa < 0.2) > 0.83$, the first two mean-field contributions nearly balance each other which leads to a major role for beyond mean-field effects. We show the relation (6.3) in figure 6.6b as a function of the peak density $n_0$. For low densities, $\frac{\partial\mu}{\partial n}$ is negative and the system is unstable, while for high enough densities it becomes positive and the system fulfils the stability condition. We plot $\frac{\partial\mu}{\partial n}$ by including quantum fluctuations as blue shaded region using the parameters $a = 95(13)\,a_0$ and $\kappa = 0.1$ (this $\kappa$ value is a factor two below the experimental upper bound, it yields $f_{\text{dip}}(\kappa) = 0.94$). And with three-body repulsions it is shown for the parameters $a = 95\,a_0$ and $\kappa_3 = 6\cdot 10^{-39}\,\hbar\mathrm{m}^6/\mathrm{s}$ as a dashed grey line. The measured peak densities are shown as orange square ($n_0^{\mathrm{TF}}$) and red circle ($n_0^{\mathrm{G}}$). Both density values are in agreement with the stabilizing density due to quantum fluctuations, while even a very high value of $\kappa_3$ is not sufficient to stabilize these densities.

---

[72] This simplifies the dipolar contribution $\Phi_{\text{dip}} = -\varepsilon_{\text{dd}} g n_0 f_{\text{dip}}(\kappa)$ and defines a peak density $n_0$ at the central position of the trap.

[73] The bulk modulus $K$ is for a thermodynamic system defined as $K = -V\frac{\partial p}{\partial V}$ which can be written for quantum gases as $K = n^2\frac{\partial\mu}{\partial n}$ [95, p. 413]. The bulk modulus measures the resistance to uniform compression. If $K$ is negative the system is unstable against a decrease in volume.

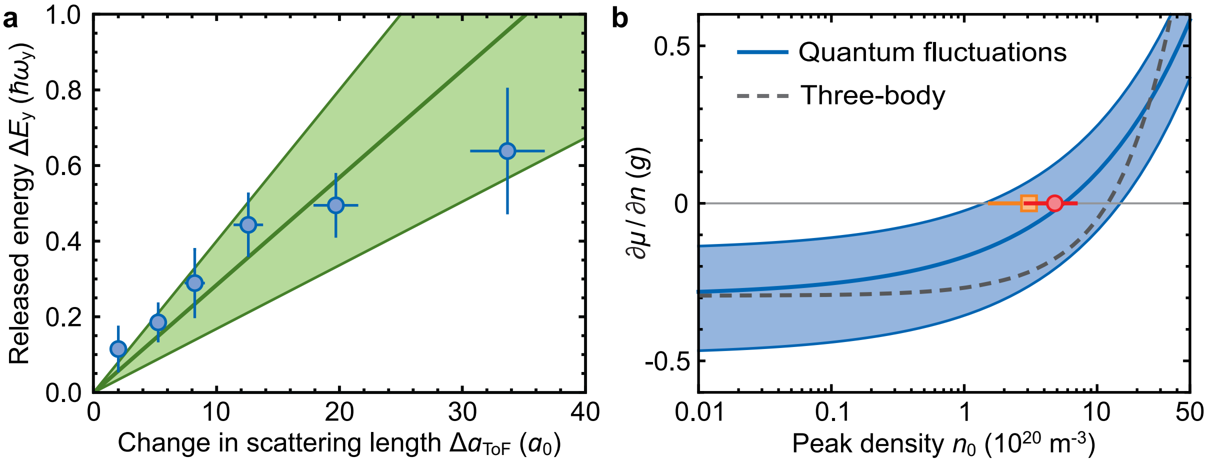

**Fig. 6.6. Results from the expansion measurements.** **a**, Difference in released energy $\Delta E_y$ with respect to $B = B_{\mathrm{drop}} = 6.66\,\mathrm{G}$ with $a_{\mathrm{drop}} = 95(13)\,a_0$. The blue points were taken for $B_{\mathrm{ToF}} = 6.73\,\mathrm{G}$ to $7.01\,\mathrm{G}$ and are plotted for the change in scattering length $\Delta a_{\mathrm{ToF}}$. The green shaded area is an estimate of the change in released energy dependent on the density as a single fit parameter, see eq. (6.2), which gives an expectation value for the density of $\langle n \rangle = 1.7(7) \cdot 10^{20}\,\mathrm{m}^{-3}$. The green shaded area represents the confidence interval. **b**, Derivative of the chemical potential with respect to density $(\partial\mu/\partial n)$ as a function of peak density $n_0$. The blue shaded area expresses our uncertainty on the scattering length. Negative values imply mechanical instability, while positive values are stable. The expectation value for the density $\langle n \rangle$ obtained from **a** is shown as peak densities assuming a Gaussian distribution (red circle) or an inverted parabola (orange square). The dashed grey line shows $\partial\mu/\partial n$ obtained using a three-body repulsion with parameters $a = 95\,a_0$ and $\kappa_3 = 6 \cdot 10^{-39}\,\hbar\mathrm{m}^{-6}/\mathrm{s}$, which stabilizes at a peak density $n_0 = 12 \cdot 10^{20}\,\mathrm{m}^{-3}$ much higher than experimentally shown.

In this chapter, we have seen that quantum droplets are self-confining due to their strong elongation along the magnetic field direction. By systematic measurements on individual droplets, we demonstrated quantitatively that quantum fluctuations mechanically stabilize them against the mean-field collapse. We observed in addition interference of several droplets indicating that each droplet remains superfluid itself. Hence, quantum droplets are a novel liquid-like state of matter stabilized by quantum fluctuations.

# 7. Conclusion and Outlook

In this thesis, we have presented the experimental observation of a new state of matter, a liquid-like quantum droplet. This state was unpredicted prior to our experimental investigations, which is a rare case in the field of cold atomic physics. Ultracold gases realize a very clean, controllable many-body model system, that can be predetermined in the framework of mean-field theory. However, our experiments have exhibited clear effects that go beyond this mean-field theory. In fact, we have shown that quantum fluctuations play a dominant role, which are neglected in mean-field theory. The studies presented in this work are the first theoretical description and experimental detection of quantum fluctuations acting as a stabilizing mechanism. We expect this to be a major discovery for the growing research field of dipolar quantum gases and to be the basis for proposals of novel achievable physics.

This discovery of quantum droplets was only possible thanks to our recently built new generation apparatus. This step forward allowed us to cool dysprosium atoms down to quantum degeneracy with advanced laser cooling schemes. In particular, the optical transport to a glass cell with high optical access enables the use of an imaging system with a high spatial resolution of $1\,\mu$m. An additional precise magnetic field control can tune the contact interaction strength by utilizing magnetic Feshbach resonances. With these experimental tools, we created a quantum ferrofluid of dysprosium atoms with a high control on internal and external properties as well as a detection method unique for dipolar gases.

Preparing this controllable system, we could induce a Rosensweig instability, known from classical ferrofluids. A classical ferrofluid forms a regular pattern of surface peaks when a strong magnetic field is present. This effect is only possible as a consequence of a competition of three different forces: surface tension, gravitation and magnetic dipole-dipole interaction. This interplay appears also as a non-monotonously increasing dispersion relation possessing a local minimum. We demonstrated in this thesis the similarities of classical and quantum ferrofluids. Quantum ferrofluids also exhibit a competition of contact interaction, external trapping and magnetic dipole-dipole interaction, which is the basis of an excitation spectrum featuring a roton minimum. By carefully tuning the contact interaction, we induced an angular roton or Rosensweig instability and created stable quantum droplets. By releasing these droplets to an optical waveguide, we could observe first properties. They are self-confining as a result of their strong elongation along the magnetic field. And they can travel without a change of shape along a waveguide and remain superfluid.

We presented a variational approach as a first theoretical framework to predict properties of the quantum droplets. For this, we inserted a parabolic density distribution in the energy functional including beyond mean-field corrections due to quantum fluctuations. With this approach, we could verify the observed effects. We could check the parameter range to observe stable droplets and understand the nature of the Rosensweig instability. The transition from a condensate to a droplet state is very similar to a first-order phase transition featuring bistability and hysteresis. We could also conclude that the droplets are strongly elongated along the magnetic field direction and behave like a liquid. However, this approach is not yet fully developed. The absolute values of the spatial extent and peak density are not consistent with experimental observations. A different approach using a stability criterion derived from the chemical potential resulted in very good agreement for the peak density and the density scaling. Future studies have to determine the appropriate density function to obtain values consistent with experiments. Very recent work describing quantum droplets numerically [299], indicates that the density distribution may be described with a function $\propto (1-\frac{z^2}{R_z^2})^{2/3}$ along the magnetic field direction and a Gaussian function perpendicular to it. However, this probably changes the geometry dependent dipolar anisotropic function $f_{\mathrm{dip}}(\kappa)$ and complicates the variational approach.

**Outlook**

We achieved further progress in the understanding of quantum droplets with numerical calculations using the Gross-Pitaevskii equation (2.12) including an additional term attributed to quantum fluctuations. We already used this new tool for numerical calculations in this thesis shown in figure 2.5b and 4.10e. One of the first simulations on quantum droplets is depicted in figure 7.1a. We could reproduce elongated droplets with a high atomic density. These studies will help to predict basic properties such as peak density, spatial extent and stability properties, but also more complicated characteristics such as collective oscillation frequencies, droplet collision physics or free expansion.

Of course, the above mentioned aspects can be also experimentally investigated. Unfortunately, the droplet creation remains a statistical process with varying number of droplets and spatial position. But our apparatus offers the possibility to create time-averaged tailored trapping potentials using a green laser guided through an electro-optical deflector (EOD) system and the microscope objective. In figure 7.1b,c we show first results with two different potentials imprinted on a dysprosium condensate. With this possibility to create almost arbitrary potentials, we could seed single droplets at well defined positions. Alternatively, we could create a single big quantum droplet by circumventing the roton instability and inducing the phonon instability to the droplet state.

Additionally, with these tailored potentials one can visibly demonstrate the long-range character of the dipolar interaction. In a linear three-well system with controllable tunnelling and particle interaction various phases are expected to occur [315–317]. In on of these phases, the atoms may be found on the two outer wells, while the central one is depopulated. The tailored potential may also allow to observe dipolar condensate in toroidal traps (see figure 7.1c). There, the condensate is predicted to form a self-induced Josephson junction [318].

For all these experiments we use the magnetic Feshbach resonances to tune the contact interaction strength. However, the microscopic scattering process and the properties of the

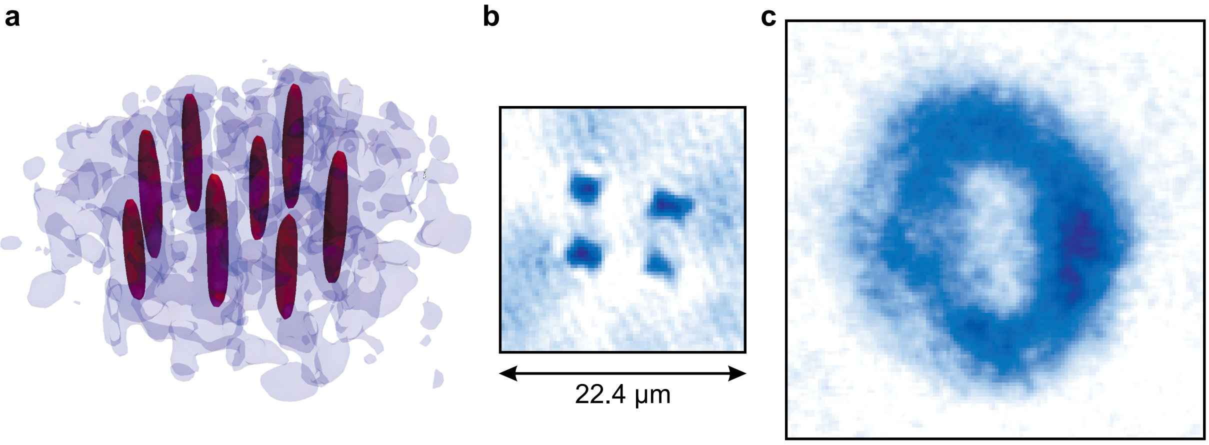

**Fig. 7.1. Control over quantum droplets and tailored potentials. a**, Numerical simulation of the Rosensweig instability of a quantum ferrofluid. The figure shows isodensity surfaces for a high density droplet state (red) and a much lower density (blue) in a side view. **b,c**, First tailored potentials written on a dysprosium condensate. For these potentials we used a green laser, two electro-optical deflectors (EOD) and the microscope objective. Exemplary, we show a four-well system (**b**) and a toroidal ring potential (**c**).

molecular potentials for the closed channel remains unclear. In addition, many Feshbach resonances seem to be temperature dependent, even in a temperature range when only s-wave scattering should be dominant. By investigating in detail the two-body interaction it might be even possible to create bound dimers of dysprosium atoms, which exhibit even higher dipole-dipole interaction.

Besides, we can utilize the Feshbach resonances to investigate interesting few-body physics. For non-dipolar quantum gases universal Efimov states, trimer bound states, were observed [14]. By including very strong dipolar interaction the Efimov trimers persist. Moreover, the dipolar interaction adds new physical aspects to Efimov states [319]. In particular, for dipolar interaction lengths larger than the contact interaction range, the positions of the Efimov resonances are universally determined by the two-dipole physics only. The same is predicted for three identical fermionic dipoles, that also show a long-lived three-dipole state [320].

Finally, we want to mention the rich atomic energy spectrum of lanthanides. For dipolar atoms, there exists a cooling method that is in principle lossless. The demagnetization cooling developed for chromium atoms [46] has shown a good cooling potential in recent experiments [321, 322]. Early studies with dysprosium atoms [177] using a transition at a wavelength of 684 nm [323] need further effort, but could help to create colder atomic samples with a higher atom number.

This list is of course far from being complete. Especially, as we are not restricted to bosonic dipolar gases. We were able to generate fermionic ultracold gases consisting dysprosium atoms [178]. In principle our apparatus was designed to work with Bose-Fermi mixtures using two dysprosium isotopes at the same time. This shows the variety of ultracold gases and the multitude of possibilities for our apparatus.

# A. Appendix

## A.1. Fourier transform of the binary interactions

The binary interactions (2.8) may be expressed in Fourier space, as the mean-field interaction potential (2.13) can thereby be simplified. By using the definition of a convolution on the mean-field interaction potential $\Phi_{\text{int}}(\boldsymbol{r})$, one reads

$$\Phi_{\text{int}}(\boldsymbol{r}) = \int \mathrm{d}^3 r' \, U_{\text{int}}(\boldsymbol{r} - \boldsymbol{r}') n(\boldsymbol{r}') = U_{\text{int}}(\boldsymbol{r}) * n(\boldsymbol{r}) \ . \tag{A.1}$$

In the following, we use this convention for the three-dimensional Fourier transform

$$\tilde{f}(\boldsymbol{k}) = \mathcal{F}\left\{f(\boldsymbol{r})\right\} = \int \mathrm{d}^3 r \, f(\boldsymbol{r}) \, \mathrm{e}^{-i\boldsymbol{k}\boldsymbol{r}} \tag{A.2a}$$

$$f(\boldsymbol{r}) = \mathcal{F}^{-1}\left\{\tilde{f}(\boldsymbol{k})\right\} = \int \mathrm{d}^3 k \, \tilde{f}(\boldsymbol{k}) \, \mathrm{e}^{i\boldsymbol{k}\boldsymbol{r}} (2\pi)^{-3} \tag{A.2b}$$

to calculate the Fourier transform of the mean-field interaction potential $\Phi_{\text{int}}(\boldsymbol{r})$ and use the convolution theorem. This theorem means that a convolution in coordinate space is equal to the multiplication in the Fourier space

$$\mathcal{F}\left\{\Phi_{\text{int}}\right\} = \mathcal{F}\left\{U_{\text{int}} * n\right\} = \mathcal{F}\left\{U_{\text{int}}\right\} \cdot \mathcal{F}\left\{n\right\} = (\tilde{U}_{\text{dd}} + \tilde{U}_{\text{contact}}) \cdot \tilde{n} \ . \tag{A.3}$$

The computation of the dipolar interaction in Fourier space $\tilde{U}_{\text{dd}}$ results in [26, 324, 325]

$$\tilde{U}_{\text{dd}}(\boldsymbol{k}) = 3 g_{\text{dd}} \left(1 - 3\cos^2\alpha\right) \left[\frac{\cos(kb)}{(kb)^2} - \frac{\sin(kb)}{(kb)^3}\right] \ , \tag{A.4}$$

where $b$ is a distance below which atoms overlap[74] and $\alpha$ is the angle between the polarization direction $\boldsymbol{\mu}_{\text{m}}$ and the wave propagation $\boldsymbol{k}$. In the limit $b \to 0$ the right term in brackets of eq. (A.4) is -1/3 and the Fourier transform of the dipolar interaction gives

$$\mathcal{F}\left\{U_{\text{dd}}\right\}(\boldsymbol{k}) = \tilde{U}_{\text{dd}}(\boldsymbol{k}) = -g_{\text{dd}} \left(1 - 3\cos^2\alpha\right) \ , \tag{A.5}$$

and the contact interaction in Fourier space is easily calculated as

$$\mathcal{F}\left\{U_{\text{contact}}\right\}(\boldsymbol{k}) = \tilde{U}_{\text{contact}}(\boldsymbol{k}) = g \ . \tag{A.6}$$

---

[74] One has to use this short distance cut-off around the origin to keep the previous integrals finite.

## A.2. Excitation spectrum of a 3D homogeneous dipolar gas

In this appendix we will derive the excitation spectrum of a homogeneous dipolar condensates in three dimensions. We follow an approach [95, p. 188] focusing on collective excitations using the hydrodynamic equations as derived in section 4.4.1. We repeat for convenience the Euler equations (4.19) and (4.23) of a compressible dipolar condensate with a different notation

$$\frac{\partial n}{\partial t} = -\nabla \cdot (n\boldsymbol{v}) \ , \tag{A.7a}$$

$$m\frac{\partial \boldsymbol{v}}{\partial t} = -\nabla \left(\mu + \frac{mv^2}{2}\right) \ , \tag{A.7b}$$

$$\mu = gn + V_{\text{ext}} + \Phi_{\text{dip}} - \frac{\hbar^2}{2m\sqrt{n}}\nabla^2\sqrt{n} \ , \tag{A.7c}$$

with $\mu$ the chemical potential. Elementary excitations can be investigated by considering small density and velocity perturbations of the equilibrium state. We choose to linearise eq. (A.7) with the velocity $\boldsymbol{v}(\boldsymbol{r}) = \boldsymbol{v_0} + \delta\boldsymbol{v}(\boldsymbol{r})$ and the density $n(\boldsymbol{r}) = n_0 + \delta n(\boldsymbol{r})$, where $\boldsymbol{v_0}$ and $n_0$ are the equilibrium values and $\delta\boldsymbol{v}$ and $\delta n$ the departure from its equilibrium. By assuming the case of a three-dimensional homogeneous condensate[75] ($n_0 =$ const, $\boldsymbol{v_0} = 0$ and $V_{\text{ext}} = 0$) and neglecting any second order terms, we get[76]

$$\frac{\partial\,\delta n}{\partial t} = -\nabla \cdot (n_0\delta\boldsymbol{v}) \ , \tag{A.8a}$$

$$m\frac{\partial\,\delta\boldsymbol{v}}{\partial t} = -\nabla\delta\mu \ , \tag{A.8b}$$

$$\delta\mu = g\delta n + \delta\Phi_{\text{dip}} - \frac{\hbar^2}{4mn_0}\nabla^2\delta n \ , \tag{A.8c}$$

with $\delta\mu$ the linear perturbation of the chemical potential and $\delta\Phi_{\text{dip}}$ the linear perturbation of the dipolar mean-field potential, that will be simplified later. Taking the time derivative of (A.8a) and eliminating the velocity with (A.8b) results in the hydrodynamic equation of motion for the perturbation

$$m\frac{\partial^2\delta n}{\partial t^2} = \nabla \cdot (n_0\nabla\delta\mu) \ . \tag{A.9}$$

---

[75] The wave function for a homogeneous condensate is given by $\Psi = \sqrt{n_0}\mathrm{e}^{i\frac{\mu}{\hbar}t}$, hence the velocity of the condensate $\boldsymbol{v_0}$ is zero.

[76] (A.8a) Inserting $\delta v$ and $n$ in (A.7a) gives $\frac{\partial n_0}{\partial t} + \frac{\partial\,\delta n}{\partial t} = -\nabla \cdot (n_0\delta\boldsymbol{v}) - \nabla \cdot (\delta n\delta\boldsymbol{v})$. Neglecting second order terms and $n_0 =$ const gives the result.

(A.8b) As before inserting the ansatz and neglect second order terms in the velocity. The equilibrium density $n_0$ and velocity $\boldsymbol{v}$ fulfill eq. (A.7b) and thus the zero order terms cancel each other.

(A.8c) We need a Taylor expansion for the quantum pressure term: $\sqrt{n} \approx \sqrt{n_0} + \frac{\delta n}{2\sqrt{n_0}}$. Using this approximation for (A.7c) and $\nabla n_0 = 0$ results in the above.

As we are interested in travelling-wave perturbations, we set for the perturbed density plane waves $\delta n = \delta n_{\boldsymbol{q}}(\boldsymbol{r}, t) = \delta\hat{n} \exp(i\boldsymbol{q}\boldsymbol{r} - i\omega t)$ with amplitude $\delta\hat{n}$, quasi-momentum $\hbar\boldsymbol{q}$ and energy $\hbar\omega$. With this ansatz, we can further simplify the perturbed chemical potential from eq. (A.8c) and derive[77]

$$\delta\mu = \delta\mu_{\boldsymbol{q}} = g\delta n_{\boldsymbol{q}} + \tilde{U}_{\mathrm{dd}}(\boldsymbol{q})\delta n_{\boldsymbol{q}} + \frac{\hbar^2 q^2}{4mn_0}\delta n_{\boldsymbol{q}} \ , \tag{A.10}$$

with $\tilde{U}_{\mathrm{dd}}(\boldsymbol{q})$ the Fourier transform of the dipolar mean field potential as calculated in eq. (A.5). Finally, with the plane wave ansatz, the equation of motion (A.9) and the chemical perturbation (A.10), we obtain the dispersion relation

$$m\omega^2 = n_0 g q^2 - n_0 g_{\mathrm{dd}} \left(1 - 3\cos^2\alpha\right) q^2 + \frac{\hbar^2 q^4}{4m} \ . \tag{A.11}$$

To make contact with a microscopic description, it is convenient to describe the dispersion relation with the energy $E(\boldsymbol{q}) = \hbar\omega(\boldsymbol{q})$ of an excitation. After a simple rearrangement of the relation (A.11), the excitation spectrum reads

$$E(\boldsymbol{q}) = \hbar\omega(\boldsymbol{q}) = \sqrt{\left(\frac{\hbar^2 q^2}{2m}\right)^2 + \frac{\hbar^2 q^2}{2m} 2n_0 \left[g - g_{\mathrm{dd}}(1 - 3\cos^2\alpha)\right]} \tag{A.12}$$

with $\hbar^2 q^2/2m$ the free particle energy $E_{\mathrm{free}}(q)$.

The terms in the square brackets represent the Fourier transform of the two-body interactions including dipolar and contact scattering, see eq. (A.5) and (A.6). Hence, we finally rewrite the excitation spectrum in a simplified way

$$E(\boldsymbol{q}) = \sqrt{E_{\mathrm{free}}(q) \left[E_{\mathrm{free}}(q) + 2n_0 \tilde{U}_{\mathrm{int}}(\boldsymbol{q})\right]} \ . \tag{A.13}$$

---

[77] We use the plane wave ansatz to simplify the perturbed dipolar mean-field potential defined in (2.15): $\delta\Phi_{\mathrm{dip}} = \int \mathrm{d}^3 r' \, U_{\mathrm{dd}}(\boldsymbol{r} - \boldsymbol{r}') \, \delta\hat{n} \, \mathrm{e}^{(i\boldsymbol{q}\boldsymbol{r}' - i\omega t)}$. With the substitution $\boldsymbol{r'} = \boldsymbol{r} - \boldsymbol{r'}$, the potential is written as $\delta\Phi_{\mathrm{dip}} = \int \mathrm{d}^3 r' \, U_{\mathrm{dd}}(\boldsymbol{r}') \, \mathrm{e}^{-i\boldsymbol{q}\boldsymbol{r}'} \delta\hat{n} \, \mathrm{e}^{(i\boldsymbol{q}\boldsymbol{r} - i\omega t)}$. All the terms dependent on $\boldsymbol{r}'$ are equal to the Fourier transform of the dipolar interaction $\tilde{U}_{\mathrm{dd}}(\boldsymbol{q})$ as defined in eq. (A.2a) and (A.5), whereas the other terms are the plane wave $\delta n_{\boldsymbol{q}}(\boldsymbol{r})$.

## A.3. Excitation spectrum of a 2D homogeneous dipolar gas

To derive the excitation spectrum of a two dimensional (2D) dipolar gas, we start first with the notation of the interaction energy from eq. (2.16) in Fourier space [250]

$$\begin{aligned} E_{\text{int}} &\overset{(\text{A.1})}{=} \frac{1}{2}\int \mathrm{d}^3 r\, n(\boldsymbol{r}) \cdot (U_{\text{int}}(\boldsymbol{r}) * n(\boldsymbol{r})) \\ &\overset{(\text{A.3})}{=} \frac{1}{2}\int \mathrm{d}^3 r\, n(\boldsymbol{r}) \cdot \mathcal{F}^{-1}\{\mathcal{F}\{U_{\text{int}}\} \cdot \mathcal{F}\{n\}\} \\ &\overset{(\text{A.2b})}{=} \frac{1}{2(2\pi)^3}\int \mathrm{d}^3 q \int \mathrm{d}^3 r\, n(\boldsymbol{r})\, \mathrm{e}^{i\boldsymbol{q}\boldsymbol{r}} \tilde{U}_{\text{int}}(\boldsymbol{q})\tilde{n}(\boldsymbol{q}) \\ &\overset{(\text{A.2a})}{=} \frac{1}{2(2\pi)^3}\int \mathrm{d}^3 q\, \tilde{n}(-\boldsymbol{q})\tilde{U}_{\text{int}}(\boldsymbol{q})\tilde{n}(\boldsymbol{q}) \ . \end{aligned} \tag{A.14}$$

For a quasi-2D gas, the density along one direction is restricted to the ground state of the harmonic oscillator. We then take as a general ansatz for a Gaussian density distribution $n(\boldsymbol{r}) = n(\rho)(\sigma_z\sqrt{\pi})^{-1}\exp(-z^2/\sigma_z^2)$ with the width $\sigma_z$ along the $z$-direction and $n(\rho)$ the normalized radial 2D density. The density in Fourier space is $\tilde{n}(\boldsymbol{q}) = \tilde{n}(q_\perp)\exp(-q_z^2\sigma_z^2/4)$ with the radial and axial quasi-momenta $q_\perp$ and $q_z$. By using the Fourier transform of the binary interactions from eq. (A.5) and (A.6), with subsequent integrating eq. (A.14) over the $q_z$-direction, the interaction energy is then given by

$$\begin{aligned} E_{\text{int}} &= \frac{1}{2(2\pi)^2}\int \mathrm{d}^2 q\, \tilde{n}(q_\perp)^2 \int_{-\infty}^{\infty} \mathrm{d}q_z \frac{1}{2\pi}\left[g + g_{\text{dd}}\left(\frac{3q_\perp^2}{q_\perp^2+q_z^2} - 1\right)\right] \mathrm{e}^{-q_z^2\sigma_z^2/2} \\ &= \frac{1}{2(2\pi)^2}\int \mathrm{d}^2 q\, \tilde{n}(q_\perp)^2\ \tilde{U}_{\text{int}}^{\text{2D}}(q_\perp) \ , \end{aligned} \tag{A.15}$$

where we used the relation $\cos^2\alpha = q_z^2/q^2 = q_z^2/q_\perp^2 + q_z^2$ and defined the effective 2D interaction potential in Fourier space [251]

$$\tilde{U}_{\text{int}}^{\text{2D}}(q_\perp) = \frac{1}{\sqrt{2\pi}\sigma_z}\left[g + 2g_{\text{dd}}H_{\text{2D}}\left(\frac{q_\perp\sigma_z}{\sqrt{2}}\right)\right] \ . \tag{A.16}$$

The function $H_{\text{2D}}$ is given by $H_{\text{2D}} = 1 - \frac{3\sqrt{\pi}}{2}\,|x|\,\mathrm{erfc}(x)\,\mathrm{e}^{x^2}$, with $\mathrm{erfc}(x)$ the complementary error function. Finally, by replacing in the 3D excitation spectrum (A.13) each term with its 2D counterpart, meaning $q \to q_\perp, \tilde{U}_{\text{int}} \to \tilde{U}_{\text{int}}^{\text{2D}}$ and $n_0 \to n_{\text{2D}}$ with $n_{\text{2D}} = \sqrt{2\pi}\sigma_z n_0$, we obtain the excitation spectrum of a 2D homogeneous dipolar gas

$$E(q_\perp) = \sqrt{\left(\frac{\hbar^2 q_\perp^2}{2m}\right)^2 + \frac{\hbar^2 q_\perp^2}{2m} 2n_0\left[g + g_{\text{dd}}H_{\text{2D}}\left(\frac{q_\perp\sigma_z}{\sqrt{2}}\right)\right]} \ . \tag{A.17}$$

## A.4. Dipolar interaction between two condensates

In section 6.1.3, we calculated the droplet spatial extent only with the knowledge of the harmonic trap and the droplet distance. For this we used the inter-droplet dipolar interaction, that is derived in this section. We perform here similar calculations as in [70, 326], but with a different geometry of the droplets. The dipolar interaction energy of two droplets, described with the density distributions $n_-$ and $n_+$, can be calculated as

$$\begin{aligned} E_{\mathrm{dd,inter}} &= \int \mathrm{d}^3 r \int \mathrm{d}^3 r' \, n_-(\boldsymbol{r}) \, U_{\mathrm{dd}}(\boldsymbol{r}-\boldsymbol{r}') \, n_+(\boldsymbol{r}) \\ &= \frac{1}{(2\pi)^3} \int \mathrm{d}^3 q \, \tilde{n}_-(-\boldsymbol{q}) \, \tilde{U}_{\mathrm{dd}}(\boldsymbol{q}) \, \tilde{n}_+(\boldsymbol{q}) \, , \end{aligned} \tag{A.18}$$

where we used to derive the second term the convolution theorem similar to eq. (A.14). We assume the density distribution to be a Gaussian function with cylindrical symmetry, and the droplets are separated by a distance $d$, which is much larger than their radial extent $\sigma_\rho$

$$n_\pm(\boldsymbol{r}) = \frac{N}{\pi^{3/2}\sigma_\rho^2\sigma_z} \exp\left(-\frac{(x \pm \frac{d}{2})^2}{\sigma_\rho^2} - \frac{y^2}{\sigma_\rho^2} - \frac{z^2}{\sigma_z^2}\right) . \tag{A.19}$$

The Fourier transform with the definition from eq. (A.2a) gives

$$\tilde{n}_\pm(\boldsymbol{q}) = N \exp\left(-\frac{q_x^2\sigma_\rho^2}{4} - \frac{q_y^2\sigma_\rho^2}{4} - \frac{q_z^2\sigma_z^2}{4} \mp i\frac{q_x d}{2}\right) . \tag{A.20}$$

We can now calculate the dipolar inter-droplet interaction by inserting eq. (A.20) and $\tilde{U}_{\mathrm{dd}}$ from eq. (A.5) with $\cos^2\alpha = q_z^2/q^2$ in eq. (A.18)

$$\begin{aligned} E_{\mathrm{dd,inter}} &= -\frac{g_{\mathrm{dd}}N^2}{(2\pi)^3} \int \mathrm{d}^3 q \left(1 - 3\frac{q_z^2}{q^2}\right) \exp\left(-\frac{q_x^2\sigma_\rho^2}{2} - \frac{q_y^2\sigma_\rho^2}{2} - \frac{q_z^2\sigma_z^2}{2} - i q_x d\right) \\ &= -\frac{g_{\mathrm{dd}}N^2}{(2\pi\sigma_\rho)^3} \int \mathrm{d}^3 \bar{q} \left(1 - 3\frac{\bar{q}_z^2}{\bar{q}^2}\right) \exp\left(-\frac{\bar{q}_x^2}{2} - \frac{\bar{q}_y^2}{2} - \frac{\bar{q}_z^2}{2\kappa^2} - i\bar{q}_x \bar{d}\right) , \end{aligned} \tag{A.21}$$

where we used for the second term dimensionless variables $\bar{\boldsymbol{q}} = \sigma_\rho \boldsymbol{q}$ and $\bar{d} = d/\sigma_\rho$. We further use the condensate ratio $\kappa = \sigma_\rho/\sigma_z$ and spherical coordinates $(\bar{q}, \vartheta, \varphi)$ and define $u = \cos\vartheta$ to perform the integration

$$\begin{aligned} E_{\mathrm{dd,inter}} &= -\frac{g_{\mathrm{dd}}N^2}{(2\pi\sigma_\rho)^3} \int_0^\infty \mathrm{d}\bar{q} \int_0^1 \mathrm{d}u \, \bar{q}^2 \left(1 - 3u^2\right) \mathrm{e}^{-\frac{1}{2}\bar{q}^2\left(1-u^2+u^2\kappa^{-2}\right)} \int_0^{2\pi} \mathrm{d}\varphi \, \mathrm{e}^{-i\bar{q}\bar{d}\sqrt{1-u^2}\cos\varphi} \\ &= -\frac{g_{\mathrm{dd}}N^2}{(2\pi\sigma_\rho)^3} \int_0^\infty \mathrm{d}\bar{q} \int_0^1 \mathrm{d}u \, \bar{q}^2 \left(1 - 3u^2\right) \mathrm{e}^{-\frac{1}{2}\bar{q}^2\left(1-u^2+u^2\kappa^{-2}\right)} \, 2\pi J_0(\bar{q}\bar{d}\sqrt{1-u^2}) \, , \end{aligned} \tag{A.22}$$

where the integration over $\varphi$ results in a Bessel-function of the first kind $J_0$. Eq. (A.22) cannot be further simplified in general and is the final result.

## A.5. Energy expressions in the Thomas-Fermi limit

We present the energy expressions in Thomas-Fermi approximation for an external radial symmetric trapping

$$V_{\text{ext}}(\rho, z) = \frac{m}{2}\left(\omega_\rho \rho^2 + \omega_z z^2\right) = \frac{m}{2}\frac{\overline{\omega}}{\lambda^{2/3}}\left(\rho^2 + \lambda^2 z^2\right) \tag{A.23a}$$

and recalling the trap aspect ratio $\lambda = \omega_z/\omega_\rho$ and the mean of the trap frequencies $\overline{\omega} = (\omega_\rho^2 \omega_z)^{1/3}$. Inserting the radial symmetric parabolic density distribution

$$n_{\text{TF}}(\rho, z) = |\psi_{\text{TF}}(\rho, z)|^2 = \frac{15N}{8\pi R_\rho^2 R_z}\left[1 - \frac{\rho^2}{R_\rho^2} - \frac{z^2}{R_z^2}\right] \text{ for } n_{\text{TF}} \geq 0 \tag{A.23b}$$

in the energy functional from eq. (2.16) with neglected kinetic energy term results in the contributing energy terms [258, 259]. We express these with the characteristic oscillator length $\overline{a} = \sqrt{\hbar/m\overline{\omega}}$ and the cloud aspect ratio $\kappa = R_\rho/R_z$. The potential energy of the external trap writes

$$\frac{E_{\text{ext}}}{\hbar\overline{\omega}} = \frac{N}{14\overline{a}^2\lambda^{2/3}}\left(2R_\rho^2 + \lambda^2 R_z^2\right) \tag{A.24a}$$

and the mean-field interaction energy (contact and dipolar interaction)

$$\frac{E_{\text{contact}} + E_{\text{dip}}}{\hbar\overline{\omega}} = \frac{15N^2}{7}\frac{\overline{a}^2 a}{R_\rho^2 R_z}\left(1 - \varepsilon_{\text{dd}} f_{\text{dip}}(\kappa)\right) \tag{A.24b}$$

with the geometry-dependent function

$$f_{\text{dip}}(\kappa) = \frac{1 + 2\kappa^2}{1 - \kappa^2} - \frac{3\kappa^2 \operatorname{arctanh}\sqrt{1 - \kappa^2}}{(1 - \kappa^2)^{3/2}}\,. \tag{A.24c}$$

By including terms beyond mean-field theory, as motivated in section 5.2, we get two further terms as expressed in the energy functional (5.7). First, the quantum fluctuations [291]

$$\frac{E_{\text{qf}}}{\hbar\overline{\omega}} = \frac{5}{2}\left(\frac{15}{8}\right)^{3/2}\left(\frac{Na}{\overline{a}}\right)^{5/2}\left(\frac{\overline{a}^3}{R_\rho^2 R_z}\right)^{3/2} Q_5(\varepsilon_{\text{dd}}) \tag{A.25}$$

with the function $Q_5(\varepsilon_{\text{dd}}) \approx 1 + \frac{3}{2}\varepsilon_{\text{dd}}^2$. And second the three-body term

$$\frac{E_3}{\hbar\overline{\omega}} = \frac{25}{112\pi^2}\frac{\kappa_3 N^3}{R_\rho^4 R_z^2}\frac{1}{\hbar\overline{\omega}} \tag{A.26}$$

with the three-body coupling strength $\kappa_3$.

## A.6. Energy expressions in Gaussian approximation

We present the energy expressions in Gaussian approximation for an external radial symmetric trapping

$$V_{\text{ext}}(\rho, z) = \frac{m}{2}\left(\omega_\rho \rho^2 + \omega_z z^2\right) = \frac{m}{2}\frac{\overline{\omega}}{\lambda^{2/3}}\left(\rho^2 + \lambda^2 z^2\right) \tag{A.27a}$$

and recalling the trap aspect ratio $\lambda = \omega_z/\omega_\rho$ and the mean of the trap frequencies $\overline{\omega} = (\omega_\rho^2 \omega_z)^{1/3}$. Inserting the radial symmetric Gaussian trial function

$$n_{\text{G}}(\rho, z) = |\psi_{\text{G}}(\rho, z)|^2 = \frac{N}{\pi^{3/2}\sigma_\rho^2 \sigma_z} \exp\left(-\frac{\rho^2}{\sigma_\rho^2} - \frac{z^2}{\sigma_z^2}\right) \tag{A.27b}$$

in the energy functional from eq. (2.16) results in the contributing energy terms [39, 164]. We express these with the characteristic oscillator length $\overline{a} = \sqrt{\hbar/m\overline{\omega}}$ and the cloud aspect ratio $\kappa = \sigma_\rho/\sigma_z$. The kinetic or quantum pressure term writes

$$\frac{E_{\text{kin}}}{\hbar\overline{\omega}} = \frac{N\overline{a}^2}{4}\left(\frac{2}{\sigma_\rho^2} + \frac{1}{\sigma_z^2}\right), \tag{A.28a}$$

the potential energy

$$\frac{E_{\text{ext}}}{\hbar\overline{\omega}} = \frac{N}{4\overline{a}^2\lambda^{2/3}}\left(2\sigma_r^2 + \lambda^2\sigma_z^2\right) \tag{A.28b}$$

and the mean-field interaction energy (contact and dipolar interaction)

$$\frac{E_{\text{contact}} + E_{\text{dip}}}{\hbar\overline{\omega}} = \frac{N^2}{\sqrt{2\pi}}\frac{\overline{a}^2 a}{\sigma_\rho^2\sigma_z}\left(1 - \varepsilon_{\text{dd}} f_{\text{dip}}(\kappa)\right) \tag{A.28c}$$

with the geometry-dependent function

$$f_{\text{dip}}(\kappa) = \frac{1 + 2\kappa^2}{1 - \kappa^2} - \frac{3\kappa^2 \operatorname{arctanh}\sqrt{1-\kappa^2}}{(1-\kappa^2)^{3/2}}\,. \tag{A.28d}$$

By including terms beyond mean-field theory, as motivated in section 5.2, we get two further terms as expressed in the energy functional (5.7). First, the quantum fluctuations [291]

$$\frac{E_{\text{qf}}}{\hbar\overline{\omega}} = \frac{512\sqrt{2}}{75\sqrt{5}\pi^{7/4}}\left(\frac{Na}{\overline{a}}\right)^{5/2}\left(\frac{\overline{a}^3}{\sigma_\rho^2\sigma_z}\right)^{3/2} Q_5(\varepsilon_{\text{dd}}) \tag{A.29}$$

with the function $Q_5(\varepsilon_{\text{dd}}) \approx 1 + \frac{3}{2}\varepsilon_{\text{dd}}^2$. And second the three-body term

$$\frac{E_3}{\hbar\overline{\omega}} = \frac{1}{18\sqrt{3}\pi^3}\frac{\kappa_3\, N^3}{\sigma_\rho^4\sigma_z^2}\frac{1}{\hbar\overline{\omega}} \tag{A.30}$$

with the three-body coupling strength $\kappa_3$.

## A.7. Droplet peak density and lifetime

In this appendix, we give further information on the quantum droplets. We use the mechanical stability condition $\frac{\partial \mu}{\partial n} \geq 0$ from eq. (6.3) to derive a minimum peak density for the droplet state. For convenience we present the stability condition again and it reads

$$\left.\frac{\partial \mu}{\partial n}\right|_{r=0} = g\left[1 - \varepsilon_{\mathrm{dd}} f_{\mathrm{dip}}(\kappa)\right] + \begin{cases} 16 g \sqrt{n_0 a^3/\pi}\,(1 + \frac{3}{2}\varepsilon_{\mathrm{dd}}^2) & \text{Quantum fluctuations} \\ \kappa_3 n_0 & \text{Three-body repulsion} \end{cases} . \tag{A.31}$$

From this equation one can easily derive the minimum needed central density $n_0$ to stabilize a droplet. For the case of quantum fluctuations the minimum peak density is given by

$$n_0 = \frac{\pi}{a^3}\left(\frac{\varepsilon_{\mathrm{dd}} f_{\mathrm{dip}}(\kappa) - 1}{16(1 + 3\varepsilon_{\mathrm{dd}}^2/2)}\right)^2 \tag{A.32}$$

and when neglecting quantum fluctuations and assuming three-body repulsion this density becomes

$$n_0 = g\frac{\varepsilon_{\mathrm{dd}} f_{\mathrm{dip}}(\kappa) - 1}{\kappa_3} . \tag{A.33}$$

For both equations the central density does not depend on the atom number but only on the scattering length $a$ and very weakly on the aspect ratio $\kappa$, which is characteristic of a liquid-like state.

In section 6.2.1, we investigates the lifetime of quantum droplets. There we used the above mentioned peak densities to give the ratio of the lifetime at two different scattering lengths $a_{\mathrm{f}}$ and $a_{\mathrm{r}}$. The relation between lifetimes limited by three-body losses and peak densities is given by eq. (6.1) and reads $\tau_{\mathrm{f}}/\tau_{\mathrm{r}} = n_{0,\mathrm{r}}^2/n_{0,\mathrm{f}}^2$. With equations (A.32) for quantum fluctuations and (A.33) for three-body repulsion one can calculate $\tau_{\mathrm{f}}/\tau_{\mathrm{r}}$ without difficulty. For a fixed aspect ratio $\kappa$ it depends only on two parameters which we chose to be $\varepsilon_{\mathrm{dd,r}} = a_{\mathrm{dd}}/a_{\mathrm{r}}$ and $a_{\mathrm{f/r}} = a_{\mathrm{f}}/a_{\mathrm{r}}$. Then the ratio of the lifetime reads for quantum fluctuations

$$\frac{\tau_{\mathrm{f}}}{\tau_{\mathrm{r}}} = (a_{\mathrm{f/r}})^6 \left(\frac{\varepsilon_{\mathrm{dd,r}} f_{\mathrm{dip}}(\kappa) - 1}{\frac{\varepsilon_{\mathrm{dd,r}}}{a_{\mathrm{f/r}}} f_{\mathrm{dip}}(\kappa) - 1}\,\frac{1 + \frac{3}{2}\left(\frac{\varepsilon_{\mathrm{dd,r}}}{a_{\mathrm{f/r}}}\right)^2}{1 + \frac{3}{2}\varepsilon_{\mathrm{dd,r}}^2}\right)^4 \tag{A.34}$$

and for three-body repulsion

$$\frac{\tau_{\mathrm{f}}}{\tau_{\mathrm{r}}} = (a_{\mathrm{f/r}})^{-2}\left(\frac{\varepsilon_{\mathrm{dd,r}} f_{\mathrm{dip}}(\kappa) - 1}{\frac{\varepsilon_{\mathrm{dd,r}}}{a_{\mathrm{f/r}}} f_{\mathrm{dip}}(\kappa) - 1}\right)^2 . \tag{A.35}$$

These two functions are shown in figure 6.4b and are used to identify quantum fluctuations to be the stabilizing mechanism for droplets.

## A.8. Perturbative magnetic field of a ferrofluid surface

In this part, we derive the perturbative magnetic field of a ferrofluid for surface deflections similar to [209, p. 185-187]. This analysis is restricted to linear magnetic material, for which $\boldsymbol{B} = \mu_0\mu_\mathrm{r}\boldsymbol{H}$, and restricted to the magnetostatic field equations. These equations are the Gauss's law for magnetism

$$\nabla \cdot \boldsymbol{B} = 0 \quad (\nabla \cdot \boldsymbol{H} = 0 \text{ for linear media}) \tag{A.36}$$

and Ampère's law

$$\nabla \times \boldsymbol{H} = 0 \tag{A.37}$$

without current flow. Consistently with section 4.2.2 we consider an initially flat layer of ferrofluid occupying the region of space $z < 0$ with a relative permeability $\mu_\mathrm{r} > 0$, while the upper half $z > 0$ is a non-magnetic phase (see figure 4.2).

To linearize the magnetic field problem, we define $\boldsymbol{B'} = \boldsymbol{B} + \boldsymbol{b}$ and $\boldsymbol{H'} = \boldsymbol{H} + \boldsymbol{h}$, where the magnitudes of $\boldsymbol{b}$ and $\boldsymbol{h}$ are assumed to be small perturbations created by the fluid surface. The initial field $\boldsymbol{H}$ is uniform in the $z$-direction and we will use in the following $\boldsymbol{H} = (0, 0, H)$ and $\boldsymbol{B} = (0, 0, B)$. Due to Ampère's law (A.37) $\boldsymbol{h}$ can be described in terms of

$$\boldsymbol{h} = -\nabla\Phi^\mathrm{m} \tag{A.38}$$

with $\Phi^\mathrm{m}$ the magnetic perturbation potential. By using Gauss's law (A.36), the potential also obeys Laplace's equation $\nabla^2\Phi^\mathrm{m} = 0$. This equation has to be fulfilled in both magnetic and non-magnetic media, thus if $\Phi^\mathrm{m}_1$ is the potential in the magnetic phase and $\Phi^\mathrm{m}_2$ the potential in the non-magnetic one, the following magnetic potentials may be found similarly to eq. (4.5)

$$\Phi^\mathrm{m}_1 = \hat{\Phi}^\mathrm{m}_1\zeta\mathrm{e}^{kz}, \quad \Phi^\mathrm{m}_2 = \hat{\Phi}^\mathrm{m}_2\zeta\mathrm{e}^{-kz} \tag{A.39}$$

where $\hat{\Phi}^\mathrm{m}_1, \hat{\Phi}^\mathrm{m}_2$ are amplitudes independent of spatial position and $\zeta = \zeta(x, y, t)$ is the $z$-coordinate of a point on the surface.

The magnetic potentials need further boundary conditions. We will use media changing surface conditions for magnetic field components of $H$ and $B$. The first condition at a material discontinuity is the continuous tangential component of the field $\boldsymbol{H'}$. This means $\boldsymbol{n} \times (\boldsymbol{H'_2} - \boldsymbol{H'_1}) = 0$ with the normal $\boldsymbol{n} = (n_x, n_y, n_z) = (-\partial\zeta/\partial x, -\partial\zeta/\partial y, 1)$ and $\boldsymbol{H'_2} - \boldsymbol{H'_1} = (h_x, h_y, H)$. Calculating this expression leads to

$$-\frac{\partial\zeta}{\partial y}H - h_y = 0, \quad h_x + \frac{\partial\zeta}{\partial x}H \quad \text{and} \quad -\frac{\partial\zeta}{\partial x}H + \frac{\partial\zeta}{\partial y}H = 0\ . \tag{A.40}$$

By using the definition of the magnetic potential (A.38) and the second term of the previous equation (A.40) has to be valid at the interface, we derive the first boundary condition for the potential $\Phi^{\mathrm{m}}$

$$\frac{\partial \Phi_1^{\mathrm{m}}}{\partial x} + H_1 \frac{\partial \zeta}{\partial x} = \frac{\partial \Phi_2^{\mathrm{m}}}{\partial x} + H_2 \frac{\partial \zeta}{\partial x} \ , \tag{A.41}$$

that will be further simplified later.

The second condition at a material discontinuity is that the normal component of magnetic field $B$ is continuous. This condition is mathematically written as $\boldsymbol{n} \cdot (\boldsymbol{B}_2' - \boldsymbol{B}_1') = 0$ that can be split up in two conditions $\boldsymbol{n} \cdot (\boldsymbol{B}_2 - \boldsymbol{B}_1) = \boldsymbol{n} \cdot (\boldsymbol{b}_2 - \boldsymbol{b}_1) = 0$. Hence, we can state $B_1 = B_2$ and

$$-\frac{\partial \zeta}{\partial x}(b_{x,2} - b_{x,1}) - \frac{\partial \zeta}{\partial y}(b_{y,2} - b_{y,1}) + (b_{z,2} - b_{z,1}) = 0 \xrightarrow{\text{1st order}} (b_{z,2} - b_{z,1}) = 0 \ . \tag{A.42}$$

By using the potential definition (A.38) and the relation $B = \mu_0 \mu_{\mathrm{r}} H$, we get the second boundary condition

$$\mu_{\mathrm{r}} \frac{\partial \Phi_1^{\mathrm{m}}}{\partial z} = \frac{\partial \Phi_2^{\mathrm{m}}}{\partial z} \tag{A.43}$$

for the magnetic potential $\Phi^{\mathrm{m}}$.

Further simplification of the first condition (A.41) is done by integrating in respect to $x$ and get $(\Phi_1^{\mathrm{m}} - \Phi_2^{\mathrm{m}})/\zeta = H_2 - H_1$. Then with the knowledge on the magnetic field along the $z$-direction, we use $H_1 = B_1/\mu_0 + M$ and $H_2 = B_2/\mu_0$ with $B_1 = B_2$ to state

$$\Phi_1^{\mathrm{m}} - \Phi_2^{\mathrm{m}} = \zeta M \ . \tag{A.44}$$

Finally, we apply the boundary conditions (A.43) and (A.44) to the magnetic potential (A.39) at the position $z = 0$ to get $\hat{\Phi}_1^{\mathrm{m}} - \hat{\Phi}_2^{\mathrm{m}} = M$ and $\mu_{\mathrm{r}} \hat{\Phi}_1^{\mathrm{m}} = -\hat{\Phi}_2^{\mathrm{m}}$ and resulting for the magnetic potential

$$\Phi_1^{\mathrm{m}} = \frac{M}{1 + \mu_{\mathrm{r}}} \zeta \mathrm{e}^{kz}, \quad \Phi_2^{\mathrm{m}} = \frac{-\mu_{\mathrm{r}} M}{1 + \mu_{\mathrm{r}}} \zeta \mathrm{e}^{-kz} \ . \tag{A.45}$$

Thus, finally the perturbative magnetic field created by the fluid surface in the $z$-direction can be calculated. As the perturbative field $\boldsymbol{b}$ is continuous normal to the interface (in good approximation along the $z$-direction), we get using the second part of eq. (A.45)

$$b_{z,1} = b_{z,2} = \mu_0 h_{z,2} = \mu_0 \left( \frac{\partial \Phi_2^{\mathrm{m}}}{\partial z} \right)_{z=0} = \mu_0 \frac{k \mu_{\mathrm{r}} M \zeta}{1 + \mu_{\mathrm{r}}} \ . \tag{A.46}$$

The final equation (A.46) includes a flux concentration at the peaks where $\zeta$ is maximal, as illustrated in figure 4.2.

# A.9. Calculations on the aspect ratio of magnetic drops

In section 4.3 the deformation of ferrofluid drops in a uniform magnetic field is discussed. In this appendix, we indicate the calculations needed to find extrema of the total energy given as a sum of eq. (4.15) and (4.16). The introduced demagnetization factor $D_\mathrm{m}$ in eq. (4.17) is presented again in a different but equal form

$$D_\mathrm{m}(\kappa) = \frac{\kappa^2(\operatorname{artanh}\epsilon - \epsilon)}{\epsilon^3} \; . \tag{A.47}$$

Finding the extrema is achieved by simple mathematical analysis on the first derivative of $E_\mathrm{s} + E_\mathrm{m}$. Straightforward calculations[78] lead finally to an expression

$$\mu_0 H^2 R_0/\sigma_\mathrm{s} = g(\kappa) \tag{A.48}$$

with the function

$$g(\kappa) = \left(\frac{1}{\mu_\mathrm{r} - 1} + D_\mathrm{m}(\kappa)\right)^2 \frac{\epsilon^2\kappa^{-4/3}(1 + 2\kappa^2 + (1-4\kappa^2)\epsilon^{-1}\kappa^{-1}\arcsin\epsilon)}{-3 + (2+\kappa^2)\epsilon^{-1}\operatorname{artanh}\epsilon} \; . \tag{A.49}$$

---

[78] The only used tricks are $\frac{\mathrm{d}}{\mathrm{d}\kappa}\arcsin\epsilon = \frac{1}{\kappa}$ and $\frac{\mathrm{d}}{\mathrm{d}\kappa}\operatorname{artanh}\epsilon = \frac{1}{\kappa^2}$. To simplify the fractions one should use the obvious relation $\epsilon^2 = 1 - \kappa^2$.

# Bibliography

[1] M. H. Anderson, J. R. Ensher, M. R. Matthews, C. E. Wieman and E. A. Cornell, *Observation of Bose-Einstein Condensation in a Dilute Atomic Vapor*, Science, **269**, 198–201 (1995).

[2] K. B. Davis, M. O. Mewes, M. R. Andrews, N. J. van Druten, D. S. Durfee, D. M. Kurn and W. Ketterle, *Bose-Einstein Condensation in a Gas of Sodium Atoms*, Phys. Rev. Lett., **75**, 3969–3973 (1995).

[3] C. C. Bradley, C. A. Sackett, J. J. Tollett and R. G. Hulet, *Evidence of Bose-Einstein Condensation in an Atomic Gas with Attractive Interactions*, Phys. Rev. Lett., **75**, 1687–1690 (1995).

[4] M. R. Andrews, C. G. Townsend, H.-J. Miesner, D. S. Durfee, D. M. Kurn and W. Ketterle, *Observation of Interference Between Two Bose Condensates*, Science, **275**, 637–641 (1997).

[5] K. W. Madison, F. Chevy, W. Wohlleben and J. Dalibard, *Vortex Formation in a Stirred Bose-Einstein Condensate*, Phys. Rev. Lett., **84**, 806–809 (2000).

[6] I. Bloch, J. Dalibard and W. Zwerger, *Many-body physics with ultracold gases*, Rev. Mod. Phys., **80**, 885–964 (2008).

[7] S. Inouye, M. R. Andrews, J. Stenger, H.-J. Miesner, D. M. Stamper-Kurn and W. Ketterle, *Observation of Feshbach resonances in a Bose-Einstein condensate*, Nature, **392**, 151–154 (1998).

[8] C. Chin, R. Grimm, P. Julienne and E. Tiesinga, *Feshbach resonances in ultracold gases*, Rev. Mod. Phys., **82**, 1225–1286 (2010).

[9] S. Jochim, M. Bartenstein, A. Altmeyer, G. Hendl, S. Riedl, C. Chin, J. Hecker Denschlag and R. Grimm, *Bose-Einstein Condensation of Molecules*, Science, **302**, 2101–2103 (2003).

[10] M. W. Zwierlein, C. A. Stan, C. H. Schunck, S. M. F. Raupach, S. Gupta, Z. Hadzibabic and W. Ketterle, *Observation of Bose-Einstein Condensation of Molecules*, Phys. Rev. Lett., **91**, 250401 (2003).

[11] M. Greiner, C. A. Regal and D. S. Jin, *Emergence of a molecular Bose-Einstein condensate from a Fermi gas*, Nature, **426**, 537–540 (2003).

[12] B. DeMarco and D. S. Jin, *Onset of Fermi Degeneracy in a Trapped Atomic Gas*, Science, **285**, 1703–1706 (1999).

[13] W. Zwerger, *The BCS-BEC Crossover and the Unitary Fermi Gas*, Springer, Berlin, Heidelberg (2012).

[14] T. Kraemer, M. Mark, P. Waldburger, J. G. Danzl, C. Chin, B. Engeser, A. D. Lange, K. Pilch, A. Jaakkola, H.-C. Nägerl and R. Grimm, *Evidence for Efimov quantum states in an ultracold gas of caesium atoms*, Nature, **440**, 315–318 (2006).

[15] I. Bloch, *Ultracold quantum gases in optical lattices*, Nat Phys, **1**, 23–30 (2005).

[16] O. Morsch and M. Oberthaler, *Dynamics of Bose-Einstein condensates in optical lattices*, Rev. Mod. Phys., **78**, 179–215 (2006).

[17] M. Greiner, O. Mandel, T. Esslinger, T. W. Hänsch and I. Bloch, *Quantum phase transition from a superfluid to a Mott insulator in a gas of ultracold atoms*, Nature, **415**, 39–44 (2002).

[18] J. Billy, V. Josse, Z. Zuo, A. Bernard, B. Hambrecht, P. Lugan, D. Clement, L. Sanchez-Palencia, P. Bouyer and A. Aspect, *Direct observation of Anderson localization of matter waves in a controlled disorder*, Nature, **453**, 891–894 (2008).

[19] G. Roati, C. D'Errico, L. Fallani, M. Fattori, C. Fort, M. Zaccanti, G. Modugno, M. Modugno and M. Inguscio, *Anderson localization of a non-interacting Bose-Einstein condensate*, Nature, **453**, 895–898 (2008).

[20] W. S. Bakr, J. I. Gillen, A. Peng, S. Fölling and M. Greiner, *A quantum gas microscope for detecting single atoms in a Hubbard-regime optical lattice*, Nature, **462**, 74–77 (2009).

[21] J. F. Sherson, C. Weitenberg, M. Endres, M. Cheneau, I. Bloch and S. Kuhr, *Single-atom-resolved fluorescence imaging of an atomic Mott insulator*, Nature, **467**, 68–72 (2010).

[22] J. Simon, W. S. Bakr, R. Ma, M. E. Tai, P. M. Preiss and M. Greiner, *Quantum simulation of antiferromagnetic spin chains in an optical lattice*, Nature, **472**, 307–312 (2011).

[23] I. M. Georgescu, S. Ashhab and F. Nori, *Quantum simulation*, Rev. Mod. Phys., **86**, 153–185 (2014).

[24] I. Bloch, J. Dalibard and S. Nascimbene, *Quantum simulations with ultracold quantum gases*, Nat Phys, **8**, 267–276 (2012).

[25] A. Griesmaier, J. Werner, S. Hensler, J. Stuhler and T. Pfau, *Bose-Einstein Condensation of Chromium*, Phys. Rev. Lett., **94**, 160401 (2005).

[26] T. Lahaye, C. Menotti, L. Santos, M. Lewenstein and T. Pfau, *The physics of dipolar bosonic quantum gases*, Reports on Progress in Physics, **72**, 126401 (2009).

[27] M. Baranov, *Theoretical progress in many-body physics with ultracold dipolar gases*, Physics Reports, **464**, 71 – 111 (2008).

[28] M. A. Baranov, M. Dalmonte, G. Pupillo and P. Zoller, *Condensed Matter Theory of Dipolar Quantum Gases*, Chemical Reviews, **112**, 5012–5061 (2012).

[29] K. Góral, L. Santos and M. Lewenstein, *Quantum Phases of Dipolar Bosons in Optical Lattices*, Phys. Rev. Lett., **88**, 170406 (2002).

[30] I. Danshita and C. A. R. Sá de Melo, *Stability of Superfluid and Supersolid Phases of Dipolar Bosons in Optical Lattices*, Phys. Rev. Lett., **103**, 225301 (2009).

[31] S. Ronen, D. C. E. Bortolotti and J. L. Bohn, *Radial and Angular Rotons in Trapped Dipolar Gases*, Phys. Rev. Lett., **98**, 030406 (2007).

[32] O. Dutta and P. Meystre, *Ground-state structure and stability of dipolar condensates in anisotropic traps*, Phys. Rev. A, **75**, 053604 (2007).

[33] L. Santos, G. V. Shlyapnikov and M. Lewenstein, *Roton-Maxon Spectrum and Stability of Trapped Dipolar Bose-Einstein Condensates*, Phys. Rev. Lett., **90**, 250403 (2003).

[34] D. G. Henshaw and A. D. B. Woods, *Modes of Atomic Motions in Liquid Helium by Inelastic Scattering of Neutrons*, Phys. Rev., **121**, 1266–1274 (1961).

[35] Q. Beaufils, R. Chicireanu, T. Zanon, B. Laburthe-Tolra, E. Maréchal, L. Vernac, J.-C. Keller and O. Gorceix, *All-optical production of chromium Bose-Einstein condensates*, Phys. Rev. A, **77**, 061601 (2008).

[36] T. Lahaye, T. Koch, B. Fröhlich, M. Fattori, J. Metz, A. Griesmaier, S. Giovanazzi and T. Pfau, *Strong dipolar effects in a quantum ferrofluid*, Nature, **448**, 672–675 (2007).

[37] J. Stuhler, A. Griesmaier, T. Koch, M. Fattori, T. Pfau, S. Giovanazzi, P. Pedri and L. Santos, *Observation of Dipole-Dipole Interaction in a Degenerate Quantum Gas*, Phys. Rev. Lett., **95**, 150406 (2005).

[38] S. Giovanazzi, P. Pedri, L. Santos, A. Griesmaier, M. Fattori, T. Koch, J. Stuhler and T. Pfau, *Expansion dynamics of a dipolar Bose-Einstein condensate*, Phys. Rev. A, **74**, 013621 (2006).

[39] T. Koch, T. Lahaye, J. Metz, B. Fröhlich, A. Griesmaier and T. Pfau, *Stabilization of a purely dipolar quantum gas against collapse*, Nature Physics, **4**, 218–222 (2008).

[40] S. Müller, J. Billy, E. A. L. Henn, H. Kadau, A. Griesmaier, M. Jona-Lasinio, L. Santos and T. Pfau, *Stability of a dipolar Bose-Einstein condensate in a one-dimensional lattice*, Phys. Rev. A, **84**, 053601 (2011).

[41] T. Lahaye, J. Metz, B. Fröhlich, T. Koch, M. Meister, A. Griesmaier, T. Pfau, H. Saito, Y. Kawaguchi and M. Ueda, *d-Wave Collapse and Explosion of a Dipolar Bose-Einstein Condensate*, Phys. Rev. Lett., **101**, 080401 (2008).

[42] J. Metz, T. Lahaye, B. Fröhlich, A. Griesmaier, T. Pfau, H. Saito, Y. Kawaguchi and M. Ueda, *Coherent collapses of dipolar Bose-Einstein condensates for different trap geometries*, New Journal of Physics, **11**, 055032 (2009).

[43] J. Billy, E. A. L. Henn, S. Müller, T. Maier, H. Kadau, A. Griesmaier, M. Jona-Lasinio, L. Santos and T. Pfau, *Deconfinement-induced collapse of a coherent array of dipolar Bose-Einstein condensates*, Phys. Rev. A, **86**, 051603 (2012).

[44] S. Hensler, J. Werner, A. Griesmaier, P. Schmidt, A. Görlitz, T. Pfau, S. Giovanazzi and K. Rzążewski, *Dipolar relaxation in an ultra-cold gas of magnetically trapped chromium atoms*, Applied Physics B, **77**, 765–772 (2003).

[45] B. Pasquiou, G. Bismut, Q. Beaufils, A. Crubellier, E. Maréchal, P. Pedri, L. Vernac, O. Gorceix and B. Laburthe-Tolra, *Control of dipolar relaxation in external fields*, Phys. Rev. A, **81**, 042716 (2010).

[46] M. Fattori, T. Koch, S. Goetz, A. Griesmaier, S. Hensler, J. Stuhler and T. Pfau, *Demagnetization cooling of a gas*, Nature Physics, **2**, 765–768 (2006).

[47] B. Pasquiou, E. Maréchal, G. Bismut, P. Pedri, L. Vernac, O. Gorceix and B. Laburthe-Tolra, *Spontaneous Demagnetization of a Dipolar Spinor Bose Gas in an Ultralow Magnetic Field*, Phys. Rev. Lett., **106**, 255303 (2011).

[48] B. Pasquiou, E. Maréchal, L. Vernac, O. Gorceix and B. Laburthe-Tolra, *Thermodynamics of a Bose-Einstein Condensate with Free Magnetization*, Phys. Rev. Lett., **108**, 045307 (2012).

[49] B. Pasquiou, G. Bismut, E. Maréchal, P. Pedri, L. Vernac, O. Gorceix and B. Laburthe-Tolra, *Spin Relaxation and Band Excitation of a Dipolar Bose-Einstein Condensate in 2D Optical Lattices*, Phys. Rev. Lett., **106**, 015301 (2011).

[50] A. de Paz, A. Chotia, E. Maréchal, P. Pedri, L. Vernac, O. Gorceix and B. Laburthe-Tolra, *Resonant demagnetization of a dipolar Bose-Einstein condensate in a three-dimensional optical lattice*, Phys. Rev. A, **87**, 051609 (2013).

[51] A. de Paz, A. Sharma, A. Chotia, E. Maréchal, J. H. Huckans, P. Pedri, L. Santos, O. Gorceix, L. Vernac and B. Laburthe-Tolra, *Nonequilibrium Quantum Magnetism in a Dipolar Lattice Gas*, Phys. Rev. Lett., **111**, 185305 (2013).

[52] A. de Paz, P. Pedri, A. Sharma, M. Efremov, B. Naylor, O. Gorceix, E. Maréchal, L. Vernac and B. Laburthe-Tolra, *Probing spin dynamics from the Mott insulating to the superfluid regime in a dipolar lattice gas*, Phys. Rev. A, **93**, 021603 (2016).

[53] G. Bismut, B. Pasquiou, E. Maréchal, P. Pedri, L. Vernac, O. Gorceix and B. Laburthe-Tolra, *Collective Excitations of a Dipolar Bose-Einstein Condensate*, Phys. Rev. Lett., **105**, 040404 (2010).

[54] G. Bismut, B. Laburthe-Tolra, E. Maréchal, P. Pedri, O. Gorceix and L. Vernac, *Anisotropic Excitation Spectrum of a Dipolar Quantum Bose Gas*, Phys. Rev. Lett., **109**, 155302 (2012).

[55] R. Heidemann, U. Raitzsch, V. Bendkowsky, B. Butscher, R. Löw and T. Pfau, *Rydberg Excitation of Bose-Einstein Condensates*, Phys. Rev. Lett., **100**, 033601 (2008).

[56] M. Saffman, T. G. Walker and K. Mølmer, *Quantum information with Rydberg atoms*, Rev. Mod. Phys., **82**, 2313–2363 (2010).

[57] G. Quéméner and P. S. Julienne, *Ultracold Molecules under Control!*, Chemical Reviews, **112**, 4949–5011 (2012).

[58] K.-K. Ni, S. Ospelkaus, M. H. G. de Miranda, A. Pe'er, B. Neyenhuis, J. J. Zirbel, S. Kotochigova, P. S. Julienne, D. S. Jin and J. Ye, *A High Phase-Space-Density Gas of Polar Molecules*, Science, **322**, 231–235 (2008).

[59] S. Ospelkaus, K.-K. Ni, D. Wang, M. H. G. de Miranda, B. Neyenhuis, G. Quéméner, P. S. Julienne, J. L. Bohn, D. S. Jin and J. Ye, *Quantum-State Controlled Chemical Reactions of Ultracold Potassium-Rubidium Molecules*, Science, **327**, 853–857 (2010).

[60] K.-K. Ni, S. Ospelkaus, D. Wang, G. Quemener, B. Neyenhuis, M. H. G. de Miranda, J. L. Bohn, J. Ye and D. S. Jin, *Dipolar collisions of polar molecules in the quantum regime*, Nature, **464**, 1324–1328 (2010).

[61] J. W. Park, S. A. Will and M. W. Zwierlein, *Ultracold Dipolar Gas of Fermionic* $^{23}$Na$^{40}$K *Molecules in Their Absolute Ground State*, Phys. Rev. Lett., **114**, 205302 (2015).

[62] J. Deiglmayr, A. Grochola, M. Repp, K. Mörtlbauer, C. Glück, J. Lange, O. Dulieu, R. Wester and M. Weidemüller, *Formation of Ultracold Polar Molecules in the Rovibrational Ground State*, Phys. Rev. Lett., **101**, 133004 (2008).

[63] K. Aikawa, D. Akamatsu, M. Hayashi, K. Oasa, J. Kobayashi, P. Naidon, T. Kishimoto, M. Ueda and S. Inouye, *Coherent Transfer of Photoassociated Molecules into the Rovibrational Ground State*, Phys. Rev. Lett., **105**, 203001 (2010).

[64] T. Shimasaki, M. Bellos, C. D. Bruzewicz, Z. Lasner and D. DeMille, *Production of rovibronic-ground-state RbCs molecules via two-photon-cascade decay*, Phys. Rev. A, **91**, 021401 (2015).

[65] T. Takekoshi, L. Reichsöllner, A. Schindewolf, J. M. Hutson, C. R. Le Sueur, O. Dulieu, F. Ferlaino, R. Grimm and H.-C. Nägerl, *Ultracold Dense Samples of Dipolar RbCs Molecules in the Rovibrational and Hyperfine Ground State*, Phys. Rev. Lett., **113**, 205301 (2014).

[66] P. K. Molony, P. D. Gregory, Z. Ji, B. Lu, M. P. Köppinger, C. R. Le Sueur, C. L. Blackley, J. M. Hutson and S. L. Cornish, *Creation of Ultracold* $^{87}$Rb$^{133}$Cs *Molecules in the Rovibrational Ground State*, Phys. Rev. Lett., **113**, 255301 (2014).

[67] M. Guo, B. Zhu, B. Lu, X. Ye, F. Wang, R. Vexiau, N. Bouloufa-Maafa, G. Quéméner, O. Dulieu and D. Wang, *Creation of an Ultracold Gas of Ground-State Dipolar* $^{23}$Na$^{87}$Rb *Molecules*, Phys. Rev. Lett., **116**, 205303 (2016).

[68] B. Yan, S. A. Moses, B. Gadway, J. P. Covey, K. R. A. Hazzard, A. M. Rey, D. S. Jin and J. Ye, *Observation of dipolar spin-exchange interactions with lattice-confined polar molecules*, Nature, **501**, 521–525 (2013).

[69] S. E. Pollack, D. Dries, M. Junker, Y. P. Chen, T. A. Corcovilos and R. G. Hulet, *Extreme Tunability of Interactions in a* $^{7}$Li *Bose-Einstein Condensate*, Phys. Rev. Lett., **102**, 090402 (2009).

[70] M. Fattori, G. Roati, B. Deissler, C. D'Errico, M. Zaccanti, M. Jona-Lasinio, L. Santos, M. Inguscio and G. Modugno, *Magnetic Dipolar Interaction in a Bose-Einstein Condensate Atomic Interferometer*, Phys. Rev. Lett., **101**, 190405 (2008).

[71] M. Vengalattore, S. R. Leslie, J. Guzman and D. M. Stamper-Kurn, *Spontaneously Modulated Spin Textures in a Dipolar Spinor Bose-Einstein Condensate*, Phys. Rev. Lett., **100**, 170403 (2008).

[72] G. E. Marti, A. MacRae, R. Olf, S. Lourette, F. Fang and D. M. Stamper-Kurn, *Coherent Magnon Optics in a Ferromagnetic Spinor Bose-Einstein Condensate*, Phys. Rev. Lett., **113**, 155302 (2014).

[73] K. Aikawa, A. Frisch, M. Mark, S. Baier, A. Rietzler, R. Grimm and F. Ferlaino, *Bose-Einstein Condensation of Erbium*, Phys. Rev. Lett., **108**, 210401 (2012).

[74] K. Aikawa, A. Frisch, M. Mark, S. Baier, R. Grimm and F. Ferlaino, *Reaching Fermi Degeneracy via Universal Dipolar Scattering*, Phys. Rev. Lett., **112**, 010404 (2014).

[75] M. Lu, N. Q. Burdick, S. H. Youn and B. L. Lev, *Strongly Dipolar Bose-Einstein Condensate of Dysprosium*, Phys. Rev. Lett., **107**, 190401 (2011).

[76] M. Lu, N. Q. Burdick and B. L. Lev, *Quantum Degenerate Dipolar Fermi Gas*, Phys. Rev. Lett., **108**, 215301 (2012).

[77] J. L. Bohn, M. Cavagnero and C. Ticknor, *Quasi-universal dipolar scattering in cold and ultracold gases*, New Journal of Physics, **11**, 055039 (2009).

[78] A. Frisch, M. Mark, K. Aikawa, F. Ferlaino, J. L. Bohn, C. Makrides, A. Petrov and S. Kotochigova, *Quantum chaos in ultracold collisions of gas-phase erbium atoms*, Nature, **507**, 475–479 (2014).

[79] T. Maier, H. Kadau, M. Schmitt, M. Wenzel, I. Ferrier-Barbut, T. Pfau, A. Frisch, S. Baier, K. Aikawa, L. Chomaz, M. J. Mark, F. Ferlaino, C. Makrides, E. Tiesinga, A. Petrov and S. Kotochigova, *Emergence of Chaotic Scattering in Ultracold Er and Dy*, Phys. Rev. X, **5**, 041029 (2015).

[80] A. Frisch, M. Mark, K. Aikawa, S. Baier, R. Grimm, A. Petrov, S. Kotochigova, G. Quéméner, M. Lepers, O. Dulieu and F. Ferlaino, *Ultracold Dipolar Molecules Composed of Strongly Magnetic Atoms*, Phys. Rev. Lett., **115**, 203201 (2015).

[81] T. Maier, I. Ferrier-Barbut, H. Kadau, M. Schmitt, M. Wenzel, C. Wink, T. Pfau, K. Jachymski and P. S. Julienne, *Broad universal Feshbach resonances in the chaotic spectrum of dysprosium atoms*, Phys. Rev. A, **92**, 060702 (2015).

[82] S. Baier, M. J. Mark, D. Petter, K. Aikawa, L. Chomaz, Z. Cai, M. Baranov, P. Zoller and F. Ferlaino, *Extended Bose-Hubbard models with ultracold magnetic atoms*, Science, **352**, 201–205 (2016).

[83] K. Aikawa, S. Baier, A. Frisch, M. Mark, C. Ravensbergen and F. Ferlaino, *Observation of Fermi surface deformation in a dipolar quantum gas*, Science, **345**, 1484–1487 (2014).

[84] K. Aikawa, A. Frisch, M. Mark, S. Baier, R. Grimm, J. L. Bohn, D. S. Jin, G. M. Bruun and F. Ferlaino, *Anisotropic Relaxation Dynamics in a Dipolar Fermi Gas Driven Out of Equilibrium*, Phys. Rev. Lett., **113**, 263201 (2014).

[85] N. Q. Burdick, K. Baumann, Y. Tang, M. Lu and B. L. Lev, *Fermionic Suppression of Dipolar Relaxation*, Phys. Rev. Lett., **114**, 023201 (2015).

[86] M. D. Cowley and R. E. Rosensweig, *The interfacial stability of a ferromagnetic fluid*, Journal of Fluid Mechanics, **30**, 671–688 (1967).

[87] H. Kadau, M. Schmitt, M. Wenzel, C. Wink, T. Maier, I. Ferrier-Barbut and T. Pfau, *Observing the Rosensweig instability of a quantum ferrofluid*, Nature, **530**, 194–197 (2016).

[88] I. Ferrier-Barbut, H. Kadau, M. Schmitt, M. Wenzel and T. Pfau, *Observation of Quantum Droplets in a Strongly Dipolar Bose Gas*, Phys. Rev. Lett., **116**, 215301 (2016).

[89] J. Weiner, V. S. Bagnato, S. Zilio and P. S. Julienne, *Experiments and theory in cold and ultracold collisions*, Rev. Mod. Phys., **71**, 1–85 (1999).

[90] S. Bose, *Plancks Gesetz und Lichtquantenhypothese*, Zeitschrift für Physik, **26**, 178–181 (1924).

[91] A. Einstein, *Quantentheorie des einatomigen idealen Gases*, Sitzungsberichte der Preussischen Akademie der Wissenschaften, pages 261–267 (1924).

[92] A. Einstein, *Quantentheorie des einatomigen idealen Gases: Zweite Abhandlung*, Sitzungsberichte der Preussischen Akademie der Wissenschaften, pages 3–14 (1925).

[93] L. De Broglie, *Recherches sur la théorie des Quanta*, Theses, Migration - université en cours d'affectation (1924).

[94] L. Pitaevskii and S. Stringari, *Bose-Einstein Condensation (International Series of Monographs on Physics)*, Clarendon Press (2003).

[95] C. J. Pethick and H. Smith, *Bose-Einstein Condensation in Dilute Gases*, Cambridge University Press (2008).

[96] W. Heisenberg, *Mehrkörperproblem und Resonanz in der Quantenmechanik*, Zeitschrift für Physik, **38**, 411–426 (1926).

[97] P. A. M. Dirac, *On the Theory of Quantum Mechanics*, Proceedings of the Royal Society of London A: Mathematical, Physical and Engineering Sciences, **112**, 661–677 (1926).

[98] A. J. Leggett, *Quantum Liquids: Bose Condensation and Cooper Pairing in Condensed-Matter Systems (Oxford Graduate Texts)*, Oxford University Press (2006).

[99] J. F. Allen and A. D. Misener, *Flow of Liquid Helium II*, Nature, **141**, 75 (1938).

[100] P. Kapitza, *Viscosity of Liquid Helium below the $\lambda$-Point*, Nature, **141**, 74 (1938).

[101] L. Landau, *Theory of the Superfluidity of Helium II*, Phys. Rev., **60**, 356–358 (1941).

[102] F. London, *The $\lambda$-Phenomenon of Liquid Helium and the Bose-Einstein Degeneracy*, Nature, **141**, 643–644 (1938).

[103] F. London, *On the Bose-Einstein Condensation*, Phys. Rev., **54**, 947–954 (1938).

[104] O. Penrose and L. Onsager, *Bose-Einstein Condensation and Liquid Helium*, Phys. Rev., **104**, 576–584 (1956).

[105] O. Penrose, *CXXXVI. On the quantum mechanics of helium II*, The London, Edinburgh, and Dublin Philosophical Magazine and Journal of Science, **42**, 1373–1377 (1951).

[106] H. R. Glyde, *Bose-Einstein Condensation Measurements and Superflow in Condensed Helium*, Journal of Low Temperature Physics, **172**, 364–387 (2013).

[107] W. D. Phillips, *Nobel Lecture: Laser cooling and trapping of neutral atoms*, Rev. Mod. Phys., **70**, 721–741 (1998).

[108] D. G. Fried, T. C. Killian, L. Willmann, D. Landhuis, S. C. Moss, D. Kleppner and T. J. Greytak, *Bose-Einstein Condensation of Atomic Hydrogen*, Phys. Rev. Lett., **81**, 3811–3814 (1998).

[109] A. Robert, O. Sirjean, A. Browaeys, J. Poupard, S. Nowak, D. Boiron, C. I. Westbrook and A. Aspect, *A Bose-Einstein Condensate of Metastable Atoms*, Science, **292**, 461–464 (2001).

[110] F. Pereira Dos Santos, J. Léonard, J. Wang, C. J. Barrelet, F. Perales, E. Rasel, C. S. Unnikrishnan, M. Leduc and C. Cohen-Tannoudji, *Bose-Einstein Condensation of Metastable Helium*, Phys. Rev. Lett., **86**, 3459–3462 (2001).

[111] C. C. Bradley, C. A. Sackett and R. G. Hulet, *Bose-Einstein Condensation of Lithium: Observation of Limited Condensate Number*, Phys. Rev. Lett., **78**, 985–989 (1997).

[112] G. Roati, M. Zaccanti, C. D'Errico, J. Catani, M. Modugno, A. Simoni, M. Inguscio and G. Modugno, $^{39}$K *Bose-Einstein Condensate with Tunable Interactions*, Phys. Rev. Lett., **99**, 010403 (2007).

[113] G. Modugno, G. Ferrari, G. Roati, R. J. Brecha, A. Simoni and M. Inguscio, *Bose-Einstein Condensation of Potassium Atoms by Sympathetic Cooling*, Science, **294**, 1320–1322 (2001).

[114] S. Kraft, F. Vogt, O. Appel, F. Riehle and U. Sterr, *Bose-Einstein Condensation of Alkaline Earth Atoms:* $^{40}$Ca, Phys. Rev. Lett., **103**, 130401 (2009).

[115] S. L. Cornish, N. R. Claussen, J. L. Roberts, E. A. Cornell and C. E. Wieman, *Stable* $^{85}$Rb *Bose-Einstein Condensates with Widely Tunable Interactions*, Phys. Rev. Lett., **85**, 1795–1798 (2000).

[116] S. Stellmer, M. K. Tey, B. Huang, R. Grimm and F. Schreck, *Bose-Einstein Condensation of Strontium*, Phys. Rev. Lett., **103**, 200401 (2009).

[117] Y. N. M. de Escobar, P. G. Mickelson, M. Yan, B. J. DeSalvo, S. B. Nagel and T. C. Killian, *Bose-Einstein Condensation of* $^{84}$Sr, Phys. Rev. Lett., **103**, 200402 (2009).

[118] S. Stellmer, M. K. Tey, R. Grimm and F. Schreck, *Bose-Einstein condensation of* $^{86}$Sr, Phys. Rev. A, **82**, 041602 (2010).

[119] P. G. Mickelson, Y. N. Martinez de Escobar, M. Yan, B. J. DeSalvo and T. C. Killian, *Bose-Einstein condensation of* $^{88}$Sr *through sympathetic cooling with* $^{87}$Sr, Phys. Rev. A, **81**, 051601 (2010).

[120] T. Weber, J. Herbig, M. Mark, H.-C. Nägerl and R. Grimm, *Bose-Einstein Condensation of Cesium*, Science, **299**, 232–235 (2003).

[121] Y. Tang, N. Q. Burdick, K. Baumann and B. L. Lev, *Bose-Einstein condensation of 162 Dy and 160 Dy*, New Journal of Physics, **17**, 045006 (2015).

[122] A. Frisch, *Dipolar quantum gases of erbium*, Ph.D. thesis, Universität Innsbruck (2014).

[123] S. Sugawa, R. Yamazaki, S. Taie and Y. Takahashi, *Bose-Einstein condensate in gases of rare atomic species*, Phys. Rev. A, **84**, 011610 (2011).

[124] T. Fukuhara, S. Sugawa and Y. Takahashi, *Bose-Einstein condensation of an ytterbium isotope*, Phys. Rev. A, **76**, 051604 (2007).

[125] Y. Takasu, K. Maki, K. Komori, T. Takano, K. Honda, M. Kumakura, T. Yabuzaki and Y. Takahashi, *Spin-Singlet Bose-Einstein Condensation of Two-Electron Atoms*, Phys. Rev. Lett., **91**, 040404 (2003).

[126] T. Fukuhara, S. Sugawa, Y. Takasu and Y. Takahashi, *All-optical formation of quantum degenerate mixtures*, Phys. Rev. A, **79**, 021601 (2009).

[127] J. M. McNamara, T. Jeltes, A. S. Tychkov, W. Hogervorst and W. Vassen, *Degenerate Bose-Fermi Mixture of Metastable Atoms*, Phys. Rev. Lett., **97**, 080404 (2006).

[128] A. G. Truscott, K. E. Strecker, W. I. McAlexander, G. B. Partridge and R. G. Hulet, *Observation of Fermi Pressure in a Gas of Trapped Atoms*, Science, **291**, 2570–2572 (2001).

[129] F. Schreck, L. Khaykovich, K. L. Corwin, G. Ferrari, T. Bourdel, J. Cubizolles and C. Salomon, *Quasipure Bose-Einstein Condensate Immersed in a Fermi Sea*, Phys. Rev. Lett., **87**, 080403 (2001).

[130] B. Naylor, A. Reigue, E. Maréchal, O. Gorceix, B. Laburthe-Tolra and L. Vernac, *Chromium dipolar Fermi sea*, Phys. Rev. A, **91**, 011603 (2015).

[131] B. J. DeSalvo, M. Yan, P. G. Mickelson, Y. N. Martinez de Escobar and T. C. Killian, *Degenerate Fermi Gas of* $^{87}$Sr, Phys. Rev. Lett., **105**, 030402 (2010).

[132] M. K. Tey, S. Stellmer, R. Grimm and F. Schreck, *Double-degenerate Bose-Fermi mixture of strontium*, Phys. Rev. A, **82**, 011608 (2010).

[133] T. Fukuhara, Y. Takasu, S. Sugawa and Y. Takahashi, *Quantum Degenerate Fermi Gases of Ytterbium Atoms*, Journal of Low Temperature Physics, **148**, 441–445 (2007).

[134] T. Fukuhara, Y. Takasu, M. Kumakura and Y. Takahashi, *Degenerate Fermi Gases of Ytterbium*, Phys. Rev. Lett., **98**, 030401 (2007).

[135] C. E. Hecht, *The possible superfluid behaviour of hydrogen atom gases and liquids*, Physica, **25**, 1159–1161 (1959).

[136] W. C. Stwalley and L. H. Nosanow, *Possible "New" Quantum Systems*, Phys. Rev. Lett., **36**, 910–913 (1976).

[137] I. F. Silvera and J. T. M. Walraven, *Stabilization of Atomic Hydrogen at Low Temperature*, Phys. Rev. Lett., **44**, 164–168 (1980).

[138] D. Koester and G. Chanmugam, *Physics of white dwarf stars*, Reports on Progress in Physics, **53**, 837 (1990).

[139] J. M. Lattimer and M. Prakash, *The Physics of Neutron Stars*, Science, **304**, 536–542 (2004).

[140] J. Tuoriniemi, *Physics at its coolest*, Nat Phys, **12**, 11–14 (2016).

[141] R. Olf, F. Fang, G. E. Marti, A. MacRae and D. M. Stamper-Kurn, *Thermometry and cooling of a Bose gas to 0.02 times the condensation temperature*, Nat Phys, **11**, 720–723 (2015).

[142] A. E. Leanhardt, T. A. Pasquini, M. Saba, A. Schirotzek, Y. Shin, D. Kielpinski, D. E. Pritchard and W. Ketterle, *Cooling Bose-Einstein Condensates Below 500 Picokelvin*, Science, **301**, 1513–1515 (2003).

[143] T. Nikuni, M. Oshikawa, A. Oosawa and H. Tanaka, *Bose-Einstein Condensation of Dilute Magnons in* $TlCuCl_3$, Phys. Rev. Lett., **84**, 5868–5871 (2000).

[144] S. O. Demokritov, V. E. Demidov, O. Dzyapko, G. A. Melkov, A. A. Serga, B. Hillebrands and A. N. Slavin, *Bose-Einstein condensation of quasi-equilibrium magnons at room temperature under pumping*, Nature, **443**, 430–433 (2006).

[145] J. P. Eisenstein and A. H. MacDonald, *Bose-Einstein condensation of excitons in bilayer electron systems*, Nature, **432**, 691–694 (2004).

[146] J. Kasprzak, M. Richard, S. Kundermann, A. Baas, P. Jeambrun, J. M. J. Keeling, F. M. Marchetti, M. H. Szymanska, R. Andre, J. L. Staehli, V. Savona, P. B. Littlewood, B. Deveaud and L. S. Dang, *Bose-Einstein condensation of exciton polaritons*, Nature, **443**, 409–414 (2006).

[147] R. Balili, V. Hartwell, D. Snoke, L. Pfeiffer and K. West, *Bose-Einstein Condensation of Microcavity Polaritons in a Trap*, Science, **316**, 1007–1010 (2007).

[148] J. Klaers, J. Schmitt, F. Vewinger and M. Weitz, *Bose-Einstein condensation of photons in an optical microcavity*, Nature, **468**, 545–548 (2010).

[149] A. J. Moerdijk, H. M. J. M. Boesten and B. J. Verhaar, *Decay of trapped ultracold alkali atoms by recombination*, Phys. Rev. A, **53**, 916–920 (1996).

[150] L. S. Butcher, D. N. Stacey, C. J. Foot and K. Burnett, *Ultracold collisions for Bose-Einstein condensation*, Philosophical Transactions of the Royal Society of London A: Mathematical, Physical and Engineering Sciences, **357**, 1421–1439 (1999).

[151] C. J. Foot, *Atomic physics*, Oxford University Press, USA (2005).

[152] J. Dalibard, *Collisional dynamics of ultra-cold atomic gases*, in *Bose-Einstein Condensation in Atomic Gases*, volume 140 of *Proceedings of the International School of Physics "Enrico Fermi"*, pages 321–349, IOS Press Amsterdam (1999).

[153] T. Dauxois, S. Ruffo, E. Arimondo and M. Wilkens, *Dynamics and Thermodynamics of Systems with Long-Range Interactions*, chapter Dynamics and Thermodynamics of Systems with Long-Range Interactions: An Introduction, pages 1–19, Springer, Berlin, Heidelberg (2002).

[154] G. E. Astrakharchik and Y. E. Lozovik, *Super-Tonks-Girardeau regime in trapped one-dimensional dipolar gases*, Phys. Rev. A, **77**, 013404 (2008).

[155] C. Ticknor, *Collisional Control of Ground State Polar Molecules and Universal Dipolar Scattering*, Phys. Rev. Lett., **100**, 133202 (2008).

[156] D. M. Stamper-Kurn and M. Ueda, *Spinor Bose gases: Symmetries, magnetism, and quantum dynamics*, Rev. Mod. Phys., **85**, 1191–1244 (2013).

[157] Y. Tang, A. Sykes, N. Q. Burdick, J. L. Bohn and B. L. Lev, *s-wave scattering lengths of the strongly dipolar bosons* $^{162}$Dy *and* $^{164}$Dy, Phys. Rev. A, **92**, 022703 (2015).

[158] F. Dalfovo, S. Giorgini, L. P. Pitaevskii and S. Stringari, *Theory of Bose-Einstein condensation in trapped gases*, Rev. Mod. Phys., **71**, 463–512 (1999).

[159] N. N. Bogolyubov, *On the theory of superfluidity*, J. Phys. (USSR), **11**, 23–32 (1947).

[160] G. Baym and C. J. Pethick, *Ground-State Properties of Magnetically Trapped Bose-Condensed Rubidium Gas*, Phys. Rev. Lett., **76**, 6–9 (1996).

[161] Y. Kagan, G. V. Shlyapnikov and J. T. M. Walraven, *Bose-Einstein Condensation in Trapped Atomic Gases*, Phys. Rev. Lett., **76**, 2670–2673 (1996).

[162] V. M. Pérez-García, H. Michinel, J. I. Cirac, M. Lewenstein and P. Zoller, *Low Energy Excitations of a Bose-Einstein Condensate: A Time-Dependent Variational Analysis*, Phys. Rev. Lett., **77**, 5320–5323 (1996).

[163] V. M. Pérez-García, H. Michinel, J. I. Cirac, M. Lewenstein and P. Zoller, *Dynamics of Bose-Einstein condensates: Variational solutions of the Gross-Pitaevskii equations*, Phys. Rev. A, **56**, 1424–1432 (1997).

[164] S. Yi and L. You, *Trapped atomic condensates with anisotropic interactions*, Phys. Rev. A, **61**, 041604 (2000).

[165] M. Edwards and K. Burnett, *Numerical solution of the nonlinear Schrödinger equation for small samples of trapped neutral atoms*, Phys. Rev. A, **51**, 1382–1386 (1995).

[166] L. Vestergaard Hau, B. D. Busch, C. Liu, Z. Dutton, M. M. Burns and J. A. Golovchenko, *Near-resonant spatial images of confined Bose-Einstein condensates in a 4-Dee magnetic bottle*, Phys. Rev. A, **58**, R54–R57 (1998).

[167] M. Schilling, *Stabilisierung eines Lasersystems zur Präzisionsspektroskopie an Dysprosiumatomen*, Bachelor thesis, Universität Stuttgart (2012).

[168] S. Ristok, *Eine optische Pinzette für ultrakalte Dysprosium-Atome*, Bachelor thesis, Universität Stuttgart (2012).

[169] B. Docters, *Ein Lasersystem zur Kühlung von Dysprosiumatomen*, Bachelor thesis, Universität Stuttgart (2013).

[170] N. Zuber, *Ein Lasersystem zum optischen Pumpen von Dysprosium*, Bachelor thesis, Universität Stuttgart (2013).

[171] M. Feldmaier, *Stabilisierung eines schmalbandigen Lasersystems zur Spektroskopie an Dysprosium*, Bachelor thesis, Universität Stuttgart (2013).

[172] I. Reis, *Hochauflösendes Abbildungssystem für ultrakalte Atome*, Bachelor thesis, Universität Stuttgart (2014).

[173] N. Uhl, *Charakterisierung eines hochauflösenden in-situ-Abbildungssystems*, Bachelor thesis, Universität Stuttgart (2015).

[174] M. Schmitt, *High Resolution Laser Spectroscopy of Dysprosium*, Master thesis, Universität Stuttgart (2012).

[175] M. Nickel, *Laser Cooling of Dysprosium Atoms*, Diploma thesis, Universität Stuttgart (2013).

[176] M. Wenzel, *A dysprosium quantum gas in highly controllable optical traps*, Master thesis, Universität Stuttgart (2015).

[177] C. Wink, *Dipolar and universal scattering of ultracold dysprosium atoms - Demagnetization cooling and broad Feshbach resonances*, Master thesis, Universität Stuttgart (2015).

[178] T. Maier, *Interactions in a Quantum Gas of Dysprosium Atoms*, Ph.D. thesis, Universität Stuttgart (2015).

[179] I. Segal, L. Halicz and I. T. Platzner, *Isotope ratio measurements of dysprosium by multiple collection inductively coupled plasma mass spectrometry*, International Journal of Mass Spectrometry, **216**, 177 – 184 (2002).

[180] D. R. Lide, *CRC Handbook Chemistry and Physics, 85th Edition*, CRC Press (2005).

[181] J. J. McClelland and J. L. Hanssen, *Laser Cooling without Repumping: A Magneto-Optical Trap for Erbium Atoms*, Phys. Rev. Lett., **96**, 143005 (2006).

[182] M. Lu, S. H. Youn and B. L. Lev, *Trapping Ultracold Dysprosium: A Highly Magnetic Gas for Dipolar Physics*, Phys. Rev. Lett., **104**, 063001 (2010).

[183] T. Maier, H. Kadau, M. Schmitt, A. Griesmaier and T. Pfau, *Narrow-line magneto-optical trap for dysprosium atoms*, Opt. Lett., **39**, 3138–3141 (2014).

[184] J. Miao, J. Hostetter, G. Stratis and M. Saffman, *Magneto-optical trapping of holmium atoms*, Phys. Rev. A, **89**, 041401 (2014).

[185] B. Hemmerling, G. K. Drayna, E. Chae, A. Ravi and J. M. Doyle, *Buffer gas loaded magneto-optical traps for Yb, Tm, Er and Ho*, New Journal of Physics, **16**, 063070 (2014).

[186] A. J. Berglund, J. L. Hanssen and J. J. McClelland, *Narrow-Line Magneto-Optical Cooling and Trapping of Strongly Magnetic Atoms*, Phys. Rev. Lett., **100**, 113002 (2008).

[187] A. Frisch, K. Aikawa, M. Mark, A. Rietzler, J. Schindler, E. Zupanič, R. Grimm and F. Ferlaino, *Narrow-line magneto-optical trap for erbium*, Phys. Rev. A, **85**, 051401 (2012).

[188] D. Sukachev, A. Sokolov, K. Chebakov, A. Akimov, S. Kanorsky, N. Kolachevsky and V. Sorokin, *Magneto-optical trap for thulium atoms*, Phys. Rev. A, **82**, 011405 (2010).

[189] D. D. Sukachev, E. S. Kalganova, A. V. Sokolov, S. A. Fedorov, G. A. Vishnyakova, A. V. Akimov, N. N. Kolachevsky and V. N. Sorokin, *Secondary laser cooling and capturing of thulium atoms in traps*, Quantum Electronics, **44**, 515 (2014).

[190] K. Honda, Y. Takahashi, T. Kuwamoto, M. Fujimoto, K. Toyoda, K. Ishikawa and T. Yabuzaki, *Magneto-optical trapping of Yb atoms and a limit on the branching ratio of the $^1P_1$ state*, Phys. Rev. A, **59**, R934–R937 (1999).

[191] T. Kuwamoto, K. Honda, Y. Takahashi and T. Yabuzaki, *Magneto-optical trapping of Yb atoms using an intercombination transition*, Phys. Rev. A, **60**, R745–R748 (1999).

[192] N. Leefer, C. T. M. Weber, A. Cingöz, J. R. Torgerson and D. Budker, *New Limits on Variation of the Fine-Structure Constant Using Atomic Dysprosium*, Phys. Rev. Lett., **111**, 060801 (2013).

[193] K. Van Tilburg, N. Leefer, L. Bougas and D. Budker, *Search for Ultralight Scalar Dark Matter with Atomic Spectroscopy*, Phys. Rev. Lett., **115**, 011802 (2015).

[194] N. Hinkley, J. A. Sherman, N. B. Phillips, M. Schioppo, N. D. Lemke, K. Beloy, M. Pizzocaro, C. W. Oates and A. D. Ludlow, *An Atomic Clock with 10–18 Instability*, Science, **341**, 1215–1218 (2013).

[195] B. J. Bloom, T. L. Nicholson, J. R. Williams, S. L. Campbell, M. Bishof, X. Zhang, W. Zhang, S. L. Bromley and J. Ye, *An optical lattice clock with accuracy and stability at the 10-18 level*, Nature, **506**, 71–75 (2014).

[196] M. Lu, S. H. Youn and B. L. Lev, *Spectroscopy of a narrow-line laser-cooling transition in atomic dysprosium*, Phys. Rev. A, **83**, 012510 (2011).

[197] M. Gustavsson, H. Lundberg, L. Nilsson and S. Svanberg, *Lifetime measurements for excited states of rare-earth atoms using pulse modulation of a cw dye-laser beam*, J. Opt. Soc. Am., **69**, 984–992 (1979).

[198] W. C. Martin, R. Zalubas and L. Hagan, *Atomic energy levels–the rare-earth elements: the spectra of lanthanum, cerium, praseodymium, neodymium, promethium, samarium, europium, gadolinium, terbium, dysprosium, holmium, erbium, thulium, ytterbium, and lutetium*, Washington: U.S. Dept. of Commerce, National Bureau of Standards (1978).

[199] C. J. Dedman, J. Nes, T. M. Hanna, R. G. Dall, K. G. H. Baldwin and A. G. Truscott, *Optimum design and construction of a Zeeman slower for use with a magneto-optic trap*, Review of Scientific Instruments, **75**, 5136–5142 (2004).

[200] T. L. Gustavson, A. P. Chikkatur, A. E. Leanhardt, A. Görlitz, S. Gupta, D. E. Pritchard and W. Ketterle, *Transport of Bose-Einstein Condensates with Optical Tweezers*, Phys. Rev. Lett., **88**, 020401 (2001).

[201] T. Lauber, J. Küber, O. Wille and G. Birkl, *Optimized Bose-Einstein-condensate production in a dipole trap based on a 1070-nm multifrequency laser: Influence of enhanced two-body loss on the evaporation process*, Phys. Rev. A, **84**, 043641 (2011).

[202] B. Fröhlich, T. Lahaye, B. Kaltenhäuser, H. Kübler, S. Müller, T. Koch, M. Fattori and T. Pfau, *Two-frequency acousto-optic modulator driver to improve the beam pointing stability during intensity ramps*, Review of Scientific Instruments, **78**, 043101 (2007).

[203] W. Ketterle and N. V. Druten, *Evaporative Cooling of Trapped Atoms*, Advances In Atomic, Molecular and Optical Physics, **37**, 181 – 236 (1996).

[204] M. Marinescu and L. You, *Controlling Atom-Atom Interaction at Ultralow Temperatures by dc Electric Fields*, Phys. Rev. Lett., **81**, 4596–4599 (1998).

[205] H. Feshbach, *Unified theory of nuclear reactions*, Annals of Physics, **5**, 357 – 390 (1958).

[206] U. Fano, *Effects of Configuration Interaction on Intensities and Phase Shifts*, Phys. Rev., **124**, 1866–1878 (1961).

[207] K. Baumann, N. Q. Burdick, M. Lu and B. L. Lev, *Observation of low-field Fano-Feshbach resonances in ultracold gases of dysprosium*, Phys. Rev. A, **89**, 020701 (2014).

[208] J. Stenger, S. Inouye, M. R. Andrews, H.-J. Miesner, D. M. Stamper-Kurn and W. Ketterle, *Strongly Enhanced Inelastic Collisions in a Bose-Einstein Condensate near Feshbach Resonances*, Phys. Rev. Lett., **82**, 2422–2425 (1999).

[209] R. Rosensweig, *Ferrohydrodynamics*, Cambridge Monographs on Mechanics, Cambridge University Press (1985).

[210] C. Scherer and A. M. Figueiredo Neto, *Ferrofluids: properties and applications*, Brazilian Journal of Physics, **35**, 718 – 727 (2005).

[211] S. S. Papell, *Low viscosity magnetic fluid obtained by the colloidal suspension of magnetic particles* (1965), US Patent No. 3,215,572.

[212] K. Raj and R. Moskowitz, *Commercial applications of ferrofluids*, Journal of Magnetism and Magnetic Materials, **85**, 233 – 245 (1990).

[213] R. Rosensweig, *Heating magnetic fluid with alternating magnetic field*, Journal of Magnetism and Magnetic Materials, **252**, 370 – 374 (2002), proceedings of the 9th International Conference on Magnetic Fluids.

[214] M. P. Perry and T. B. Jones, *Dynamic loading of a single-stage ferromagnetic liquid seal*, Journal of Applied Physics, **49**, 2334–2338 (1978).

[215] J. King, *Method for making loudspeaker with magnetic fluid enveloping the voice coil* (1977), US Patent No. 4,017,694.

[216] Q. A. Pankhurst, J. Connolly, S. K. Jones and J. Dobson, *Applications of magnetic nanoparticles in biomedicine*, Journal of Physics D: Applied Physics, **36**, R167 (2003).

[217] K. Maier-Hauff, F. Ulrich, D. Nestler, H. Niehoff, P. Wust, B. Thiesen, H. Orawa, V. Budach and A. Jordan, *Efficacy and safety of intratumoral thermotherapy using magnetic iron-oxide nanoparticles combined with external beam radiotherapy on patients with recurrent glioblastoma multiforme*, Journal of Neuro-Oncology, **103**, 317–324 (2011).

[218] C. Alexiou, R. Schmid, R. Jurgons, C. Bergemann, W. Arnold and F. Parak, *Targeted Tumor Therapy with "Magnetic Drug Targeting": Therapeutic Efficacy of Ferrofluid Bound Mitoxantrone*, in *Ferrofluids*, volume 594 of *Lecture Notes in Physics*, pages 233–251, Springer Berlin Heidelberg (2002).

[219] R. Weissleder, G. Elizondo, J. Wittenberg, C. A. Rabito, H. H. Bengele and L. Josephson, *Ultrasmall superparamagnetic iron oxide: characterization of a new class of contrast agents for MR imaging.*, Radiology, **175**, 489–493 (1990).

[220] L. Romankiw, M. Slusarczuk and D. Thompson, *Liquid magnetic bubbles*, IEEE Transactions on Magnetics, **11**, 25–28 (1975).

[221] I. Torres-Diaz and C. Rinaldi, *Recent progress in ferrofluids research: novel applications of magnetically controllable and tunable fluids*, Soft Matter, **10**, 8584–8602 (2014).

[222] R. M. Erb, H. S. Son, B. Samanta, V. M. Rotello and B. B. Yellen, *Magnetic assembly of colloidal superstructures with multipole symmetry*, Nature, **457**, 999–1002 (2009).

[223] R. Richter and A. Lange, *Surface Instabilities of Ferrofluids*, in *Colloidal Magnetic Fluids*, volume 763 of *Lecture Notes in Physics*, pages 1–91, Springer Berlin Heidelberg (2009).

[224] L. D. Landau and E. M. Lifshitz, *Electrodynamics of Continuous Media*, Course of Theoretical Physics Volume 8, Pergamon Press, New York (1960).

[225] M. Liu and K. Stierstadt, *Thermodynamics, Electrodynamics, and Ferrofluid Dynamics*, in *Colloidal Magnetic Fluids*, volume 763 of *Lecture Notes in Physics*, pages 1–74, Springer Berlin Heidelberg (2009).

[226] L. D. Landau, E. M. Lifshitz, J. B. Sykes and W. H. Reid, *Fluid Mechanics*, Course of Theoretical Physics Volume 6, Pergamon Press Oxford (1959).

[227] M. S. Amin, S. Elborai, S.-H. Lee, X. He and M. Zahn, *Surface tension measurement techniques of magnetic fluids at an interface between different fluids using perpendicular field instability*, Journal of Applied Physics, **97**, 10R308 (2005).

[228] S. Bohlius, *The Rosensweig instability in isotropic magnetic gels*, Ph.D. thesis, Universität Bayreuth (2008).

[229] J.-C. Bacri and D. Salin, *First-order transition in the instability of a magnetic fluid interface*, J. Physique Lett., **45**, 559–564 (1984).

[230] J. Joule, *XVII. On the effects of magnetism upon the dimensions of iron and steel bars*, Philosophical Magazine Series 3, **30**, 76–87 (1847).

[231] Y. D. B. V. I. Arkhipenko and V. G. Bashtovoi, *Shape of a drop of magnetized fluid in a homogeneous magnetic field*, Magnetohydrodynamics, **14**, 373–376 (1978).

[232] J. Bacri and D. Salin, *Instability of ferrofluid magnetic drops under magnetic field*, J. Physique Lett., **43**, 649–654 (1982).

[233] S. Afkhami, A. J. Tyler, Y. Renardy, M. Renardy, T. G. St. Pierre, R. C. Woodward and J. S. Riffle, *Deformation of a hydrophobic ferrofluid droplet suspended in a viscous medium under uniform magnetic fields*, Journal of Fluid Mechanics, **663**, 358–384 (2010).

[234] J. A. Stratton, *Electromagnetic Theory*, Wiley-IEEE Press (2007).

[235] A. F. Pshenichnikov and A. V. Lebedev, *Low-temperature susceptibility of concentrated magnetic fluids*, The Journal of Chemical Physics, **121**, 5455–5467 (2004).

[236] A. Lebedev, *Dipole interparticle interaction in magnetic fluids*, Colloid Journal, **76**, 334–341 (2014).

[237] T. Jamin, C. Py and E. Falcon, *Instability of the Origami of a Ferrofluid Drop in a Magnetic Field*, Phys. Rev. Lett., **107**, 204503 (2011).

[238] G.-P. Zhu, N.-T. Nguyen, R. V. Ramanujan and X.-Y. Huang, *Nonlinear Deformation of a Ferrofluid Droplet in a Uniform Magnetic Field*, Langmuir, **27**, 14834–14841 (2011).

[239] J. V. I. Timonen, M. Latikka, L. Leibler, R. H. A. Ras and O. Ikkala, *Switchable Static and Dynamic Self-Assembly of Magnetic Droplets on Superhydrophobic Surfaces*, Science, **341**, 253–257 (2013).

[240] L. Landau, *On the theory of superfluidity of Helium II*, J. Phys. (USSR), **11**, 91–92 (1947).

[241] M.-O. Mewes, M. R. Andrews, N. J. van Druten, D. M. Kurn, D. S. Durfee, C. G. Townsend and W. Ketterle, *Collective Excitations of a Bose-Einstein Condensate in a Magnetic Trap*, Phys. Rev. Lett., **77**, 988–991 (1996).

[242] J. Steinhauer, R. Ozeri, N. Katz and N. Davidson, *Excitation Spectrum of a Bose-Einstein Condensate*, Phys. Rev. Lett., **88**, 120407 (2002).

[243] F. Zambelli, L. Pitaevskii, D. M. Stamper-Kurn and S. Stringari, *Dynamic structure factor and momentum distribution of a trapped Bose gas*, Phys. Rev. A, **61**, 063608 (2000).

[244] J. Stenger, S. Inouye, A. P. Chikkatur, D. M. Stamper-Kurn, D. E. Pritchard and W. Ketterle, *Bragg Spectroscopy of a Bose-Einstein Condensate*, Phys. Rev. Lett., **82**, 4569–4573 (1999).

[245] D. M. Stamper-Kurn, A. P. Chikkatur, A. Görlitz, S. Inouye, S. Gupta, D. E. Pritchard and W. Ketterle, *Excitation of Phonons in a Bose-Einstein Condensate by Light Scattering*, Phys. Rev. Lett., **83**, 2876–2879 (1999).

[246] J. D. Parsons, *Sound velocity in a magnetic fluid*, Journal of Physics D: Applied Physics, **8**, 1219 (1975).

[247] D. Y. Chung and W. E. Isler, *Ultrasonic velocity anisotropy in ferrofluids under the influence of a magnetic field*, Journal of Applied Physics, **49**, 1809–1811 (1978).

[248] S. Taketomi, *The Anisotropy of the Sound Attenuation in Magnetic Fluid under an External Magnetic Field*, Journal of the Physical Society of Japan, **55**, 838–844 (1986).

[249] V. Polunin, *Acoustics of Nanodispersed Magnetic Fluids*, CRC Press (2015).

[250] U. R. Fischer, *Stability of quasi-two-dimensional Bose-Einstein condensates with dominant dipole-dipole interactions*, Phys. Rev. A, **73**, 031602 (2006).

[251] M. Klawunn and L. Santos, *Hybrid multisite excitations in dipolar condensates in optical lattices*, Phys. Rev. A, **80**, 013611 (2009).

[252] R. P. Feynman, *Atomic Theory of the Two-Fluid Model of Liquid Helium*, Phys. Rev., **94**, 262–277 (1954).

[253] H. Saito, Y. Kawaguchi and M. Ueda, *Ferrofluidity in a Two-Component Dipolar Bose-Einstein Condensate*, Phys. Rev. Lett., **102**, 230403 (2009).

[254] R. M. Wilson, S. Ronen and J. L. Bohn, *Angular collapse of dipolar Bose-Einstein condensates*, Phys. Rev. A, **80**, 023614 (2009).

[255] R. M. Wilson, S. Ronen, J. L. Bohn and H. Pu, *Manifestations of the Roton Mode in Dipolar Bose-Einstein Condensates*, Phys. Rev. Lett., **100**, 245302 (2008).

[256] P. B. Blakie, D. Baillie and R. N. Bisset, *Roton spectroscopy in a harmonically trapped dipolar Bose-Einstein condensate*, Phys. Rev. A, **86**, 021604 (2012).

[257] M. Jona-Lasinio, K. Łakomy and L. Santos, *Roton confinement in trapped dipolar Bose-Einstein condensates*, Phys. Rev. A, **88**, 013619 (2013).

[258] D. H. J. O'Dell, S. Giovanazzi and C. Eberlein, *Exact Hydrodynamics of a Trapped Dipolar Bose-Einstein Condensate*, Phys. Rev. Lett., **92**, 250401 (2004).

[259] C. Eberlein, S. Giovanazzi and D. H. J. O'Dell, *Exact solution of the Thomas-Fermi equation for a trapped Bose-Einstein condensate with dipole-dipole interactions*, Phys. Rev. A, **71**, 033618 (2005).

[260] S. Giovanazzi, A. Görlitz and T. Pfau, *Tuning the Dipolar Interaction in Quantum Gases*, Phys. Rev. Lett., **89**, 130401 (2002).

[261] N. G. Parker and D. H. J. O'Dell, *Thomas-Fermi versus one- and two-dimensional regimes of a trapped dipolar Bose-Einstein condensate*, Phys. Rev. A, **78**, 041601 (2008).

[262] J. L. Bohn, R. M. Wilson and S. Ronen, *How does a dipolar Bose-Einstein condensate collapse?*, Laser Physics, **19**, 547–549 (2009).

[263] H. P. Büchler, E. Demler, M. Lukin, A. Micheli, N. Prokof'ev, G. Pupillo and P. Zoller, *Strongly Correlated 2D Quantum Phases with Cold Polar Molecules: Controlling the Shape of the Interaction Potential*, Phys. Rev. Lett., **98**, 060404 (2007).

[264] J. Söding, D. Guéry-Odelin, P. Desbiolles, F. Chevy, H. Inamori and J. Dalibard, *Three-body decay of a rubidium Bose–Einstein condensate*, Applied Physics B, **69**, 257–261 (2014).

[265] A. F. Andreev and I. M. Lifshitz, *Quantum Theory of Defects in Crystals*, Sov. Phys. JETP, **29**, 1107–1113 (1969).

[266] G. V. Chester, *Speculations on Bose-Einstein Condensation and Quantum Crystals*, Phys. Rev. A, **2**, 256–258 (1970).

[267] A. J. Leggett, *Can a Solid Be "Superfluid"?*, Phys. Rev. Lett., **25**, 1543–1546 (1970).

[268] M. Boninsegni and N. V. Prokof'ev, *Colloquium: Supersolids: What and where are they?*, Rev. Mod. Phys., **84**, 759–776 (2012).

[269] E. Kim and M. H. W. Chan, *Probable observation of a supersolid helium phase*, Nature, **427**, 225–227 (2004).

[270] E. Kim and M. H. W. Chan, *Observation of Superflow in Solid Helium*, Science, **305**, 1941–1944 (2004).

[271] D. Y. Kim and M. H. W. Chan, *Absence of Supersolidity in Solid Helium in Porous Vycor Glass*, Phys. Rev. Lett., **109**, 155301 (2012).

[272] M. D. Lukin, M. Fleischhauer, R. Cote, L. M. Duan, D. Jaksch, J. I. Cirac and P. Zoller, *Dipole Blockade and Quantum Information Processing in Mesoscopic Atomic Ensembles*, Phys. Rev. Lett., **87**, 037901 (2001).

[273] N. Henkel, R. Nath and T. Pohl, *Three-Dimensional Roton Excitations and Supersolid Formation in Rydberg-Excited Bose-Einstein Condensates*, Phys. Rev. Lett., **104**, 195302 (2010).

[274] F. Cinti, P. Jain, M. Boninsegni, A. Micheli, P. Zoller and G. Pupillo, *Supersolid Droplet Crystal in a Dipole-Blockaded Gas*, Phys. Rev. Lett., **105**, 135301 (2010).

[275] G. E. Astrakharchik, J. Boronat, I. L. Kurbakov and Y. E. Lozovik, *Quantum Phase Transition in a Two-Dimensional System of Dipoles*, Phys. Rev. Lett., **98**, 060405 (2007).

[276] S. Komineas and N. R. Cooper, *Vortex lattices in Bose-Einstein condensates with dipolar interactions beyond the weak-interaction limit*, Phys. Rev. A, **75**, 023623 (2007).

[277] K.-T. Xi and H. Saito, *Droplet formation in a Bose-Einstein condensate with strong dipole-dipole interaction*, Phys. Rev. A, **93**, 011604 (2016).

[278] R. N. Bisset and P. B. Blakie, *Crystallization of a dilute atomic dipolar condensate*, Phys. Rev. A, **92**, 061603 (2015).

[279] W. Lenz, *Die Wellenfunktion und Geschwindigkeitsverteilung des entarteten Gases*, Zeitschrift für Physik, **56**, 778–789 (1929).

[280] T. D. Lee and C. N. Yang, *Many-Body Problem in Quantum Mechanics and Quantum Statistical Mechanics*, Phys. Rev., **105**, 1119–1120 (1957).

[281] T. D. Lee, K. Huang and C. N. Yang, *Eigenvalues and Eigenfunctions of a Bose System of Hard Spheres and Its Low-Temperature Properties*, Phys. Rev., **106**, 1135–1145 (1957).

[282] T. T. Wu, *Ground State of a Bose System of Hard Spheres*, Phys. Rev., **115**, 1390–1404 (1959).

[283] N. M. Hugenholtz and D. Pines, *Ground-State Energy and Excitation Spectrum of a System of Interacting Bosons*, Phys. Rev., **116**, 489–506 (1959).

[284] K. Sawada, *Ground-State Energy of Bose-Einstein Gas with Repulsive Interaction*, Phys. Rev., **116**, 1344–1358 (1959).

[285] E. Braaten and A. Nieto, *Quantum corrections to the energy density of a homogeneous Bose gas*, The European Physical Journal B - Condensed Matter and Complex Systems, **11**, 143–159 (2012).

[286] T. Köhler, *Three-Body Problem in a Dilute Bose-Einstein Condensate*, Phys. Rev. Lett., **89**, 210404 (2002).

[287] R. Schützhold, M. Uhlmann, Y. Xu and U. R. Fischer, *Mean-Field expansion in Bose-Einstein condensates with finite-range interactions*, International Journal of Modern Physics B, **20**, 3555–3565 (2006).

[288] E. Braaten and A. Nieto, *Quantum corrections to the ground state of a trapped Bose-Einstein condensate*, Phys. Rev. B, **56**, 14745–14765 (1997).

[289] D. Blume and C. H. Greene, *Quantum corrections to the ground-state energy of a trapped Bose-Einstein condensate: A diffusion Monte Carlo calculation*, Phys. Rev. A, **63**, 063601 (2001).

[290] A. R. P. Lima and A. Pelster, *Quantum fluctuations in dipolar Bose gases*, Phys. Rev. A, **84**, 041604 (2011).

[291] A. R. P. Lima and A. Pelster, *Beyond mean-field low-lying excitations of dipolar Bose gases*, Phys. Rev. A, **86**, 063609 (2012).

[292] H. Bateman, *Higher transcendental functions. Volume I*, McGraw-Hill Book Company, New-York, Toronto, London (1953).

[293] A. Altmeyer, S. Riedl, C. Kohstall, M. J. Wright, R. Geursen, M. Bartenstein, C. Chin, J. H. Denschlag and R. Grimm, *Precision Measurements of Collective Oscillations in the BEC-BCS Crossover*, Phys. Rev. Lett., **98**, 040401 (2007).

[294] Y. Shin, A. Schirotzek, C. H. Schunck and W. Ketterle, *Realization of a Strongly Interacting Bose-Fermi Mixture from a Two-Component Fermi Gas*, Phys. Rev. Lett., **101**, 070404 (2008).

[295] N. Navon, S. Nascimbène, F. Chevy and C. Salomon, *The Equation of State of a Low-Temperature Fermi Gas with Tunable Interactions*, Science, **328**, 729–732 (2010).

[296] N. Navon, S. Piatecki, K. Günter, B. Rem, T. C. Nguyen, F. Chevy, W. Krauth and C. Salomon, *Dynamics and Thermodynamics of the Low-Temperature Strongly Interacting Bose Gas*, Phys. Rev. Lett., **107**, 135301 (2011).

[297] S. B. Papp, J. M. Pino, R. J. Wild, S. Ronen, C. E. Wieman, D. S. Jin and E. A. Cornell, *Bragg Spectroscopy of a Strongly Interacting* $^{85}$Rb *Bose-Einstein Condensate*, Phys. Rev. Lett., **101**, 135301 (2008).

[298] D. S. Petrov, *Quantum Mechanical Stabilization of a Collapsing Bose-Bose Mixture*, Phys. Rev. Lett., **115**, 155302 (2015).

[299] F. Wächtler and L. Santos, *Quantum filaments in dipolar Bose-Einstein condensates*, arXiv:1601.04501 (2016).

[300] H. Saito, *Path-Integral Monte Carlo Study on a Droplet of a Dipolar Bose–Einstein Condensate Stabilized by Quantum Fluctuation*, Journal of the Physical Society of Japan, **85**, 053001 (2016).

[301] P. B. Blakie, *Properties of a dipolar condensate with three-body interactions*, Phys. Rev. A, **93**, 033644 (2016).

[302] A. Gammal, T. Frederico, L. Tomio and P. Chomaz, *Liquid-gas phase transition in Bose-Einstein condensates with time evolution*, Phys. Rev. A, **61**, 051602 (2000).

[303] A. Gammal, T. Frederico, L. Tomio and P. Chomaz, *Atomic Bose-Einstein condensation with three-body interactions and collective excitations*, Journal of Physics B: Atomic, Molecular and Optical Physics, **33**, 4053 (2000).

[304] A. Bulgac, *Dilute Quantum Droplets*, Phys. Rev. Lett., **89**, 050402 (2002).

[305] F. Dalfovo, A. Lastri, L. Pricaupenko, S. Stringari and J. Treiner, *Structural and dynamical properties of superfluid helium: A density-functional approach*, Phys. Rev. B, **52**, 1193–1209 (1995).

[306] M. Bender, P.-H. Heenen and P.-G. Reinhard, *Self-consistent mean-field models for nuclear structure*, Rev. Mod. Phys., **75**, 121–180 (2003).

[307] K. E. Strecker, G. B. Partridge, A. G. Truscott and R. G. Hulet, *Formation and propagation of matter-wave soliton trains*, Nature, **417**, 150–153 (2002).

[308] L. Khaykovich, F. Schreck, G. Ferrari, T. Bourdel, J. Cubizolles, L. D. Carr, Y. Castin and C. Salomon, *Formation of a Matter-Wave Bright Soliton*, Science, **296**, 1290–1293 (2002).

[309] U. Al Khawaja, H. T. C. Stoof, R. G. Hulet, K. E. Strecker and G. B. Partridge, *Bright Soliton Trains of Trapped Bose-Einstein Condensates*, Phys. Rev. Lett., **89**, 200404 (2002).

[310] J. H. V. Nguyen, P. Dyke, D. Luo, B. A. Malomed and R. G. Hulet, *Collisions of matter-wave solitons*, Nat Phys, **10**, 918–922 (2014).

[311] P. Pedri and L. Santos, *Two-Dimensional Bright Solitons in Dipolar Bose-Einstein Condensates*, Phys. Rev. Lett., **95**, 200404 (2005).

[312] I. Tikhonenkov, B. A. Malomed and A. Vardi, *Anisotropic Solitons in Dipolar Bose-Einstein Condensates*, Phys. Rev. Lett., **100**, 090406 (2008).

[313] R. Richter and I. V. Barashenkov, *Two-Dimensional Solitons on the Surface of Magnetic Fluids*, Phys. Rev. Lett., **94**, 184503 (2005).

[314] M. J. Holland, D. S. Jin, M. L. Chiofalo and J. Cooper, *Emergence of Interaction Effects in Bose-Einstein Condensation*, Phys. Rev. Lett., **78**, 3801–3805 (1997).

[315] T. Lahaye, T. Pfau and L. Santos, *Mesoscopic Ensembles of Polar Bosons in Triple-Well Potentials*, Phys. Rev. Lett., **104**, 170404 (2010).

[316] D. Peter, K. Pawłowski, T. Pfau and K. Rzążewski, *Mean-field description of dipolar bosons in triple-well potentials*, Journal of Physics B: Atomic, Molecular and Optical Physics, **45**, 225302 (2012).

[317] B. Chatterjee, I. Brouzos, L. Cao and P. Schmelcher, *Ultracold dipolar few-boson ensembles in a triple-well trap*, Journal of Physics B: Atomic, Molecular and Optical Physics, **46**, 085304 (2013).

[318] M. Abad, M. Guilleumas, R. Mayol, M. Pi and D. M. Jezek, *A dipolar self-induced bosonic Josephson junction*, EPL (Europhysics Letters), **94**, 10004 (2011).

[319] Y. Wang, J. P. D'Incao and C. H. Greene, *Efimov Effect for Three Interacting Bosonic Dipoles*, Phys. Rev. Lett., **106**, 233201 (2011).

[320] Y. Wang, J. P. D'Incao and C. H. Greene, *Universal Three-Body Physics for Fermionic Dipoles*, Phys. Rev. Lett., **107**, 233201 (2011).

[321] V. V. Volchkov, J. Rührig, T. Pfau and A. Griesmaier, *Efficient demagnetization cooling of atoms and its limits*, Phys. Rev. A, **89**, 043417 (2014).

[322] J. Rührig, T. Bäuerle, A. Griesmaier and T. Pfau, *High efficiency demagnetization cooling by suppression of light-assisted collisions*, Opt. Express, **23**, 5596–5606 (2015).

[323] M. Schmitt, E. A. L. Henn, J. Billy, H. Kadau, T. Maier, A. Griesmaier and T. Pfau, *Spectroscopy of a narrow-line optical pumping transition in atomic dysprosium*, Opt. Lett., **38**, 637–639 (2013).

[324] K. Góral, K. Rzążewski and T. Pfau, *Bose-Einstein condensation with magnetic dipole-dipole forces*, Phys. Rev. A, **61**, 051601 (2000).

[325] J. Metz, *Collapse of dipolar Bose-Einstein condensates for different trap geometries*, Ph.D. thesis, Universität Stuttgart (2010).

[326] S. Müller, *Stability and Collapse Dynamics of Dipolar Bose-Einstein Condensates in One-Dimensional Optical Lattices*, Ph.D. thesis, Universität Stuttgart (2012).

# Danksagung

Der erste Dank geht an Prof. Dr. Tilman Pfau, der mich bereits Ende 2009 innerhalb eines Hauptseminars für den Forschungsbereich der ultrakalten Atome begeistern konnte. Bereits während meiner Diplomarbeit habe ich deine Begeisterung für das Quantenverhalten von Atomen bewundert. Besonders deine Unermüdlichkeit half in schweren Zeiten weiter, wenn das Experiment nicht vorankam und hat zu neuen Lösungswegen geführt. Vielen Dank für die Möglichkeit in die verwirrende Quantenwelt eintauchen zu können.

Ich danke auch Prof. Dr. Hans Peter Büchler für die Übernahme des Prüfungsvorsitzes und hilfreiche Diskussionen um unsere Ergebnisse besser verstehen zu können. Außerdem danke ich Prof. Dr. Martin Dressel für die Übernahme des Mitberichts.

Grundlegendes Wissen über Elektronik, Optik und kalte Atome konnte ich bereits während meiner Diplomarbeit von Stefan Müller lernen. Deine große Motivation für die Forschung, das auch einen hohen zeitlichen Aufwand mit sich bringt, ist auf mich übergegangen und hat meinen Entschluss gefestigt meine Dissertation zu beginnen. Ebenso danke ich Juliette Billy und Emanuel Henn für die Betreuung meiner Diplomarbeit und die Hilfe bei der Planung für das neue Dysprosiumexperiment. Eine weitere wichtige Person in meinen ersten Jahren war Axel Griesmaier. Mit deinem außerordentlichen Wissen und langjähriger Erfahrung warst du die erste Ansprechperson bei kleineren und größeren Schwierigkeiten.

Ein ganz besonderer Dank geht an Thomas Maier, der mit mir über 4 Jahre hinweg die Maschine zum Laufen gebracht hat. Deine Tatkraft und dein Fleiß waren unentbehrlich für die Entwicklung und den Erfolg unserer Experimente. Ohne deinen täglichen Ansporn ('Schaff mer was') hätte unsere gemeinsame Reise in der Quantenwelt noch länger angedauert.

Auf dieser Reise in der Quantenwelt haben uns auch Matthias Schmitt und Matthias Wenzel begleitet. Ihr habt beide sehr erfolgreiche Masterarbeiten durchgeführt, die unser Experiment deutlich vorangebracht haben. Vielen Dank für eure Mithilfe und eure positive Stimmung. Nun dürft ihr unsere Dysprosiummaschine an seine Grenzen führen. Ich wünsche euch zügige und interessante wissenschaftliche Erfolge.

Außerdem danke ich den ganzen Bachelor-, Diplom- und Master-Studenten, die ich betreut habe: Micha Schilling, Simon Ristok, Bernd Docters, Nicolas Zuber, Matthias Feldmaier, Isabel Reis, Niklas Uhl, Michaela Nickel und Clarissa Wink. Ihr alle habt zum Fortschritt des Experiments beigetragen und meinen Dank verdient.

Obwohl unser Gruppenleiter Igor Ferrier-Barbut das neueste Mitglied am Experiment ist, ist er doch derjenige mit dem größten physikalischen Wissen. Dieses hast du auch für uns eingesetzt um unsere Experimente zu deuten und in eine vielversprechende Richtung zu lenken. Ich wünsche dir eine erfolgreiche Zukunft in der Wissenschaft.

Auch danke ich den anderen Gruppenleitern Harald Kübler, Robert Löw und Sebastian Hofferberth. Ihr habt mir mit eurem technischen und wissenschaftlichen Wissen in vielen Situationen weiterhelfen können.

Kein Experiment an unserem Institut würde existieren, wenn unsere Finanzen nicht ordentlich verwaltet werden. Im Laufe meiner Dissertation haben sich darum Beatrice Olgun-Lichtenberg, Karin Hauff, Astrid Buck, Oliver Nagel, Nadine Prellwitz, Britta Lenz, Katrin Maier und Karin Otter gekümmert. Vielen Dank für das Verwalten der Finanzen, das Organisieren von Tagungen und Vorträgen und den täglichen Postverkehr.

Natürlich haben auch alle anderen am Institut ihren Beitrag für die gute Stimmung in unseren Arbeitsgruppen geleistet. Ich denke gerne an unsere gemeinsamen Frühstücke, Mittagspausen, Kaffeepausen und das wohlverdiente Bier am Abend zurück.

Meine gesamte Studienzeit wäre nicht dieselbe gewesen ohne ganz besondere Kommilitonen. Vielen Dank an Fabian Hargart, David Peter, Andreas Wünsch, Sebastian Zaiser, Mathias Eichler und Patrick Herlinger für die unzähligen Brett- und Kartenspiele und viele andere Erinnerungen.

Ich danke auch meinen Eltern für die Unterstützung während meiner Dissertation. Ihr hattet immer Verständnis für mein Studium und meine Doktorarbeit, so dass ich die Freiheit hatte meinen Wünschen nachgehen zu können. Vielen Dank auch an meine Geschwister und Freunde für die nicht wissenschaftlichen Gespräche.

Zu guter Letzt ein ganz großes Dankeschön an meine Frau Alexandra. Du hast es die letzten Jahre immer ertragen, wenn es bei mir wieder später wurde. Vielen Dank, dass du mir während dieser Zeit vieles abgenommen hast und für die gemeinsame Zeit ohne Physik.